Universidad de Oviedo

Programa de Doctorado en Análisis Químico, Bioquímico y Estructural y Modelización Computacional

TESIS DOCTORAL

Síntesis Fotoasistida de Materiales de Carbono Nanoporosos

Photoassisted Synthesis of Nanoporous Carbon Materials

MARÍA COCINA FERNÁNDEZ DE CÓRDOBA

AÑO 2021

RESUMEN DEL CONTENIDO DE TESIS DOCTORAL

1.- Título de la Tesis	
Español/Otro Idioma (Francés): **Síntesis Fotoasistida de Materiales de Carbono Nanoporosos / Synthèse de matériaux carbonés nanoporeux**	Inglés: **Photoassisted Synthesis of Nanoporous Carbon Materials**

2.- Autor	
Nombre: **María Cocina Fernández de Córdoba**	DNI/Pasaporte/NIE: 3
Programa de Doctorado: **Análisis Químico, Bioquímico y Estructural y Modelización Computacional**	
Órgano responsable: **Centro Internacional de Postgrado (CIP)**	

RESUMEN (en español)

El objetivo principal de esta tesis fue explorar la posibilidad de utilizar reacciones fotoasistidas para preparar carbones porosos y nanohíbridos de metal/carbono. Así, se implementó la policondensación fotoinducida por UV para fijar las estructuras autoorganizadas formadas por ciertos polifenoles, que son capaces de atrapar nanopartículas metálicas de Ag o Au. La pirólisis de estos precursores orgánicos abre el camino a materiales híbridos nanoporosos con propiedades texturales y fisicoquímicas controladas. Mediante la elección adecuada del precursor orgánico y de los parámetros de síntesis, fue posible controlar la morfología, el orden estructural y la distribución del tamaño de los poros de los materiales de carbono finales en toda la gama micro/mesoporosa.

El grado de reticulación de la resina fotopolimerizada se determinó por la estructura (lineal, cíclica), así como por el número de posiciones reactivas en los precursores orgánicos (es decir, las posiciones ortosustituidas o parasustituidas de las moléculas de los grupos hidroxilo y aldehído). Así, la estructura lineal del bisfenol A, por ejemplo, dio lugar a grupos muy ramificados que curan para formar la resina de tipo fenólico en una estructura con una porosidad densa compuesta principalmente por microporos estrechos. Por otro lado, los precursores orgánicos aromáticos son capaces de ensamblarse en grandes racimos reticulados, creando una estructura más abierta.

La incorporación de iones metálicos (Au3+, Ag+) durante el proceso de un solo paso permitió la policondensación fotoasistida simultánea de las unidades fenólicas y la fotorreducción de los iones metálicos dando lugar a nanopartículas metálicas. Los materiales resultantes contienen nanopartículas metálicas altamente dispersas en la matriz de carbono, lo que induce ligeros cambios en la porosidad, principalmente en el volumen de los poros y especialmente en el tamaño medio de los mesoporos.

También se llevaron a cabo caracterizaciones morfológicas, texturales y fisicoquímicas de los nuevos nanomateriales de carbono y de los híbridos metal/carbono para evaluar la influencia de los parámetros sintéticos en los materiales resultantes.

Esta técnica fotoasistida, rápida, sencilla y económica, abre interesantes perspectivas en la síntesis de carbones porosos y materiales híbridos que podrían utilizarse, por ejemplo, como fotocatalizadores en el tratamiento de aguas residuales y en procesos de oxidación avanzada.

Universidad de Oviedo
Universidá d'Uviéu
University of Oviedo

RESUMEN (en Inglés)

The main objective of this thesis was to explore the possibility of using photo-assisted reactions to prepare porous carbons and metal/carbon nanohybrids. Thus, UV photoinduced polycondensation was implemented to freeze the auto-organized structures formed by certain polyphenols, which are capable of trapping Ag or Au metal nanoparticles. The pyrolysis of these organic precursors opens the way to nanoporous hybrid materials with controlled textural and physicochemical properties.

By appropriate choice of the organic precursor and synthesis parameters, it was possible to control the morphology, structural order, and pore size distribution of the final carbon materials throughout the micro/mesoporous range. The degree of crosslinking of the photopolymerized resin was determined by the structure (linear, cyclic) as well as the number of reactive positions in the organic precursors (i.e., the ortho- or para-substituted positions of the hydroxyl and aldehyde group moieties). Thus, the linear structure of bisphenol A, for example, resulted in highly branched clusters that cure to form the phenol-type resin in a structure with dense porosity composed primarily of narrow micropores. On the other hand, aromatic precursors are able to assemble into large crosslinked clusters, creating a more open structure.

The incorporation of metal ions (Au^{3+}, Ag^+) during the one-pot process allowed the simultaneous photoassisted polycondensation of phenolic units and photoreduction of metal ions yielding metal nanoparticles. The resulting materials contain highly dispersed metal nanoparticles in the carbon matrix, which induces slight changes in porosity, mainly in pore volume and especially in the average mesopore size.

Morphological, textural and physicochemical characterizations of the new carbon and metal/carbon hybrid nanomaterials were also carried out in order to assess the influence of synthetic parameters on the resulting materials.

This fast, simple and cost-effective photoassisted approach opens up interesting prospects in the synthesis of porous carbons and hybrid materials that could be used, for example, as photocatalysts in wastewater treatment and advanced oxidation processes.

SR. PRESIDENTE DE LA COMISIÓN ACADÉMICA DEL PROGRAMA DE DOCTORADO
EN *Análisis Químico Bioquímico y Estructural y Modelización Computacional*

THÈSE présentée par

MARÍA COCINA FERNÁNDEZ DE CÓRDOBA

Soutenance prévue Septembre 2021

pour obtenir le grade de:

Docteur de l'Université De Haute Alsace et de L'Universidad de Oviedo

Discipline/ Spécialité: Chimie de Materiaux

Synthèse de matériaux carbonés nanoporeux Photoassisted Synthesis of Nanoporous Carbon Materials

THÈSE dirigée par :

Mme OVÍN ANIA María Concepción	Investigador Científico, CSIC, Spain & Directeur de recherche, CNRS, France
Mme BALAN Lavinia	Directeur de recherche, CNRS, France

RAPPORTEURS :

M. SILVESTRE ALBERO Joaquin	Professeur, Universidad de Alicante, Espagne
Mme. DIAS MESTRE Ana Sofia,	Assistant Researcher, Universidade de Lisboa, Portugal

JURY :

Mme TROBAJO FERNANDEZ Camino	Professeur, Universidad de Oviedo, Espagne
M. SILVESTRE ALBERO Joaquin	Professeur, Universidad de Alicante, Espagne
Mme. DIAS MESTRE Ana Sofia	Assistant Researcher, Universidade de Lisboa, Portugal
Mme OVÍN ANIA María Concepción	Investigador Científico, CSIC, Spain & Directeur de recherche, CNRS, France
Mme BALAN Lavinia	Directeur de recherche, CNRS, France

"The real voyage of discovery consists not only in seeking new landscapes,

but in having new eyes."

Marcel Proust

A mis padres y hermanos

Acknowledgements

As well I am grateful for the welcome I was given by my colleagues at the IS2M. Mariam, Justine, Marine, Mohamed, Étienne and especially to Leïla and Hoang already my friends.

Thanks to Dr. Parra, por todos los mensajes de ánimo durante estos años ya fuera del INCAR.

I would also like to specially thank the NaFMAT members during my stay. Cristina, Alicia, Ana, Edurne, Eder, Getaneh, Mariví, etc. Some of you have become closer friends. Gracias! (Getaneh I know you understand) Thank you for you scientific and personal support all these years. Cristina! recuerda tenemos muchos planes pendientes, gracias por tooodo el apoyo estos años. Alicia, Ana se os echa de menos.

Outside of the research I could not have had such a great time without the people I was lucky to meet. Andrea, que alegría conocernos! Ricmari, te a-do-ro! espero verte pronto de nuevo. Andrea, por todos los buenos momentos y aventuras compartidas, por intentar hacerme ver la vida desde otro ángulo... ya me dirás a cuánto asciende la factura de psi toupeira.

To Rémy, thank you *u*. Thank you for having endured my "worst motivation" moments... and having helped me out of them ~~without cyanide~~. I've been lucky and very happy to count on you. P.S. remind me to renew the subscription ;p

Gracias a mis amigos de antes y de siempre. Alba (amore!!), Ana (mi rubia<3), Pedro, gracias por seguir a mi lado a pesar del tiempo y la distancia. Cuánto os echo de menos! Javier, gracias por saber que siempre cuento con tu apoyo, 24/7...dónde quiera que esté, donde quiera que estés... gracias se queda corto.

A la familia, Inmaculada (me muero de ganas de verte), María, Fran, gracias por estar a mi lado, siempre pendientes.

Por último agradecer muy en especial a mis padres y a mis hermanos. Gracias por apoyarme, por todo el amor, la paciencia! por creer en mí, y renovar mis fuerzas.

Table of contents

Table of contents

List of symbols and abbreviations

2D-NLDFT	Two dimensional- non local density functional theory
aka	As known as
BA	Bisphenol A
BET	Brunauer-Emmett-Teller
ca.	Circa, from Latin "around, about, approximately"
CBET	BET constant
CDC	Carbide derived carbons
Ch	Chromophore
CP	Cross Polarization
CP-MAS	Cross Polarization- magic angle spinning
CT	Catechol
cte	Constant
CVD	Chemical vapour deposition
DN	Dihydroxynaphthalene
e.g.	Exempli gratia, from Latin "for example"
EISA	Evaporation induced self-assembly
EtOH	Ethanol
F	Formaldehyde
GA	Gallacetophenone or 2',3',4' trihydroxybenzophenone
H	Enthalpy (refer to bond energy)
hpdec	High power decoupling pulse program
hpdec-MAS	High power decoupling pulse program- magic angle spinning
HS	Heterogeneous surface
HTC	Hydrothermal carbonization
i.e.	Id est, from Latin "that is"
IR	Infrared
IUPAC	International Union of Pure and Applied Chemistry
L	Micropores size
MAS	Magic Angle Spinning
MOFs	Metal-organic framework
MT	Mimosa tannin
NMR	Nuclear magnetic resonance

List of symbols and abbreviations

NPs	nanoparticles
OMC	Ordered mesoporous carbons
p	Pressure
p/p0	Relative pressure
p0	Gas saturated equilibrium vapour pressure
PG	Pyrogallol
PGA	Pyrogallol-4-carboxylic acid or 2',3',4' trihydroxybenzoic acid
PH	Phenol
ppm	Parts per million
PSD	Pore size distribution
PZC	Point zero charge
R	Resorcinol
r.t.	Room temperature
R-F	Resorcinol- formaldehyde
rpm	Revolutions per minute
RS	Resorcinol
SS	Simulated Solar light
SSA	Specific surface area
T	Temperature
t	Time
TEM	Transmission electron microscopy
THBA	2',4',6' trihydroxybenzoic acid
THF	Tetrahydrofurane
TMS	Tetramethylsilane
TNA	Tannic acid
UV	Ultraviolet
vis	Visible
Vmeso	Mesopore volume
Vmicro	Micropore volume
Vmicro N_2	Micropore volume (DR equation) applied to N2 adsorption
Vt	Volume of titrant
V_{Total}	Total pore volume
W	Volume occupied by adsorbed phase (DR equation)
W_0	Micropore volume (DR equation) applied CO2 adsorption

wt	Weight
x	Relative pressure p/p0
XPS	X-ray photoelectron spectrometry
XRD	X-Ray Diffraction
ZTC	Zeolite template carbons

List of Figures

List of Tables

List of Tables

Layout

This thesis fulfilled all the requirements for obtaining doctor of philosophy in chemistry according to the regulation of the doctoral Program Análisis Químico, Bioquímico y Estructural y Modelización Computacional of Departamento de Química Física y Analítica at Universidad de Oviedo (Spain), and the doctoral school Physique et chimie-physique (ED 182) at Université de Haute Alsace (Mulhouse, France) in the framework of an international joint PhD agreement (convention de cotutelle internationale) between both universities. According to this agreement, and as a mean of broadening its diffusion in the scientific field, the English language is used throughout the text, and the defense will also be carried out in English. To facilitate the diffusion of the PhD thesis in the official languages of both Universities, abstracts summarizing the content of the manuscript will also be provided in Spanish and French.

The PhD was funded by project PHOROSOL (ERC-Consolidator Grant 648161) and the research has been performed at Instituto de Ciencia y Tecnología del Carbono (INCAR, CSIC) in Oviedo (Spain), CEMHTI (Conditions Extremes Materiaux: Haute Temperature et Irradiation) UPR 3079 of CNRS (Centre National de la Recherche Scientifique) in Orléans (France), and at Institut de Sciences de Materiaux de Mulhouse (UMR 7361) of CNRS in Mulhouse (France) as associated unit to Université de Haute Alsace, under the direction of Dr. Conchi Ania (Investigador Cientifico of CSIC and Directrice de Recherche of CNRS) and Dr. Lavinia Balan (Directrice de Recherche CNRS).

A scientific internship of 6 months was carried out at Unidad de Desarrollo Tecnológico (UDT) belonging to Universidad de Concepcion in Chile, under the supervision of Dr. Matos, to work on photocatalytic application of carbon-based semiconductors.

The thesis mainly focused on the use of photo-assisted polymerization reactions of different organic precursors for the preparation of nanoporous carbons and metal-decorated carbons with controlled textural and physicochemical properties. The thesis divided in six principal chapters. The first chapter provides an introduction on the fundamentals of the methods for the preparation of carbon material and the state of the art on photoassisted methods for the synthesis of materials, along with a description of the overall goal of the thesis and the specific objectives programmed for its achievement. The second chapter gives a detailed description of the materials used, the experimental procedures followed during the

research work, as well as the fundamentals of the characterization techniques. Chapters 3 to 6 compile the results and discussion of the thesis: chapter 3 focuses on demonstrating the feasibility of a novel photoinduced methodology for the preparation of porous carbons using a set of different polyhydroxylated benzenes as organic precursors, and on establishing a correlation between the functionalization of the precursor and the physicochemical properties of the prepared carbon materials. Chapter 4 focuses on exploring the impact of various chemical parameters (i.e. the use of HCl as catalyst, the presence of a photoinitiator, different reagents concentration) on the textural properties and surface chemistry of the developed carbon materials. To undertake such optimization study, gallacetophenone and pyrogallol were selected as precursors. Chapter 5 is devoted to evaluate the impact of further functionalization of the aromatic ring in the organic precursor (e.g., carboxylic acid, carbonyl moieties) in the photoassisted polycondensation reaction and the physicochemical features of the carbons. Chapter 6 focuses on demonstrating the possibility of carrying out the simultaneous photoinduced polycondensation reaction of a precursor's mixture with the photoreduction of a metallic precursor, leading to materials with well-developed textural features and dispersion of metallic nanoparticles.

Finally, chapter 7 provides a summary of the main findings of the work, along with a vision of the perspectives generated from this PhD thesis, with specific details on the ongoing and future work.

Resumen

El objetivo principal de esta tesis fue explorar la posibilidad de utilizar reacciones fotoasistidas para preparar carbones porosos y nanohíbridos de metal/carbono. Así, se implementó la policondensación fotoinducida por UV para fijar las estructuras autoorganizadas formadas por ciertos polifenoles, que son capaces de atrapar nanopartículas metálicas de Ag o Au. La pirólisis de estos precursores orgánicos abre el camino a materiales híbridos nanoporosos con propiedades texturales y fisicoquímicas controladas.

Mediante la elección adecuada del precursor orgánico y de los parámetros de síntesis, fue posible controlar la morfología, el orden estructural y la distribución del tamaño de los poros de los materiales de carbono finales en toda la gama micro/mesoporosa. El grado de reticulación de la resina fotopolimerizada se determinó por la estructura (lineal, cíclica), así como por el número de posiciones reactivas en los precursores orgánicos (es decir, las posiciones ortosustituidas o parasustituidas de las moléculas de los grupos hidroxilo y aldehído). Así, la estructura lineal del bisfenol A, por ejemplo, dio lugar a grupos muy ramificados que curan para formar la resina de tipo fenólico en una estructura con una porosidad densa compuesta principalmente por microporos estrechos. Por otro lado, los precursores orgánicos aromáticos son capaces de ensamblarse en grandes racimos reticulados, creando una estructura más abierta.

La incorporación de iones metálicos (Au^{3+}, Ag^+) durante el proceso de un solo paso permitió la policondensación fotoasistida simultánea de las unidades fenólicas y la fotorreducción de los iones metálicos dando lugar a nanopartículas metálicas. Los materiales resultantes contienen nanopartículas metálicas altamente dispersas en la matriz de carbono, lo que induce ligeros cambios en la porosidad, principalmente en el volumen de los poros y especialmente en el tamaño medio de los mesoporos.

También se llevaron a cabo caracterizaciones morfológicas, texturales y fisicoquímicas de los nuevos nanomateriales de carbono y de los híbridos metal/carbono para evaluar la influencia de los parámetros sintéticos en los materiales resultantes.
Esta técnica fotoasistida, rápida, sencilla y económica, abre interesantes perspectivas en la síntesis de carbones porosos y materiales híbridos que podrían utilizarse, por ejemplo, como fotocatalizadores en el tratamiento de aguas residuales y en procesos de oxidación avanzada.

Résumé

L'objectif principal de cette thèse était d'explorer la possibilité d'utiliser des réactions photo-assistées pour préparer des carbones poreux et des nanohybrides métal/carbone. La polycondensation photoinduite par UV a ainsi, été mise en œuvre pour figer les structures auto-organisées formées par certains polyphénols, capables de piéger des nanoparticules métalliques d'Ag ou d'Au. La pyrolyse de ces précurseurs organiques ouvre la voie vers des matériaux hybrides nanoporeux aux propriétés texturales et physicochimiques contrôlées.

Par un choix approprié du précurseur organique et des paramètres de synthèse, il a été possible de contrôler la morphologie, l'ordre structurel et la distribution de taille des pores des matériaux carbonés finaux dans toute la gamme micro/mésoporeuse. Le degré de réticulation de la résine photopolymérisée est déterminé par la structure (linéaire, cyclique) ainsi que par le nombre de positions réactives dans les précurseurs organiques (c'est-à-dire les positions ortho- ou para-substituées par rapport aux groupes hydroxyle et aldéhyde). Ainsi, la structure linéaire du bisphénol A, par exemple, induit la formation d'amas hautement ramifiés qui durcissent pour former la résine de type phénol dans une structure à porosité dense composée principalement de micropores étroits. D'autre part, les précurseurs organiques aromatiques sont capables de s'assembler en grands clusters réticulés, créant ainsi une structure plus ouverte.

L'incorporation d'ions métalliques (Au^{3+}, Ag^+) au cours du processus "one-pot" a permis de réaliser simultanément la polycondensation photoassistée d'unités phénoliques et la photoréduction d'ions métalliques produisant des nanoparticules métalliques. Les matériaux obtenus contiennent des nanoparticules métalliques très dispersées dans la matrice de carbone, ce qui induit de légers changements dans la porosité, principalement dans le volume des pores et surtout dans la taille moyenne des mésopores.

Des caractérisations morphologiques, texturales et physicochimiques des nouveaux nanomatériaux en carbone et hybrides métal/carbone ont également été réalisées afin d'évaluer l'influence des paramètres de synthèse sur les matériaux obtenus.

Cette approche photoassistée rapide, simple et économique ouvre des perspectives intéressantes dans la synthèse de carbones poreux et de matériaux hybrides qui pourraient être utilisés, par exemple, comme photocatalyseurs dans le traitement des eaux usées et les processus d'oxydation avancés.

Résumé

Abstract

The main objective of this thesis was to explore the possibility of using photo-assisted reactions to prepare porous carbons and metal/carbon nanohybrids. Thus, UV photoinduced polycondensation was implemented to freeze the auto-organized structures formed by certain polyphenols, which are capable of trapping Ag or Au metal nanoparticles. The pyrolysis of these organic precursors opens the way to nanoporous hybrid materials with controlled textural and physicochemical properties.

By appropriate choice of the organic precursor and synthesis parameters, it was possible to control the morphology, structural order, and pore size distribution of the final carbon materials throughout the micro/mesoporous range. The degree of crosslinking of the photopolymerized resin was determined by the structure (linear, cyclic) as well as the number of reactive positions in the organic precursors (i.e., the *ortho-* or *para-*substituted positions of the hydroxyl and aldehyde group moieties). Thus, the linear structure of bisphenol A, for example, resulted in highly branched clusters that cure to form the phenol-type resin in a structure with dense porosity composed primarily of narrow micropores. On the other hand, aromatic organic precursors are able to assemble into large crosslinked clusters, creating a more open structure.

The incorporation of metal ions (Au^{3+}, Ag^+) during the one-pot process allowed the simultaneous photoassisted polycondensation of phenolic units and photoreduction of metal ions yielding metal nanoparticles. The resulting materials contain highly dispersed metal nanoparticles in the carbon matrix, which induces slight changes in porosity, mainly in pore volume and especially in the average mesopore size.

Morphological, textural and physicochemical characterizations of the new carbon and metal/carbon hybrid nanomaterials were also carried out in order to assess the influence of synthetic parameters on the resulting materials.

This fast, simple and cost-effective photoassisted approach opens up interesting prospects in the synthesis of porous carbons and hybrid materials that could be used, for example, as photocatalysts in wastewater treatment and advanced oxidation processes.

CHAPTER 1

Introduction

1.1 Synthesis of nanoporous carbons

Nanoporous carbons (aka activated carbons) are unique materials that have been extensively used in many specialized applications from gas adsorption and separation, environmental remediation, catalysis and energy storage [Marsh 2006]. Such variety of applications stems from the unique textural, electronic and physicochemical features, along with their ability to bind heteroatoms, leading to the development of multifunctional materials [Bandosz 2006; Stein 2009; Tascon 2012; Zhang 2015; Hesse 2015; Sheng 2014].

From a structural point of view, nanoporous carbons are composed of distorted graphene-like layers of sp^2 domains of carbon atoms also rich in defects (free edge sites), heteroatoms located at the edges (predominantly) or inserted in the basal-planes, and carbon atoms in sp3 configurations [Guo 2012]. The distorted graphene layers are stacked by weak Van der Waals forces either in an ordered or turbostratic structure with different degrees of planarity depending on the graphitization extent of the materials. Regarding porosity, nanoporous carbons can display a hierarchical pore structure and exist in 3D architectures reaching specific surface areas over 1000 m^2/g, and displaying a high fraction of pores of nanometric dimensions [Marsh 200; Bandosz 2006].

The preparation of activated carbons from charcoals is an ancient artwork, and extensive work has been done to enhance the porosity of the resulting carbon adsorbents by the use of different activating agents, the choice of precursors, the optimization of the activation conditions (temperature, heating rate, gas flow), and the usage of various impregnation methods (soaking, stirring). However, conventional activation methods for the synthesis of nanoporous carbons do not allow a precise control of the pore size and volume. Furthermore, the formation of pores is usually accompanied by significant mass loss (hence low overall yield) and high energy consumption. Thus, introducing a rational design and new approaches that allow to control the porosity at a nanometric scale has received much attention.

Most relevant methodologies to control the porosity in the synthesis of carbons are based on nanocasting techniques [Wang 2012; Lee 2006; Lu 2006; Chuenchom 2012], carbonization of metal–organic frameworks (MOFs) [Jiang 2011; Chaikittisilp 21013; Jin 2018], sol-gel polycondensation reactions [Pekala 1989; Al-Muhtaseb, S.A., 2003 Isaacs-Páez 2015; Rasines 2015], hydrothermal carbonization approaches [Titirici 2008; Hu 2010], or carbide-derived carbons [Gogotsi 2003; Yushin 2017].

Despite the interesting features of the carbons synthesized following these approaches, most of these methodologies would hardly adapt to large-scale fabrication processes due to the complexity of the long time and high energy consuming processes. Thus the open question still remains on

whether if the performance of such highly featured carbons with ad-hoc porous features can overcome the cost associated to the synthesis for a scale-up, hence granting their practical application.

In this PhD thesis we have explored a new concept for the preparation of such carbon materials with tunable nanopore structure in the nanometric range, consisting in the photoassisted polycondensation of different organic precursors in the presence of a non-ionic surfactant as a structural director. The obtained polymer resins were further carbonized to obtain the carbon materials. In this regard, the use of light has emerged as a powerful strategy in material's synthesis [Fouassier 1995], as it offer several advantages over conventional approaches such as a shorter time scale, and the versatility of precursors owing to the specificity of the light-assisted reactions. This would open the door to the upscaling of the fabrication process.

The flowing sections provide an overview on most widely used synthetic approaches for the preparation of activated carbons (covering conventional activations methods and new approaches) based on a rational material's design to control the porosity.

1.1.1 Conventional activation methods

Activated carbons are produced at industrial scale by so-called conventional activation methods (i.e., physical and chemical activation). Most processes start with a carbonization (pyrolysis) or an oxidation step of the precursor, followed by the exposure of the carbonized material to a reactive atmosphere in the presence of an activating agent that allows the development of a porous structure. The preparation of activated carbons from charcoals is an ancient artwork, and extensive work has been done to enhance the porosity of the resulting carbon adsorbents by the use of different activating agents, the choice of precursors, the optimization of the activation conditions (temperature, heating rate, gas flow), and the usage of various impregnation methods (soaking, stirring) [Marsh 2006].

a) Carbonization

Carbonization or pyrolysis involves the thermal transformation of a material to moderate/high temperatures in an inert atmosphere, with the purpose of eliminating most of the volatiles of the precursor. The residual solid obtained is a carbonaceous char, which is composed of carbon atoms arrangement in a cross-linked condensed aromatic structure in a random manner. The disorganized structure of the carbon atoms leaves interstices between the aromatic layers

(incipient porosity, eventually filled with the tars formed during the carbonization). A subsequent activation of the char enlarges the incipient porosity and creates new pores.

The temperature of the pyrolysis has an important effect in the development of the porosity. At low heating rates, the internal surface area development is strictly correlated to the degree of devolatilization and to the formation of cracks inside the matrix. Mild thermal conditions of ca. 400 °C favor the development of a macroporous structure due to the removal of large amounts of volatile matter. At about 500 °C, micropores and mesopores are created, leading to an increase in surface area and porosity; and at T>800 °C, the structure and micropore coalescence lead to low values of SSA [Andrade 2012; Ragucci 2013]. For certain precursors (e.g., high rank coals), a preoxidation step in air is needed for boosting the incipient porosity of the char [Ruiz 2006].

b) Physical activation

The term thermal or physical activation refers to the development porosity in the gas phase, usually by reaction of a char with oxygen air, CO_2, steam or their mixtures. The reaction is generally at elevated temperatures (between 750-1100 ºC) and proceeds through the formation of surface oxygen complexes. A detailed review on the understanding of the chemical reactions, thermodynamics and kinetics of the physical activation with these gases can be found in [Marsh 2006]. The objective of the activation is to enlarge and open the incipient porosity developed during the carbonization. This is carried out under a reactive atmosphere in the presence of oxidants such as oxygen (or air), steam, and carbon dioxide, according to:

$C + O_2 \rightarrow CO_2$ $\qquad$ AH = -406 kJ/mol
$C + CO_2 \rightarrow 2CO$ $\qquad$ AH = +159 kJ/mol
$C + H_2O \rightarrow CO + H_2$ $\qquad$ AH = +117 kJ/mol
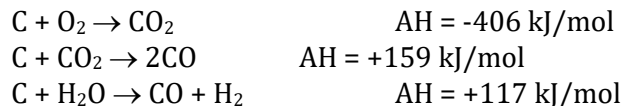
The gasification of chars under CO_2 and steam (and their mixtures) is preferred over the use of oxygen (air) due to the high exothermic enthalpy of the latter, which makes the reaction temperature difficult to control. As a result, oxygen does not penetrate inside the particles of the char, and a fast gasification occurs in the external surface, leading to the complete burn-out of the carbon material rather than to the formation of pores. In the case of CO_2 or steam the reactions are endothermic, thus an external heat supply is required, allowing an accurate control of the experimental conditions.

Physical activation is commonly carried out as a two-stage process, starting by the carbonization of the precursor and further activation of the obtained char. The use of a single-stage process is also possible, and it does not seem to have a significant impact in the porous features of the activated

carbon in terms of micropore volume (V_{micro}) and SSA [Rodriguez-Reinoso 1984]. Many experimental conditions can influence the final textural features of an activated carbon: the precursor origin and reactivity, the heating rate, the gas flow rate, the temperature and dwelling time of the activation, the activating agent, and so forth. A comprehensive review of all of them and the impact on the resulting porosity can be found in [Marsh 2006; Tascón 2012; Ania 2018].

c) Chemical activation

In general terms, chemical activation is considered as a reaction between a solid precursor and a chemical activating agent during the heating of the mixture in an inert atmosphere. The most studied precursors are lignocellulosic materials, coals and chars; as activating agents the most used are $ZnCl_2$, H_3PO_4 and alkali hydroxides (e.g., KOH and NaOH). Chemical activation has recognized advantages for the production of activated carbons with high developed porosity, as it leads to higher yields and allows the use of lower temperatures than physical activation. Additionally, the activation mechanisms are different in both processes, and so it is the porosity of the resulting activated carbons. A detailed review on the mechanism of the different chemical activation reactions for various activating agents can be found in [Marsh 2006; Tascón 2012; Ania 2018].

The main parameters affecting the porous characteristics of chemically activated carbons (in terms of SSA, pore size and pore size distribution) are impregnation ratio, activation temperature, activation time and activating atmosphere. The activating agent is generally in solution where concentration can be varied but in some cases, as for NaOH, a direct mixing of the solid chemical and the precursor results more efficient for developing high SSA [Lillo-Ródenas 2001]. The impregnation ratio is the correlation between the weights of chemical agent and the precursor. A general trend, increasing the impregnation ratio also increases the SSA of the resulting activated carbon up to a maximum value. A drop in the SSA is generally observed at high impregnation ratios due to the collapse of micropores and to an extensive gasification of pore walls. Regarding the pore sizes and pore volumes, there is a strong development of porosity when increasing the impregnation ratio.

1.1.2 Unconventional synthetic methods

Conventional activation methods for the synthesis of nanoporous carbons do not allow a precise control of the pore size and volume. Furthermore, the formation of pores is usually accompanied by significant mass loss (hence low overall yield) and high energy consumption. Thus, introducing a rational design and new approaches that allow to control the porosity at a nanometric scale has

received much attention. In the following sections, we will summarize most relevant methodologies to control the porosity in the synthesis of carbons, emphasizing on the generation of microporous carbons.

a) Hydrothermal Carbonization

A hydrothermal carbonization (HTC) is a thermochemical process in subcritical water for the conversion of wet/dry biomass to carbon materials. Typically, the yield of the solid fraction in HTC is higher than in hydrothermal gasification (e.g., above the supercritical temperature, with the gas fraction as primary product) and 'hydrothermal liquefaction' (e.g., close to 400 ºC, with the predominant production of liquid hydrocarbons). Thus, it has proven to be a powerful technique for the synthesis of carbons from biomass. The first studies reporting the hydrothermal transformation of biomass sources into coal-like materials were reported long ago, but the interest for the use of this technique as a simple method to obtain carbon materials (hydrochars) at mild conditions has growth much just in the last 20 years [Bergius 1913; Berl 1932].

During hydrothermal carbonization, water acts as a solvent and a catalyst, facilitating hydrolysis reactions and accelerating the decomposition of the biomass oligomers and monomers in smaller fragments, leading to the formation of a carbonaceous solid [Demir-Cakan 2009]. The choice of the hydrothermal carbonization conditions (temperature, residence time, pressure and so forth) depends on the nature of the precursor and its thermal stability [Titirici 2010; Jain 2016]. As a general rule, increasing the temperature and pressure of the hydrothermal conditions results in an increase in the conversion of the biomass feedstock into carbon particles. Both high-temperature and low-temperature HTC processes can be applied for the preparation of carbon materials. The first one, typically between 300-800 ºC is beyond the stability of biomass components and other natural or organic precursors, and it has been mainly described for the synthesis of carbon filaments and graphitic carbons [Fujino 2002]. The low-temperature HTC process performs below 300 ºC, and is commonly used for the preparation of hydrochars and activated carbon derivatives, either based on direct solid conversion of biomass feedstocks [Dinjus 2011] or the polymerization of the monomers generated upon the decomposition of biomass (carbohydrates/cellulose) [Sevilla 2009].

The effect of the various operating parameters of HTC on the quality and yield of the products (solid char, liquid and gas) has been extensively investigated [Fujino 2002; Titirici 2010; Jain 2016]. It would seem that once the composition of the precursor is known, the hydrothermal conditions could be adapted in order to obtain carbon materials with optimized features. Most hydrochars

obtained from HTC using water as dispersion medium display poor textural parameters (e.g., SSAs typically below 50 m^2/g). Post-synthesis activation of the hydrochars is another alternative for producing activated carbons with high SSAs [Jain 2016; Falco 2013]. Recent studies [Fechler 2013] have reported hydrochars with SSAs of 673 m^2/g from the HTC of glucose under hypersaline conditions or in the presence of iron nanoparticles [Cui 2006]. The incorporation of a catalyst (acid, oxidant, metallic salt) during the hydrothermal carbonization process also enhances the development of the pore structure in the subsequent activation step.

b) Nanocasting techniques

Nanocasting techniques are classified into two categories depending on the template used: endo- and exo-templating routes, also called soft- and hard-templating, respectively. The concept soft-templating refers to the preparation of porous material using an organic template (e.g., surfactants) that is self-assembled in a solvent in the present of a polymerizable carbon precursor. The carbon material is obtained after a carbonization process, where the template is either consumed becoming a carbon precursor or sacrificed generating the final porous carbon [Chuenchom 2012]. It has been mainly used for obtaining mesoporous carbons through the self-assembly of block copolymers and precursors such as phenolic resins or resorcinol. The exotemplating approach consists on using a porous solid as sacrificial scaffold, so that the porous material obtained is an inverse replica of the template used. Zeolites of varied topology, mesoporous silica/oxides and opals or colloidal silica templates have been used as scaffolds to obtain micro-, meso- and macroporous materials, respectively [Lu 2006].

Hard-templating

Hard-template techniques consist in the use of an appropriate porous material as sacrificial scaffold to replicate its porosity and structure through the infiltration of a carbon precursor followed by carbonization of the composite and removal of the template. The obtained carbon is a negative replica of the template, meaning that the carbon skeletal structure is related to the pores of the template, while the porosity of the carbon is related to the walls of the template after the chemical etching. Even though hard-templating has marked a milestone in controlling the pore structure of carbons, the process is quite challenging and complex, and still has to face a great disadvantage for scaling up applications due to the need to remove the template.

Pioneering research studies on preparing microporous carbons via nanocasting methods were performed by Kyotani and co-workers using zeolites and layered clay minerals as templates

[Kyotani 1998; Kyotani 1997] and resulted to be particularly suitable for the synthesis of carbons with a desired structure of micropores of uniform sizes and shape. These materials are commonly referred to as zeolite templated carbons (ZTC), and due to the well-defined three-dimensional structure of most zeolites, very often present a periodic arrangement of micropores in the range of 1–2 nm [Nishihara 2012; Ma 2000; Ma 2002]. Besides zeolites, the research has been extended to a wide variety of hard templates such as multilayered clays, colloid crystals, mesoporous silica and several MOFs [Matsuoka 2005; Xia 2010].

Nanocasting techniques have important limitations, typically related to the infiltration of the carbon precursor within the narrow channels of the zeolites, or the restricted polymerization in small pores that bring about a low carbon yields, and ultimately provokes the collapse of the carbon after the etching off the template [Nishihara 2012]. The topology of the scaffold is important as it define the size of the cavities and their connectivity; the acidity of the scaffold also plays a role, as it affects the formation of the carbon layer when the infiltration is made by chemical vapor deposition (avoiding the deposit of pyrolyzed carbon outside the zeolite particles). Regarding the carbon precursor, CVD of small hydrocarbon gases, polymer carbonization of organic monomers, and the combination of both have been mainly explored. In general, a two-step infiltration method is recommended for obtaining a uniform carbon deposition and a robust carbon framework with high SSA [Kyotani 1997; Ma 2000; Matsuoka 2005].

Soft templating

Soft-templating approaches are based on the formation of supramolecular arrangements of precursor molecules (e.g., carbon precursor) with a template (e.g., surfactants), stabilization of the carbon matrix by polymerization and the removal of the template. The microphase separation induced by the usually well-ordered phases of the templates is responsible for the ultimate structure of the resulting materials. One of the advantages of this approach is that the template is either destroyed or consumed as carbon precursor during the carbonization process, avoiding the need of a chemical etching off. However the scaling-up is still economically and environmentally questionable, due to the synthetic origin of most of the templates.

The interest of soft-templating approaches has been mostly directed towards the preparation of carbon materials with hierarchical meso- and macroporosity [Chuenchom 2012] but it can also be extended to microporous carbons with high pore volumes and/or molecular sieving. In this regard, the preparation of carbon materials with pores of different sizes is intimately related to the nature of the template. For instance, polyethylene oxide (PEO) blocks in block copolymeric surfactants

tend to produce microporosity, ionic surfactants produce micropores and small mesopores (2-4 nm), whereas non-ionic surfactants (e.g., Brij and Pluronics) generate mesopores of up to 10 nm [Petkovich 2013]. The morphology of the carbon materials can also be modulated by adjusting the concentration of the surfactant or block copolymer, the pH of the solution or the temperature of the reaction [Mai 2012].

Precursor molecules typically employed in the resin formation that precedes the synthesis of soft-templated carbons are hydroxylated aromatic molecules (e.g., phenol, resorcinol, phloroglucinol, resol) or functionalized compounds (e.g., melamine, pyrrol) if doped-carbons are targeted. The chemical cross-linking of these molecules is often carried out in the presence of an aldehyde (formaldehyde, glyoxal) acting as a linker, to form the oligomer that co-assemble with the template micelles. The chemical composition of the polymeric carbon precursor controls the interaction strength with the template polymer, and thus the degree of cross-linking that will define the porosity of the soft-templated carbon.

c) Sol-Gel Approaches

Sol-gel techniques are bottom-up approaches that enable a precise control over the synthesis parameters, and thus over the final characteristics of the porous material. In 1989, Pekala et al. [Pekala 1989] reported the preparation of organic sol-gel based materials through the polycondensation of resorcinol-formaldehyde (RF) mixtures in the presence of acid or base catalysts in aqueous media. The resulting materials contain abundant oxygen functionalities and thus are commonly referred to as organic gels or resins. A final carbonization step would convert them into carbon gels.

The sol-gel process starts with the polymerization and condensation of the precursors (typically R and F), initially through an addition reaction to form hydroxymethyl derivatives that subsequently condensate to form methylene and methylene ether bridged-compound. When the reaction starts, polymer chains grow into aggregated clusters of a few nanometers in diameter; the cross-linking of these colloidal particles lead to the stiffening of an organic gel with an interconnected structure. To prepare the polymerization of the reactants, these are mixed with the catalyst and the solvent, stirred for form a homogenous mixture and allowed to gelate and polymerize at moderate temperatures in sealed vessels to minimize the solvent evaporation. Dynamic viscosity measurements have shown that the initial cluster formation and particle growth takes about 1 h [Job 2007], at this stage, the mixture constitutes a colloidal solution of clusters of monomeric particles. This general mechanism depends on the solution pH, the components molar

ratios and the temperature, among others [Al-Muhtaseb 2003]. The next stage is the covalent crosslinking of the clusters until they become unstable and undergo spinodal decomposition leading to the solidification of the gel. The sol–gel polycondensation of R-F mixtures in the presence of a catalyst is endothermic, and then heating is required to provide the necessary energy for this reaction. The typical temperature for this reaction in aqueous medium is ca. 80 ºC [117], although it may be decreased when longer gelation times [Pröbstle 2002] or alternative solvents to water are used [Berthon 2001]. The curing step is also important since it allows the polymeric clusters to crosslinking and form the final shape of the gel. This is usually carried out at 80-90 ºC for about a week to prevent the swelling during the drying stage [Job 2005, 2007].

Carbonization of the organic gels under an inert atmosphere provokes the removal of the volatiles and the densification of the carbon gel. The carbonization typically provokes a partial collapse of the mesoporosity, but if favors the formation of a microporous structure [Al-Muhtaseb 2003]. The carbonized gels can be further activated to enhance the porosity, in a similar pathway as that of any other carbon precursor [Gomis-Berenguer 2017].

After the pioneering work of Pekala [1989] much of the effort has focused on how different synthetic parameters affect the final organic gels and carbons, optimizing the porosity within the full nanometric scale. The nature of the catalyst and its concentration also affect the porosity of the carbon gel. The most widely used catalyst is Na_2CO_3; as a general trend, low R/C molar ratio favor the formation of predominantly microporous carbon gels with low SSAs and poor mechanical properties [Al-Muhtaseb 2003; Job 2005, 2007; Chuenchom 2012,].

Other monomers have been used as alternative precursors to resorcinol, including cathecol, hydroquinone, phloroglucinol, phenol and other substituted phenolic rings, as well as heteroatom-containing monomers (e.g., urea, melamine, 3-hydroxypyridine) for the preparation of doped-carbons [Rasines 2015a,b; Chuenchom 2012] and deep eutectic solvents [Lopez-Salas 2014,6; Carriazo 2010]. The differences in the polycondensation reaction kinetics of these molecules define the features of the carbon gels. In this regard, phloroglucinol, being a more reactive molecule towards polycondensation reactions than resorcinol promotes the formation of highly crosslinked polymers with a microporous structure. On the other hand, the presence of only one hydroxyl group in phenol makes its reactivity slower in compare to both phloroglucinol and resorcinol [Chuenchom 2012]. Low cost precursors (e.g., biomass, furfuryl alcohol) have also been explored as an economic alternative to the RF sol-gel process [Szczurek 2011]. Antonietti and coworkers reported that the general principles of sol-gel chemistry can be transferred to a sustainable

preparation of carbon materials following a hydrothermal approach of low cost and available precursors such as carbohydrates, saccharides or biowastes [Titirici 2008].

d) Self-activation

Self-activation generally occurs during a single-step pyrolysis of a carbon precursor that results in in porosity development without incorporating any additional activating agent. In this sense, self-activation of polymer based precursors or biomass carbons have been reported if an alkali-rich precursor is carbonized under an inert gas flow or if the own gas products of the pyrolysis of the precursor are used as activating agents. For some particular precursors, the method is very efficient for producing highly microporous carbons for being used as gas adsorbents.

The carbonization of organic salts has recently considering a facile synthesis strategy towards the preparation of highly microporous carbons using more sustainable approaches compared to chemical activation with harsh KOH. Highly porous carbons with different textural properties have been obtained by direct carbonization of organic polymers and their salts (i.e., gluconates, alginates, citrates, sulfonates, maleic acid) as precursors. These compounds combine a carbon precursor (i.e, the organic moiety) and certain elements that during the heat-treatment generate species capable of operating as activating agents [Raymundo-Piñero 2006; Sevilla 2013].

Following the same principle, dynamic carbonization templating of metal-loaded organic polymers has been reported, giving rise to polymer-derived carbons with a predominantly microporous structure [Nakagawa 1999; Ania 2006; Hines 2006]. The porosity of the material was deepening on the nature of the cation exchanged, with Na and Ni favoring the formation of microporous carbons, and Cu, Fe and Co mesoporous materials. Self-activation of polymers or biomass can be also performed by using the pyrolysis gases to prepare microporous activated carbons without any physical or chemical agent [Bommier 2015; Jeon 2015; Xia 2016]. As a result, in-situ activation reactions between the resulting carbon and the gases that are evolved during pyrolysis of cellulose are allowed to take place over a wide range of temperatures. The high amount of oxygen present in certain precursors favors porosity development during the carbonization.

e) Carbide Derived Carbons

Carbide derived carbons, CDCs, are produced by selective etching of metals from crystalline metal carbides. In such a way the metal carbide lattice has the role of template as metal is extracted layer by layer. The transformation is conformal and an atomic level control can be achieved at the

same time that the carbide sample size and shape is maintained. Depending on the carbide used as precursor and the synthesis conditions, different carbon allotropes can be produced ranging from amorphous carbon to graphite or even nanocrystalline diamond [Yushin 2006].

Several methods have been reported for selective removal of metal or metalloid atoms from carbides as hydrothermal leaching, thermal decomposition, etching at high temperatures in molten salts, halogenation or electrochemical etching at room temperature. Hydrothermal leaching, thermal decomposition and electrochemical etching at high temperatures drives to non-porous or low porosity carbons whereas halogenation and electrochemical etching at room temperature are the most suitable routes for obtaining nanoporous carbons [Lukatskaya 2014; Messner 2018; Batisse 2010].

Halogenation is the most suitable for obtaining nanoporous carbons. The general reaction involved in the synthesis of carbon from metal carbides by halogenation can be written as: $Me_xC_y(s) + (z/2) X_2(g) \rightarrow x MeX_z(g) + y C(s)$ where Me represents metal and X the halogen The most commonly used etching agent is Cl_2 but other halogens such as F_2 and XeF_2 can be used instead of Cl_2 [Batisse 2010].

The factors controlling the porous textures of the carbons produced by chlorination of carbides are related to the initial carbide chemistry and porosity, some processing parameters as gas mixtures or chlorination temperature, and post-halogen treatment [Presser V2011; Thomberg 2010]. Overall, increasing the chlorination temperature increases the average micropore size of the CDC. In general, at low chlorination temperatures, N_2 or Ar adsorption isotherms of the resultant carbons are of type I since they become of type IV when increasing temperature indicating the presence of mesopores [Urbonaite 2008].

1.2. Light assisted reactions

Photochemical processes have been the directors for the origin of the life. Thus, the study of the interaction between light and matter is a central theme that connects multiple areas of scientific research. Photochemical reactions are referred to any chemical reaction which occurs as a result of light absorption [Braslavsky 2007]. From the ozone formation and dissociation in the atmosphere, to the photosynthesis in the plants and other organisms, sunlight is the source of energy for almost all life. Photochemistry have been often associated with high energy photons at UV wavelengths, however UV, visible, or infrared radiations are also concerned. Photons are near-ideal reagents: they generate no waste after its action unlike other activating agents or catalysts, and they can be

obtained from renewable sources [Protti 2007; Ciamician 1908, 19012]. From the point of view of atom economy, photochemical reactions are often advantageous too, because they provoke transformations at deep-seated molecular level, achieving in a single stage what would otherwise require several steps. Moreover, photochemistry has been employed to enable transformations that are, at times, just inaccessible by other methods.

For example, photochemical paths offer the advantage over thermal methods of forming thermodynamically disfavored products, overcoming large activation barriers [Protti 2007], i.e. under mild conditions, photochemical reactions can undergo the formation of thermodynamically instable species, usually more reactive their ground-state counterparts, giving rise to reactions allowing access to exceptional molecular structures that cannot be obtained by conventional means [Stephenson 2016]. We can say that, photochemical reactions are a green alternative to thermal processes. Thus photochemical strategies have turned into a powerful synthetic tool in diverse fields, with applications across the breadth of modern chemistry research.

As mentioned above, photochemical reactions favor transformations at deep-seated molecular level. The high energy that is transferred to a molecule by absorption of light facilitates reaction pathways that cannot be accessed by conventional methods. And a result, unexpected transformations take place. The excitation of a molecule is based on the electronic transition from its ground state to an upper energy level. The excitation of a molecule might occur by different ways. On the one hand, direct irradiation consists in the absorption of a photon with the appropriate energy. This absorption promotes an electron from its ground state to an excited state through an allowed transition, thus, the energy of the photon absorbed should be the same the energy GAP between both states. On the other hand, indirect transitions can also occur, such as photo-induced electron transfer reactions [Prier 2013] or energy transfer by photosensitization [Zao 2013].

Since many molecules and atoms are capable of undergoing chemical changes upon light absorption, there are many ground state reactions which have photochemical counterparts and thus, there is a large number of photochemical reactions that have been carried out with different purposes. Examples of photochemical reactions can be found in organic synthesis (photoadditions, photoeliminations, photoenolizations, photo-Fries rearrangements, photoisomerizations, photooxidations, photoreductions, photosubstitutions, etc.) [Fouassier 1995; Allen 2010; Ramamurthy 2000]; photochemical transformations that have also been extensively employed in the synthesis of natural products [Kärkäs 2016; Bach 2011], heterogeneous photocatalysis [Yasser 2021], the synthesis of materials [Sakamoto 2009; Jiang 2020], and the pharmaceutical field

[Politano 2018]. Moreover, photo-induced electron transfer (PET) phenomena have been of particular importance in the development of diverse research areas, as photoredox catalysis for organic synthesis [Stephenson 2016]**,** energy conversion in solar cells [O'Regan 1991; Lewis 2006] and the production of solar fuels [Gray 2009].

In the field of materials' science and the synthesis of materials, photochemical reactions are also of great relevance. Scientist and engineers are increasingly thinking in a sustainable design of their research programs and photochemistry can contribute efficiently to development of Green Chemistry [Sanderson 2011;Protti 2007; Ciamician 1908]. As an example, in polymer sciences the use of light to control and fine-tune the formation, structure, structure and properties (e.g., bio-chemo-, mechanical) of polymeric materials represents one of the most powerful and rapidly evolving approaches. Indeed, the use of light presents important advantages over other analogous methods used in polymer chemistry. It allows some processes that are unable to occur by other means at ambient temperature, on reasonable time scales after a photo-initiation. A comprehensive review of the fundamental basis for the main photochemical processes implemented in polymer systems, (e.g. synthesis, polymerization, degradation, functionalization, crosslinking reactions) can be found in [Chatani 2014]. Additionally, future perspectives in the development of scale-up strategies, combining photochemical reactions in the continuous flow multistep synthesis are being as well developed [Galant 2020].

Another important application of light induced reactions in material's synthesis can be found in photolithography techniques, also known optical lithography or UV lithography [Tanaka 2015]. Photolithography allows the micro-fabrication of pattern parts on a thin film or the bulk of a substrate; a locally deposit of a photoresist serves as a protective mask during the shaping of a substrate or a thin layer. This technique uses a beam of photons to transfer a pattern written on an optical mask to the substrate surface. Photolithography is widely used in the semiconductor industry and large-scale mass production of Si-based devices down to several tens of nanometers. Also in functional oxides, it has been applied to the preparation of prototype devices: for example, magnetic oxide tunneling junctions, field effect transistors, etc. [Rossum 2005; Tanaka 2015].

Finally, UV light is also very much used to carry out surface treatments. For example UV coating process is a technique where a compound is applied and then instantly curing by ultraviolet light. Several types of compounds can be used; from polymers to metal nanoparticles and inorganic composites. UV coatings can protect, for example from the UV radiation's harmful effects, or modify the surface properties of other materials (surface resistance, antibacterial effects, modify the finishes of the surface e.g. shine, anticorrosive or waterproof effects, etc.). Indeed, in the recent

years many studies have been done about UV-curable coating materials due to their versatility. UV coating technology can be apply to protect or modify many different materials as paper, wood, plastic, glass, metals, etc. [Shukla 2004; Sharmin 2015; Liu 2020].

1.2.1 Light-assisted methods for the synthesis of metal nanoparticles

The studies on the photochemical synthesis of metal nanoparticles (NPs) date back to a discovery in the 18th century, with the observations of the darkening of certain silver salts upon light exposure [Albini 2009; Watanabe 2006]. Since then, a variety of photo-induced methods have been developed to obtain well-defined monometallic and bimetallic NPs, as well as composite materials. The essential of the photochemical approach is the formation of zero valence metal nanoparticles under the conditions that prevent their precipitation. Photoreduction has been established as an important technique for NPs synthesis, where the zero valence metal, (M^0) is formed through the direct excitation of a metal source.

The method has an enormous advantage over other chemical methods, as it does not need the addition of reducing agents, as they are typically generated in-situ by the photochemical reaction. The photochemical synthesis enables one to fabricate NPs in various media including emulsion, surfactant micelles, polymer films, glasses, cells, etc. what confers to this approach a great versatility. This allows the stabilization of the NPs along with the functionalization of the materials (e.g., in-situ synthesis of metal NPs/polymer composites).

The classical photochemical synthesis of metal NPs proceeds either through a direct photo-reduction of the metallic precursor (metal salt or complex), or through a photosensitization reaction involving photoinitiators or other intermediate species such as excited molecules or radicals [Sakamoto 2009].

1.2.1 Light assisted methods for the synthesis of carbon materials

Recently, the use of light has attracted the attention of the scientific community with interest in carbon materials for the potential to promote controlled photooxidation/reactions. Particularly with the focus on the reparation of graphene derivatives from the photoréduction of graphene oxide (GO). Indeed, this chemical approach is considered one of the most viable alternatives to produce highly quality graphene and defective graphene derivatives (reduced graphene oxides, rGO) of interest in many different fields. The photoreduction of GO has been reported using a variety of lamp sources (UV, solar, laser, IR) and compared to the classical reduction methods based

on wet chemistry, plasma, thermal or electrochemical reduction processes. Interesting reviews on the topic can be found elsewhere [Li 2013; Singh 2016; Niu 2020; Agarwal 2021].

The irradiation is most commonly carried out using high energy lasers and UV light, and in the presence of catalysts aiming to boost the full exploitation of solar light [Williams 2008; Hasani 2014; Zhang 2014; Guardia 2012]. In most cases, the mechanism is described as a photothermal reduction process, where the interaction of GO with a high energy pulse locally induces the heating of the GO layers, thereby generating the decomposition of the oxygen- functionalities of the material. More recently, it has been reported that illumination of the graphene oxide thin film electrodes with low irradiance simulated solar light brings about the photoassisted reduction of the material with negligible photothermal effects [Quezada-Renteria 2020], and the selective removal of epoxides and hydroxyl groups rendering a reduced graphene oxide with a high density of defects (high reactivity).

Some other authors have reported the use of light for the formation of plasmon-assisted phase transformation of carbon on metal nanoparticles [Kulkarni 2012], and the synthesis porous carbons from phenolic resins upon exposure to UV and IR laser irradiation [Sopronyi 2016; Cao 2007]. For instance, Cao et al. showed a localized photothermal growth of carbon nanotubes and silicon nanowires on metal nanoparticles exposed to a focused light beam due to the heat generated at the metallic surface plasmons exposed to irradiation [Cao, 2007].

The same principle based on the light absorption properties of a metallic component has been used to induce the phase transformation of amorphous carbon deposited on nanoparticulated metal films, thereby obtaining carbon materials with enhanced electrical properties (graphitization) [Kularni, 20128].

Vinu et al. reported the photofunctionalization of a carbon matrix with carboxylic moieties by exposing the sample to UV light and oxygen at room temperature [Jia 2012]. The preparation of porous carbons using polyhydroxylated aromatic precursors based on photoinduced evaporation reactions has also been reported using a triblock copolymer as sacrificial template [Sopronyi 2016; Balan 2017]. The main advantage of the photoinduced synthesis, compared to the conventional endotemplating route (using the same precursors) is the time scale, since the aging step needed to induce the cross-linking of the polymeric precursor is significantly reduced due to the energy provided by the UV irradiation.

1.3. Objectives

The main objective of this thesis is to explore the use of photo-assisted polymerization reactions of different organic precursors for the preparation of nanoporous carbons and resins as well as metal-decorated materials by the incorporation of Ag and Au metallic nanoparticles with controlled textural and physicochemical properties. The final goal is to control not only the chemical and textural parameters but also the metallic nanoparticles size and distribution within the carbon matrix.

The specific objectives set in order to achieve the main purpose of this thesis are:

a) To prepare nanoporous carbon and metal-loaded carbon materials through photo-induced synthetic strategies using various precursors.

b) To characterize the morphological, textural and physicochemical features of the polymeric resins and the nanoporous carbons in order to study the influence of synthetic conditions on the final physicochemical properties of the carbon materials. The nature of the organic precursors (e.g., composition, type of surface moieties) were found to play a key role in the polycondensation rate of the monomers, and thus in the porosity (type, connectivity) of the obtained carbons in the full micropore and mesopore range. Thus, special emphasis has been put in the characterization of the porosity of the materials using advanced characterization techniques combining gas adsorption of various probes and scanning of the hysteresis loops.

c) To elucidate the impact of the different synthetic parameters (e.g., pH, irradiation time and source, use of photoinitiators, nature -type, composition, functionalization- of the organic precursor) on the characteristics of the obtained carbon materials.

d) To unravel the mechanisms occurring during the photoinduced reactions leading to the polycondensation of the reactants, and/or the photoreduction of metallic precursors. To this end, the reactant's mixtures, the final polymeric resins and the carbon materials were analysed using solid-state NMR. Comparison with classical polycondensation reactions (non photoassisted) have allowed to understand the reaction mechanism boosted by the light source.

e) To extend the application of UV-assisted polycondensation of organic monomers in the presence of metallic salts to prepare metal-containing carbon materials. The use of light allows the simultaneous photoreduction of the metallic precursor in solution, which is expected to render

metal-containing carbon materials with well-dispersed metal nanoparticles within the porous carbon matrix.

f) To extend the proof of concept on the use of light for a fast preparation of carbon materials to the use of solar light, green precursors (biomass-derived molecules) and the incorporation of additives (e.g., carbon black) to obtain carbon materials with a controlled porosity and improved characteristics for various potential applications.

CHAPTER 2

Experimental

2.1. Reactives

Gallacetophenone (GA), 2,3-dihydroxynaphtalene (DN), pyrogallol (PG), bisphenol A (BA), phenol (PH), catechol (CT), resorcinol (RS), pyrogallol carboxylic acid (PGA) and tannic acid (TNA) were select as organic precursors; glyoxal (40 wt.% aqueous solution) was used as polymeric linker; Pluronic F127 (poly(ethyleneoxide)-block-poly(propylene oxide)-block-poly-(ethylene oxide) $PEO_{106}PPO_{70}PEO_{106}$ (molecular weight, 12600 Da) was used as surfactant; 37 % HCl was used as acidic catalyst; 2-Hydroxy-4'-(2-hydroxyethoxy)-2-methylpropiophenone (98 %) was used as photoinitiator; silver nitrate $AgNO_3$ and gold (III) bromide ($AuBr_3$). All the chemicals were purchased from Sigma-Aldrich with the highest purity, and were used as received without any further purification.

2.2. Synthesis of the polymeric resins

About 1.6-2.2 g of the selected organic precursor and 3.2 g of surfactant were dissolved in ethanol. At this step, HCl or/and the photoinitiator were also added if necessary. The solution was magnetically stirred at 290 rpm at 27ºC until all the reactives were dissolved. Then, 1.6 mL of glyoxal 40 wt.% were added; the solution was transferred to glass dishes and exposed to irradiation for various periods (i.e., up to 60 min). The fixed molar ratio, OP: glyoxal: pluronic F127 was 1: 1.4: 0.03. The irradiation source was a lightning cure device fitted with a 365 nm elliptical reflector (ca. 170mW/cm² at UVA band). An anticaloric filter was used to avoid heating during irradiation (monitored temperature was constant). The progress of the photoassisted reaction was monitored via UV-visible absorption spectroscopy using a Thermo Fisher Scientific Evolution 200 spectrophotometer. Brownish viscous solids were obtained. The nomenclature assigned for the resins after light exposure is r-OP-X-Y, where OP stands for the organic precursor (PH, CT, RS, BA, DN, PG, GA, PGA, TNA and THBA,), X indicates the presence (H) or absence (0) of acid, and (Y) indicates the presence (Ch) of absence (0) of photoinitiator. For the series of metal-containing materials, the adequate amounts of $AgNO_3$ or $AuBr_3$ were added to the precursor's mixtures before the irradiation. The amount of $AgNO_3$ was added 5 min after incorporating the glyoxal solution to the relative's mixture, whereas $AuBr_3$ was incorporated to the ethanol solution at the same time than the OP. The nomenclature of these resins is r-OP-X-Y-A, where A stands for Ag or Au.

2.3. Synthesis of the carbon materials

The brownish viscous solids (series r-OP-X-Y or r-OP-X-Y-A) obtained after the irradiation were recovered from the glass dishes and carbonized at 600 ºC under N_2 atmosphere (ca. 120 ml/min,

heating rate 2 ºC/min, 2 hours) to obtain the carbon materials. The nomenclature of the carbonized samples is C-OP-X-Y or C-OP-X-Y-A.

2.4. Characterization Techniques

2.4.1 Textural characterisation

Gas adsorption (particularly, physisorption) at a constant temperature is the most suitable method used for textural characterisation of all types of solids. Adsorption is defined as the enrichment of molecules, atoms or ions in the vicinity of an interface that occurs whenever the surface of a solid (adsorbent) is exposed to a gas or liquid (adsorptive). According to the nature of such interactions a distinction can be made between chemisorption -formation of a chemical bond with the solid- and physisorption -no chemical bond formed-. The pore size is generally specified as the pore width, defined as the distance between the two opposite walls. Pore sizes are classified by IUPAC as follows [Thommes 2015]:

> *Micropores*: pore widths not exceeding about 2 nm.
> *Mesopores*: pore widths between 2 nm and 50 nm.
> *Macropores*: pore widths exceeding about 50 nm.

Recently, IUPAC has accepted the term *nanopores* to include the above three categories of pores, with an upper limit close to 100 nm width [Thommes 2015]. In addition, some other authors proposed other classifications to distinguish *ultramicropores* or *narrow micropores* (widths less than 0.7 nm), *medium sized micropores* (corresponding to a widths between 0.7 and 1.4 nm) and *supermicropores* (widths between 1.4 and 3.4 nm) [Brunauer 1970; Dubinin 1979].

The amount of gas adsorbed by a solid, n, per mass of solid depends on the pressure, p, the temperature, T, and the nature of the gas-solid system. For a given gas adsorbed on a particular solid at a constant temperature, and if the gas is below its critical temperature, the number of moles of gas adsorbed may be expressed as:

$$n = f\left(\frac{p}{p_0}\right)_{T,gas,solid} \qquad \text{equation 2.1}$$

where p_0 is the gas saturation pressure and p/p_0 is the relative pressure.

This equation is a general expression for an adsorption isotherm [Gregg 1982] which represents the relation, at constant temperature, between the amount adsorbed by unit mass of solid and the equilibrium pressure (or relative pressure).

Experimental adsorption isotherms for gas-solid systems are usually presented in graphical form (adsorbed gas amount *vs* relative pressure), and display various characteristic. According to classification proposed by IUPAC in 2015 [Thommes 2015], all experimental adsorption isotherms should fit at least one, or a combination of two or more, of the six recognised types (Figure 2.1). Each type of isotherm is associated to a particular mechanism (physical adsorption, chemical adsorption, capillary condensation), consequently, a simple observation of the experimental adsorption isotherm allows to draw some conclusions on the porous texture of the analysed material.
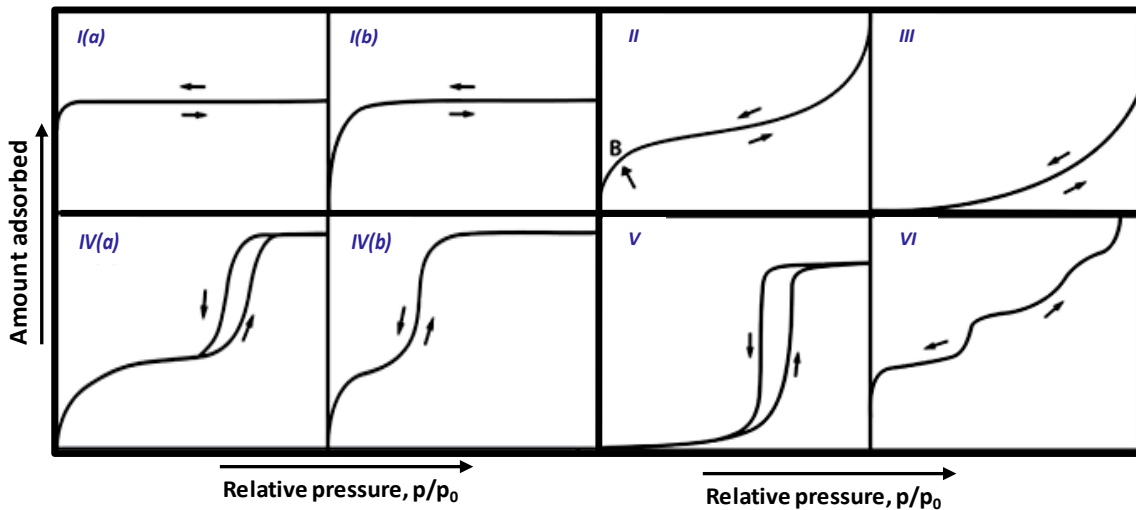
Figure 2.1 Classification of adsorption isotherms from IUPAC. Adapted from [Thommes 2015].

Reversible Type I(a) and I(b) isotherms are concave to the p/p_0 axis and are characterised by a limiting value of the amount adsorbed, which begins to set at relatively low relative pressure and is extended to the saturation pressure. They are given by microporous solids presenting small external surface areas, as is the case for some activated carbons, molecular sieve zeolites and certain porous oxides. Type I(a) isotherms are given by microporous materials having mainly narrow micropores, whereas Type I(b) isotherms indicates the presence of wider pore size distributions on the materials.

Type II isotherms are given by the adsorption of most gases on non-porous or macroporous adsorbents, with unrestricted monolayer-multilayer adsorption up to high relative pressure. These isotherms are reversible and concave relative to the x-axis up to a certain point normally referred to as Point B, when the middle almost linear section starts. If the knee is sharp, Point B usually corresponds to the completion of monolayer coverage. After this almost straight section, the slope increases and the curve becomes convex to pressure axis.

The Type III isotherms are convex in relation to the axis of the abscissas over to complete range and consequently do not present a Point B, with no monolayer formation. This shape indicates that the adsorbent-adsorbate interactions are relatively weak and the adsorbed molecules are clustered around the most favourable sites on the surface of a non-porous or macroporous solid.

Type IV isotherms are characteristic of mesoporous adsorbents, as many oxide gels, industrial adsorbents and mesoporous molecular sieves. The adsorption behaviour in mesopores is governed by the adsorbent-adsorptive interactions and the interactions between the molecules in the condensed state. The shape of the initial region is closely related to Type II reaching a characteristic saturation plateau at high relative pressures. In Type IV(a) isotherms present hysteresis loop associated with capillary condensation that occurs when pore exceeds a certain critical width, depending on the adsorption system and temperature. Completely reversible Type IV(b) are observed for adsorbents having mesopores of smaller width.

Type V isotherms are convex to x-axis and, to a certain pressure value, similar to the isotherms of Type III, which is indicative of relatively weak adsorbent-adsorbate interactions.

Reversible stepped Type VI isotherms are associated with layer-by-layer adsorption on highly uniform non-porous surfaces. Type VI isotherms are typically obtained with argon or krypton at low temperature of graphitized carbon blacks.

Hysteresis loops are associated with capillary condensation occurring in the mesopores and can be attributed to thermodynamic effects (adsorption metastability) and/or network effects (percolation, cavitation). In a complex pore networks, if wide pores have access to the external surface only through narrow necks (known as ink-bottle pore shape), the desorption vapour pressures are dependent on the size and spatial distribution of the necks, if the neck diameters are not too small, the porous structure may empty at a relative pressure corresponding to a characteristic percolation threshold. In addition, hysteresis may also be caused by the effects of connectivity of the pores [Choma 2006]. Then, useful information concerning the neck size and pore

network can be obtained from the desorption branch of the isotherm. Six different forms of loops have been reported by the extended IUPAC classification [Thommes 2015] associated with certain well-defined pore structure (Figure 2.2).

Type H1 is a narrow loop with very steep and almost parallel adsorption and desorption branches indicating the delayed condensation of the adsorption branch. It is observed in porous materials with a narrow range of uniform mesopores. Hysteresis loop Type H2 is given by complex pore structures in which network effects are important. The desorption branch is nearly vertical, which is a characteristic feature of H2(a) loops; this steep desorption can be attributed either to pore-blocking/percolation in a narrow range of pore necks or to cavitation-induced evaporation. The type H2(b) loop, also associated with pore blocking, is obtained for larger size distribution of neck widths. Two distinctive features characterize the Type H3 loop: the resemblance of the adsorption branch of the Type II isotherm; the lower limit of the desorption branch is normally located at the cavitation-induced p/p_0. The adsorption branch of Type H4 loop is now a composite of Types I and II isotherms, the more pronounced uptake at low relative pressure being associated with the filling of micropores. Type H5 loop has a distinctive form associated with certain pore structures containing open and partially blocked mesopores.
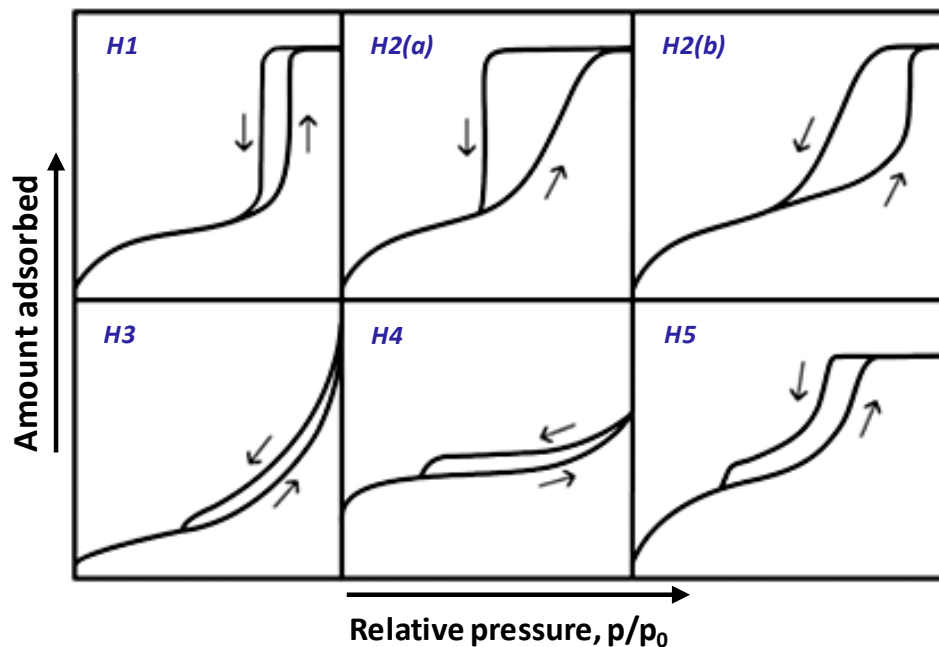
Figure 2.2 IUPAC classification of hysteresis loops. Adapted from [Thommes 2015].

In this thesis, the textural properties of the materials have been characterised by physical adsorption of various gases. Volumetric analysers were used for the measurement of the adsorption isotherms of N_2 at -196 °C and CO_2 at 0 °C (3Flex and TRISTAR 3020, Micromeritics). All samples were previously outgassed under vacuum (ca. 10^{-1} Pa) at 120 °C (heating rate of 2 °C/min) for 17 h to obtain reproducible and accurate data [Figini-Albisetti 2010]. Each isotherm was recorded at least in duplicate on fresh sample aliquots, to guarantee the accuracy and reproducibility of the experiments (error was below 2 %). The specific surface area, pore volumes and pore size distributions have been calculated using the BET model, the DR equation applied to both N_2 and CO_2 adsorption isotherms, and the 2D-NLDFT-HS approach for the distribution of pore sizes in the full nanometric scale. Further details of these equations are described below.

Surface area determination using BET method

The surface area of a porous solid is commonly calculated using the BET equation, expressed as:

$$n(p) = \frac{n_m \, C_{BET} \, p}{(p - p_0) \, [1 + (C_{BET} - 1) \, (p/p_0)]}$$

equation 2.2

where $n(p)$ is the amount of adsorbed gas at pressure p, n_m is the adsorbed amount needed to fill the monolayer, p_0 corresponds to the vapour saturation pressure and C_{BET} is designated as the BET constant which is related to the adsorbate-adsorbent interactions.

The application of this equation requires to transform an experimental physisorption isotherm into a BET plot, from that, it is possible to determinate the number of adsorbed moles in the monolayer (n_m) and the equivalent surface area (S_{BET}). BET equation can be linearised in different forms; in this thesis, the one proposed by Parra et al. in 1995 [Parra 1995] is used:

$$\frac{1}{n \, (1 - x)} = \frac{1}{n_m} + \frac{1}{n_m \, C_{BET}} \left(\frac{1 - x}{x} \right)$$

equation 2.3

where x is the relative pressure (= p/p_0).

BET theory has become a standard procedure for the determination of the surface area of a wide range of porous materials [Rouquerol 2014]. On the other hand, it is now generally recognised that the theory is based on an oversimplified model of multilayer adsorption and that the reliability of the BET method is questionable unless certain conditions are prescribed. In this regard, the BET method can be applied to many Type II and Type IV isotherms, in which the range of linearity of the BET plot is restricted to the relative pressure range between 0.05 and 0.3; at higher or lower

pressures, the BET equation provides adsorbed quantities which are, respectively, lower and higher than real. However, the BET equation needs to be applied with extreme caution for microporous materials (i.e. Type I isotherms and combinations of Types I and II or Types I and IV isotherms) because in these cases, it may be very difficult to detect the formation of the monolayer from the multilayer adsorption and micropore filling, for which the linear range of the BET plot may be difficult to locate.

The IUPAC has addressed this concern in a review in 2015 [Thommes 2015], recommending a procedure to overcome this difficulty and to avoid any subjectivity in evaluating the BET monolayer capacity. The procedure is based on various criteria: i) the C_{BET} constant should be positive (i.e. a negative intercept would indicate that the selected range of relative pressures for the application of the BET equation is not appropriate); ii) the application of the BET equation should be restricted to the range where the term $n(1 - p/p_0)$ continuously increases with p/p_0; iii) the p/p_0 value corresponding to n_m should be within the selected BET range.

In this thesis, the mathematical approach proposed by Parra et al. was used to determine the right range of relative pressures for the correct application of the BET equation. This approach complies with all the criteria recommended by IUPAC.

Micropore volume: Dubinin-Radushkevich equation

In 1947, Dubinin and Radushkevich proposed an equation for the characteristic curve in terms of the fractional filling of the micropore volume. This equation is an empirical method that takes into account the distinct adsorption energies and assumes that the micropore size follows a Gaussian distribution. The linear DR equation is given as follows:

$$\ln W = \ln W_0 - \left(\frac{R\,T}{\beta\,E_0}\right)^2 \ln^2\left(\frac{p_0}{p}\right) \qquad\qquad \text{equation 2.4}$$

where W (cm^3/g) is the volume occupied by adsorbed phase at temperature T, W_0 (cm^3/g) corresponds to total volume of micropores, β is the adsorbate-adsorbent affinity factor -ca. 0.34 for N_2 and 0.36 for CO_2 [Guillot 2001]-, and E_0 (kJ/mol) is the adsorption energy.

In this thesis, the total micropore volume (W_o, N_2) and the volume of narrow micropores (W_o, CO_2) were calculated from the N_2 and CO_2 adsorption isotherms, respectively.

Pore size distributions: Density Functional Theory

The Density Functional Theory (DFT) is widely used for the calculation of pore size distributions of porous materials; the method is based on the assumption that an experimental isotherm can be expressed as the sum of the isotherms of individual pores forming the porous solid structure [Tarazona 1987; Lastoskie 1993].

$$n(p) = \int_{w_{min}}^{w_{max}} f(w)\rho(p,w)dw \qquad \text{equation 2.5}$$

where $n(p)$ is the amount of gas adsorbed at pressure p, w_{min} and w_{max} are the minimum and maximum pores width, $f(w)$ is the distribution of the pore volume as a function of the pore width and $\rho(p,w)$ is the molar density of the adsorbate at pressure p in a pore with width w.

The first approaches using DFT to evaluate the pore size distribution made simplistic assumptions concerning the functional form of the size distribution; more recently, a generalisation was accomplished by numerical deconvolution of the isotherm data using a set of pore shape dependent model isotherm; each member of the set being representative of a unique, narrow range of pore sizes. Nowadays, more sophisticated methods based on NLDFT have succeeded in determining the pore size distribution in the entire range of pore sizes accessible by the adsorptive molecule, incorporating concepts related to the dimensionality of the pores, the surface energetic heterogeneity and geometrical corrugation in the equation (2D-NLDFT-HS) [Jagiello 2013a, 2013b; Landers 2013]. In this thesis, the 2D-NLDFT-HS approach was used to obtain the distribution of pore sizes.

2.4.2. Physicochemical and structural characterization

Elemental analysis

The determination of the content of carbon (C), oxygen (O), hydrogen (H), nitrogen (N) and sulphur (S) was based on the complete combustion of a sample applying a thermal treatment at high temperature, about 950 °C, in a stream of oxygen. The combustion products such as CO_2, H_2O, N_2 and SO_2 are measured typically using infrared spectroscopy. For the determination of the oxygen content, the sample is heated up to 1070 °C under inert atmosphere provoking the liberation of different gas molecules (CO, CO_2, H_2O). This gas mixture is passed through a bed of graphite powder to reduce them to CO, then, CO is oxidised to CO_2 in a CuO catalysts and it is detected by a chatarometric detector. Analyses were carried out by a THERMO SCIENTIFIC-FLASH2000 analyser.

The oxygen content was also measured (not calculated by difference). For comparative purposes and to eliminate the moisture, all the samples were previously dried under vacuum at 120 °C for 17 h.

Surface pH and pH of the point of zero charge

The surface pH of the materials was measured in an aqueous suspension containing 0.4 g of carbon sample powder added to 20 mL of distilled water. After equilibration under stirring overnight, the pH value was measured using a glass electrode. The pH of the point of zero charge (PZC) - the pH at which the net surface electrical charge (average of positive and negative charges) is zero- was determined by a mass titration method [Noh 1989; Ania 2007]. The experimental procedure consists in the dispersion of a fix amount of material in a suitable volume of distilled water; the suspension is continuously stirring under a nitrogen atmosphere at room-temperature until equilibrium is attained (*ca.* 48 h). After equilibration, the pH value is measured using a glass electrode; then distilled water is added to the suspension in order to obtain a new dispersion with lower solids concentration. Typical dispersions of the materials in water employed were 2, 4, 6, 8, 10 and 12 % (wt./wt.). The representation of the equilibrium pH versus solid weight percentage is a curve showing a plateau at high solids concentrations, which is taken as the PZC value of the material (typically between 8-12 wt.%).

Thermal analysis

The thermogravimetric analysis was carried out in a Labsys Setaram thermobalance. A continuous N_2 flow of 50 mL/min and a heating rate of 10 °C/min up to 900 °C of final temperature were employed for the analysis. For the samples obtained at high temperature (e.g., graphite, graphene-like and carbon black), an air flow was used as reactive atmosphere (100 mL/min). The amount of sample used for each experiment was *ca.* 20 mg.

X-Ray photoelectron spectroscopy

XPS experiments were recorded in a PHI 5000 VersaProbe II apparatus (Physical Electronics), using monochromatic Al-Kα (1486.6 eV) radiation and a dual beam charge neutralizing system. Spectra of the dried films were recorded using a 100 μm beam size, operating at 25 W and 15 KV, and using a pass energy of 23.5 eV and a 0.2 eV step size for 50 sweeps. Semi-quantitative elemental surface analyses were obtained from the survey spectra with the corresponding sensitivity factors. Processing of the collected spectra was performed using energy values referenced to the C 1s peak of adventitious carbon located at 284.6 eV, and a Shirley-type background function [Wagner 1979]. After acquisition of the spectra, MultiPak™ software package was used for data analysis. A Shirley type background was subtracted from

the signals and the recorded spectra were fitted using Gauss Lorentz (90:10) curves, in order to determine the core levels of the binding energy of each element.

Transmission electron microscopy

Transmission electron microscopy (TEM) was used to characterize the morphology of the samples, as well as the as the size and shape of the metallic nanoparticles. TEM measurements were carried out with a Philips CM200 instrument working at 200 kV with LaB6 cathode. Powder samples were dispersed in ethanol upon sonication for 10 min, and deposited on a holey carbon film supported by a copper grid.

Raman spectroscopy

Raman spectra were recorded in ambient conditions in a Renishaw InVia Qontor spectrometer equipped with 514.5 nm laser. The spectra were collected under a Leica DM2500 optical microscope with a x50 long working distance objective (*ca.* 10 mm). The scattered Raman light was dispersed by a holographic grating of 600 grooves/mm, in order to acquire the whole range of interest for carbons (500-5000 cm^{-1}). Each spectrum was recorded with an integration time of 5 s; data presented represents the average of three measurements. Raman imaging was performed using the fast Streamline mode of the spectrometer setup. A zone of *ca.* 180 x 115 μm^2 on the samples was scanned with a step of 1.3 μm in two dimensions (accounting for the spatial resolution), resulting in 12000 acquired spectra recorded over 19.5 h of experiment. The LiveTrack™ mode was used, allowing to maintain the focus automatically during the measurements whatever the surface state, which becomes essential when recording powders. Wire™ software was used to remove cosmic rays, and to perform the spectral curve fitting (line positions are obtained by a classical Gaussian/Lorentzian fitting process).

In the case of carbon materials, first-order Raman spectra (1100-1800 cm^{-1}) of most carbon forms contain two characteristic peaks labelled as G band (or graphitic band) at ~ 1580 cm^{-1} and D band (or defect band) at ~ 1360 cm^{-1}, which are related to the vibrations of the sp^2 building blocks in carbon materials and their defects, providing information on the structural order and disorder. As D band is associated to structural disorder, it grows up in terms of intensity with an increment of the disorder in the material; as a consequence, the ratio of the intensities of the D and G bands is indicative to the structural disorder. The second order Raman spectra (between 2300 and 3300 cm^{-1}) show a predominant 2D band associated with the structural order. However, theoretical and experimental studies have indicated the existence of other bands in non-crystalline nanoporous disordered carbons related to various defect-induced phenomena [Cançado 2011; López-Díaz 2017]. A broad shoulder can be appeared between the D and G peaks namely the D'' (~ 1500-1550 cm^{-1}) and is related to

amorphous phases. Another band ($\sim$ 1150-1200 cm^{-1}), D*, is related to disordered graphitic lattices provided by sp^2-sp^3 bonds. Other defect-related features such as D' and D+D' bands can be observed.

Nuclear Magnetic Resonance

Solid-state Nuclear Magnetic Resonance (ssNMR) offers information about structural and dynamic properties. However NMR in solids presents considerable difficulties. In a static solid sample, each part of it has a different orientation relative to the external magnetic field. The static NMR spectra of systems with many non-equivalent chemical sites reveal numerous broad overlapping lines. If the solids contain hydrogen atoms, all proton spins will be coupled in a common network giving rise to very broad spectra which are useless. Proton decoupling is therefore absolutely necessary in ssNMR. Moreover in the case of ^{13}C or other heavy atom isotopes, anisotropic interactions are also important. In addition, the spin- lattice relaxation of many heavy atom isotopes is extremely slow (tens or even hundreds of seconds) making experiments unreasonably long. Thus in the case of static ssNMR analysis a considerable loss of sensitivity compared to liquid state NMR will achieve.

Andrew et al. showed that a rotation of the sample around an angle of 54.74° (Magic-Angle) with respect the external magnetic field enhances sensitivity and resolution in ssNMR measurements [Andrew 1959; Lowe 1959]. MAS in the fast spinning regime removes all anisotropic issues. At very high spinning speeds, the chemical shift anisotropy (CSA) averages out and a liquid-like spectrum with only isotropic shift contributions can be obtained. The technique of Magic-angle-spinning (MAS) is obtained by aerodynamic levitation and drive of the sample inside of a rotor.

On the other hand, for a solid material having protons in the vicinity (up to several bonds away), it is possible to increase the sensitivity and reduce the relaxation delay (thus, data acquisition time) by transferring the magnetization from protons to carbons; in other words, exciting the ^{1}H and ^{13}C together with matching spin-lock pulses in a process called cross-polarization that works via dipolar coupling. In sum, cross polarization (CP), allows magnetization exchange between the abundant ^{1}H nuclei and the much less abundant ^{13}C nuclei, with the advantage that proton spin-lattice relaxation is reasonably fast [Hartman 1962]. The combination of CP with the proton decoupling [Pines 1972] and under MAS in solid materials [Schaefer 1976] provides high resolution spectra for rigid solids. If the spinning frequency is large enough, the resolution of CP-MAS spectra approaches that of the liquid state NMR. Thus CP-MAS technique is specifically for solid state, typically of rigid samples where the dipolar interaction is very strong.

^{13}C CP-MAS (cross polarization- magic angle spinning) and ^{13}C high-power proton decoupling- magic angle spinning (^{13}C hpdec- MAS) experiments were conducted. ^{13}C NMR spectra were recorded in a Bruker AVANCE HD 750 or 300 NMR spectrometers with a 17.62 T or 7.05 T wide-bore superconducting magnet, operating at frequencies of 750.1 MHz and 300.0 MHz for ^{1}H nuclei, and 188.5 and 75.5 MH for ^{13}C nuclei respectively. The chemical shifts were reported in ppm using tetramethylsilane, TMS, as reference at 0 ppm. The resins and the carbons materials were placed in a 4 mm Bruker ZrO_2 rotor; for liquid-solid phase mixture of resins reaction mixtures in EtOH and for the resins which present some degree of viscosity disposable 30 uL Kel-F insert was used inside of the zirconia rotor. The Magic Angle Spinning (MAS) rates from 4 kHz to 14.5 kHz in Bruker double resonance MAS-NMR 4 mm probes. Several spectra were recorded, with different CP contact times, in order to optimize the parameter for generating the spectra. Phenylalanine was employed to set up the experimental parameters for Hartman-Hahn conditions for the ^{13}C CP-MAS. The CP-MAS experiments lasted 3-4 days.

CHAPTER 3

Light-induced synthesis of polymeric nanoporous carbons - *Proof*

of concept

3.1. Introduction

A great variety of porous carbon materials has been prepared through the polycondensation of hydroxylated benzenes (such as phenol, catechol, resorcinol, phloroglucinol, tannic acid...) with an aldehyde (e.g. formaldehyde, furfural...), followed by the carbonization of the polymeric resins [Al-Muhtaseb 2003; Job 2007]. However, the preparation of the polymeric resins proceeds through several complex multi-stage reactions: polymerization, crosslinking, curing, and sometimes drying steps. All this typically turns out in long synthetic times, at least 2-3 days, to obtain the carbon precursor.
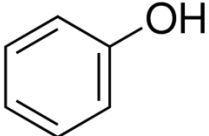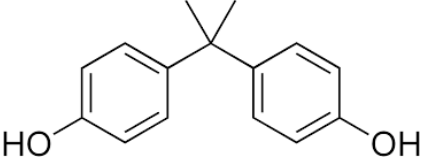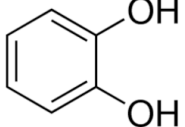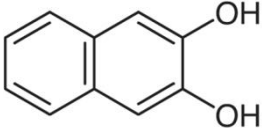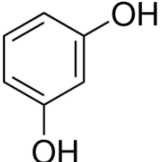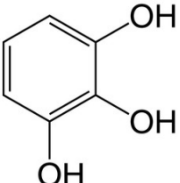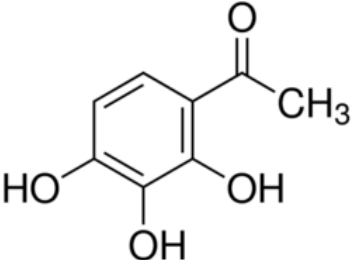
In this PhD thesis we have explored a new concept for the preparation of such carbon materials with tunable nanopore structure in the nanometric range, consisting in the photoassisted polycondensation of different organic precursors in the presence of a non-ionic surfactant as a structural director (the interactions between the resin's precursor and the surfactant are expected to direct the shape, the secondary mesostructured and hence to control the growing polymer chain. The obtained polymer resins were further carbonized to obtain the carbon materials.

To demonstrate the feasibility of this new photoinduced methodology, a set of different polyhydroxylated benzenes was selected as organic precursors (OP). The selected compounds are summarized in Table 3.1. To evaluate the link between the functionalization of the OP and the physicochemical properties of the prepared materials, organic compounds with different functionalization were selected: bisphenol A (**BP**), as an example of linear di-phenolic molecule with the two interconnected hydroxyphenol molecules; 2,3-dihydroxynaphtalene (**DN**) as polycyclic aromatic dihydroxybenzene (a fused pair of benzene rings); pyrogallol (1,2,3-trihydroxybezene, **PG**), trihydroxylated benzene with the–OH groups in adjacent positions; and gallacetophenone (2,3,4-trihydroxyacetophenone, **GA**), a trihydroxylated benzene with the hydroxyl groups in adjacent positions (asPG), also featuring additional functionalization of the aromatic ring.

It should also be highlighted that most of these **OP** were employed for the first time for the synthesis of polymeric resins; on the other hand phenol (**PH**), and 1,2- and 1,3-dihydroxybenzenes, catechol (**CT**) and resorcinol (**RS**) have been widely used for this purpose [Job 2007; Al-Muhtaseb 2003; Haro 2011; Macias 2013, 2016], and have been employed for comparative purposes. In addition, the selected aldehyde (glyoxal) is a biodegradable reactant with low toxicity, and has shown a high potential as a substitute for other aldehydes, e.g. for formaldehyde, the most

commonly used reactive in the literature [Al-Muhtaseb 2003; Rasines 2015a, 2015b], which is toxic by inhalation, swallowed and contact with the skin.

Table 3.1. Nomenclature assigned to the polyhydroxylated aromatic organic precursors (OP) selected for the study, including molecular formula and IUPAC names.

Organic Precursor (OP)	Nomenclature	Molecular Structure
Phenol IUPAC name: hydroxybenzene C_6H_6O	PH	
Bisphenol A IUPAC name: 4,4'-(propane-2,2-diyl)diphenol $C_{15}H_{16}O_2$	BA	
Catechol IUPAC name: benzene-1,2-diol $C_6H_6O_2$	CT	
Dihydroxynaphtalene IUPAC name: naphthalene-2,3-diol $C_{10}H_8O_2$	DN	
Resorcinol IUPAC name: Benzene-1,3-diol $C_6H_6O_2$	RS	
Pyrogallol IUPAC name: Benzene-1,2,3-triol $C_6H_6O_3$	PG	
Gallacetophenone IUPAC name: (2,3,4-trihydroxyphenyl)ethan-1-one $C_8H_8O_4$	GA	

3.2. Photo-assisted synthesis of polymeric resins

The photoassisted condensation reaction of glyoxal with the different organic precursors (i.e. PH, BA, CT, RS, DN, PG or GA) in the presence of Pluronic F127 as soft-template was carried out under UV light at ambient conditions and using HCl as catalyst (see experimental details in Chapter 2). The choice of HCl as catalyst (i.e. the reaction underwent under strong acidic conditions, pH~ 1), was based on the literature describing its ability to catalyse the condensation of polyhydroxylated aromatic derivatives and aldehydes through an electrophilic aromatic substitution [Mulik 2007; Granado 2019]. In our experimental conditions, it may also contribute to enhance the assembly between the hydrophilic segments of the surfactant (i.e., polyethyleneglycol blocks) and the hydroxyl groups of the organic precursor. The evolution of the reaction upon illumination of the reactants ´mixtures (OP_rm) was monitored by UV-visible (UV-VIS) absorption spectroscopy (Figure 3.1).
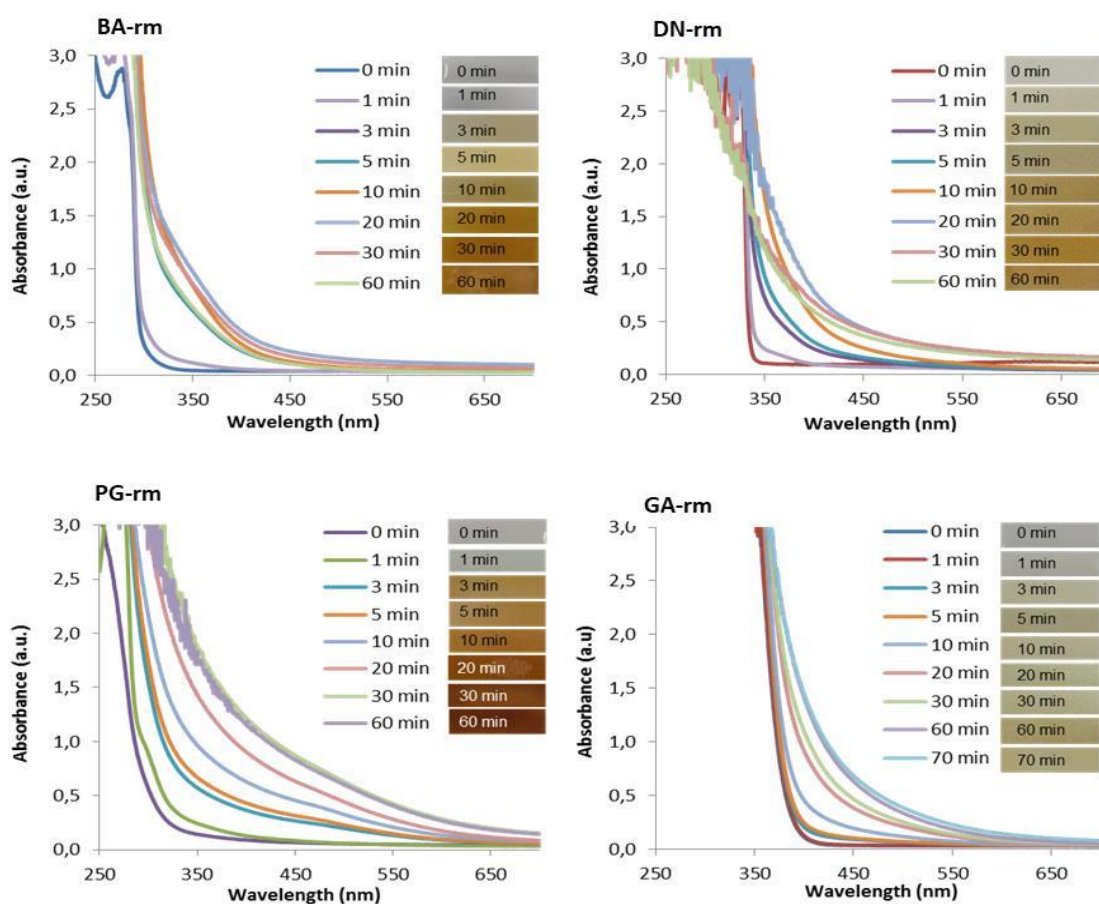
Figure 3.1. Evolution of the UV-VIS spectra for selected reactants mixtures (OP_rm) upon exposure to UV light.

The UV-VIS spectra of the initial reactants' mixtures absorbed between 200 and 400 nm. In all cases the solutions slowly darkened during the UV exposition, indicating that a photoassisted reaction took place (likely polymerization and/or oxidation of the precursors). It was possible to observe how the absorbance gradually increased with the exposition time. Moreover, the solutions not only gradually got darker with the irradiation time, but also denser, until a viscous but homogeneous brownish resin was formed (no phase separation was observed). This suggested that the condensation of the OP rendered a homogenous mixture **at macroscopic level** (Figure 3.2), and that the surfactant is either embedded inside the resin, or incorporated to it.
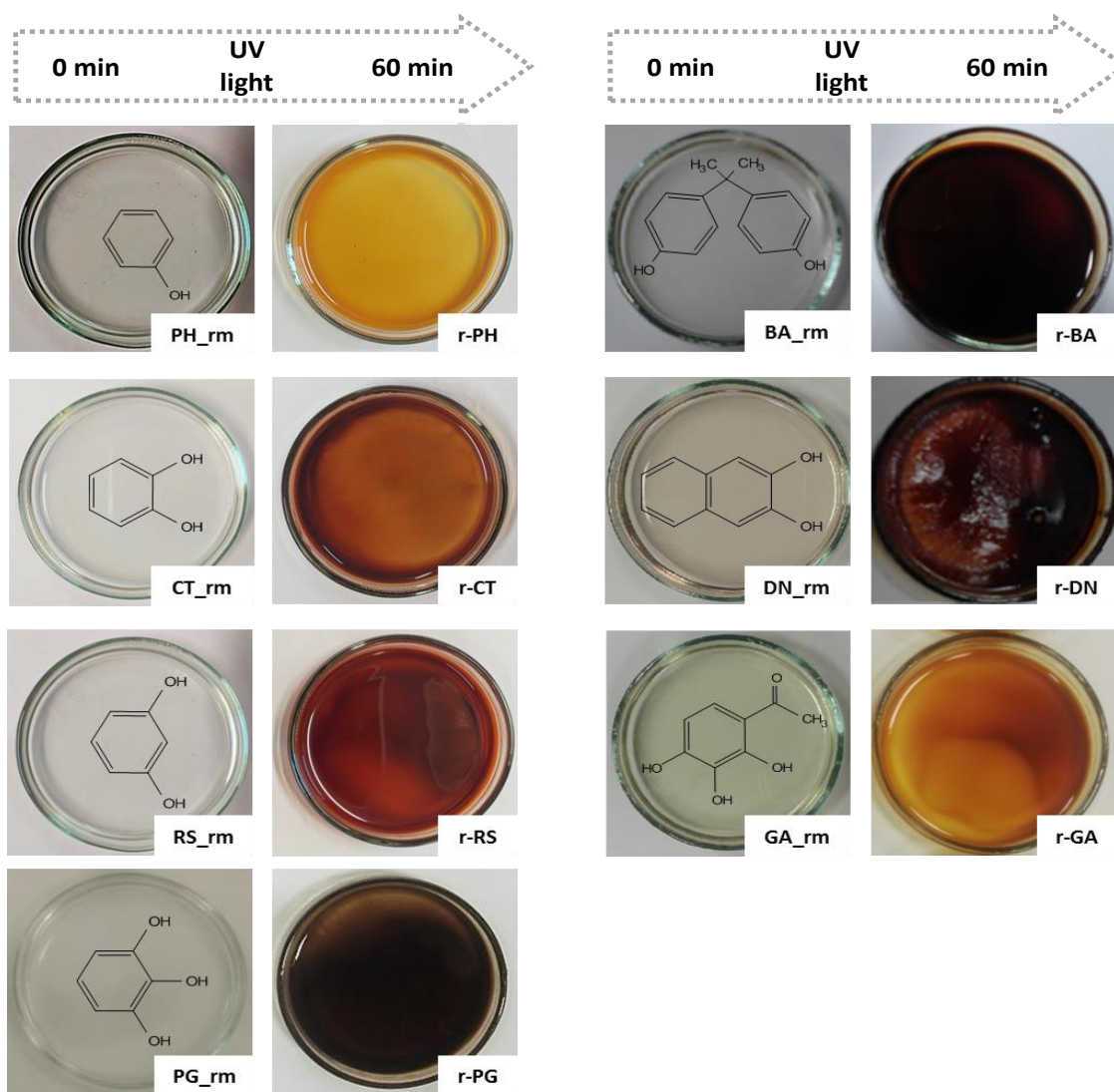
Figure 3.2. Visual changes in the starting precursors' solutions after UV irradiation: OP_rm denotes the precursors reactant's mixture at 0 min, and r-OP denotes the resin obtained after 60 min UV irradiation.

For all of them 60 min of irradiation was enough time to obtain the brownish resin. However the resins presented some differences between them; regarding appearance, resins prepared using PH and GA as precursors were lighter, with a golden yellowish colour. The ones prepared from CT and RS exhibited light brown and reddish colours, respectively, and those obtained from for PG, DN and BA were dark brown. The same differences were found in the viscosity of the samples (visual inspection), with resins from PH and GA (most faded, colorless) being the least viscous ones. However it was observed that longer exposures (e.g. 70 min) did not increase the absorbance, nor significantly modify the resin mass yield for any of the studied organic precursors. Hence, 60 min was fixed as optimized irradiation time. The as-obtained resins (r_OP) were recovered (scratched-out) from the glass dishes and analysed without any the need of further solvent evaporation or curing step.

3.3. Thermal treatment

To obtain carbon materials, a thermal treatment of the resins is necessary. For this, a thermogravimetric analysis under inert atmosphere was initially carried out to evaluate the thermal stability of the different prepared resins (Fig.3.3.a.). Differences in the overall mass loss (wt.%) and decomposition temperature (i.e., thermal stability) were observed for the precursors and their corresponding resins.

The thermogravimetric profiles show that the main mass loss for the resins appears at higher temperatures (between 300 and 400 °C) than those of their corresponding organic precursors (Figure 3.3.b). The fact that the resins (after UV exposition) showed higher stability than the organic precursors, suggested that the photopolymerization of the reactants took place, rather than just the evaporation of the solvent coupled to a partial oxidation of the reactants. Furthermore, the considering the differences in the profiles of the OP and the resins, the presence of residual amount of unreacted reagents in the resin can be discarded in all the cases, with the exception of GA. For the latter, the derivative curve showed a peak at around 238 °C, which is near the decomposition temperature of pristine gallacetophenone, 235 °C (Figure 4.3). On the other hand, given the large excess of glyoxal employed in the synthesis, this second peak in the thermogravimetric profiles might also be interpreted as the occurrence of two different polymerization mechanisms for this precursor. Thus, two different resin matrices with different thermal stability would be displayed in the thermal profiles.
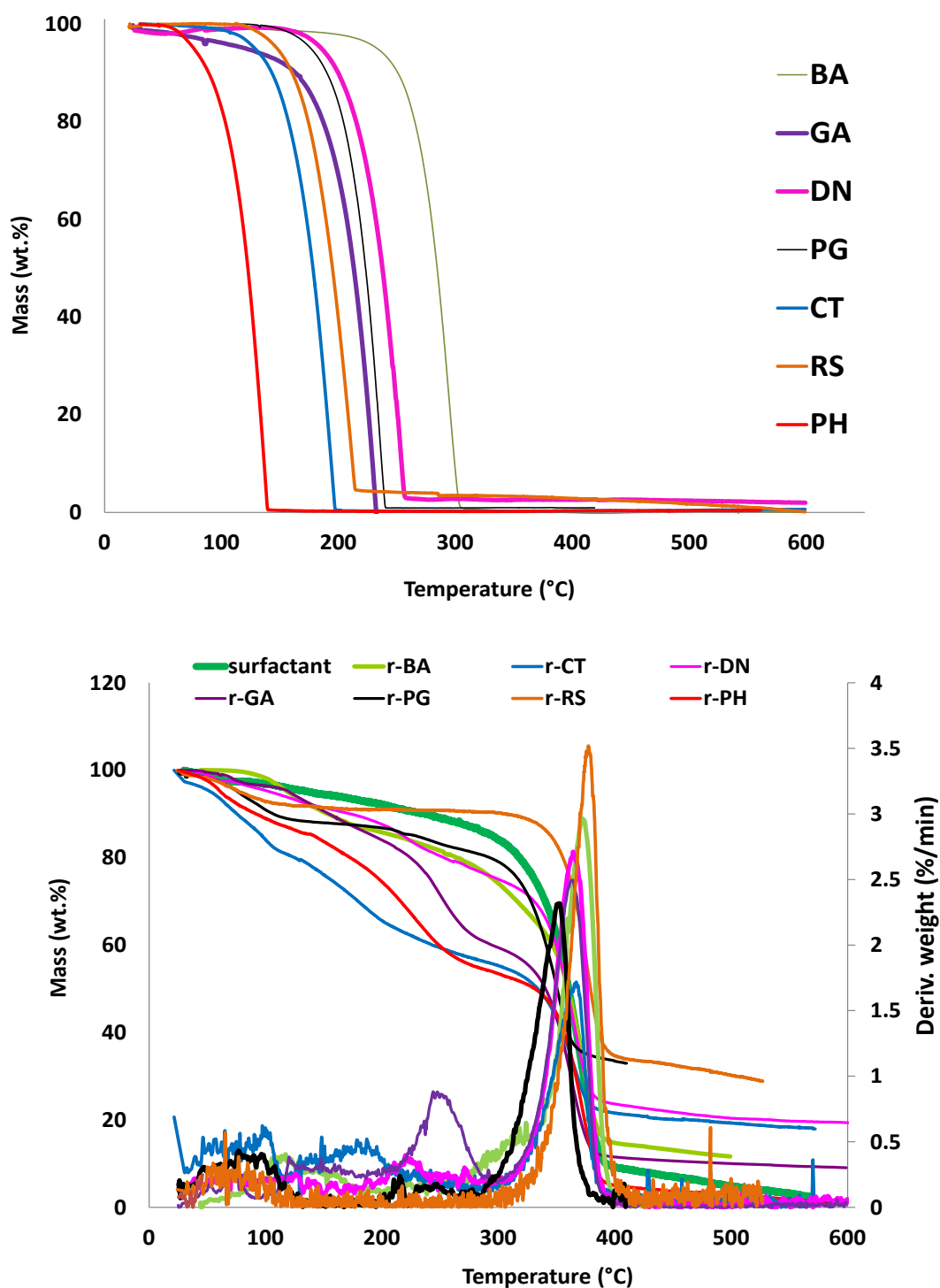
Figure 3.3. Thermogravimetric profiles under inert atmosphere of (top) the organic precursors and (down) the photopolymerized resins after 60 minutes of UV exposure (r-OP). The profile corresponding to the surfactant is included for comparison purposes.

It should be noted that the thermal profiles of the organic precursors (Fig.3.3.b.) displayed just a main weight loss, despite their different composition. For example, the gallacetophenone thermal profile showed one broad peak centred at 235 ºC, despite the molecule has two different structural motifs (i.e., hydroxyl and ketone groups). This indicates that, under the experimental conditions used, it is not possible to differentiate if various steps take place during the decomposition of the organic precursors. On the other hand, the main peak centered at 350 °C appears at a temperature close to that corresponding to the decomposition of the surfactant used as template (pluronic F127). This could be attributed partially to the presence of an excess of surfactant in the resin.

In any case, above 500 °C the decomposition was almost complete for all of the resins and the mass loss remained almost unchanged. For this, 600 °C was the selected temperature for the thermal treatment of the resins in order to obtain a carbon material. The carbonized samples are labelled as C-OP, bine OP the corresponding organic precursor.

The carbonization yields of the photopolymerized resins are shown in Table 3.2. As seen, the values strongly depend on the organic precursor, and ranged from 9 wt.% for the resins prepared from PH and GA, to 21 and 24 wt.% for RS and PG, respectively. **This finding suggests that the resins present different degree of crosslinking depending on their molecular structure, rather than on the type or number of functional groups.**

Table 3.2. Carbonization yields of the photopolymerized resins after carbonization at 600 °C.

(wt.%)	C-PH	C-CT	C-RS	C-BA	C-DN	C-PG	C-GA
Carbonization Yield	9	17	21	21	11	18	9
Carbonization Yield[a] (resin basis)	21	39	49	26	42	54	21
OP Carbon [b]	77	65	65	78	75	57	57

[a] Experimental carbonization yield recalculated on the basis of the resin (i.e. without considering the mass of Pluronic F127).
[b] Carbon content in the organic precursor, considering the molecular formula.

This is in good agreement with the differences in the physical appearance of the resins, as discussed above (Figure 3.2). Resins obtained using phenol and gallacetophenone as precursors showed a less notorious darkening upon UV irradiation, pointing out that the darkening could be related to the degree of cross-linking of the precursors. Besides this, there is no clear correlation between the carbonization yields and other parameters such as the molecular weight of the precursors, their thermal stability, or their functionalization.

Regarding the DTG curves of the carbon materials (Fig.3.4) similar thermal profiles were obtained for all the samples (in terms of profile shape, mass loss and thermal stability). Overall mass losses of about 10-12 wt.% were obtained for all the samples. As expected based on the carbonization temperature, the main mass loss occurred above 600 °C, and is attributed to the decomposition of the volatile matter remaining on the carbons after carbonization and/or to decomposition of surface functionalities anchored in the matrix.
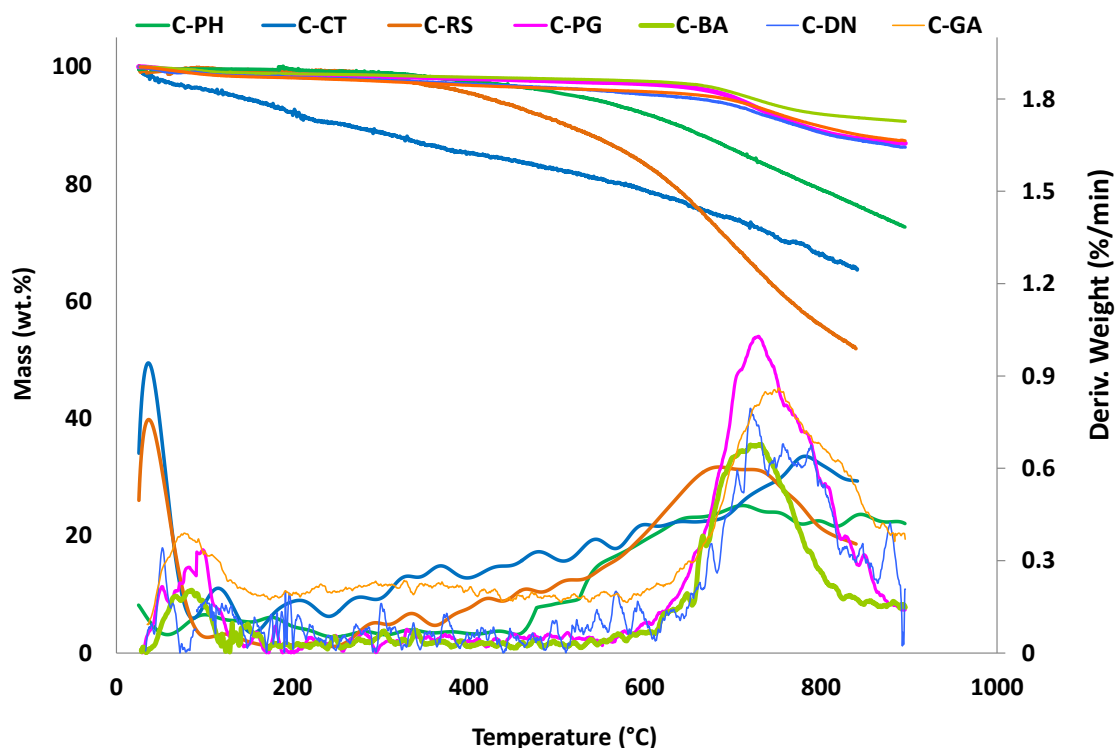
Figure 3.4. Thermogravimetric profiles under inert atmosphere of the carbons prepared by carbonization of the photopolymerized resins at 600 °C (series C-OP), mas loss (left axis) and derivative weight signal (right axis).

3.4. Physicochemical characterization of the carbons

The chemical features of the samples were analysed by elemental analysis, surface pH and XPS. As shown in Table 3.3., all the carbon materials exhibited a carbon content higher than 90 wt.% and moderate oxygen contents following the trend: BA< DN< GA< PG. The highest oxygen content values, (i.e., highest retention of oxygen) were found for C-GA and C-PG, which seems reasonable considering that both organic precursors present a higher oxygen content that is expected to be incorporated to the carbon matrix during the cross-linking reactions. The surface pH ranged from 7.3 to 9.1 for all the carbons, indicating their rather basic nature. This suggests that the oxygen is predominantly incorporated in the form of quinones, ether and/or O-bridge (basic nature functional groups), rendering carbons of hydrophobic nature [Bandosz 2006; Ania 2013].

Table 3.3. Carbonization yields (wt.%), elemental analysis (wt. %) and surface pH of the carbon materials obtained from different precursors after carbonization of the photopolymerized resins at 600 °C.

	C-BA	C-DN	C-PG	C-GA	C-PH	C-RS	C-CT
Carbonization Yield	11	18	23	9	9	21	17
Carbon	92.5	92.1	90.3	91.6	94.6	93.8	93.7
Oxygen	4.7	5.0	7.4	6.1	3.8	4.4	4.6
Hydrogen	2.8	2.9	2.4	2.3	1.6	1.8	1.7
Surface pH	8.3	7.3	8.3	9.1	8.6	8.2	8.4
OP Carbon [a]	78.9	74.7	57.1	51.6	77	79	65
Carbon (at. %) [b]	91.5	95.5	95	96.1	--	--	--
Oxygen (at. %) [b]	8.5	4.5	5	3.9	--	--	--

[a] Carbon content considering the formula of the organic precursor, OP (i.e. BA, DN, PG and GA).
[b] Evaluated from XPS spectra (at. %).

Further information about the composition of the carbonized samples was obtained by XPS. The atomic concentrations of surface carbon and oxygen surface are compiled in Table 3.3. The relative distributions of the different species (Fig. 3.5.) were obtained by deconvolution of the C 1s and O1s core level peaks. The amount of surface oxygen followed a similar trend than that obtained from elemental analysis. This confirms a homogenous distribution of the oxygen in the bulk and surface. The C 1*s* core level spectrum was deconvoluted in carbon in sp^2 configuration, and the contributions at 286.3, 287.3 and 288.5 eV were assigned to phenolic and/or ether (C-O), carbonyl (C=O) and carboxylic groups (O=C-O), respectively. As seen, for all the samples the majority of carbon is in Csp^2 configuration, and ca. 3-6 % in oxidized forms in various oxygen environments.
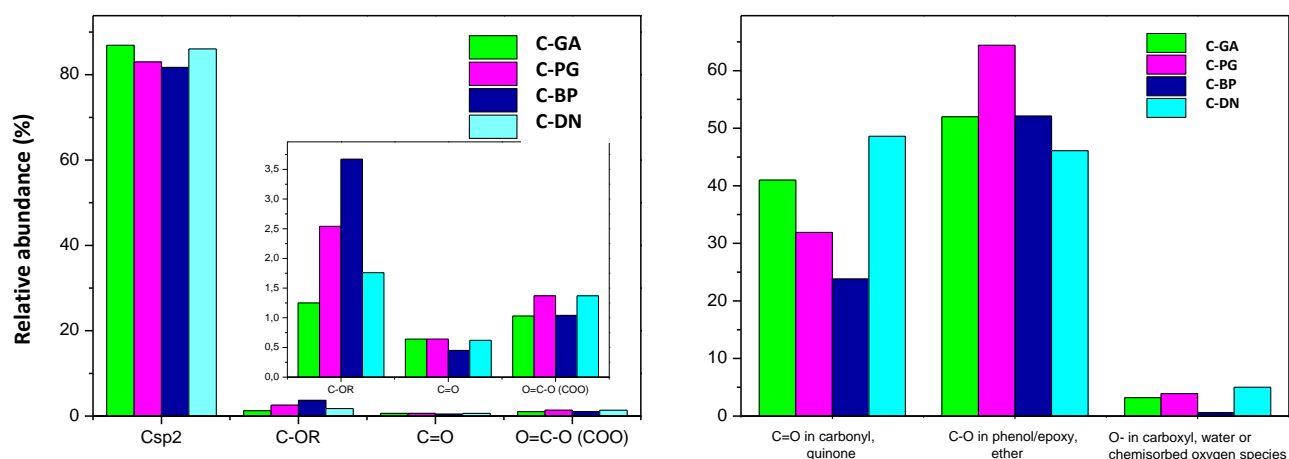
Figure 3.5. Relative abundance of carbon and oxygen species in various environments obtained by fitting the C1s and O1s core level peaks, respectively, of the XPS spectra on the prepared carbons upon carbonization at 600 °C of the photopolymerized resins.

In addition, the O 1s core level broad peaks were decomposed in three contributions at 530.6-531.9 eV, 532.2-533.9 and 533.7-535 eV, assigned to carbonyl, phenol/ epoxy, ether and carboxyl, water or chemisorbed oxygen species, respectively (Figure 3.5). The oxygen is predominantly in hydroxyl, epoxy and/or ether-like configurations, with equal distributions for all the samples.

3.5. Textural analysis

To evaluate the influence of the different OP on the structure of the obtained carbons, the porosity was analysed by gas adsorption. The nitrogen and carbon dioxide adsorption isotherms at -196 and 0 °C, respectively, of the prepared carbons are shown in Fig.3.6.a. Data corresponding to the pore size distributions obtained upon analysis of the adsorption branch of the nitrogen data is also shown. The summary of the pore structure parameters are presented in the Table 3.4.
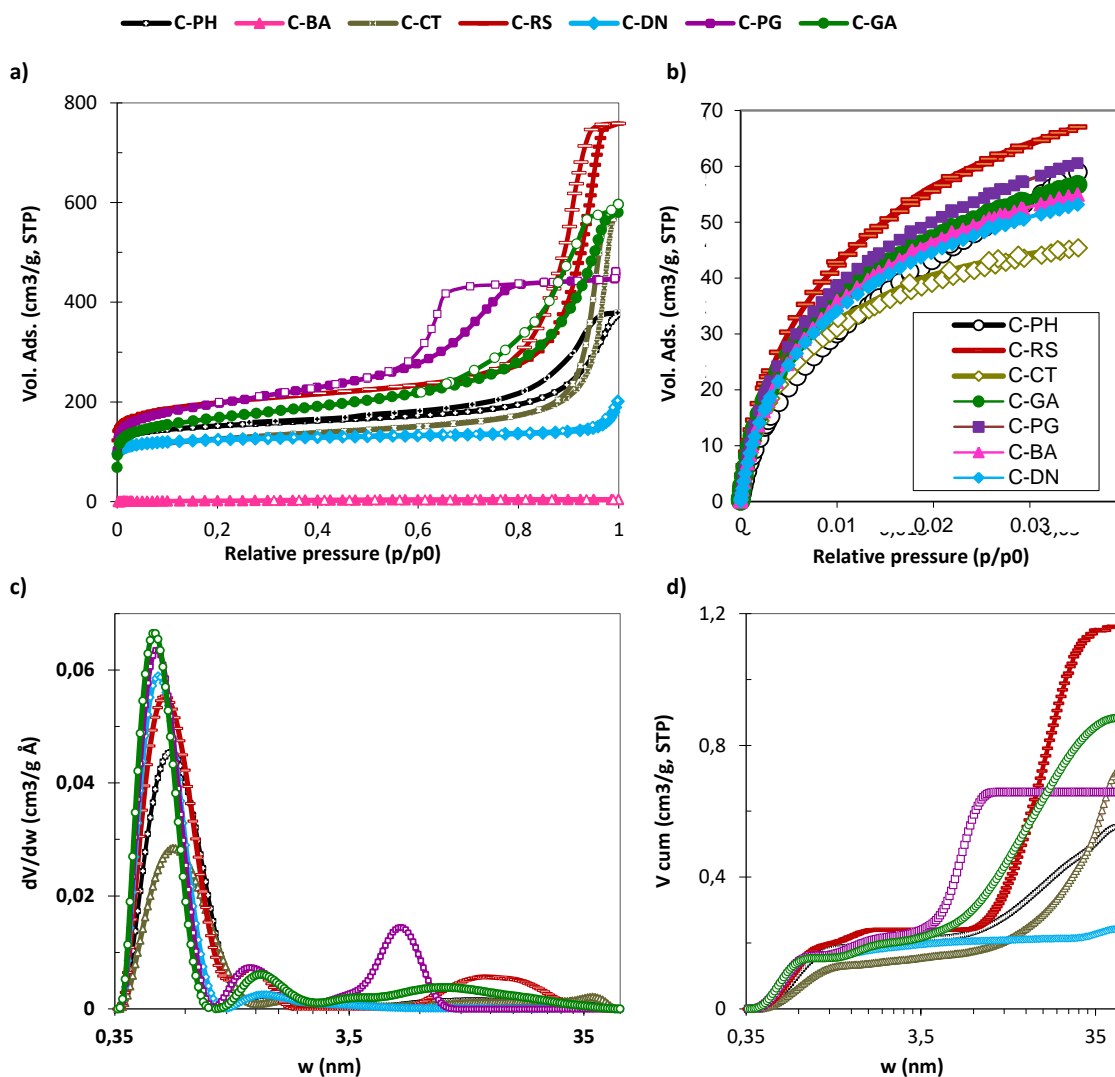
Figure 3.6. a) High resolution N_2 adsorption isotherms at -196 °C of the materials after carbonization of different photopolymerized resins from various organic precursor (full symbol: adsorption; empty symbol: desorption). b) CO_2 adsorption isotherms at 0 °C of the carbon materials. c -d) Pore size distribution (PSD) evaluated using the 2D-NLDFT-HS method from the adsorption branch of nitrogen -196 °C isotherm.

With the exception of sample C-BA, all the carbons displayed large gas uptakes, confirming the formation of nanoporosity as a result of the decomposition of the volatile matter during the carbonization of the resins. The N_2 uptake at -196 °C for sample C- BA was negligible, suggesting either a poor textural development or the presence of narrow micropores through which the diffusion of the gas at cryogenic temperatures is restricted [Thommes 2014]. To further confirm this observation, CO_2 adsorption isotherms at 0 °C were recorded (Figure 3.6.b), as this is generally accepted to evaluate the presence of narrow microporosity in carbon materials [Garrido 1987]. Data confirmed that indeed, the porous structure of C-BA is composed of narrow sized micropores, which are not accessible to nitrogen molecules at -196 °C [Cazorla-Amoros 1996; Garcia-Martinez 2000]. Interestingly, the uptake of carbon dioxide at 0 °C was quite similar for all of the carbons, as opposed to the N_2 uptake at -196 °C.

Dubinin and Radushkevich method (DR) and the Stoeckli-Ballerini equation were applied to the CO_2 adsorption isotherms at 0 °C to calculate the volume of narrow micropores (Wo, CO_2) and the average micropore size (L) respectively [Rouquerol, 2014], (Table 3.4). As a general trend, all the samples displayed similar volumes of narrow micropores, with average pore sizes of ca. 0.6 nm.

Table 3.4. Main textural parameters of the carbon materials after the thermal treatment of the resins (series C-OP) obtained from gas adsorption data.

	S_{BET}	V_{PORES}[a]	$V_{MICRO\,N2}$[b]	V_{MICRO}[c]	V_{MESO}[c]	$W_{0\,CO2}$[d]	L[e]
	(m²/g)	(cm³/g)	(cm³/g)	(cm³/g)	(cm³/g)	(cm³/g)	(nm)
C-PH	584	0.53	0.22	0.20	0.35	0.21	0.74
C-CT	439	0.79	0.17	0.14	0.58	0.14	0.56
C-RS	752	1.17	0.28	0.24	0.92	0.22	0.63
C-BA	10	0.01	0.002	0	0	0.18	0.64
C-DN	486	0.28	0.19	0.18	0.06	0.20	0.66
C-PG	720	0.69	0.22	0.214	0.445	0.21	0.63
C-GA	620	0.89	0.22	0.196	0.688	0.19	0.63

[a] Evaluated at $p/p_0 \sim 0.99$ in the N_2 adsorption isotherms at -196 °C.
[b] Micropores volume, evaluated from DR equation applied to N_2 adsorption isotherms at -196 °C.
[c] Evaluated from the 2D-NLDFT-HS method applied to N_2 adsorption isotherms at -196 °C.
[d] Narrow micropores volume, from DR equation applied to CO_2 adsorption isotherms at 0 °C.
[d] Evaluated using the Stoeckli-Ballerini equation applied to CO_2 adsorption isotherms at 0 °C

Going back to the N_2 adsorption isotherms, different features were obtained for the carbons. Sample C-DN displayed a type I (a) isotherm according to IUPAC classification [Thommes 2015],

characteristic of exclusively microporous materials. The marked knee of the isotherm at relative pressures below 0.1, and its reversibility over the entire pressure range, indicates that the porosity is composed of micropores, with an almost negligible contribution of mesopores.

For the rest of the series, the N_2 adsorption isotherms displayed type IV(b), with the presence of pronounced hysteresis loops (e.g., irreversibility between the adsorption and desorption branch at relative pressures above 0.3, associated to delayed capillary condensation in mesopores). The differences in the shape of the hysteresis loops are associated to the size, accessibility and distribution of the mesopores. A typical feature of Type IV isotherms is a final saturation plateau, easily observed for C-PG, and less visible for the rest of the samples due to the fact that the hysteresis loops is shifted upwards towards relative pressures close to unity. In the case of C-PH and C-CT, the nitrogen adsorption isotherms feature a well-defined knee at low relative pressure and the hysteresis loops at high relative pressures, indicating the presence of micropores and large mesopores. Interestingly, the adsorption branch of the isotherms was almost parallel to the abscise axis in the range between 0.2-0.7 relative pressures, indicating the lack of medium sized mesopores.

For C-RS and C-CT, the hysteresis loops (spanning from ca. 0.7 to 0.97 relative pressures) belong to type H1 according to IUPAC classification, with almost parallel adsorption/desorption branches over the gas uptake. This type of behaviour indicates materials with a narrow range of uniform mesopores (e.g., MCM-41, SBA-15), although it has also been reported for carbons with large ink-bottle mesopores, where the width of the neck is similar to the width of the main mesopore cavity [Thommes 2014].

In the case of C-PH and C-GA, the hysteresis loop expands over a larger range of relative pressures (from around 0.64 to roughly 0.97), indicating a wider distribution of mesopores. The adsorption and desorption branches displayed a sloping feature with a less parallel character, indicating type H2 loops. This is typically found in complex pore structures, where networking effects are important (i.e., desorption mechanism is influenced by the connectivity between neighbouring pores and the sizes of the necks and main cavity of the mesopores), and the pore neck widths plays an important role.

On the other hand, sample C-PG displayed a type H2 (a) hysteresis loop expanding from ca. 0.5-0.85 (hence, the average mesopore size is smaller than all of the others). The asymmetrical loop with an evaporation (desorption) branch steeper than the condensation (adsorption) one is

attributed to either pore-blocking/percolation phenomena during the emptying of porous materials (i.e., materials consisting of cavities connected to one another by constrictions, with most of the cavities having no direct access to the gas reservoir) or to cavitation-induced evaporation (i.e., the spontaneous nucleation and growth of gas bubbles in a metastable condensed fluid) [Thommes 2014]. The relative pressure of the closing loop (about 0.5, the percolation threshold of N_2 at -196 °C), suggests the presence of ink-bottle mesopores having access to the external surface through narrow necks, likely smaller than 5-6 nm. This type of H2(a) loops has been reported for silica gels, porous glasses (e.g., vycor) and some ordered mesoporous materials [Kruk 2005; Morishige 2006; Thommes 2010].

Regarding the textural parameters (Table 4.7), moderate surface areas were obtained for most of the carbons (except for C-BA as discussed above), with values ranging from 400-800 m2/g. The highest values were obtained for C-RS and C-PG. The contribution of mesopores to the total pore volume followed the trend: C-RS > C-GA> C-CAT>C-PH>C-PG>>>C-DN. No direct correlation seems to be found between this trend and the reticulation of the resin or the functionalization of the organic precursor. Interestingly, the values of narrow microporosity evaluated from the CO_2 adsorption isotherms are quite close for all the samples, regardless the composition of the organic precursor. This indicates that the latter affects mainly to large pores (medium-sized micropores and mesopores).

Figure 3.6 c-d shows the pore size distributions (PSD) of the samples obtained from the nitrogen isotherms using the 2D-NLDFT-HS method [Jagiello 2013a, 2013b]. In complex pore systems where networking effects might apply, the analysis of the PSD is not straightforward. However, the analysis of the adsorption branch can be considered as a good approximation to get a distribution of the size of the mesopore bodies (main cavities). As seen, the carbons display a wide variety of mesopore size distributions depending on the precursor, ranging from around 5 to 45 nm. Large average mesopore sizes were obtained from samples C-CT (40 nm), C-RS (15 nm), C-PH (12 nm) and C-GA (10 nm) compared to C-PG (5 nm). This is in excellent agreement with the analysis obtained from the observation of the gas adsorption isotherms, and thus validates the application of the 2D-NLDFT-HS method for the assessment of the PSD.

In order to fully characterize the mesoporosity of carbon C-PG, presenting a type H2 (a) hysteresis type typical of complex pore systems, scanning isotherms of the hysteresis loop were carried out. This methodology is useful to evaluate the nature of the networking effects in pore systems, and ideally to discriminate between the occurrence of pore blocking or cavitation effects.

It should be mentioned, that if pore blocking is the dominant mechanism, the evaporation pressure is controlled by the size of the necks (or interconnecting pores). Consequently, the analysis of the PSD using the desorption branch may be used to evaluate the size of the mesopores necks. This is not possible in the case of cavitation-induced evaporation. The recorded adsorption and desorption scanning curves corresponding to different filling/emptying states of the hysteresis loop are shown in Figure 3.7. Primary desorption scanning curves (PDSC) were recorded by reverting the isotherm before the saturation is complete (before reaching relative pressure of unity).
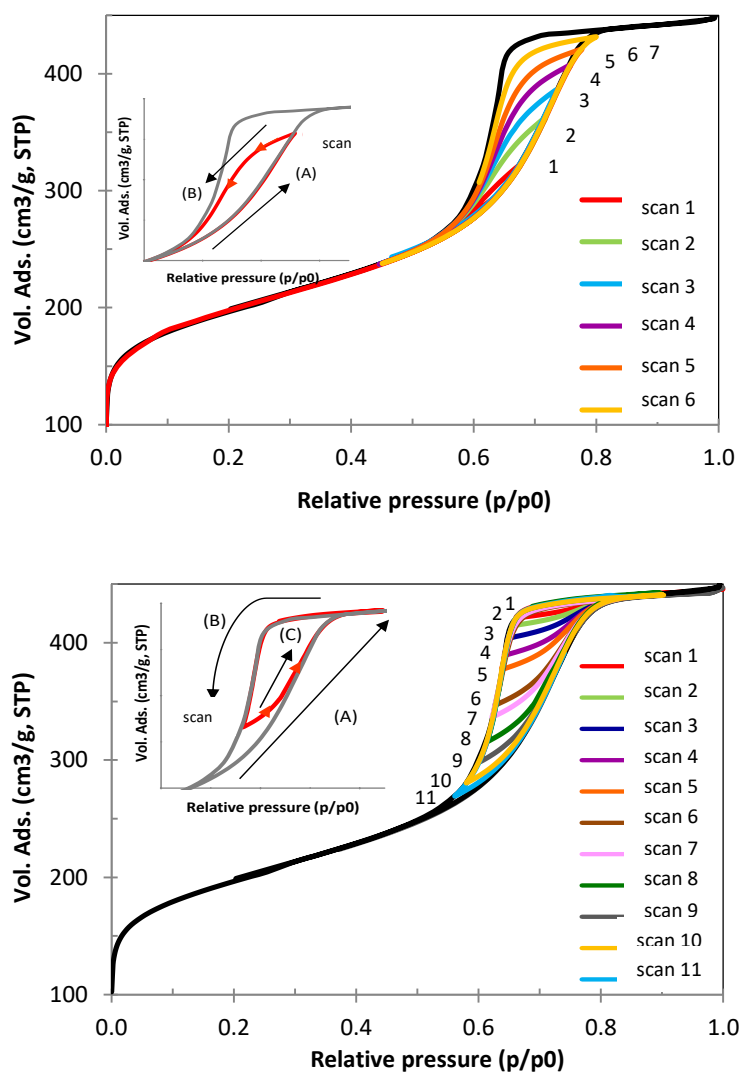
Figure 3.7. Scanning N_2 adsorption/desorption isotherms at -196 °C of sample C-PG. (a) primary desorption scanning curves (partial pore filling); (b) secondary adsorption scanning curves (partial pore emptying). Inset: schematic representation of the emptying/filling mechanisms in both cases.

51

In this situation, evaporation (desorption) starts when the porous system is not fully filled, and a filled cavity would only empty when it has a neighboring empty cavity. As a result, the hysteretic behavior of a filled cavity will depend on whether the adjacent cavities are filled or empty and the shape of the primary desorption scanning curves would differ from that of the boundary evaporation (desorption) branch.

Similarly, secondary adsorption scanning curves (SASC) were recorded by restarting the isotherm from the desorption branch before the porous system is fully emptied. In this situation, condensation (adsorption) stars when a fraction of the pores is still filled, and thus the shape of the SASC curves might differ from that of the boundary branch. In a porous system comprised of cavities connected together by constrictions (e.g., most disordered porous materials), most of the cavities would have no direct access to the gas reservoir (only indirect access through other constrictions and cavities).

Thus, if evaporation is started when the porous system is completely filled, a cavity cannot empty unless a continuous vapor path is created towards the main vapor reservoir. When this condition happens, many routes can be created and the whole porous system empties in a cascade-like manner (percolation process, giving rise to asymmetrical hysteresis loop). For clarity, a schematic representation of the PDSC and SASC is provided in the insets in Figure 3.7 a-b.

As seen in Figure 3.7a-b in the case of C-PG both the PDSC and the SASC have a similar shape than that of their corresponding boundary curves, with the main difference being the gas uptake of each scanning curve. This indicates that the emptying mechanism does not depend on the filled state of the neighboring cavities, thus pointing out to pore blocking as the main desorption pathway for this material. Thus, the evaporation of the man cavities of the pores is delayed by the constriction of the pore necks of narrower sizes. For such pore systems, the analysis of the desorption branch of the boundary and scanning curves can be considered as an accurate approximation for gathering information about the size of the pore necks (while the adsorption branch would refer to the pore cavities). Data is shown in Figure 3.8, where it can be observed that the main mesopore cavities are centered at about 4 nm, and the distribution of pore necks is quite narrow, centred at 3.8 nm.
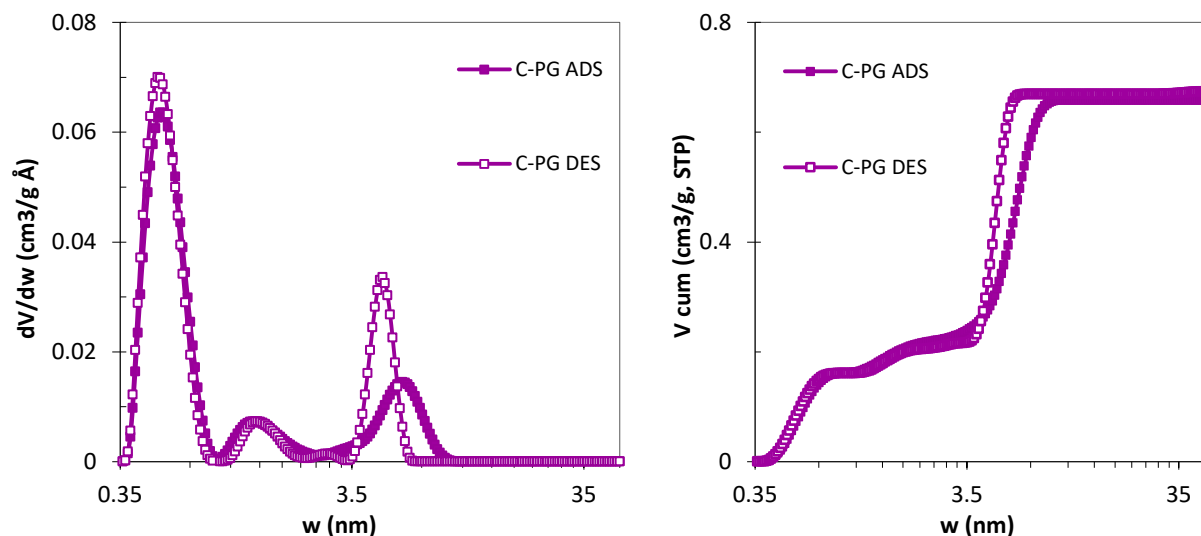
Figure 3.8. Distribution of pore sizes of sample C-PG evaluated using the 2D-NLDFT-HS method applied to desorption and adsorption branches of the N$_2$ (-196 °C) adsorption and desorption isotherms.

3.6. Morphological and structural characterization

The TEM images revealed important differences among the samples Figure 3.9, 3.10). Carbon C-BA displayed a dense structure composed of rectangular particles of nanometric dimensions (100-300 nmx 50-100 nm), which is in agreement with the low porosity measured for this material obtained by gas adsorption. This morphological feature could be related to two facts:

i) kinetic: a high reactivity or high reaction rate of BA with glyoxal (BA is well known to be a versatile building block: it is used in the synthesis of epoxy resins, is the second component or hardener in acrylate glues…). This would result in a highly cross-linked resin which would present a low interaction with the template before being condensed (too fast).

ii) mechanistic: the reaction pathway through the substitution of the –OH moieties (instead through the unsubstituted positions) which would hinder the interaction with the template.

In contrast, samples C-PH C-DN, C-RS and C-GA show the typical structure of amorphous carbon materials with disordered particle aggregates (Figures 3.9, 3.10). A closer inspection allows to point out small differences. For instance, sample DN displays ill-defined aggregates of large sizes, as well as the absence of the small voids. In the case of C-RH, small size particle aggregates with a narrow biscontinuous wormhole-like structure can be observed. Such structure of close aggregates would be in agreement with the narrow pore size distribution found for this material (ca. 10-20 nm).

53
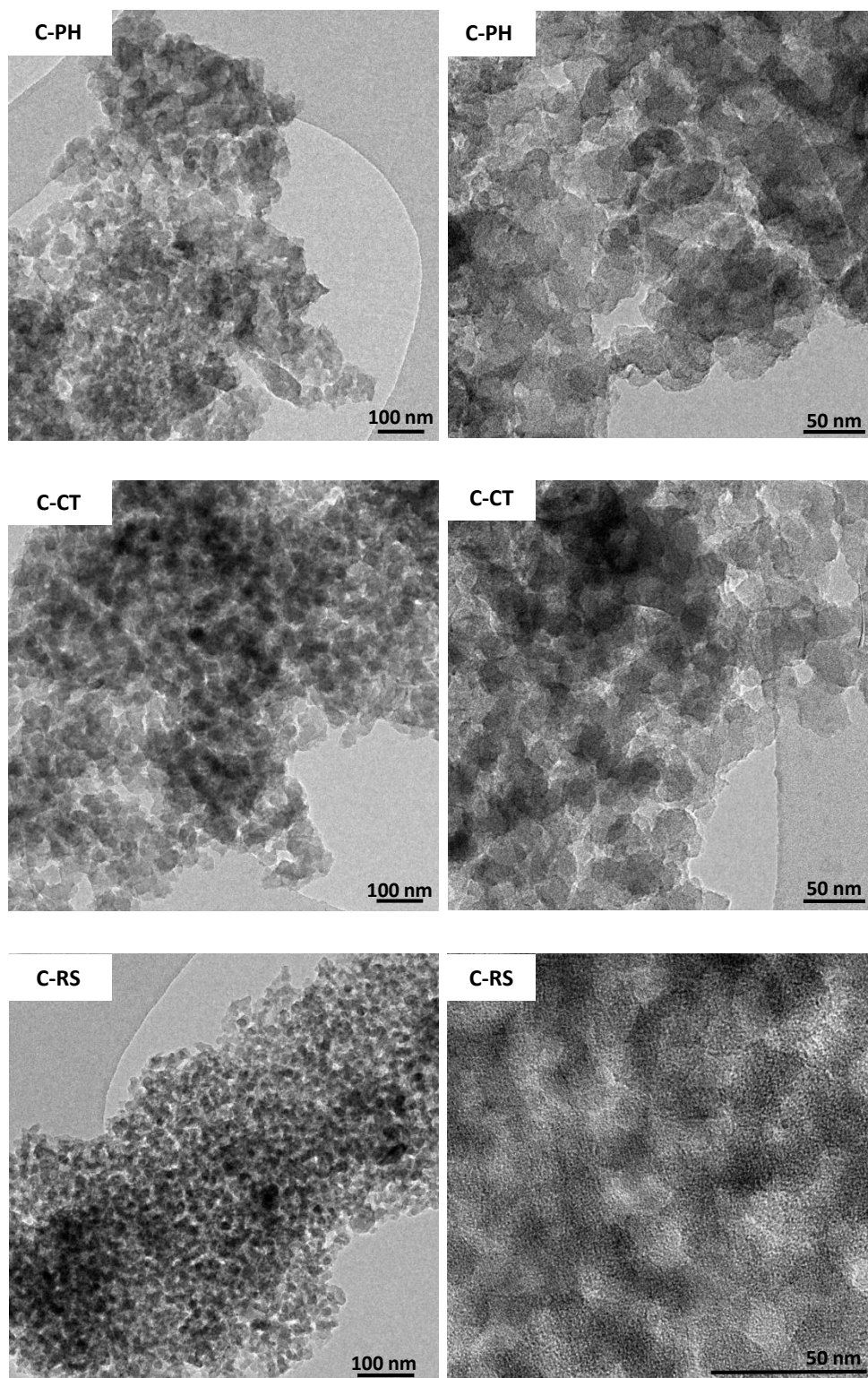
Figure 3.9. TEM images of the nanoporous carbons from the photopolymerized PH, CT, RS resins after carbonization at 600 °C.
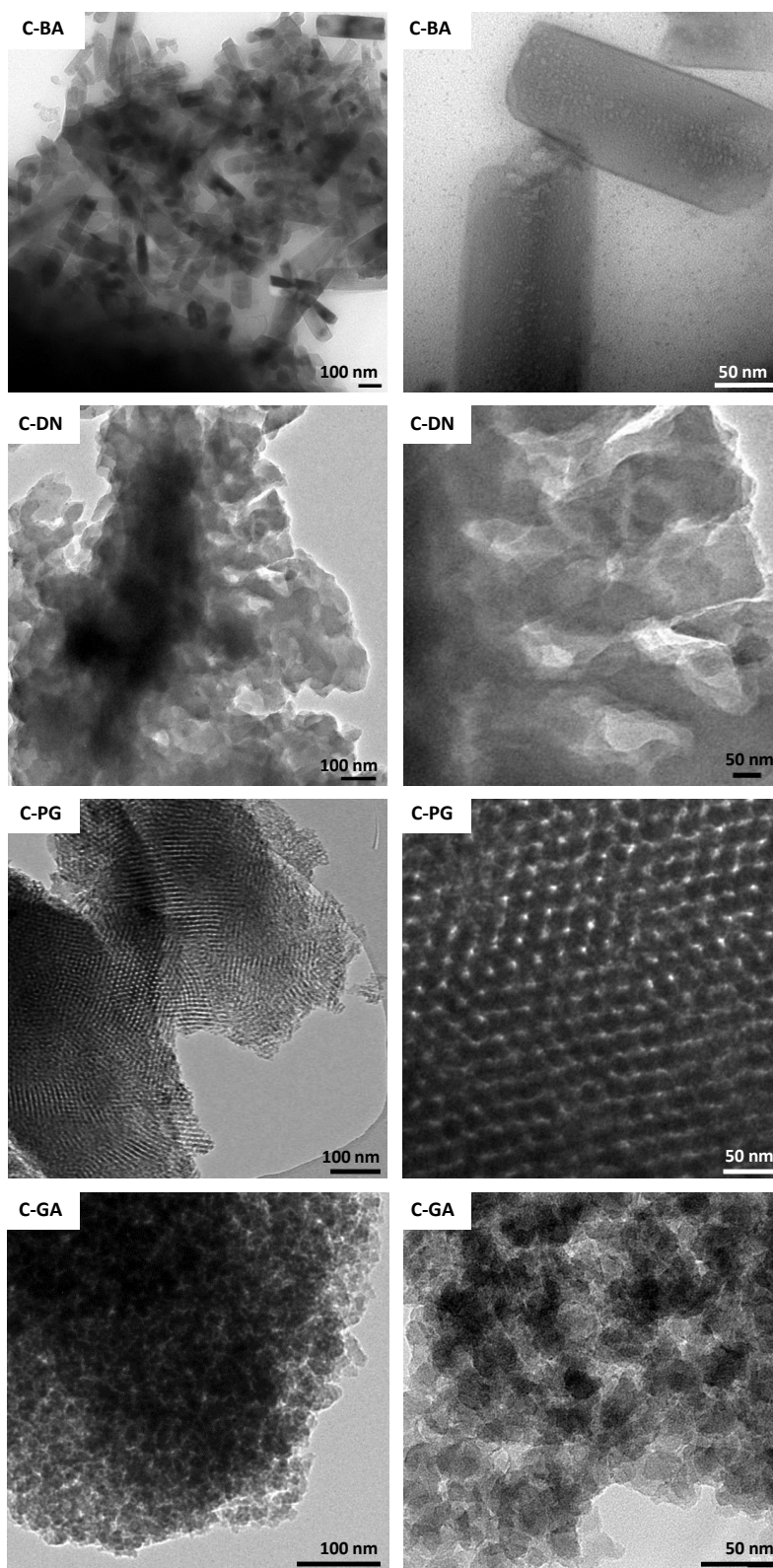
Figure 3.10. TEM images of the nanoporous carbons from the photopolymerized BA, DN, PG and GA resins after carbonization at 600 °C.

The TEM images of sample C-PG showed a fairly ordered pattern following a hexagonal symmetry typical of other ordered mesoporous materials such as SBA-15 [Liu 2010]. The TEM images confirmed the mesopore diameter of 4-5 nm which is also in agreement with the PSD data obtained from the N_2 adsorption analysis. The morphological characterization shows distinct behaviors at a microscopic level. In the first case (sample C-BA), the absence of interaction between the resin and the surfactant would prevent the formation of the mesoporous structure. Secondly, in the case of PH, RS, DN and GA, a spinodal decomposition takes place through a biscontinuous transition. Finally, for PG, a continuous dispersed phase is formed, entrapping the surfactant. In the end, at a macroscopic scale, homogenous resins would be formed due to different mechanistic situations.

The structural order of the carbons was investigated by Raman spectroscopy. The Raman spectra (Figure 3.11) showed the typical fingerprint of carbons with a rather disorganized (turbostratic) structure, dominated by the characteristic D-band (around 1350 cm^{-1}) related to the lack of long range symmetry and defects, and the G-band (around 1595 cm^{-1}) characteristic of in-plane vibrations of sp^2 bonded carbon [Ferrari, 2000]. The similarities in the Raman spectra contrast with the differences observed by TEM images regarding the morphology of the samples. This indicates that the carbon matrix present similar short-order range domains, regardless the state of the particles aggregates.

To better fit the first order spectral region, the contributions of bands D2 (D') (around 1600 cm^{-1}), D3 (D'') (around 1506 cm^{-1}) and D4 (D*) (around 1220 cm^{-1}) were introduced, following Sadezky's 5-band model (Figure 4.8) [Sadezky 2005; Jawhari 1995]. They correspond to disorder in the surface, out of plane defects, and disorder graphitic lattices and impurities, respectively.

It is also important to consider that nanoporous carbons are not graphitizable and correspond to the carbonization regime (stage 2 of the amorphization trajectory) according to the terminology proposed by Ferrari et al [2000, 2003, 2004]. According to this I_D/I_G can be used as an indicator of the size of coherent domains along the aromatic layers (i.e., La) as it is proportional to La^2 (i.e., higher I_D/I_G ratio correspond to smaller domains, i.e., more disordered structure). This is important, since the opposite conclusion would be obtained for graphitizable carbons, for which the D/G ratio is proportional to 1/La. The I_D/I_G values from the deconvolved bands followed the trend: C-DN≤ C-BA = C-PH< C-RS < C-PG < C-GA (0.61, 0.63, 0.63, 0.73, 0.78, 0.81), indicating a slightly higher structural order for C-GA.
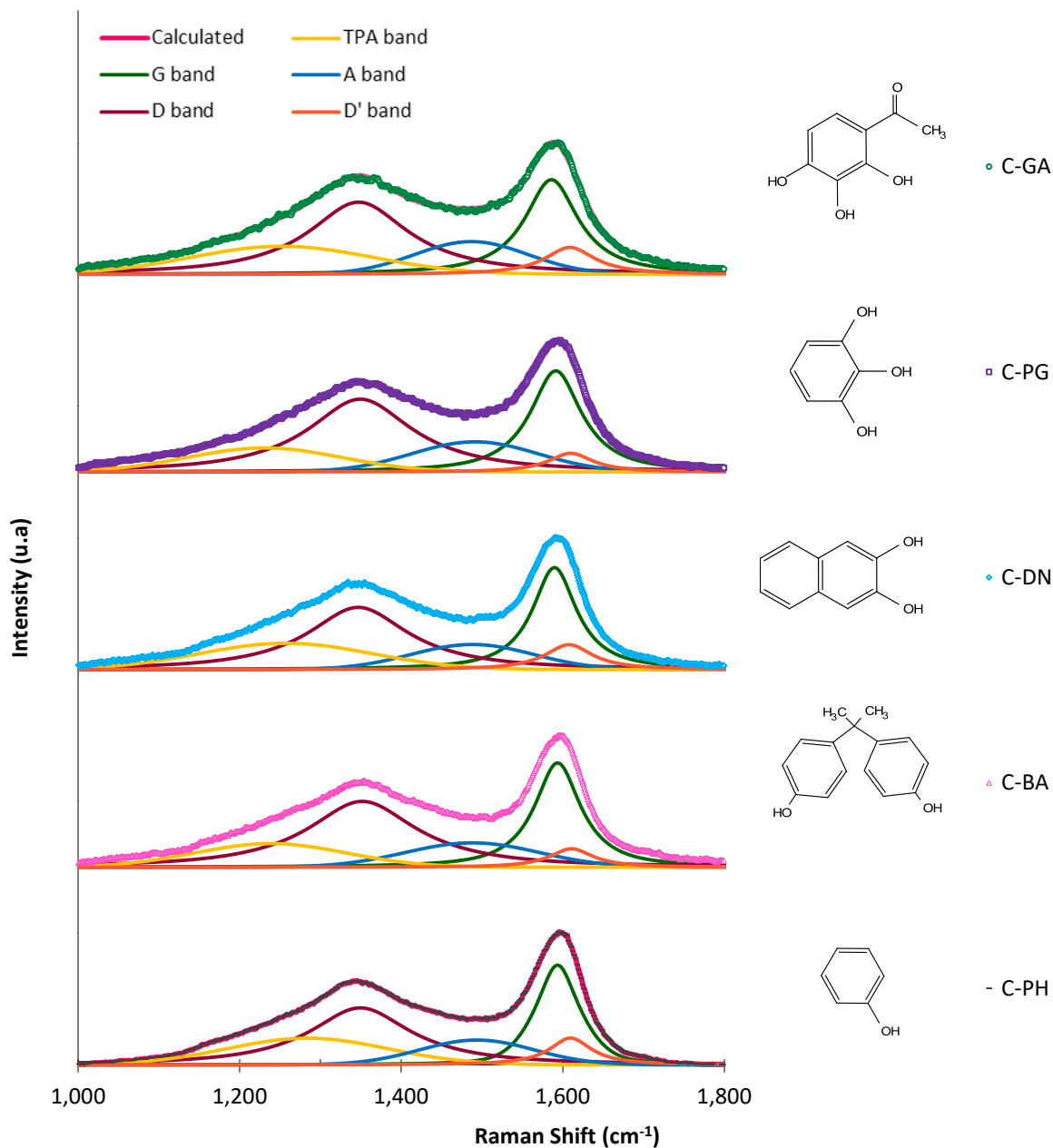
Figure 3.11. Raman profiles of the photopolymerized resins after carbonization at 600 °C. Raw data is represented in dots; calculated data after deconvolution and deconvoluted bands (TPA, D, A, G and D') are depicted in lines (see legends and color codes).

3.7. Conclusions

We have developed a simple and cost effective method for the synthesis of nanoporous carbon materials with varied textural and structural features based on the UV assisted condensation of organic polymeric precursors at room temperature for 60 min. Owing to the specificity of the organic precursors, they react differently upon UV exposure giving rise to resins, the carbonization of which renders nanoporous carbons of hydrophobic nature and varied porosity and morphology. By an adequate choice of the organic precursor, and synthetic parameters, it is possible to control the morphology, structural order and the pore size distributions of the final carbon materials within the full micro/mesoporous range.

The degree of cross-linking of the reactant is determined by the structure, as well as the number of reactive positions of the polyhydroxylated aromatic organic precursors controlled the final physicochemical properties of the carbons. Thus, the linear structure of bisphenol A gave rise to highly branched clusters that harden to form the phenol-like resin in a dense structure with close porosity mainly composed of narrow micropores. On the other hand, the aromatic organic precursors are able to assemble in large cross-linked clusters, creating a more open structure, rendering in some cases (sample C-PG) an ordered mesopore structure.

CHAPTER 4

Impact of the synthetic conditions on the development of the porosity

4.1. Introduction

In the previous chapter, we have developed a fast photoinduced methodology for the preparation of nanoporous carbons with different textural features, at room temperature in only one hour, by using HCl as catalyst [Balan 2017]. The architecture of the carbons was controlled by using different organic precursors. But the porous properties not only depend on the structure of the precursor but also in the synthetic conditions]. The type of catalyst and therefore the pH are among the main chemical parameters that control the porosity of the resulting carbons. In this regard, the HCl plays two roles; on the one hand the role of the catalyst in the polymerization reaction (favoring the formation of the carbocation by the reaction with the glyoxal (dialdheyde) inducing the polymerization through the electrophilic aromatic substitution). On the second hand, it also favors the self-assembly between the hydrophilic segments -PEO groups (polyetilenglycol-block) of the surfactant and the –OH (hydroxyl groups) from the hydroxy-benzenes present in the resin. Considering this, in this chapter we have evaluated the impact of various chemical parameters (i.e. the use of HCl as catalyst, the presence of a photoinitiator, different reagents concentration) on the textural properties and surface chemistry of the developed carbon material. To undertake the study, the photocondensation of gallacetophenone (section 4.2) and pyrogallol (section 4.3) were selected.
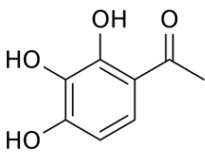
4.2. Gallacetophenone-based materials

In Chapter 3, we reported the preparation of a mesoporous carbon from the photoassisted polycondensation of gallacetophenone (sample C-GA) at acidic pH. The sample displayed a type IV(b) nitrogen adsorption isotherm, characteristic of mesoporous materials and exhibited a BET specific surface area of ca. 620 m^2/g, a total pore volume of 0.9 cm^3/g, and a distribution of mesopores centered at about ca. 14 nm (Figure 3.7, Table 3.4).

In this section, a series of materials was prepared using gallacetophenone as organic precursor as detailed in the previous chapter, but varying the pH conditions, the photoinitiator and the precursor to ethanol molar ratio (Table 4.2.1). The samples will be labeled as q-GA-X-Y where q is r or C to refer to the resin of the carbon material; X indicates the presence (H) or absence (0) of HCl, and Y indicates the presence (Ch) or absence (0) of photoinitiator. In order to explore the impact of the solvent in the synthesis, a series of samples was prepared with a lower OP/EtOH ratio (i.e., 1:40 as opposed to 1:100 used in the common synthesis described in this thesis). When such OP/EtOH ratio of 1:40 is used, the samples are labeled as cc. As an example, r-GA-0-0 is the resin prepared without acid nor photoinitiator with a OP/EtOH ratio of 1:100, and its corresponding counterpart

with a EtOH ratio of 1:40is labelled as r-GA-0-0 cc. It should be mentioned that sample r-GA-H-0 was already discussed in Chapter 3 as r-GA; it is herein re-labeled for clarity, to indicate the exact formulation of the reactant's mixture accounting for the different conditions of pH and photoinitiator.

Table 4.2.1. Summary of the parameters used in the synthesis of polymeric resins using gallacetophenone as precursor and irradiating at 365 nm for 60 minutes.

		$C_2H_2O_2$:EtOH molar ratio	HCl [0.1 M]	Photoinitiator [1 wt. %]	Final pH
	r-GA-0-0		-	no	6.16
	r-GA-H-0*	1:100	yes	no	1.01
	r-GA-0-Ch		-	yes	6.03
	r-GA-H-Ch		yes	yes	1.03
	r-GA-0-0cc		no	no	6.25
	r-GA-H-0cc	1:40	yes	no	0.87
	r-GA-0-Chcc		no	yes	6.45
	r-GA-H-Chcc		yes	yes	0.96

* This material was labeled in Chapter 3 as r-GA; it is herein re-labeled for clarity, to indicate the exact formulation of the reactant's mixture.

A gradual darkening and increase in the absorbance values were observed in all the solutions with the illumination time (Figures 4.2.1 and 4.2.2), indicating the occurrence of the photoassisted reaction regardless the synthesis conditions. In all cases after 60 min of irradiation, a brownish solid (resin) was formed. A subtle difference was observed for the solutions prepared in the presence of the photoinitiator, with the resins showing a slightly darker color (Figure 4.2.2) and a highest intensity of absorbance (sample r-GA-0-Ch).

For comparison purposes, the series of materials prepared using 1:40 glyoxal/EtOH molar ratio (i.e. 2.5 times higher concentration) were irradiated also for 60 minutes under the UV light. A similar trend was obtained regarding the color evolution of the solutions, with slightly darker color for the formulations incorporating the photoinitiator. Regarding the time of irradiation, no significant differences were observed for the samples prepared using 1:40 or 1:100 glyoxal/EtOH molar ratio, indicating that the solvent evaporation rate does not seem to influence the kinetics of polycondensation of the reactants.
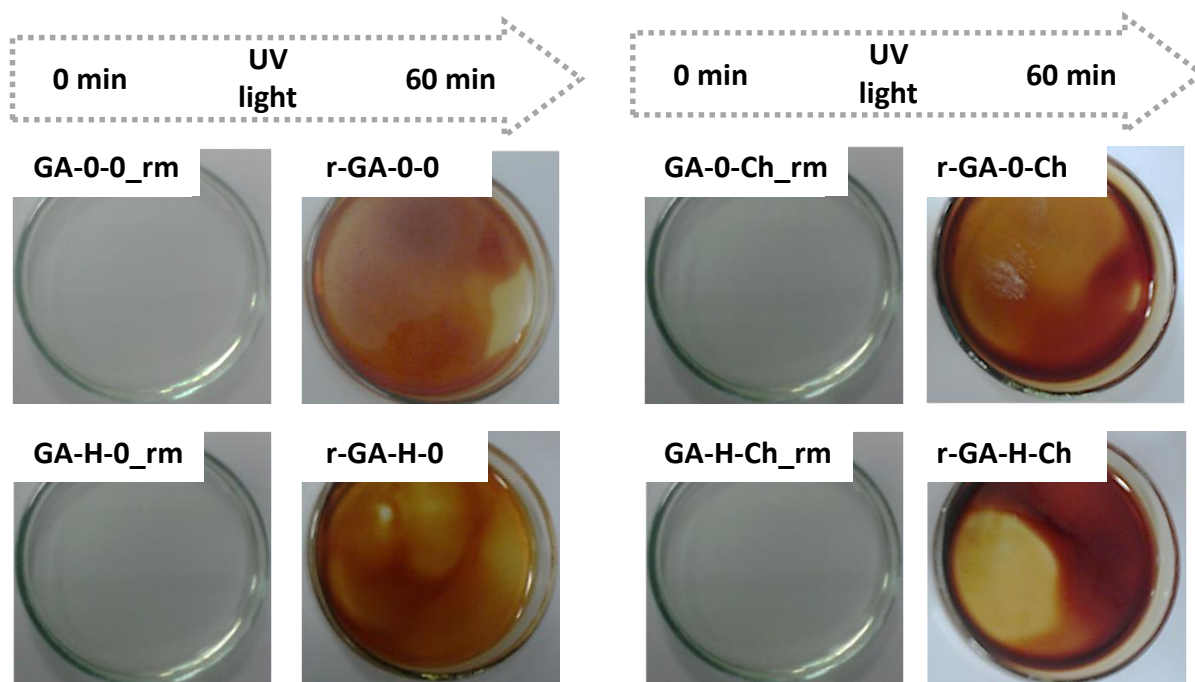
Figure 4.2.1. Visual changes in the gallacetophenone reactant's mixtures before (series rm) and after 60 minutes of UV irradiation at different experimental parameters of pH and photoinitiator (series r-GA-X-Y).
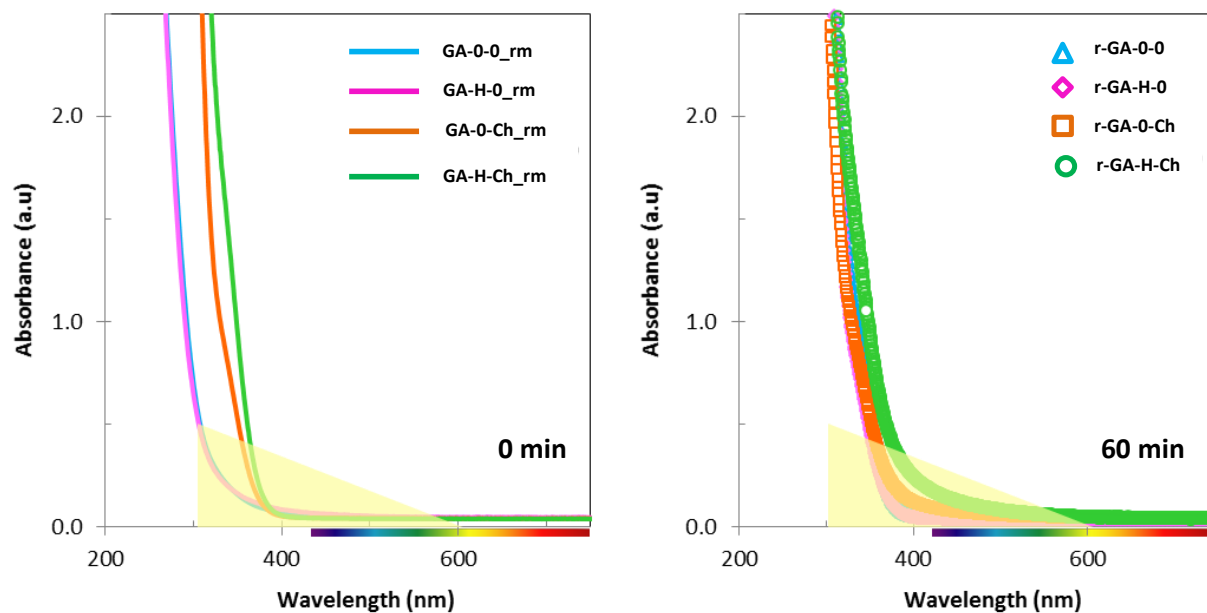
Figure 4.2.2. UV-VIS spectra of gallacetophenone reactant's mixtures before (series rm) and after 60 minutes of UV irradiation at different experimental parameters of pH and photoinitiator (series r-GA-X-Y).

4.2.1. Thermal treatment

The thermal behavior of the resins obtained solids after 60 minutes of irradiation was investigated by thermogravimetric analysis, so as to determine the optimized pyrolysis temperature. The corresponding thermogravimetric profiles under inert atmosphere are shown in Fig.4.2.3.
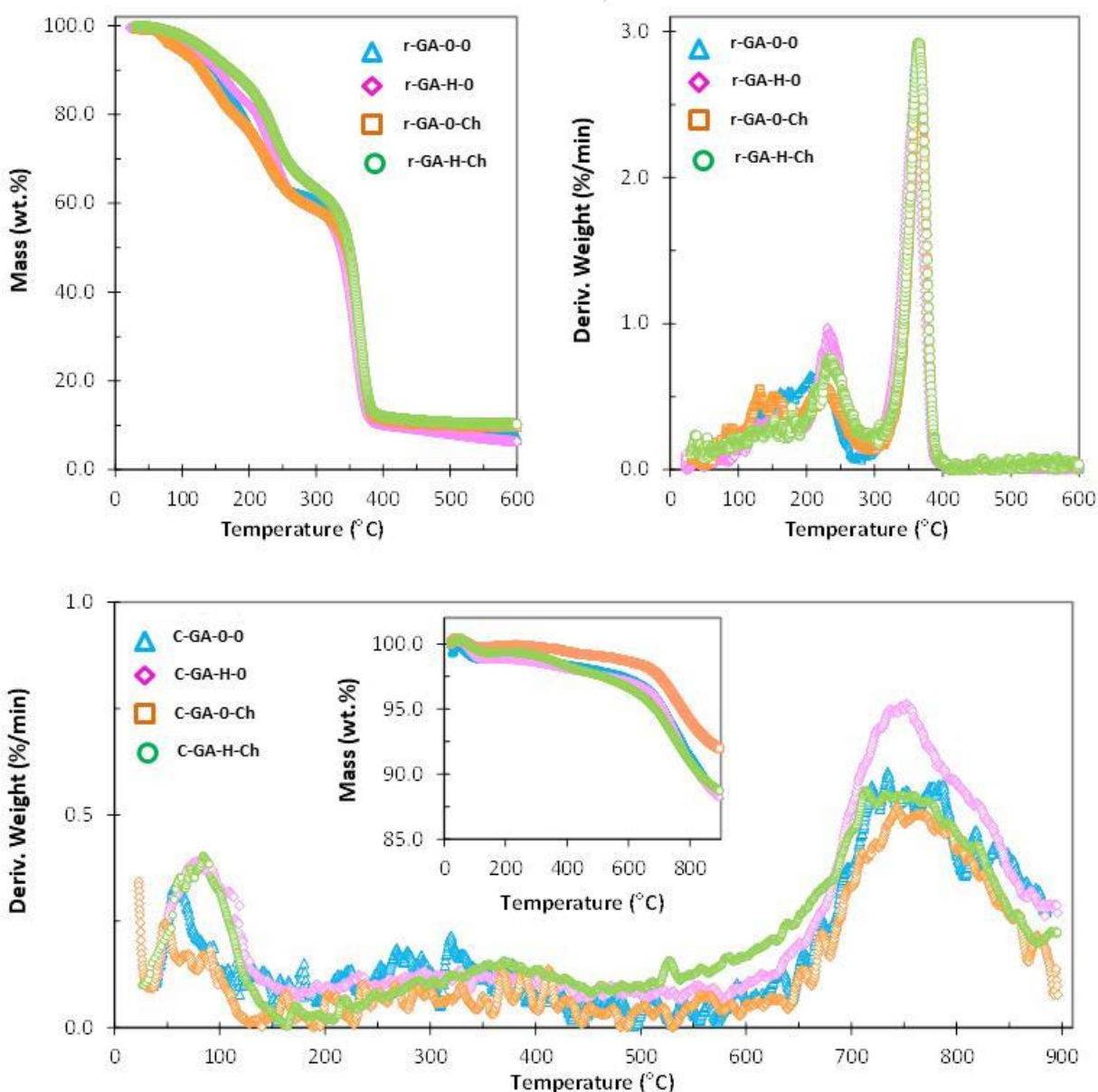
Figure. 4.2.3. a) Thermogravimetric profiles and derivative curves under inert atmosphere of the series r-GA-X-Y after 60 min of irradiation and their corresponding carbons (series C-GA-X-Y) obtained upon thermal treatment at 600 °C.

As seen, all of them present a large mass loss between 100-400 °C, with the largest mass loss fraction occurring between 300-400 °C. This range of temperatures is higher than that corresponding to the thermal decomposition of raw gallacetophenone powders (ca. 235 °C), confirming the higher stability of the resins obtained after the photopolymerization. It also points out the absence of unreacted gallacetophenone, which is also in agreement with the excess of glyoxal in the reactant´s mixture.

The DTG curves show a broad peak at 238-240 °C for all the samples, being wider in the materials synthesizes in the absence of HCl (samples r-GA-0-0 and r-GA-0-Ch). As already discussed in Chapter 3, this suggests differences in the polymerization pathway under the experimental conditions of pH and photoinitiator. As already discussed in Chapter 3, the main peak centered at 350 °C appears at a temperature close to that corresponding to the thermal decomposition of the surfactant (pluronic F127) (Figure 3.3). Thus, the interactions occurring between the surfactant and the precursor during the photoinduced polycondensation, (e.g., electrostatic, van der Waals, hydrogen bonds) are most likely giving rise to the mass loss below 350ºC. Above 500 °C the mass loss remained almost unchanged for all the resins, thus 600 °C remained a suitable temperature for the preparation of the carbon materials (via carbonization).

Table 4.2.2 shows the yields of carbonization of the photopolymerized resins after the carbonization at 600 °C. The values ranged from 8 wt.% in the case of C-GA-0-0 prepared without acid or photoinitiator, to 11 wt.% for C-GA-H-Ch prepared in the presence of both of them.

Table 4.2.2. Carbonization yields, elemental analysis data and surface pH of the carbon materials of the series C-GA-X-Y.

	C-GA-0-0	C-GA-H-0	C-GA-0-Ch	C-GA-H-Ch
Carbonization Yield (wt.%)	8	9	10	11
Carbonization Yield (resin basis) [a] (wt.%)	18	21	23	25
Carbon (wt.%)[b]	91.5	91.6	91.9	91.5
Oxygen (wt.%)[b]	6.0	6.1	5.8	6.0
Hydrogen(wt.%)[b]	2.5	2.3	2.3	2.5
Surface pH	9.2	9.1	8.5	9.2

[a] Experimental carbonization yield recalculated on the basis of the resin (i.e. without considering the mass of Pluronic F127).
[b] Evaluated from elemental analysis. The initial carbon content considering the precursor's formula is 51.6 wt.%.

The thermogravimetric analysis of the carbon materials is shown in Fig.4.1.4c. The profiles were very similar whatever the synthetic parameters used for the synthesis. The main mass loss took place above ca. 750 °C, attributed to the decomposition of volatile matter and/or O-surface functionalities still remaining on the solids after the carbonization at 600 °C. The carbon content after carbonization, measured by elemental analysis is presented in Table 4.2.2, and it shows a clear densification of all the samples compared to the initial carbon content of the precursor (ca. 51.6 wt.%). The surface pH was basic ranging from 8.5 to 9.2, suggesting the hydrophobic nature of the resulting carbon materials. Such basic nature contrasts with the moderate oxygen content of the samples (ranging between 5.5-6 w.t%), and thus suggests that most of the oxygen groups of the carbons would be in the form of quinones, ethers and/or O-bridge (basic nature functional groups)[Ania 2013].

The carbonization of the resins from the series prepared with 1:40 glyoxal:EtOH molar ratio was carried out under the same conditions; the carbonization yields in this case (Table 4.2.3) were slightly lower than those of the samples prepared with a higher amount of solvent (Table 4.2.1).

Table 4.2.3. Carbonization yields (wt.%) of the carbons materials of the series C-GA-X-Ycc.

	C-GA-0-0cc	C-GA-H-0cc	C-GA-0-cc	C-GA-H-cc
Carbonization Yield	7.5	8.0	7.4	8.3
Carbonization Yield (resin basis)[a]	16.9	18.0	17.7	18.7

[a] Experimental carbonization yield recalculated on the basis of the resin (i.e. without considering the mass of Pluronic F127).

4.2.2 Textural characterization

The nitrogen adsorption/desorption isotherms -196 °C of the carbon materials prepared of the series C-GA-X-Y and C-GA-X-Ycc are shown in (Fig. 4.1.4). As seen, the materials displayed the type IV(a) isotherms, with well-developed hysteresis loops (type H2 (b)), indicating the occurrence of mesopores for all the experimental conditions assayed. The differences in the shape of the isotherms and the pore volumes point out to an effect of the acidic conditions and the presence of the photoinitiator. A summary of the main textural parameters is presented in Table 4.2.4.
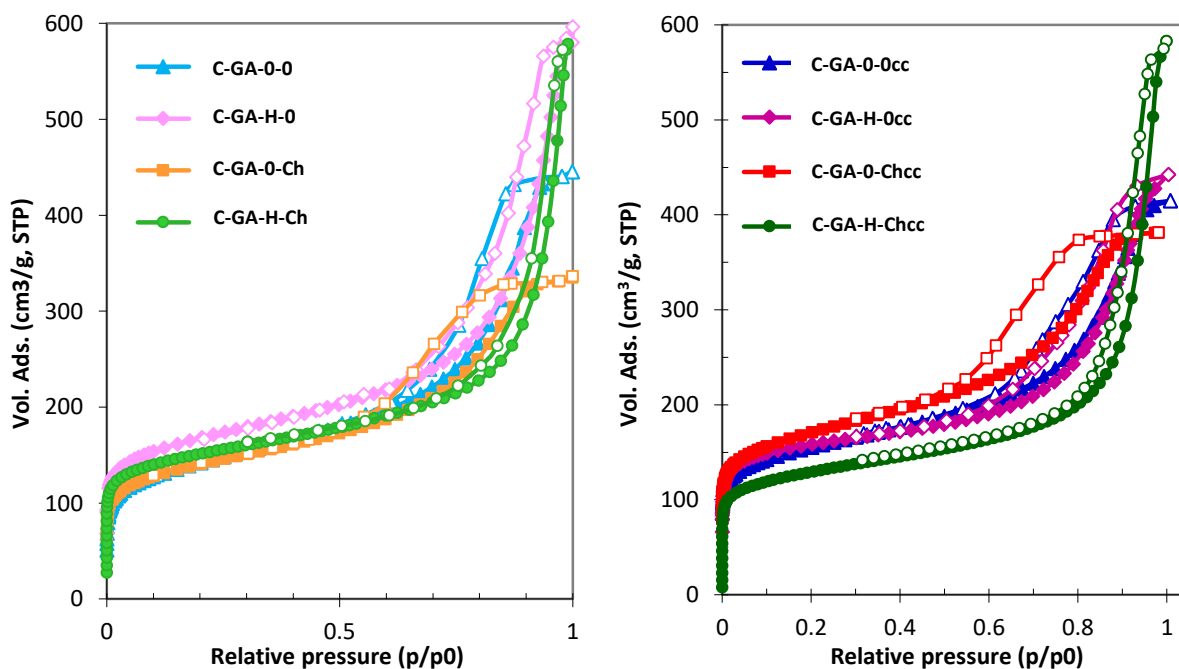
Figure 4.2.4. N_2 adsorption/desorption isotherms at -196 °C of the carbon materials obtained by the photopolycondensation of gallacetophenone at different experimental parameters of pH, photoinitiator and OP/EtOH ratio (full symbols: adsorption; empty symbols: desorption).

Comparing among the C-GA-X-Y series (1:100 glyoxal/ EtOH ratio), it can be observed that the samples prepared in the absence of HCl (solution pH during the synthesis is ca. 6) displayed lower total pore volumes (ca. 0.7 and 0.5 cm³/g for carbons C-GA-0-0 and C-GA-0-Ch, respectively) compared to the materials obtained at acidic pH (solution pH of ca. 2) with a total pore volume of 0.9 cm³/ g. for both C-GA-H-0 and C-GA-H-Ch carbons. The same trend, although less pronounced, was obtained for the carbons prepared with 1:40 glyoxal/ EtOH ratio (series cc). On the other hand, the photoinitiator has a minor impact on the porosity of the samples, as pore volumes were slightly lower. The impact of pH and photoinitiator on the position of the hysteresis loops of the isotherms was less pronounced. Overall, it can be inferred that the acidic conditions during the synthesis rendered materials with the highest total pore volumes, while the photoinitiator had a minor effect.

In the absence of HCl (sample C-GA-0-0), the hysteresis loop expands over the range 0.60-0.93 p/p_0 (Fig 4.2.5a), and the carbon displayed a narrow distribution of mesopores with the main peak in the distribution centered between 9- 10 nm (Fig. 4.2.5b). At converse, when the solution pH was

67

acidic (samples C-GA-H-0 and C-GA-H-Ch) the hysteresis loop shifted towards higher values of relative pressure, indicating the occurrence of mesopores of larger sizes. This is in agreement with the pore size distribution shown in Fig. 4.1.5b, with average mesopore sizes of 38-40 nm for the samples prepared in acidic conditions, compared to the ca. 13-15 nm for the samples prepared without adding HCl. Interestingly, sample C-GA-H-Ch showed a secondary local maximum around 38 nm. Besides the position, the shape of the hysteresis loop also changed towards a type H1 loop with parallel adsorption/desorption branches, indicating a more uniform distribution of mesopores [Thommes 2015], where the pore neck and mouths would be of similar dimensions (i.e., less constricted porosity).

Table 4.2.4. Main textural parameters from the gas adsorption data, of the carbonized GA resins at 600 °C.

	S_{BET} (m²/g)	V_{PORES}[a] (cm³/g)	$W_{0 N2}$[b] (cm³/g)	V_{MICRO}[c] (cm³/g)	V_{MESO}[c] (cm³/g)	Mesopore Size[d] (nm)	$W_{0 CO2}$[e] (cm³/g)	L[f] (nm)
C-GA-0-0	518	0.70	0.19	0.147	0.52	9	0.139	0.64
C-GA-H-0	620	0.89	0.19	0.176	0.71	14	0.148	0.63
C-GA-0-Ch	513	0.52	0.20	0.157	0.35	7	0.152	0.63
C-GA-H-Ch	563	0.91	0.20	0.183	0.652	15	0.149	0.62
C-GA-0-0 cc	572	0.64	0.20	0.18	0.45	10	0.163	0.60
C-GA-H-0 cc	602	0.67	0.21	0.19	0.47	10	0.176	0.61
C-GA-0-Ch cc	627	0.65	0.22	0.20	0.38	7	n.m.	n.m.
C-GA-H-Ch cc	478	0.88	0.17	0.15	0.71	17	0.258	0.71

[a] Evaluated at p/p₀ ~ 0.99 in the N₂ adsorption isotherms at -196 °C.
[b] Micropore volume, evaluated from DR equation applied to N₂ adsorption isotherms at -196 °C.
[c] Evaluated by applying the 2D-NLDFT-HS method to the N₂ adsorption isotherms at -196 °C.
[d] Average mesopore size determined from the PSD obtained by applying the 2D-NLDFT-HS method to the N₂ adsorption data.
[e] Narrow micropores volume, from DR equation applied to CO₂ adsorption isotherms at 0 °C.
[f] Average size of narrow micropores evaluated from the Stoeckli-Ballerini equation applied to CO₂ adsorption isotherms at 0 °C.
n.m. not measured

As for the photoinitiator also induced a shift in the position of the hysteresis loop towards lower relative pressures, indicating the presence of mesopores of small sizes. This can be observed in the

PSD, with an average pore size of ca. 7 nm. On the other hand, the surface areas were not much modified by either the pH or the photoinitiator, with values ranging between 513-620 m^2/ g for all the samples.
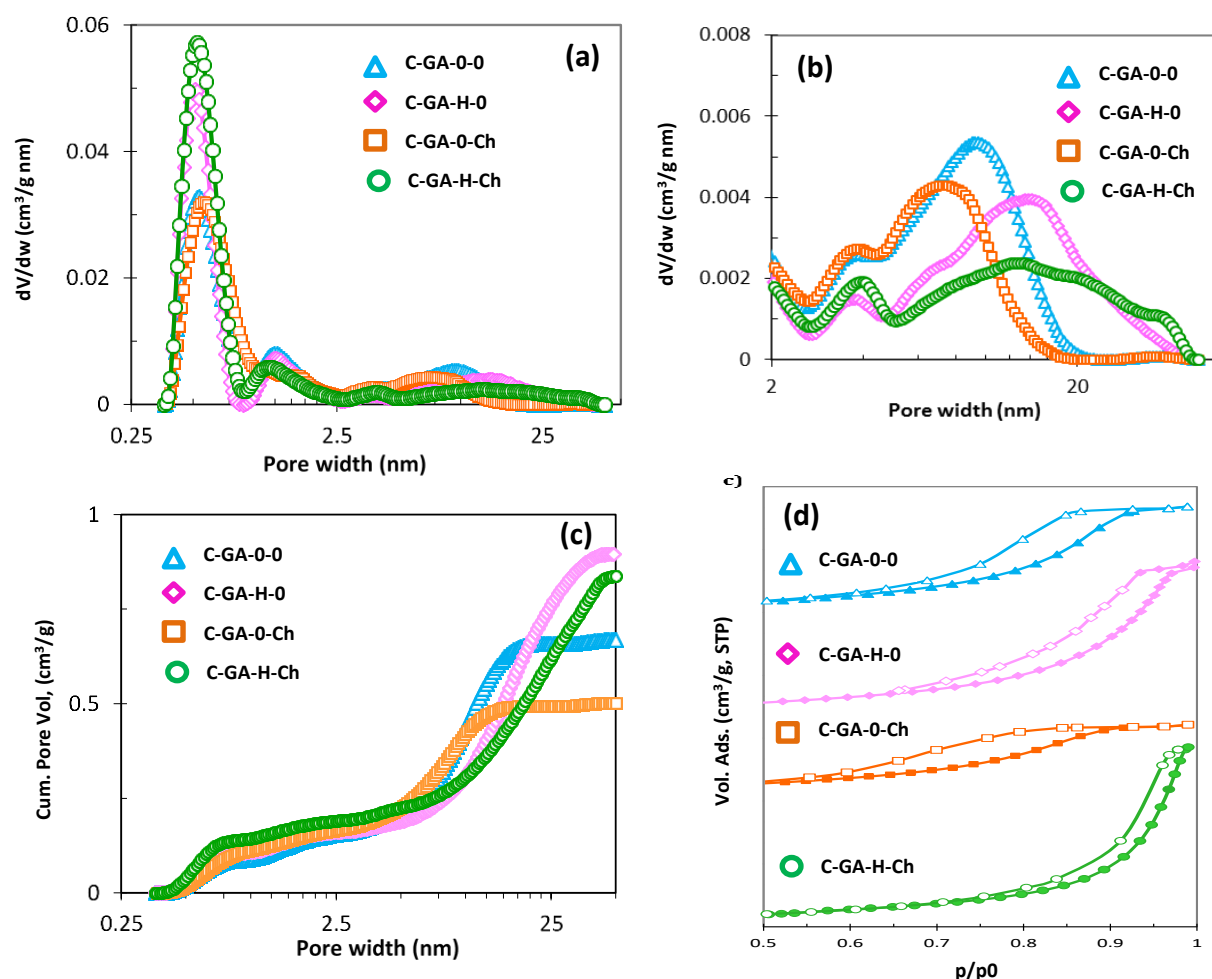
Figure 4.2.5. Derivative (a,b) and cumulative (c) distribution of pore sizes evaluated using the 2D-NLDFT-HS method applied to the adsorption branch of the nitrogen adsorption isotherms at -196 ℃ of the series C-GA-X-Y; (d) magnification of the hysteresis loops of the N_2 adsorption isotherms at -196 ℃.

Regarding the series of materials prepared with a 1:40 glyoxal/ EtOH ratio, the effect of the acidic pH on increasing the total pore volume and shifting the average mesopore size distribution was less remarkable (sample C-GA-H-0cc), being almost the same than for sample C-GA-0-0cc (Figure 4.2.8). When both acidic conditions and the photoinitiator were used, the material C-GA-H-Chcc showed similar characteristics than the one prepared with a higher glyoxal/ EtOH ratio (Table 4.2.4). The PSD was rather wide, with the main peak centered around 16.5 nm and showing a

secondary contribution between 35-40 nm (Figure 4.2.8). When just the photoinitiator was incorporated (sample C-GA-0-Chcc), the most remarkable effect was the increase in the specific surface area and micropore volume (Table 4.2.4), accompanied by a fall in the total pore volume. The sample also displayed a narrower distribution of mesopores towards smaller sizes of around 7 nm. As general trend, the presence of HCl (alone or combined with the photoinitiator) triggered the highest values of specific surface area.
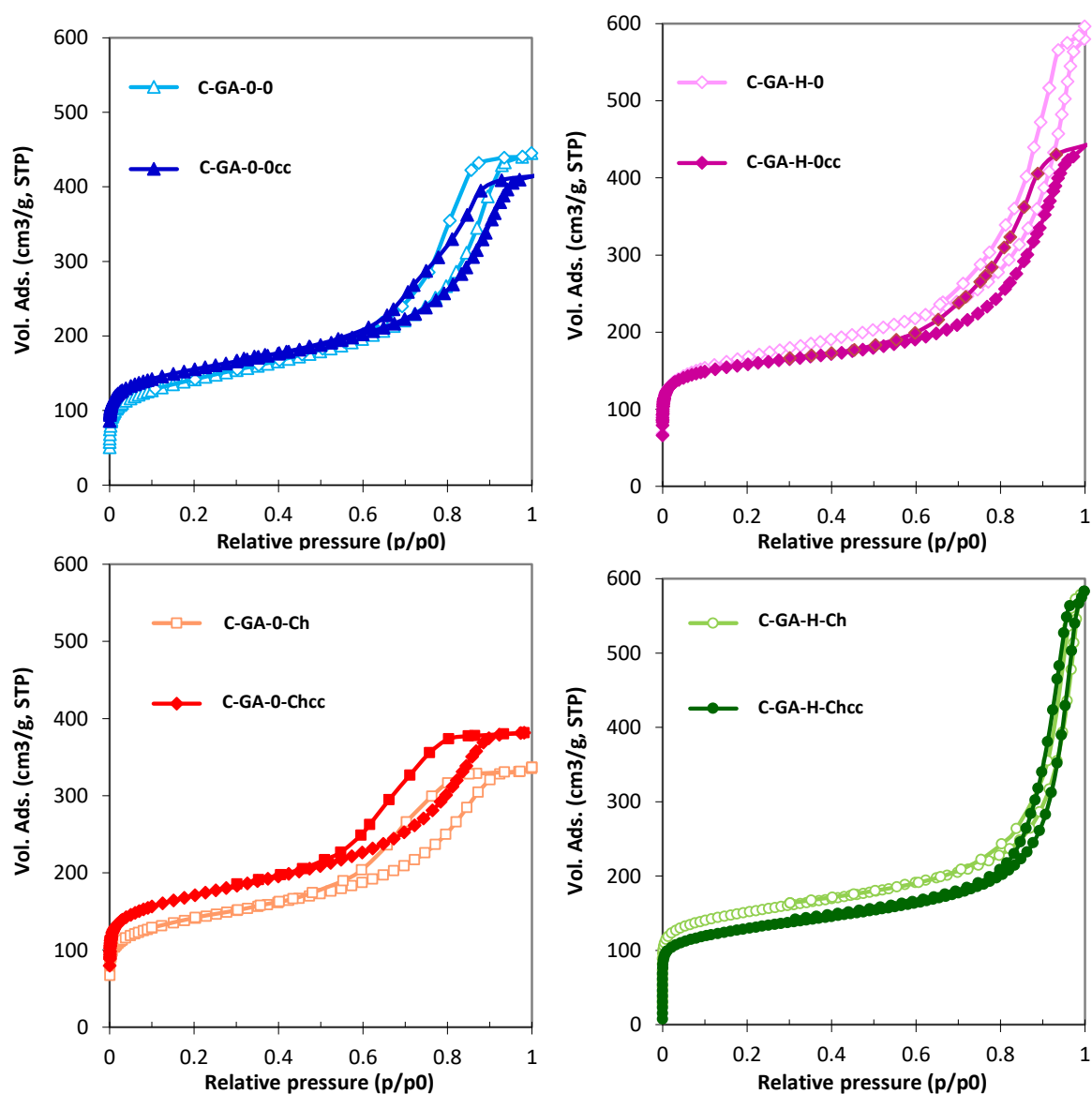
Figure 4.2.7. N_2 adsorption isotherms at -196 °C of the series C-GA-X-Ycc. Data is compared to that of the series C-GA-X-Y to show the effect of the Glyoxal: EtOH ratio.

The most remarkable differences between the two series with different glyoxal/ EtOH ratio were observed for the pairs C GA-H-0 and C GA-H-0cc (Fig. 4.2.7), where a higher volume of solvent (i.e., more diluted conditions) seemed to strongly favor the increase in the total pore volume. Also, the pair C GA-0-Ch/ C GA-0-Chcc showed that a smaller volume of solvent favored the development of the microporosity (i.e., higher W0 micropore volume).
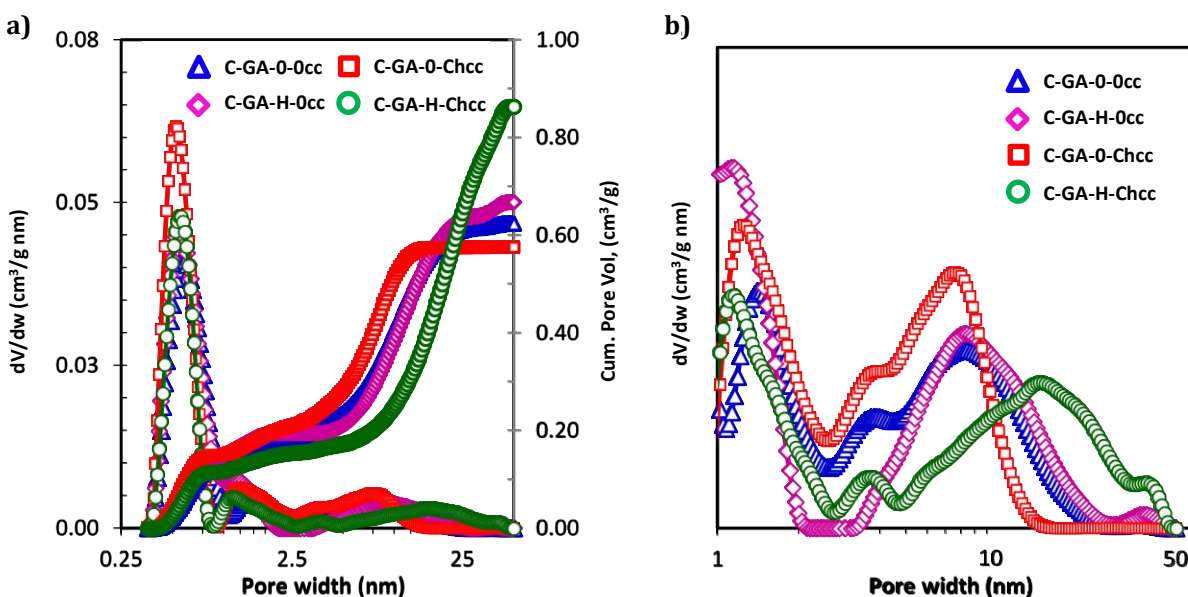
Figure 4.2.8. a) Distribution of pore sizes and cumulative pore volume evaluated using the 2D-NLDFT-HS method applied to the adsorption branch of the N_2 adsorption isotherms of the series C-GA-X-Ycc; **b)** magnification of the pore size distribution within the mesopore range.

4.2.3. Morphological and structural characterization

TEM images of the carbon materials from the C-GA-X-Y series are presented in Fig. 4.1.9. The micrographs revealed the typical disorganized structure of amorphous carbon materials. Nevertheless, some differences can be observed on the particle aggregation and their size. For instance, carbon C-GA-0-0 presented the smallest particle sizes aggregation. When the photoinitiator was used (carbon C-GA-0-Ch), more defined and spherical packed-particles were obtained, rendering smaller mesopores and pore volumes according to the textural analysis discussed above. On the other hand, the carbons prepared at low pH clearly presented larger intraparticle space. A similar observation has been reported by Lei Lu and co-workers [Lu 2010]. Moreover, when both HCl and photoinitiator were combined (carbon C-GA-H-Ch), the carbon

particles doubled in size, reaching more than 40 nm, and the intraparticular spaces became also larger.

This suggests that the acidic conditions favor the formation of long cross-linked chains in the resin that would better prevent the shrinkage during the carbonization to obtain the carbons. Otherwise, the photoinitiator would be expected to accelerate the rate of the polymerization reaction, which would lead to the formation of shorter chains/nodules around the micelles of the surfactant. Such poorly cross-linked particles would suffer from a strong shrinkage during the carbonization. A similar observation has been reported for other polymeric materials obtained by polycondensation of phenolic precursors and aldehydes [Al-Muhtaseb 2003; Job 2007; Macias 2013; Rasines 2015a,b]. These observations are also supported by the thermal analysis (Figure 4.2.4) of the carbons, as samples C-GA-0-0 and C-GA-0-Ch presented larger mass loss at lower temperatures.
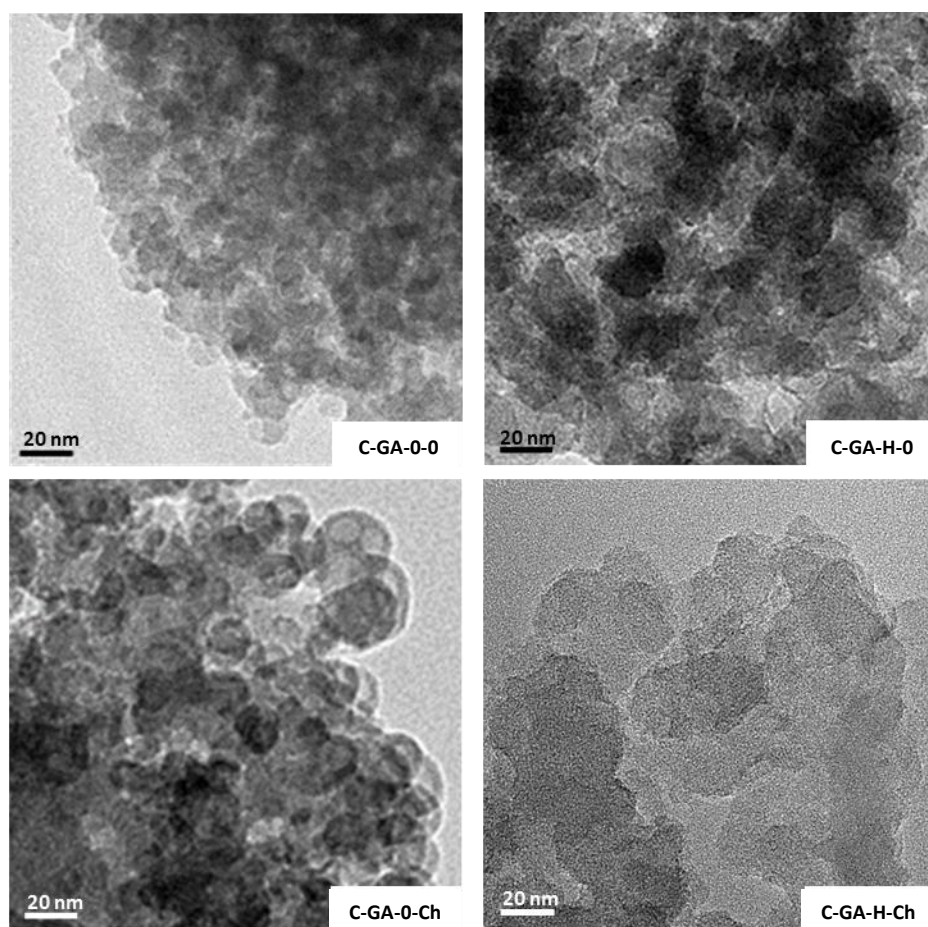
Figure 4.2.9. TEM micrographs of the carbon material from the series C-GA-X-Y.

The structural order of the carbons was evaluated by Raman spectroscopy (Figure 4.2.10.). Raman spectra presented the typical features of amorphous carbons with a disorganized turbostratic structure, with the characteristic broad G (1595 cm^{-1}) and D bands (1350 cm^{-1}). The I_D/I_G ratio after the deconvolution of the first-order spectra (see Chapter 2) are very similar for all the samples, with values typical of materials with a low crystalline short-range (ranging from 0.91, 0.71, 0.81 and 0.81 for C-GA0-0, C-GA-H-0, C-GA-H-Ch, and C-GA-0-Ch respectively). Furthermore, these values are in agreement with those reported for carbon materials upon polycondensation of organic precursors [Lopez-Salas 2016, 2017].
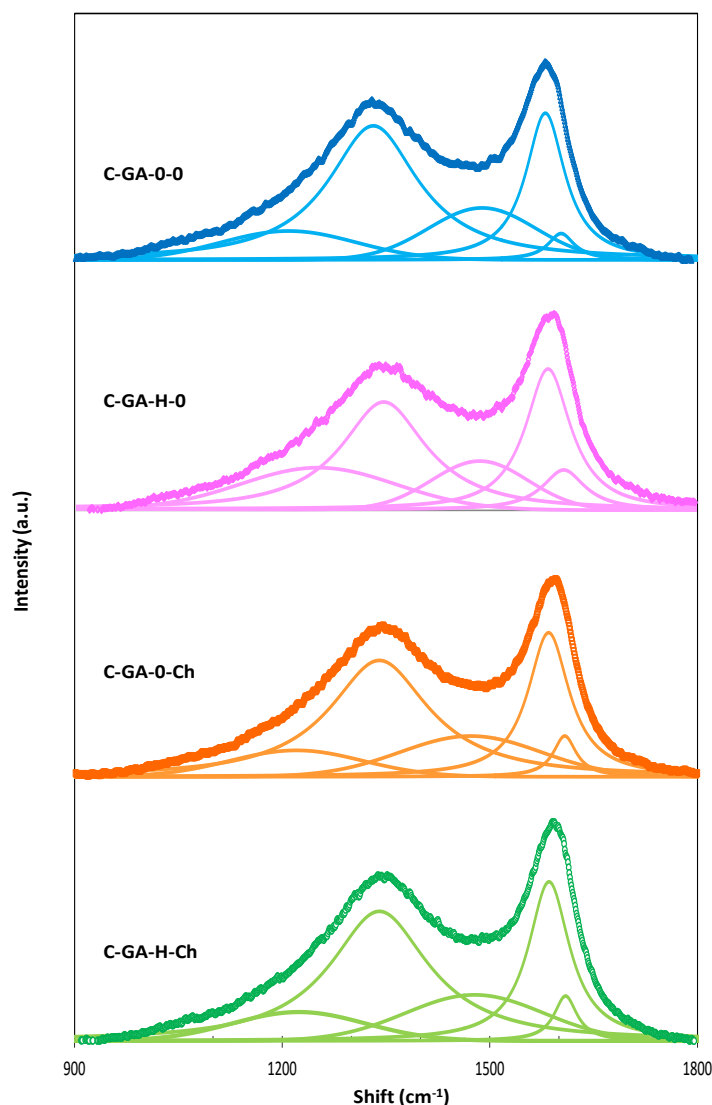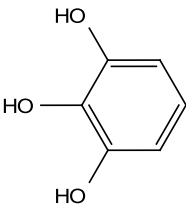
Figure 4.2.10. Raman profiles of the carbons of the series C-GA-X-Y. Original (normalized experimental data) presented in dots, and the calculated from the deconvolution of the TPA, D, A, G and D' bands by lines.

4.3. Pyrogallol-based materials

Similarly to the study on the previous section 4.2 for gallacetophenone, we have investigated the impact of various synthetic conditions on the photoinduced polycondensation of pyrogallol (1,2,3-trihydroxybezene). The choice of the precursor was made based on two facts: a) its chemical structure with three adjacent hydroxyl groups in the aromatic ring, and b) the data obtained in Chapter 3 showing that a carbon material with an ordered mesoporous structure arranged in a hexagonal matrix is obtained when the synthesis is carried out under acidic conditions and the absence of photoinitiator. Furthermore, the aromatic ring of pyrogallol is less functionalized than that of gallacetophenone (2,3,4-trihydroxyacetophenone), for which it could be expected to present a different reactivity.

The modifications induced in the synthesis are summarized in Table 4.3.1. Following the same code as before, the samples will be labeled as r-PG-X-Y or C-PG-X-Y where r denotes the resin, C the carbon, X indicates the presence (H) or absence (0) of HCl, and Y indicates the presence (Ch) or absence (0) of photoinitiator. As an example, r-PG-0-0 is the resin prepared without acid or photoinitiator.

Table 4.3.1. Summary of experimental conditions used in the photoassisted synthesis of the resins using pyrogallol as precursor upon UV irradiation for 60 min.

		HCl	*Photoinitiator*	*pH of reactants' mixture*
	r-PG-0-0	no	no	5.4
	r-PG-H-0[a]	yes	no	1.1
	r-PG_0-Ch	no	yes	6.0
	r-PG_H-Ch	yes	yes	1.2

[a] This material was labeled in Chapter 3 as r-PG; it is herein re-labeled for clarity, to indicate the exact formulation of the reactant's mixture.

As discussed in Chapter 3 and Section 4.1, the reactant's mixtures gradually darkened with the irradiation time, confirming the occurrence of the photoassisted reaction. After 60 minutes under the UV light all the resins were formed (Fig. 4.3.1) regardless the experimental conditions. However, unlike in the case of GA series, some differences were observed in the color and viscosity

of the resins (optical observation). Clearly, the resins prepared at low pH of ~1 (i.e. samples r-PG-H- and r-PG-H-Ch) were darker. Although, this feature was already observed with gallacetophenone (see section 4.1), it is more marked for PG (Figure 4.3.2), and the resins were also more viscous and sticky. Also, some of the resins presented an intense golden/orange-ish color, which could be attributed to the presence of the photoinitiator in the reactant's mixtures.
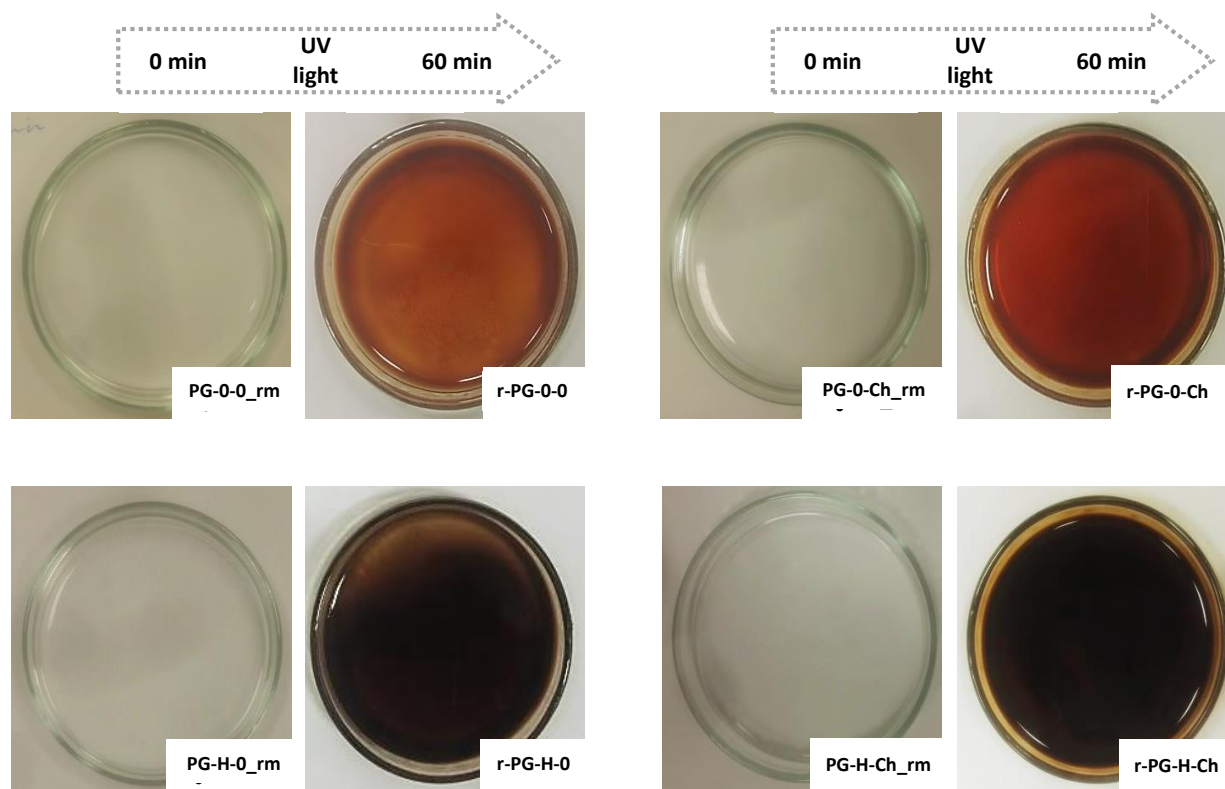
Figure 4.3.1. Visual changes in the pyrogallol reactant's mixtures before (series rm) and after 60 minutes of UV irradiation at different experimental parameters of pH and photoinitiator (series r-PG-X-Y).

The UV-Vis spectra at the initial (t0) and final states (after irradiation) present some differences between them too (Fig. 4.3.2). The UV-Vis spectra of the reactants mixtures before the irradiation were rather similar (Fig. 4.3.2a) with the onset of the absorption below 350 nm, and a small shift to higher wavelengths in the case of the solutions containing the photoinitiator). Upon irradiation, the absorbance of the solutions increased and shifted towards higher wavelengths (Fig. 4.3.2b), particularly in the case of the samples with photoinitiator. After 30 minutes of irradiation the absorbance already reached the highest value and a steady state, similar to that after 60 minutes (see example in Figure 4.3.3). However, as the solvent was not fully evaporated at 30 min, the

reaction was allowed to proceed up to 60 min (where evaporation was complete). Furthermore, no differences in the mass of resin were found after 60 minutes of irradiation.
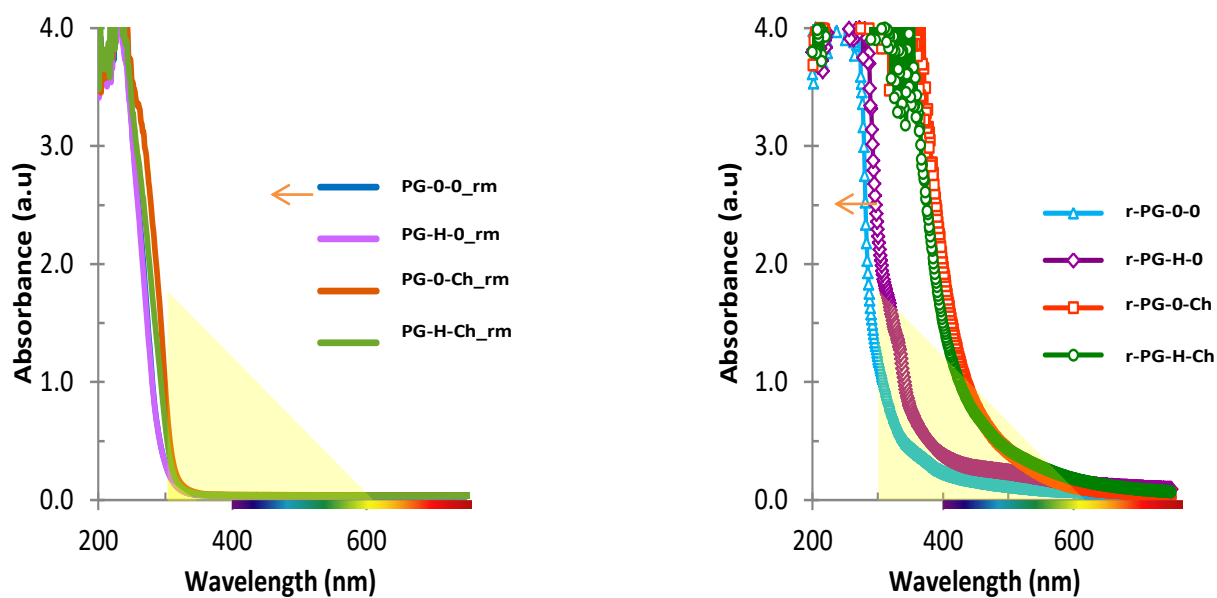
Figure 4.3.2 UV-Vis spectra of pyrogallol reactants' mixtures before (series rm) and after 60 minutes of UV irradiation at different experimental parameters of pH and photoinitiator (series r-PG-X-Y).
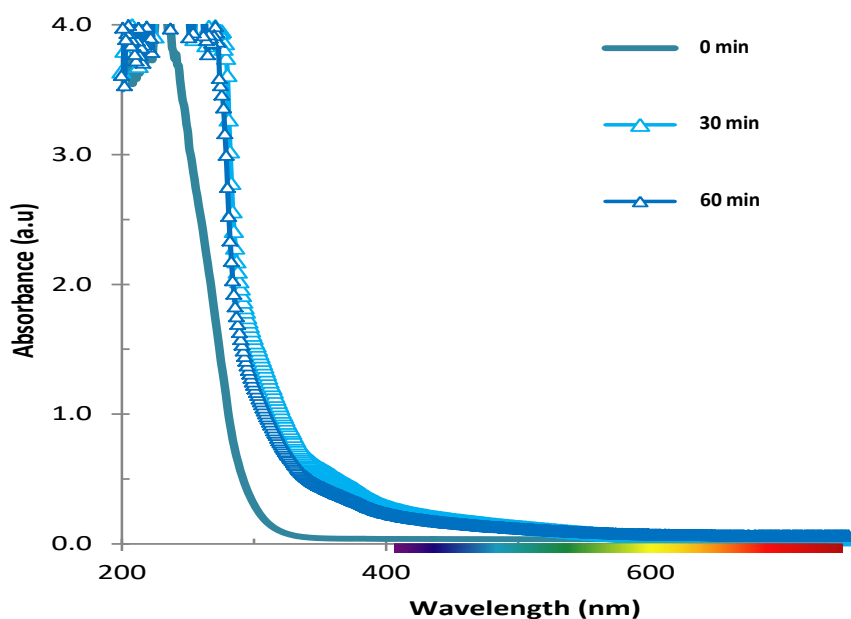
Figure 4.3.3 Evolution of the UV-Vis spectra of the reactants' mixtures PG-0-0 with the irradiation time: 0, 30 and 60 min.

4.3.1. Thermal treatment

The thermal treatment under inert atmosphere at 600 °C was performed. The carbonization yields of the PG resins series (Table 4.3.2) presented differences, greater than for the GA ones, ranged from 17 wt.% in the case of resin r-PG-0-0 prepared without acid neither, to 23 wt.% for resin r-PG-H-0 prepared in the presence of HCl.

Table 4.3.2. Carbonization yields, elemental analysis (wt.%) and surface pH of the carbon materials obtained from PG as precursor.

Sample	C-PG-0-0	C-PG-H-0	C-PG-H-Ch	C-PG-H-Ch
Pyrolysis Yield[a] (wt.%)	17.2	23.0	17.9	19.8
Resin Pyrolisis Yield[b] (wt.%)	40.0	53.5	41.6	46.1
Carbon[c] (wt.%)	90.4	90.3	90.8	90.8
Oxygen[d] (wt.%)	7.2	7.4	7.1	7.4
Hydrogen[d] (wt.%)	2.4	2.4	2.1	1.8
Surface pH	8.5	8.3	7.8	8.4

[a] Pyrolisis yield of the resin under N_2 atmosphere at 600°C calculated on the basis of the phenolic resin, without taking into account the surfactant.
[c] Evaluated from elemental analysis. The initial carbon content considering the precursor's formula is 57.1%.

The thermogravimetric profiles of the resins prepared from PG as precursor (series R-PG-X-Y) are shown in Figure 4.3.4; data corresponding to PG precursor itself is also included for comparison. As seen, the decomposition temperature of the resins in much higher than that of the organic precursor alone, evidencing the cross-linking of the reactants upon irradiation. The temperature corresponding to the main mass loss appeared is slightly lower (ca. 10 °C) for the resins prepare under lower pH. This indicates that the presence of the acid boosts the decomposition of the volatile matter at lower temperatures. This behavior has also been reported for the thermal decomposition of polymers and other polymeric resins [Mulik 2007]. In addition, for all the resins the mass loss above 500 °C was almost complete, as similarly observed for the resins prepared with other precursors (see chapter 3).
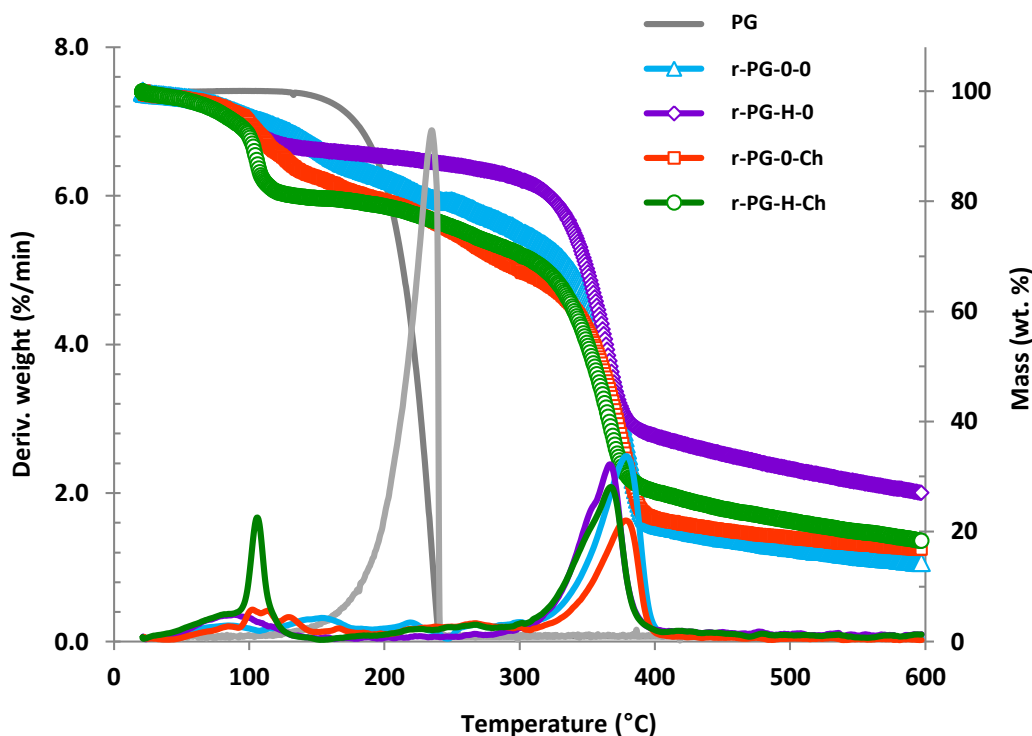
Figure 4.3.5 Thermogravimetric profiles of the series r-PG-X-Y obtained under inter atmosphere.

4.3.2. Textural characterization

In order to assess the effect of the different chemical conditions on the development of the porosity of the resulting C-PG-X-Y carbons, gas adsorption/desorption isotherms (N_2 at -196 °C and CO_2 at 0 °C) were measured. Data is shown in Fig. 4.3.5. A summary of the main textural parameters is presented in Table 4.3.3. Regardless of the synthesis conditions, all materials presented high gas uptakes, indicating their porous nature. Considering the N_2 isotherms, the presence of micro- and mesopores was confirmed for the whole series, with type IVb isotherms with marked hysteresis loops due to the capillary condensation of the gas in the mesopores [Thommes 2015].

Interestingly, while the volume of CO_2 adsorbed is similar to all the samples (indicating similar narrow microporosity), differences are observed in the nitrogen adsorption data, both in the gas uptake and the shape and position of the hysteresis loops, indicating that the synthesis conditions affect mainly the formation of the mesoporosity. Considering the shape of the nitrogen adsorption isotherms, the samples can be divided in two groups with similar porous features. The first group is constituted by the carbons prepared in free pH conditions (i.e., C-PG-0-0 and C-PG-0-Ch), which

display a type H2b hysteresis loop spanning from 0.7-0.9 relative pressures, and a slightly higher pore volume for carbon C-PG-0-0.
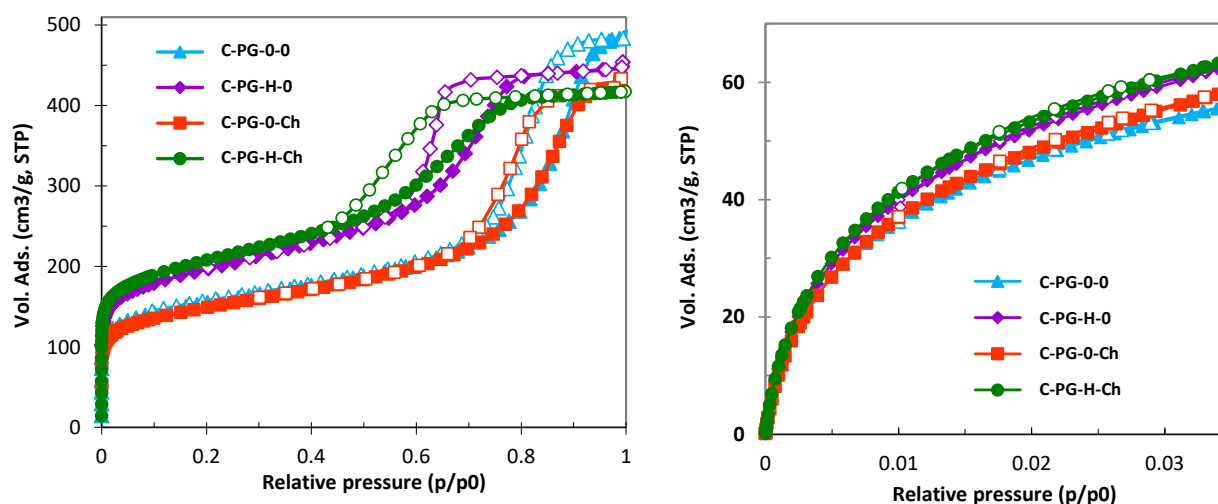
Figure 4.3.5. a) High resolution N_2 adsorption isotherms at -196 °C (a) and CO_2 adsorption isotherms at 0 °C (b) of the materials of the C-PG-X-Y series (full symbol: adsorption; empty symbol: desorption).

The second group is constituted by the carbons prepared under acidic conditions, featuring type H2a (C-PG-H-0) and H2b (C-PG-H-Ch) hysteresis loops spanning from 0.4-07 relative pressures. The lower range of relative pressures of the hysteresis loops, compared to the first group indicates the presence of mesopores of smaller sizes. Also, as in the case of the first group, the carbon prepared without the photoinitiator presented a slightly higher total pore volume. The difference in the shape of the hysteresis loop for carbon C-PG-H-0 (type H2a as opposed to type and H2b for the rest of the series) indicates the occurrence of pore blocking/ percolation in narrow pore necks of the mesopores, or cavitation-induced evaporation phenomena. The advanced characterization of this sample has been described in Chapter 3, including an analysis of the scans of the hysteresis loops in the nitrogen adsorption data to analyze the connectivity of the pores.

Regarding microporosity, at pH ≈ 5.5 conditions, the carbons displayed lower micropore volumes, also evidenced by the lower surface area values. Also, the photoinitiator does not seem to affect the microporosity of the carbons (Table 4.3.3). In general, acidic conditions promoted higher total pore volumes and mesopore volumes. Interestingly, in our conditions, the higher total pore volume was found for sample C-PG-0-0, and followed the trend: C-PG-0-0> C-PG-H-0> C-PG-0-Ch $\approx$ C-PG-H-Ch.

Table 4.3.3. Main textural parameters of the materials of the C-PG-X-Y series obtained from gas adsorption data.

	S_{BET} (m²/g)	V_{PORES}[a] (cm³/g)	Wo_{N2}[b] (cm³/g)	V_{MICRO}[c] (cm³/g)	V_{MESO}[c] (cm³/g)	$W_{0\ CO2}$[d] (cm³/g)	L[e] (nm)
C-PG-0-0	570	0.75	0.21	0.17	0.56	0.19	0.61
C-PG-H-0	722	0.69	0.26	0.22	0.45	0.21	0.62
C-PG-0-Ch	544	0.66	0.20	0.18	0.47	0.20	0.63
C-PG-H-Ch	762	0.64	0.27	0.23	0.39	0.23	0.62

[a] Evaluated at $p/p_0 \sim 0.99$ in the N_2 adsorption isotherms at -196 °C.
[b] Micropores volume evaluated from DR equation applied to N_2 adsorption at -196 °C.
[c] Evaluated from the 2D-NLDFT-HS method applied to N_2 adsorption at -196 °C.
[d] Narrow micropores volume evaluated from DR equation applied to CO_2 adsorption at 0 °C.
[e] Evaluated using the Stoeckli-Ballerini equation applied to CO_2 adsorption at 0 °C.
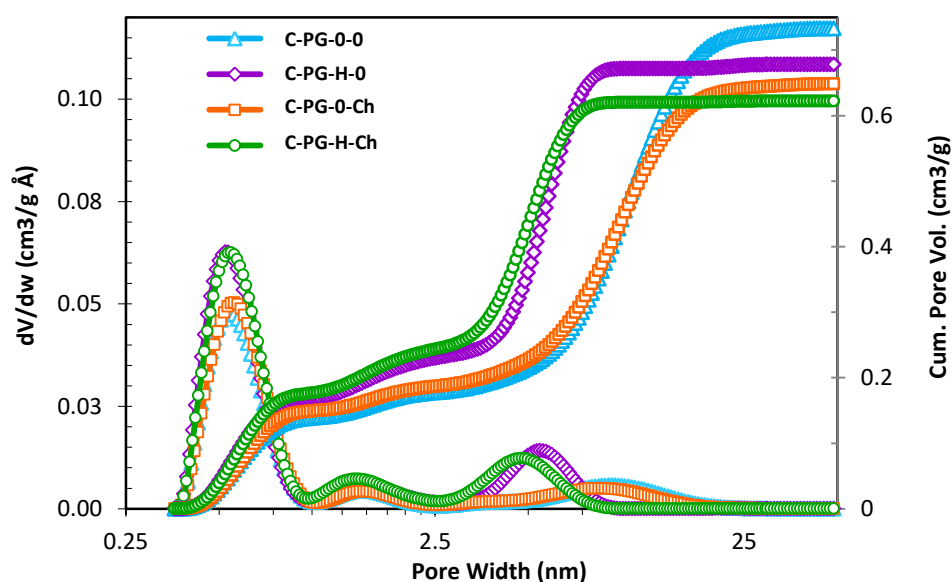
Figure 4.3.6. Pore size distribution (left -y axis) and cumulative pore volumes (right Y axis) of the carbon materials of the C-PG-X-Y series, obtained by the 2D-NLDFT-HS method applied to the adsorption branch of the N_2 adsorption isotherms at -196 °C.

In terms of the distribution of pore sizes (Fig.4.3.6), small differences were found on the samples prepared under the same pH conditions. For instance, pH ≈ 5.5 favors the formation of larger mesopores (around 9.4 and 8.8 nm for C-PG-0-0 and C-PG-0-Ch, respectively), while at pH 1, average mesopore sizes around 5 nm were obtained (i.e., 5.2 and 4.8 nm for C-PG-H-0 and C-PG-H-Ch, respectively). This highlights that the PSD is mainly controlled by the pH, while the photoinitiator would seem to favor the formation of mesopores of slightly smaller size.

4.3.3. Morphological and structural characterization

TEM micrographs revealed significant and interesting differences between the samples (Fig.4.3.7), showing two different trends in the development of the mesostructure, in agreement with the textural properties inferred from the gas adsorption data. On the one hand, samples C-PG-H-0 and C-PG-H-Ch showed an ordered pattern of well-aligned parallel channels, resembling an ordered hexagonal array of mesopores of around 5 nm size Fig.4.3.7b and d). On the other hand, the carbons prepared in free solution pH conditions (i.e., samples C-PG-0-0 and C-PG-0-Ch) showed the typical fingerprint of amorphous carbons, with disordered carbon particles aggregates (Fig.4.3.7). This confirms the outstanding role of the pH in the cross-linking mechanism and arrangement of the reactants during the synthesis, as it is the main parameter governing the size of the mesopores (see discussion above) and the arrangement of the pores. It is interesting to point out that the formation of an ordered arrangement of the mesoporosity at acidic conditions was not observed in the case of gallacetophenone (with a more functionalized aromatic ring compared to PG, due to the presence of the ketone group of electron withdrawal character).

This could be attributed to modifications in the mechanism of polycondensation, where acidic conditions would modify the cross-linking of the polymeric resin before the spinodal decomposition takes place. The latter should occur after the transition from the wormlike packing micelles to an 2D hexagonal packing cylindrical configuration [Dutra 2015; Liu 2016; Zhao 2019] and before the cloud point. For that, a good compromise between the polymerization and the self-assembly between the hydrophilic segments -PEO groups- of the template and the resin by the formation of hydrogen bonds is needed. This means that too long/slow polymerization rates will be unable to promote the formation of ordered mesostructures, while too fast polymerization might prevent the self-assembling of the surfactant (director agent) before reaching the crystalline structure, producing amorphous materials.
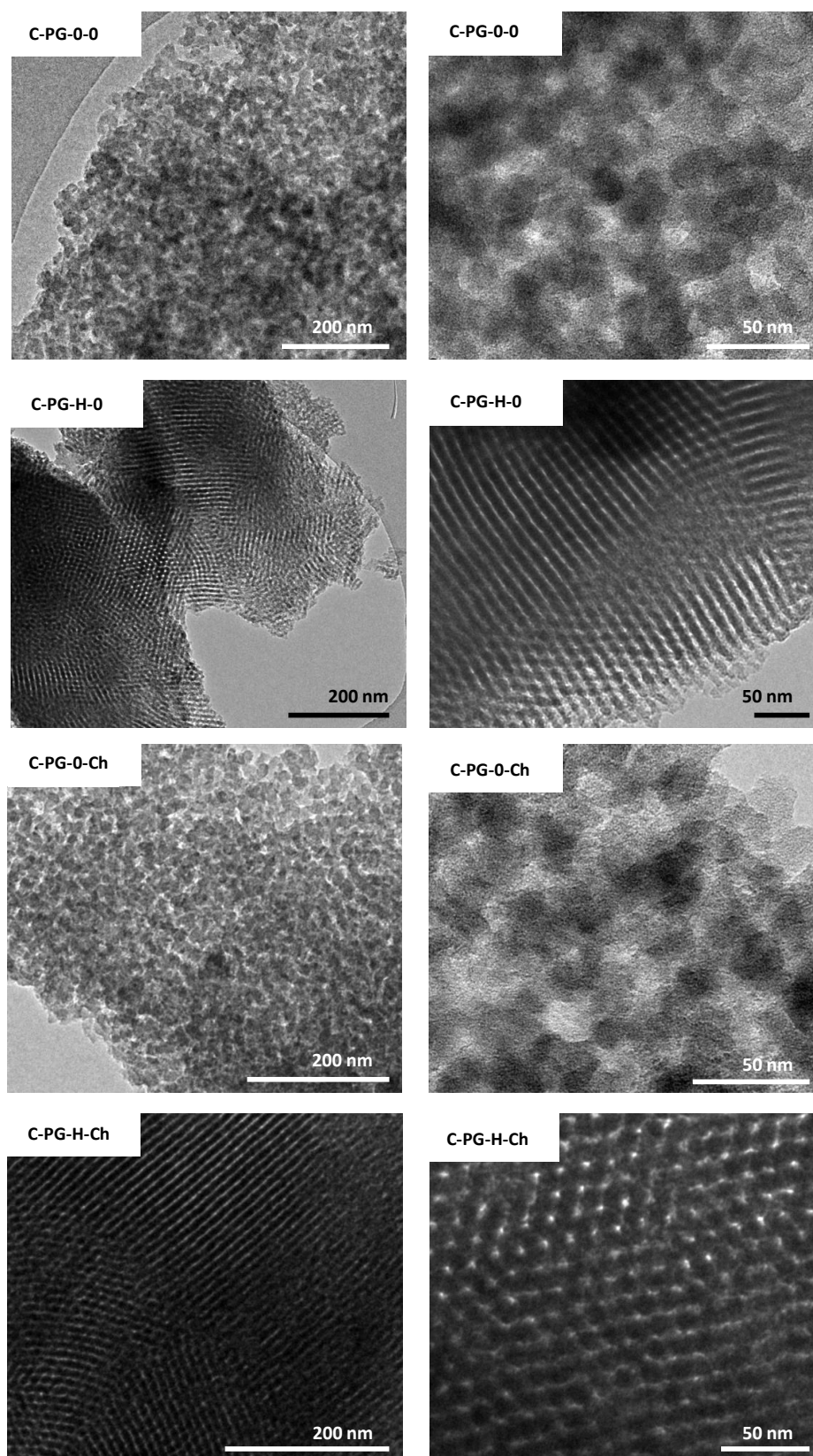
Figure 4.3.7. TEM micrographs of the carbons of the series C-PG-X-Y.

The structural order of the carbons C-PG_0 and C-PG_H were analysed by Raman spectroscopy (Figure 4.3.8.), with no differences between the samples. As in the case of the carbons described in Section 4.1 and Chapter 3 for other organic precursors, the broad G (1595 cm^{-1}) and D band (1350 cm^{-1}) in the Raman spectra confirmed the amorphous character of the carbons prepared using PG as precursor.
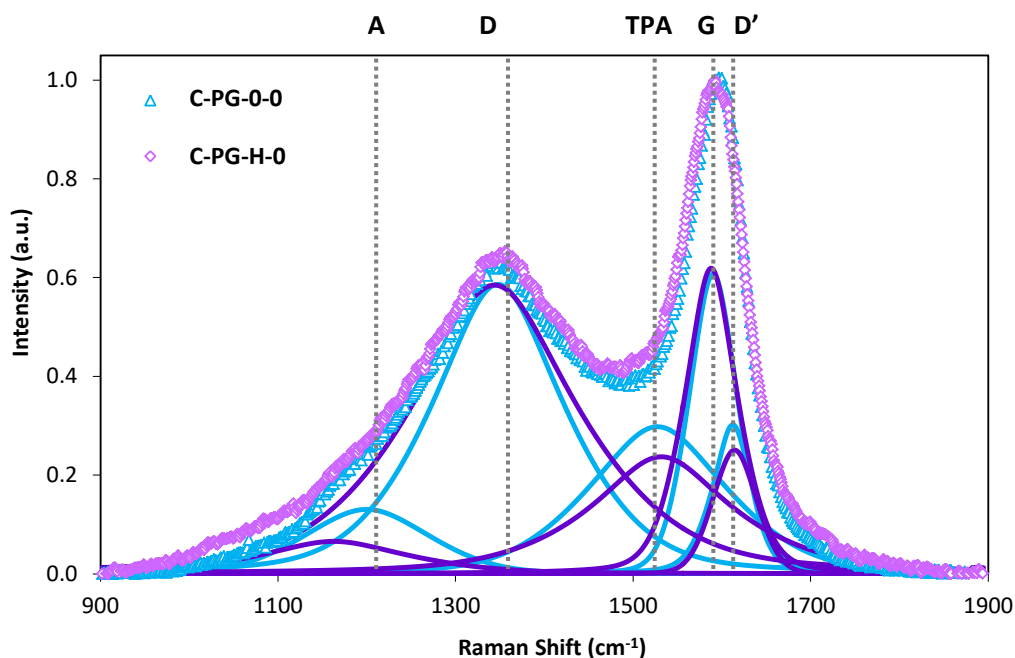
Figure 4.3.8. First-order Raman spectra of carbons C-PG-0-0 and C-PG-H-0. Symbols represent raw data and lines represent deconvoluted data (showing TPA, D, A, G and D' bands).

Indeed, the I_D/I_G values of the deconvoluted spectra rendered 0.95 and 0.94 for C-PG-0-0 and C-PG-H-0 respectively, confirming that the acidic conditions do not affect the order/disorder of the carbon matrix, and just the order/disordered arrangement of the mesopores.

4.4 Conclusions

We have investigated the effect of the solution pH and a photoinitiator in the physicochemical characteristics of the nanoporous carbons obtained upon the photoinduced polycondensation of selected organic precursors (i.e., gallacetophone and pyrogallol) and glyoxal. In both cases, data has shown that a well-developed mesoporosity can be successfully obtained through the photoassisted polymerization of **gallacetophenone and pyrogallol without the need of using acidic conditions or a photoinitiator.** This constitutes an advantage towards the preparation of materials through green synthetic routes and using less chemical reagents. At free pH conditions (i.e. pH ~6), the polymerization of both precursors and glyoxal takes place, rendering carbon materials with high porosity in the micro-/mesopore range. Strong acidic conditions have demonstrated the feasibility to produce carbon materials with high specific surface areas and total pore volumes, characterized by large mesopores, while the photoinitiator has little impact on the properties of the resulting carbons.

In the case of gallacetophenone, we have also confirmed that the synthesis can be carried out at high glyoxal/ EtOH ratio (i.e., concentrated conditions), which allows to reduce the consumption of solvent in the synthesis without sacrificing the mesoporosity of the carbons -despite there is a slight influence of the glyoxal/ EtOH ratio on the average mesopore size and total pore volume-. The absence of the acid catalyst results in carbon materials with a narrower distribution of mesopores of small sizes, as well as a slight decrease in the total pore volume. In contrast, the photoinitiator has an impact in the polymerization process, rather than in the self-assembly process, while the acidic conditions would seem to play a role in both processes.

In the case of pyrogallol, the acidic conditions enabled the formation of an ordered arrangement of the mesoporosity, which was not observed in the case of gallacetophenone. This could be attributed to modifications in the mechanism of polycondensation. Indeed, the acidic conditions would modify the cross-linking of the polymeric resin before the spinodal decomposition occurs, avoiding the transition from the wormlike packing micelles of the surfactant to a hexagonal crystalline arrangement. Too long or too fast polymerization rates will be unable to provide ordered mesostructures, rendering amorphous materials.

CHAPTER 5
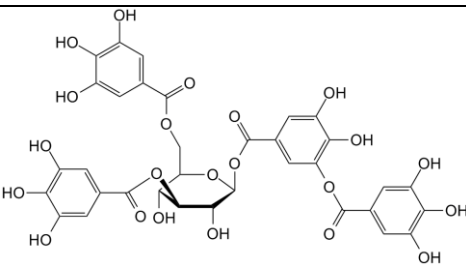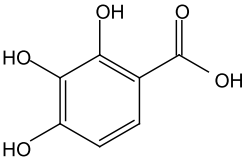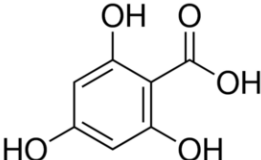
Polyhydroxylated benzoic acids *-exploring the impact of the carboxylic acid functionalization*

5.1. Introduction

In chapter 4 we have explored the impact of the pH and other synthetic parameters in the photoassisted polycondensation of pyrogallol and gallacetophenone, highlighting the important role of HCl as catalyst to control the hydrogen bond interactions between the precursors and the amphiphilic triblock copolymer. The acidic conditions have demonstrated to have **different** impacts depending on the precursor used, for this reason, this chapter is devoted to evaluate the impact of further functionalization of the aromatic ring in the organic precursor (e.g., carboxylic acid, carbonyl moieties) in the photoassisted polycondensation reaction and the physicochemical features of the obtained carbons.

In this regard, 2,4,6-trihydroxybenzoic acid (PGA), tannic acid (TNA) -as an example of a macromolecular polyhydroxylated aromatic compound- and 2, 4, 6-trihydroxybenzoic acid (THBA), were selected as precursors (Table 5.1.1).

Table 5.1.1. Nomenclature assigned to the polyhydroxylated aromatic organic precursors selected for the study, including molecular formula and IUPAC names.

Organic Precursor (OP)	Nomenclature	Molecular Structure
Tannic acid IUPAC name: 1,2,3,4,6-penta-O-{3,4-dihydroxy-5-[(3,4,5-trihydroxybenzoyl)oxy]benzoyl}-D-glucopyranose $C_{76}H_{52}O_{46}$	TNA	
Pyrogallol 4-carboxylic acid IUAC name: Benzene-2,3,4-triol $C_5H_6O_5$	PGA	
Phloroglucinol carboxylic acid IUAC name: 2,4,6tTrihydroxybenzoic acid $C_7H_6O_5$	THBA	

5.2 TNA and PGA-based materials

For the preparation of the resins using TNA and PGA as precursors, the following experimental conditions were used (similar to those of the GA and PG series); glyoxal/ EtOH 1:100 molar ratio; glyoxal: OP: Pluronic F127 molar ratio of 1.4: 1: 0.03; ethanol as solvent; illumination at 365 nm for 1 h; absence of HCl and photoinitiator. In the case of TNA and considering the large difference in molar mass compared to the rest of the aromatic precursors used, the amount of organic precursor was kept similar to the amount of PGA expressed in terms of mass (e.g., 2.21 grams -10mmol- of PGA and 2.21 grams -1.29 mmol- of TNA used in the synthesis). A summary of the experimental conditions is presented in table 5.1.2.

Table 5.2.1. Summary of experimental conditions used in the synthesis of polymeric resins using TNA and PGA as precursors, and pH of the reactant's mixtures. Data of GA and PG discussed in chapter 4 is included for comparison purposes.

	HCl	*Photoinitiator*	*pH of reactants' mixture*
r-PGA-0-0	no	no	4.9
r-PGA-H-0	yes	no	1.0
r-PGA-0Ch	no	yes	1.0
r-PGA-H-Ch	yes	yes	5.1
r-TNA-0-0	no	no	5.9
r-TNA-H-0	yes	no	2.5
r-TNA-0Ch	no	yes	2.8
r-TNA-H-Ch	yes	yes	6.2
r-PG-0-0	no	no	5.4
r-GA-0-0	no	no	6.2

As already discussed in Chapters 3 and 4 for other precursors, the solutions of the reactants' mixtures (crystalline) gradually darkened with the irradiation time, and a viscous solid was formed after 60 min of irradiation under UV light. The resulting color of the resins formed upon irradiation was lighter and less viscous than that of the resins obtained upon illumination of PG, and slightly darker and more fluid than those of GA series. In the case of TNA, the reactants' mixture was turbid before irradiation, rather than a clear crystalline solution as observed in the case of all other organic precursors (Figure 5.1.1b). Despite of this, a solid resin was retrieved upon irradiation.

Figure 5.1.2 shows the UV-vis spectra of the reactants' mixtures before and after 60 minutes of illumination; an increment in the absorbance of the samples after UV exposure can be clearly observed in all the cases. The photopolymerized resins were recovered and a thermal treatment at

600 °C under inert atmosphere was performed to obtain the carbon samples. The same carbonization conditions as in PG and GA series were selected for comparative purposes. Moderate carbonization yields between ca. 12-13 wt.%, were obtained, very similar for both precursors (i.e, TNA and PGA) despite their different molecular structure (table 5.1.3). These values were slightly higher than the ones found for gallacetophenone, and lower than the ones for pyrogallol series.
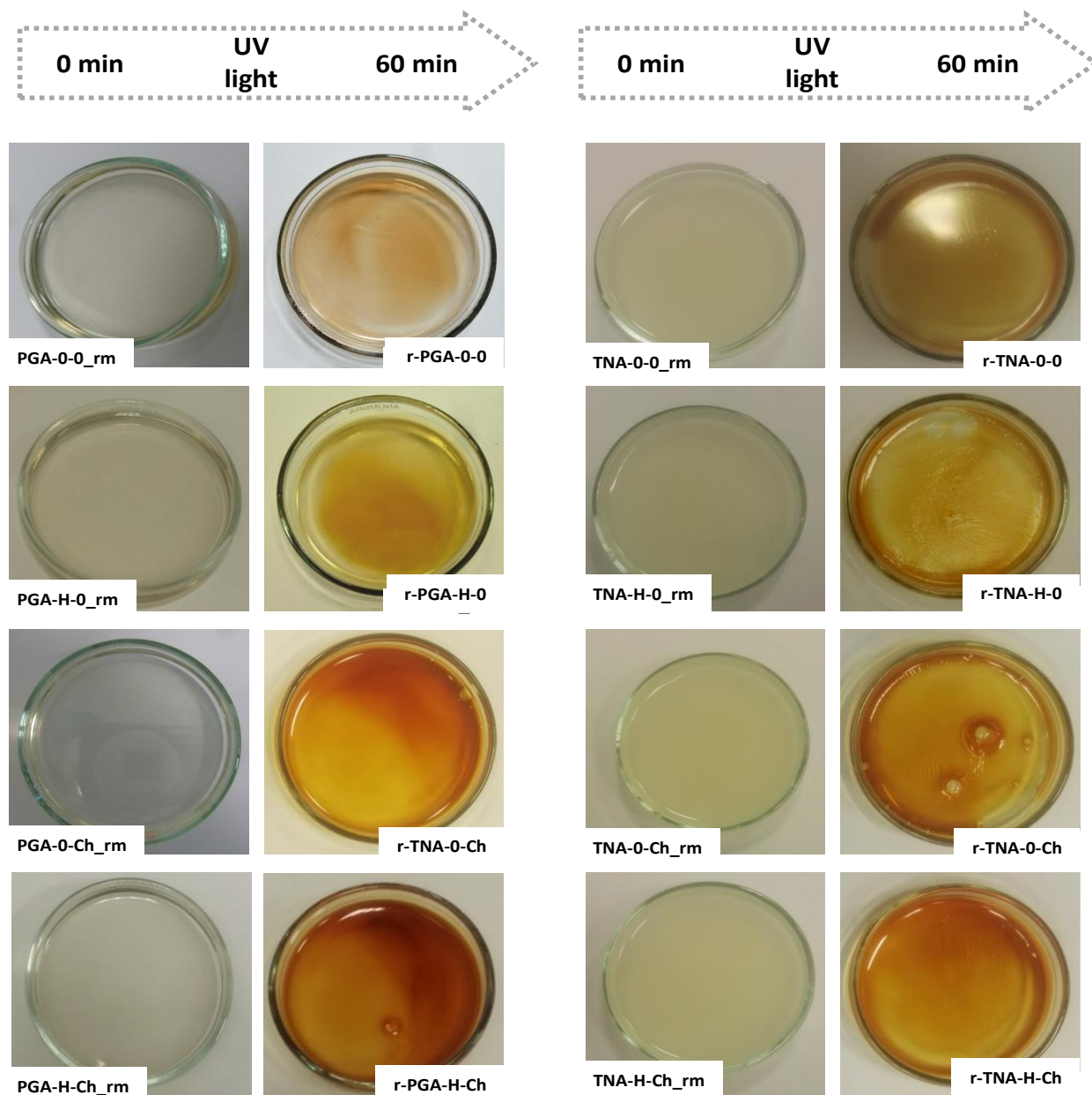
Figure 5.2.1. Visual changes in the TNA and PGA reactant's mixtures before (series rm) and after 60 minutes of UV irradiation.
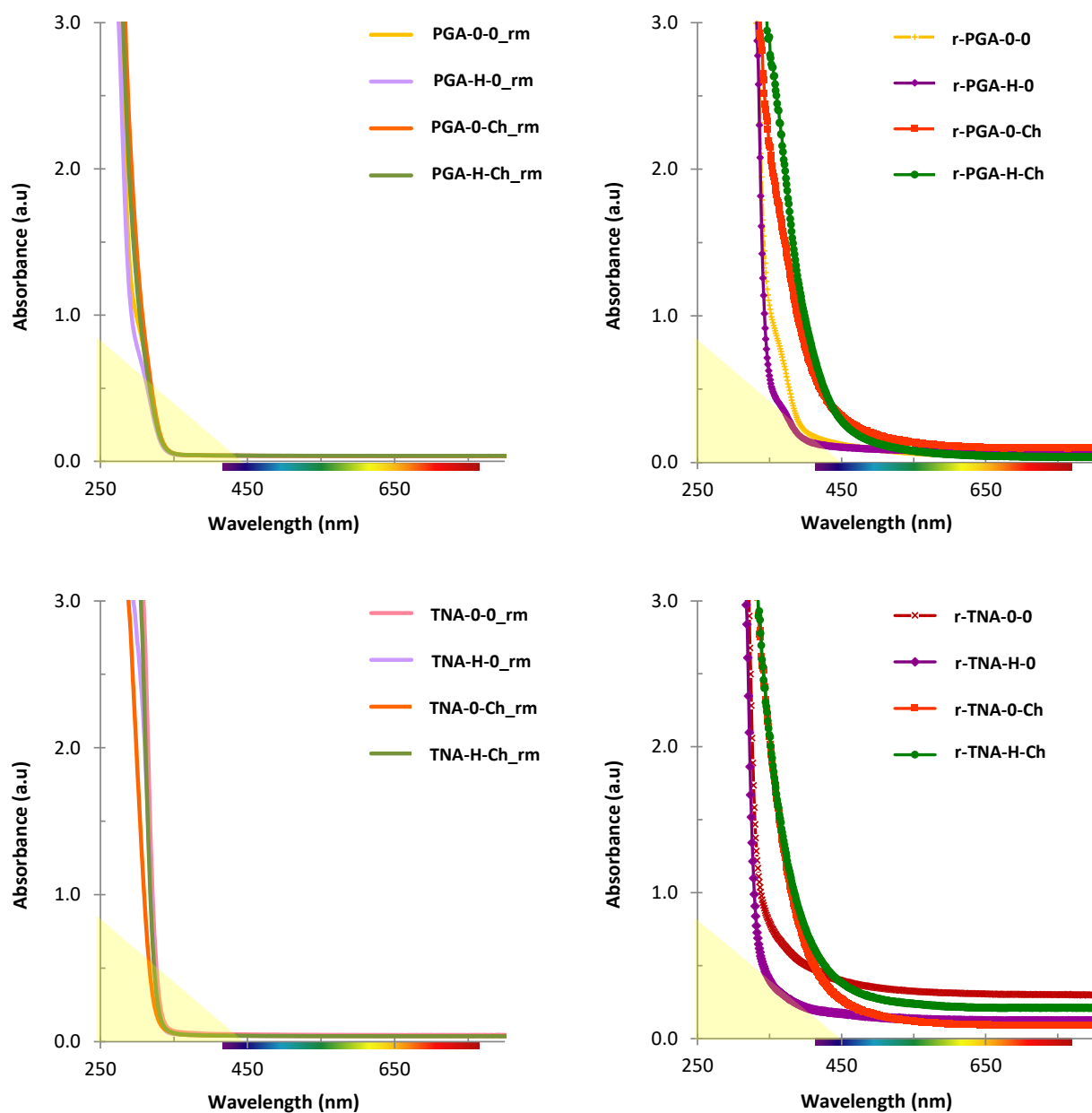
Figure 5.2.2 UV-VIS spectra of PGA and TNA reactant's mixtures before (series rm) and after 60 minutes of UV irradiation.

On the other hand, the surface pH was slightly basic in both cases, with the value corresponding to C-PGA-0-0 being the lowest, similar to that of C-DN (chapter 3). As already discussed for the rest of the series prepared from polyhydroxylated benzenes in chapter 3, these are values characteristic of hydrophobic carbons.

Table 5.2.2. Carbonization yields (wt.%) and surface pH of the carbons materials prepared using TNA and PGA as precursors.

	Carbonization Yield [a]	Carbonization Yield (resin basis)[b]	Surface pH
r-PGA-0-0	11.9	27.8	7.6
r-PGA-H-0	11.4	26.5	8.0
r-PGA-0-Ch	12.0	27.9	7.8
r-PGA-H-Ch	11.8	27.4	7.9
r-TNA-0-0	13.2	30.7	8.1
r- TNA-H-0	11.4	26.6	8.1
r- TNA-0-Ch	12.3	28.7	7.8
r- TNA-H-Ch	11.2	26.1	8.2

[a] Experimental carbonization yield under N_2 atmosphere at 600°C yield
[b] Carbonization yield recalculated on the basis of the resin (i.e. without considering the mass of Pluronic F127)

5.2.1. Textural characterization

The porosity of the samples was characterized by adsorption-desorption isotherms of N_2 at -196 °C as well as CO_2 at 0 °C. The corresponding isotherms are shown in Figure 5.1.3. As seen, the materials presented high gas uptakes of both N_2 at 196 °C and CO_2 at 0 °C, indicating the development of an open porosity in both cases. A summary of the main textural parameters is presented in Table 5.1.4.

The series of samples from PGA presented higher total pore volumes than their corresponding counterparts derived from TNA. The N_2 adsorption- desorption isotherms were in both series of type IV(a), with the presence of pronounced hysteresis loops that point out to the occurrence of large mesopores (ca. > 4nm). However, the shape and the range of relative pressures of the hysteresis loops were different in both series. The samples derived from PGA presented hysteresis loops type H2(b), typically of materials displaying networking effects (pore blocking or cavitation), with adsorption and desorption branches rather parallel, and spanning from ca. 0.69 to roughly 0.96 relative pressures. This indicates the occurrence of wide mesopores and rather uniform distributions of (meso)pore sizes. In addition, for these materials, the analysis of the desorption branch would give information about the size of the pore necks.

Table 5.2.3. Main textural parameters of the carbons of the series PGA and TNA obtained from gas adsorption analysis. Data corresponding to samples C-GA-0-0, C-GA-H-0 and C-PG-0-0 are presented for comparative purposes.

	S_{BET} (m^2/g)	V_{PORES}[a] (cm^3/g)	$V_{MICRO\,N2}$[b] (cm^3/g)	V_{MICRO}[c] (cm^3/g)	V_{MESO}[c] (cm^3/g)	$W_{0\,CO2}$[d] (cm^3/g)	L^e (nm)
C-PGA-0-0	592	0.97	0.21	0.18	0.79	0.17	0.59
C-PGA-H-0	520	1.14	0.19	0.17	0.91	0.18	0.59
C-PGA-0-Ch	559	0.89	0.20	0.18	0.69	0.18	0.58
C-PGA-H-Ch	541	0.78	0.20	0.19	0.53	0.19	0.60
C-TNA-0-0	577	0.50	0.20	0.18	0.30	0.18	0.59
C-TNA-H-0	580	0.63	0.21	0.19	0.43	0.18	0.55
C-TNA-0-Ch	565	0.38	0.21	0.20	0.18	0.19	0.59
C-TNA-H-Ch	541	0.44	0.20	0.19	0.24	0.20	0.59
C-GA-0-0	518	0.70	0.19	0.15	0.52	0.14	0.64
C-PG-0-0	570	0.75	0.21	0.17	0.56	0.19	0.61

[a] Evaluated at $p/p_0 \sim 0.99$ in the N_2 adsorption isotherms at -196 °C.
[b] Micropores volume, evaluated from DR equation applied to N_2 adsorption data at -196 °C.
[c] Evaluated from the 2D-NLDFT-HS method applied to N_2 adsorption data at -196 °C.
[d] Narrow micropores volume, from DR equation applied to CO_2 adsorption data at 0 °C.
[e] Evaluated using the Stoeckli-Ballerini equation applied to CO_2 adsorption data at 0 °C

At converse, the samples of the series TNA presented hysteresis loops type H2(a), with a smooth adsorption branch and a steep desorption branch; the loop spans from relative pressures around 0.5 to 17, indicating mesopores of narrower sizes than those of series PGA. The percolation threshold in these samples occurs in a narrow range of pore necks, while the relative pressure of the closure of the desorption branch (i.e., close to 0.5) points out to the existence of cavitation-induced evaporation. For such complex systems, the analysis of the desorption branch for the estimation of the size of the pore necks is not recommended. The analysis of the N_2 adsorption isotherms by applying the 2D- NLDFT-HS method was carried out to obtain a realistic pore size distribution of the materials (Figures 5.3.b and 5.4.b). As seen, narrower distributions of mesopores (ca. 3-10 nm) were found for samples of the series TNA, compared to the samples derived from PGA (ca. 5-25 nm).
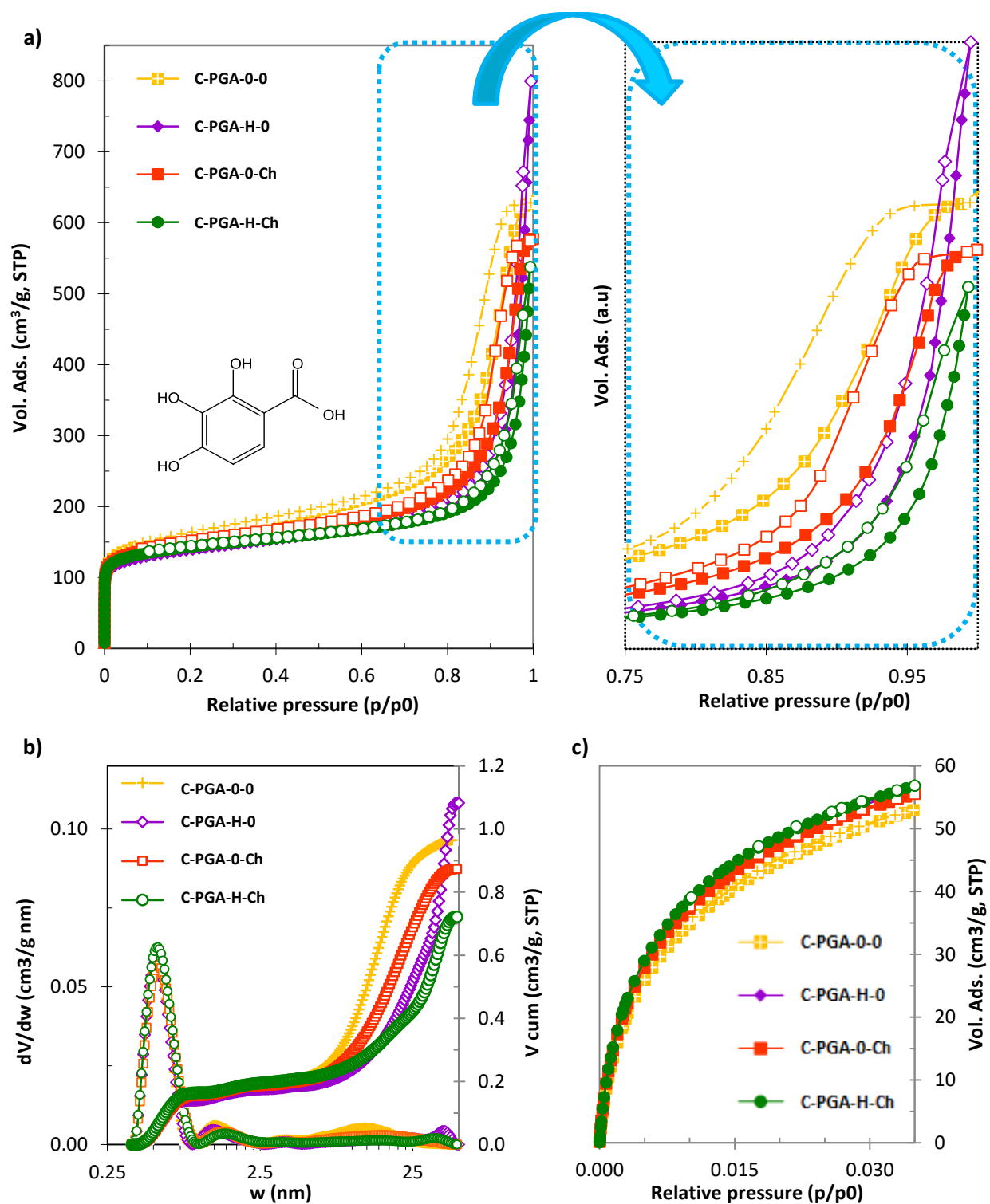
Figure 5.2.3. (top left) High resolution N_2 adsorption/desorption isotherms at -196 °C and (top right) CO_2 adsorption isotherms at 0 °C of the materials derived from PGA after carbonization (full symbol: adsorption; empty symbol: desorption); c) Pore size distribution evaluated using the 2D-NLDFT-HS method from the adsorption branch of the N_2 isotherms.
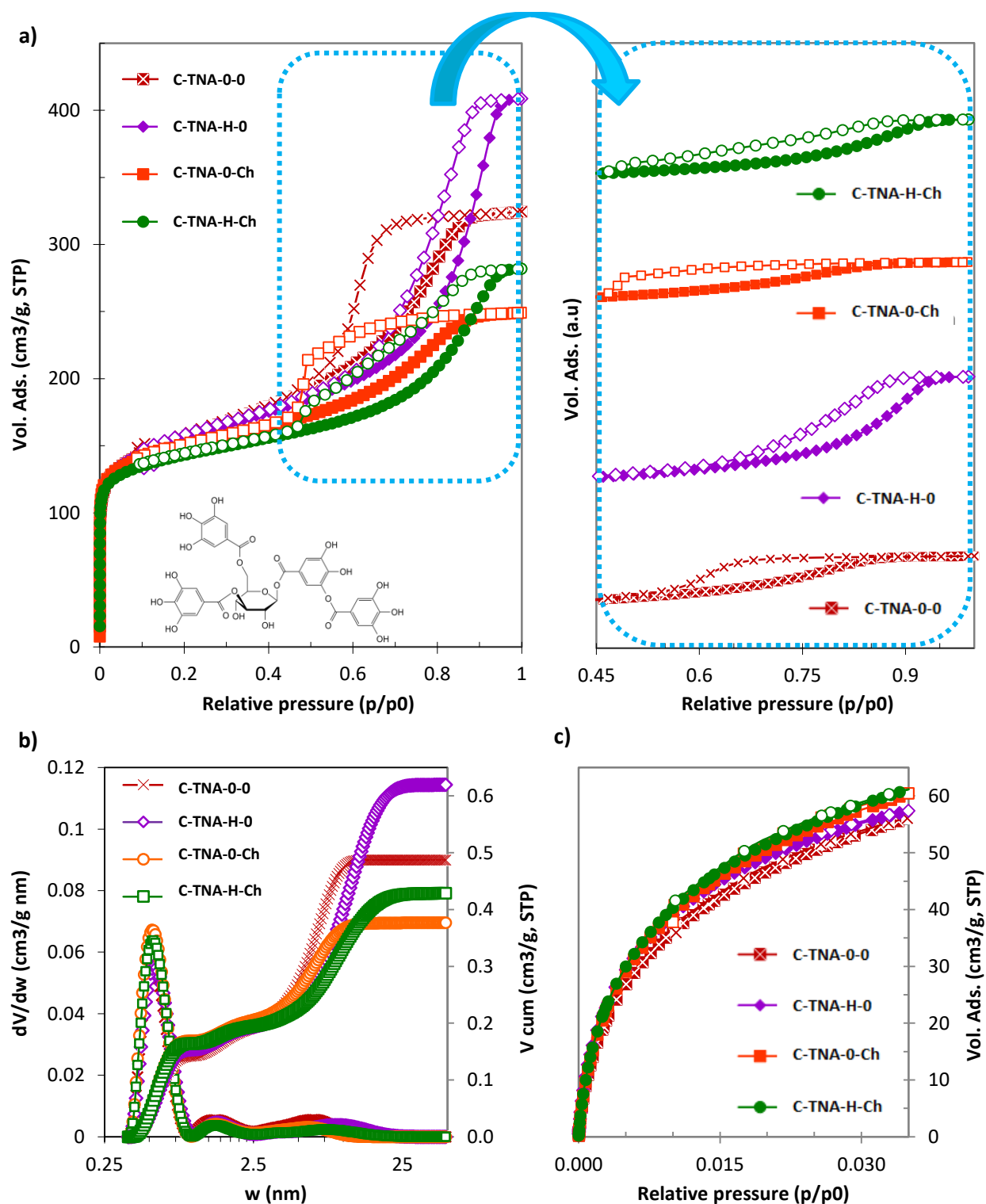
Figure 5.2.4. (top left) High resolution N_2 adsorption/desorption isotherms at -196 °C and (top right) CO_2 adsorption isotherms at 0 °C of the materials derived from TNA after carbonization (full symbol: adsorption; empty symbol: desorption); c) Pore size distribution evaluated using the 2D-NLDFT-HS method from the adsorption branch of the N_2 isotherms.

At neutral pH conditions, samples C-TNA-0-0 and C-TNA-0-Ch presented a clear **type H2(a) hysteresis loops,** extending from 0.49 to 0.86 and 0.45 to 0.86 of relative pressures for samples C-TNA-0-0 and C-TNA-0-Ch, respectively. When HCl was used, a **type H2(b)** hysteresis loop was observed for sample C-TNA-H-0 (expanding from 0.59 to 0.96 of relative pressures) and **type H5** for sample C-TNA-H-Ch (expanding from 0.45 to 0.96 of relative pressures). This data suggest that the HCl itself leads the formation of larger and more open mesopores with a larger distribution of neck sizes. In the case of C-TNA-H-0, the total pore volume is also higher. For sample C-TNA-H-Ch, the hysteresis loop occurred in the wider range of relative pressures, characteristic of a material with a wide distribution of mesopores; the shape of the loop suggests a bimodal distribution of mesopores, with a fraction of mesopores partially blocked (e.g., isolated pores with small neck sizes). Regarding surface area and microporosity, the values were very similar for both precursors (Table 5.2.4). A similar trend was obtained for the narrow microporosity evaluated from the CO_2 adsorption isotherms at 0 °C. This was expected since the carbonization yield was rather similar for all the materials. In this regard, as discussed in previous chapters, the microporosity of carbons obtained by the photoassisted polycondensation of polyhydroxylated organic precursors seems to be dependent on the nature of the resin network itself and the carbonization yield, rather than on the interactions between the resin with the surfactant during the photoassisted reaction. On the other hand, the PSD on the mesopore range followed the trend: C-PGA-0-0 $\prec$ C-PGA-0-Ch $\prec$ C-PGA-H-0 $\prec$ C-PGA-H-Ch. More in detail, **strong acidic conditions** (samples C-PGA-H-0 and C-PGA-H-Ch), **rendered materials with larger mesopores** (reaching sizes of 38-40 nm), as evidenced by the hysteresis loop expanding over higher values of relative pressure. In the presence of photoinitiator, a decrease in the V_{TOTAL} was observed. For the series of samples derived from TNA, a similar trend was observed, with acidic conditions favoring the formation of larger mesopores sizes. The PSD on the mesopore range followed the trend: C-TNA-0-0 $\prec$ C-TNA-0-Ch $\prec$ C-TNA-H-0 $\prec$ C-TNA-H-Ch. Moreover, larger pore volumes were favored when acidic conditions were used, as compared to the presence of photoinitiator. The later, itself, did not modify the average pore size (remaining practically the same at about 6-6.5 nm) but caused a reduction of about 0.25 cm^3/g in the pore volume (Figure 5.2.4).

5.2.2. Morphological characterization

The TEM micrographs of the carbons derived from TNA and PGA are shown in Figure 5.1.5). Both precursors rendered amorphous carbons, which contrasts with the trend observed for PG with an ordered pore network arrangement.

a)

b)
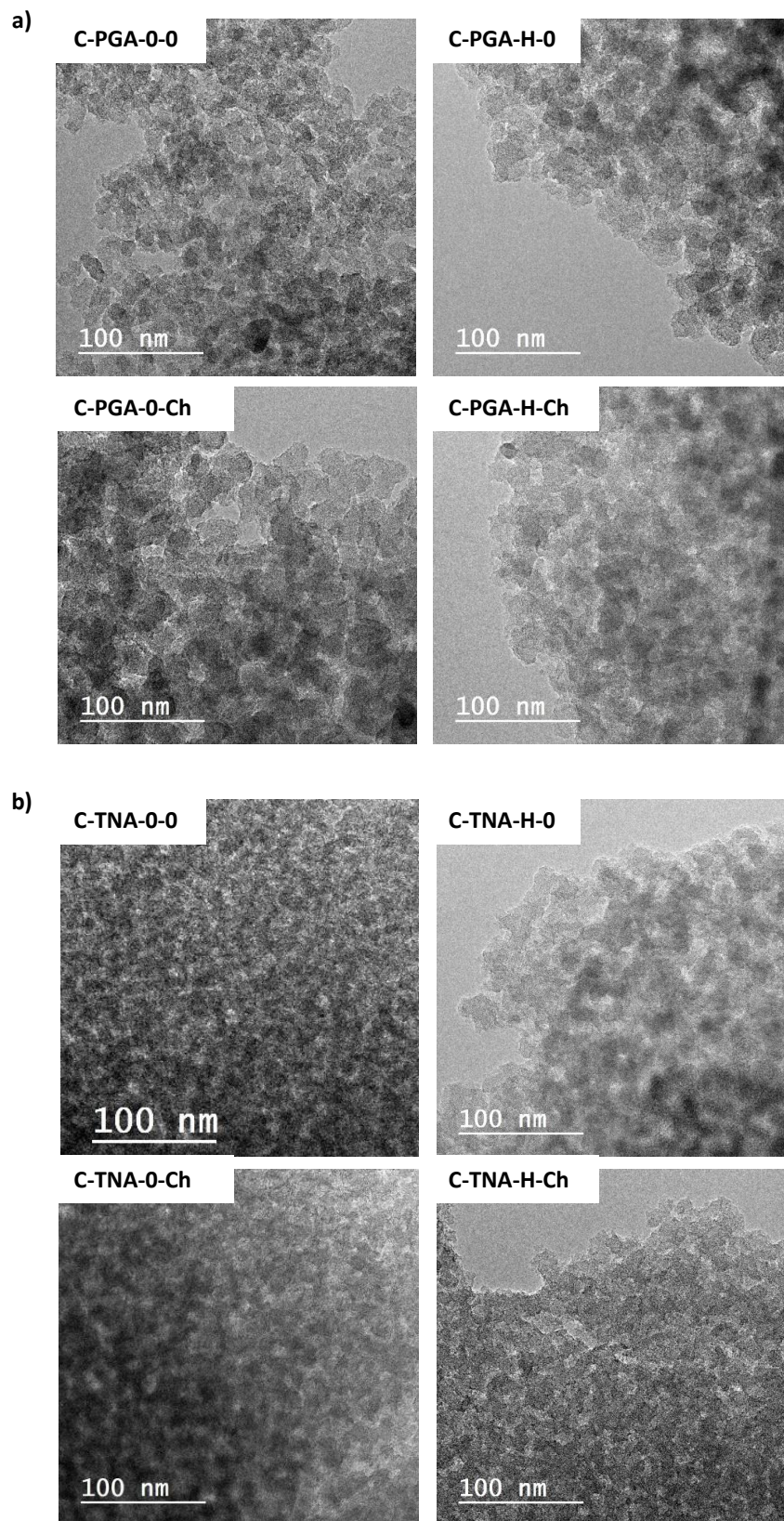
Figure 5.2.4. TEM images of the carbon materials obtained using TNA and PGA as precursors.

A worm-like morphology is observed in all the samples, with mesopores connected by channels arranged in a disordered structure. All this suggests that the interactions between the resin and the surfactant are greater in the case of TNA, leading to a denser assembly of particle nodules [Liu 2010] or high crosslinked resin leaving less mobility for surfactant reorganization during the heat treatment, resulting in narrower mesoporosity. Such interactions could be attributed to either the higher density of –OH groups in TNA precursor, and/or a kinetic effect, since the PGA reacts faster with glyoxal, giving rise to a less branched polymeric resin (less crosslinked) with polymer chains roughly distributed around the micelles.

5.3. THBA-based materials

One of the key parameters for the generation of highly ordered mesostructures that might yield ordered carbon materials through the self-assembly of a phenolic resin and the surfactant, is the number of hydrogen bonding of the organic precursor with the -PEO groups of the surfactant, that would lead to strong interactions between both species [Liang 2004]. In this regard, after having explored the trihydroxybenzoic acids PGA (2, 4, 6-trihydroxybenzoic acid), were the three -OH groups and the carboxylic acid are in adjacent positions, and TNA with three -OH groups of the aromatic rings in adjacent positions, we decided to investigate the use of 2, 4, 6-trihydroxybenzoic acid (THBA), where the–OH groups are in non-adjacent positions (Table 5.1.1). The experimental procedure used was the same as indicated for PGA and TNA (glyoxal/ EtOH 1:100 molar ratio; glyoxal: OP: Pluronic F127 molar ratio of 1.4: 1: 0.03; ethanol as solvent; illumination at 365 nm for 1 h), varying the experimental parameters concerning the acid and photoinitiator as compiled in Table 5.3.2. Due to the nature of THBA precursor, all the reactant's mixtures presented a marked acidic character, regardless the incorporation of HCl in the synthesis.

Table 5.3.1. Summary of experimental conditions used in the synthesis of polymeric resins using THBA as precursor, and pH of the reactant's mixtures.

	HCl	*Photoinitiator*	*pH of reactants' mixture*
r-THBA-0-0	no	no	2.1
r-THBA-H-0	yes	no	1.0
r-THBA-0-Ch	no	yes	2.2
r-THBA-H-Ch	yes	yes	1.0

After 60 minutes of irradiation, the solids were recovered. A polymer film was formed in all cases for THBA resin series, being possible to remove them in one piece from the petri dish (Figure 5.3.1). The as-obtained polymeric resins presented a rather elastic character (e.g., r-THBA-0-0, r-THBA-0-Ch and r-THBA-H-Ch), being more elastic those resins prepared in the presence of photoinitiator. For sample r-THBA-H-0, a more fragile film was obtained. It's important to remark that all this series of materials presented a different rheology, compared with the resins prepared from other tri-hydroxylated precursors (i.e. GA, PG, PGA, TNA) with a rather soft character.
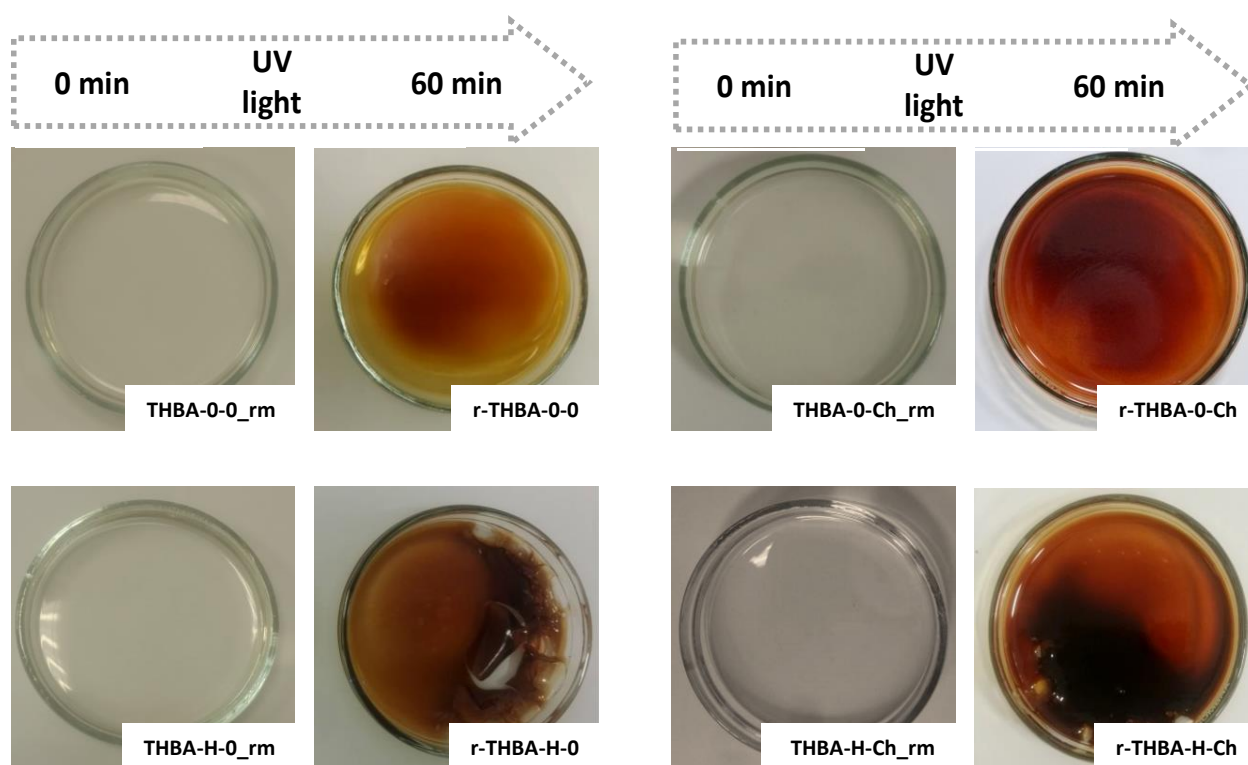
Figure 5.3.1. Visual changes in the THBA reactant's mixtures before (series rm) and after 60 minutes of UV irradiation.

The UV-vis spectra of the samples (Figure 5.3.2) show the increase in the absorbance of the mixtures after the exposure to the 365 nm UV light.

The thermal treatment of the resins at 600 °C under inert atmosphere rendered carbonization yields between 18-20 wt.% (Table 5.3.2), with values slightly lower when the photoinitiator was employed. These values were similar to those of the PG series (i.e. ~20 wt.%). The surface pH of the carbons was rather neutral in all cases, as also obtained for most of the carbon materials, regardless the precursor used. Slight higher pH values were obtained in the samples with photoinitiator.
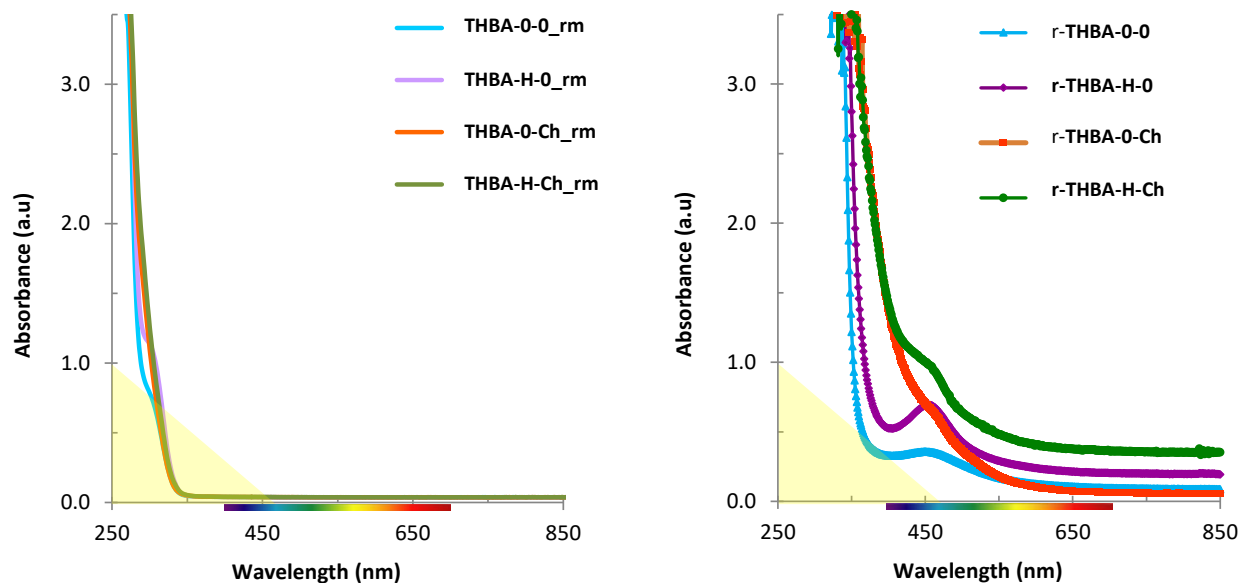
Figure 5.3.2. UV-VIS spectra of THBA reactant's mixtures before (series rm) and after 60 minutes of UV irradiation.

Table 5.3.2. Carbonization yields (wt.%) and surface pH of the carbons materials prepared using THBA as precursor.

	Carbonization Yield [a]	Carbonization Yield (resin basis)[b]	Surface pH
r-THBA-0-0	20.4	47.1	6.8
r-THBA-H-0	20.5	47.7	6.9
r-THBA -0-Ch	18.3	42.5	7.3
r-THBA -H-Ch	18.0	41.9	7.4

[a] Experimental carbonization yield under N_2 atmosphere at 600°C yield
[b] Carbonization yield recalculated on the basis of the resin (i.e. without considering the mass of Pluronic F127)

5.3.1. Textural characterization

The adsorption-desorption isotherms of N_2 at -196 °C and CO_2 at 0 °C are shown in Figure 5.3.3. A summary of the main textural parameters is presented in Table 5.3.4. The materials presented high N_2 and CO_2 adsorption uptakes, indicating a well-developed porosity.

The appearance of hysteresis loops confirmed the presence of large mesopores (type IVb isotherms). Interestingly, the main difference among the sample is the shape of the hysteresis loop.

The closing point in the desorption branch of the loops is similar in all the samples (spanning from 0.42 vs 0.44 of relative pressures), but the starting point is different for the materials, spanning towards higher relative pressures for the samples prepared in the presence of HCl. Indeed, the starting point of the loop for carbons C-THBA-0-0 and C-THBA-0-Ch expanded from relative pressures of ca. 0.66 and 0.65, respectively, and to ca. 0.80 and 0.77 for samples C-THBA-H-0 and C-THBA-H-Ch, respectively. This indicates the presence of mesopores of narrower sizes for the former. Furthermore, in the absence of HCl the hysteresis loops present a shape classified as type H2(a), as opposed to type H2(b) in the presence of acid. This points out to important differences in the pore network of the samples [Thommes 2006, 2014]. A similar behavior was observed for the carbons of the series C-PG-X-Y (see chapter 4.2); in that case, the carbons also presented an ordered pore structure of open mesopores. Regarding PSD, all the samples presented a monomodal narrow distribution of mesopores, with average pore sizes ranging from 3.9 nm for C-THBA-0-Ch to 4.7 nm for C-THBA-H-0.

Table 5.3.4. Main textural parameters of the carbons of the series THBA obtained from gas adsorption analysis.

	S_{BET} (m^2/g)	V_{PORES}[a] (cm^3/g)	$V_{MICRO\ N2}$[b] (cm^3/g)	V_{MICRO}[c] (cm^3/g)	V_{MESO}[c] (cm^3/g)	$W_{0\ CO2}$[d] (cm^3/g)	L[e] (nm)
C-THBA-0-0	903	0.75	0.31	0.26	0.46	0.19	0.60
C-THBA-H-0	912	0.84	0.30	0.25	0.56	0.23	0.63
C-THBA-0-Ch	850	0.63	0.28	0.26	0.35	0.22	0.60
C-THBA-H-Ch	847	0.71	0.28	0.24	0.44	0.20	0.60

[a] Evaluated at $p/p_0 \sim 0.99$ in the N_2 adsorption isotherms at -196 °C.
[b] Micropores volume, evaluated from DR equation applied to N_2 adsorption data at -196 °C.
[c] Evaluated from the 2D-NLDFT-HS method applied to N_2 adsorption data at -196 °C.
[d] Narrow micropores volume, from DR equation applied to CO_2 adsorption data at 0 °C.
[e] Evaluated using the Stoeckli-Ballerini equation applied to CO_2 adsorption data at 0 °C

While the closure point of the hysteresis loop (desorpton branch) for the series of THABA is quite similar, differences are evident regarding the shape of the desorption. Indeed, the desorption brach falls steep and almost vertical for samples C-THBA-0-0 and C-THBA-0-Ch, which suggests that cavitation effect was taking place. In contrast, for samples prepared under acidic conditions (i.e., C-THBA-H-0 and C-THBA-H-Ch), the desorption branch is smoother (Figure 5.3.3 insets). **Thus, the obtained data suggests that we are witnessing a transition of desorption mechanisms from a desorption controlled by cavitation to pore blocking depending** on the pH of the materials

synthesis. Similar observations have been reported for highly ordered mesoporous silica [Morishige 2006], where the diameter of the pore necks increased with the temperature of the hydrothermal treatment, being able to switch between cavitation to pore blocking evaporation (also pointed out by the evolution of the hysteresis loops from H2(a) to H2(b) type).

Another remarkable, differences is the total pore volume of the samples, with slightly higher values for the samples of the series H, compared to their corresponding counterparts prepared in the absence of acid. On the other hand, high values of S_{BET} were obtained for all the samples, ranging from 850 to 910 m^2/g, with no significant differences observed among the samples. This is in agreement with previous observations for other precursors suggesting that the microporosity seems to be related to the nature of the precursor with a lower impact of the rest of experimental conditions -perhaps values slightly higher for the samples prepared in the absence of photoinitiator, although differences might not be meaningful-. The materials also displayed similar volumes of narrow micropores (ca. 0.19 to 0.23 cm^3/g) with not clear trend correlating to the differences in the experimental conditions.

In order to further evaluate the nature of the networking effects in complex pore systems, sample C-THBA-0-0 was analyzed by scanning the hysteresis loop of the nitrogen adsorption/desorption data. As already indicated in Chapter 3, this methodology allows to discriminate between the occurrence of pore blocking or cavitation effects; if pore blocking is the dominant mechanism, the evaporation pressure is controlled by the size of the pore necks (or interconnecting pores), and the analysis of the PSD using the desorption branch may be used to evaluate the size of those mesopores necks. This is not possible in the case of cavitation-induced evaporation. The recorded adsorption and desorption scanning curves corresponding to different filling/emptying states of the hysteresis loop are shown in Figure 5.3.4.

The primary desorption scanning curves (PDSC) recorded by reverting the isotherm before the saturation is complete indicate that the partial pore filling of the sample has an important effect on the shape of the scans. Indeed, the uptake of the PDSC scanning curves decrease smoothly up to a point where they converge the boundary evaporation branch (full desorption). This trend is opposed to the behaviour observed in Chapter 3 for sample C-PG (displaying an ordered mesopores structure), and indicates that while a fraction of the -desorption scan will present different shape than the initial desorption curve [Cimino, 2013]. An analysis of the volume freely desorbed in the PDSC scanning curves indicates that, for instance, the fraction of mesoporosity that would

evaporate freely at the different scans in Figure 5.3.4 represents ca. 80 % (the remaining mesopore fraction would be constricted through pores of smaller dimensions).
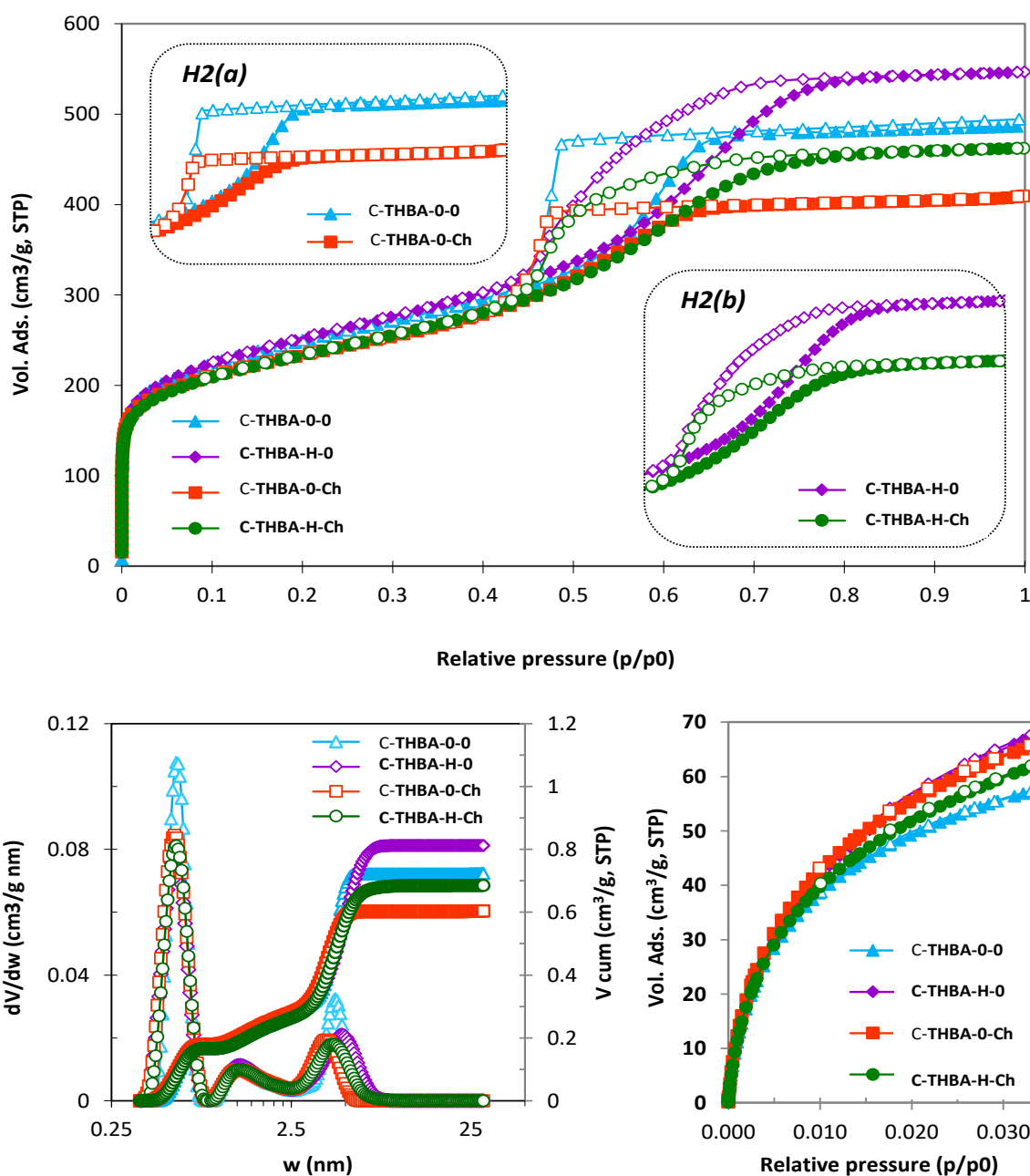
Figure 5.3.3. a) High resolution N_2 adsorption isotherms at -196 °C of the materials after carbonization (full symbol: adsorption branch; empty symbol: desorption branch); (down, left) Pore size distribution (PSD) evaluated using the 2D-NLDFT-HS method from the adsorption branch of N_2 isotherm; (down, right) CO_2 adsorption isotherms at 0 °C.
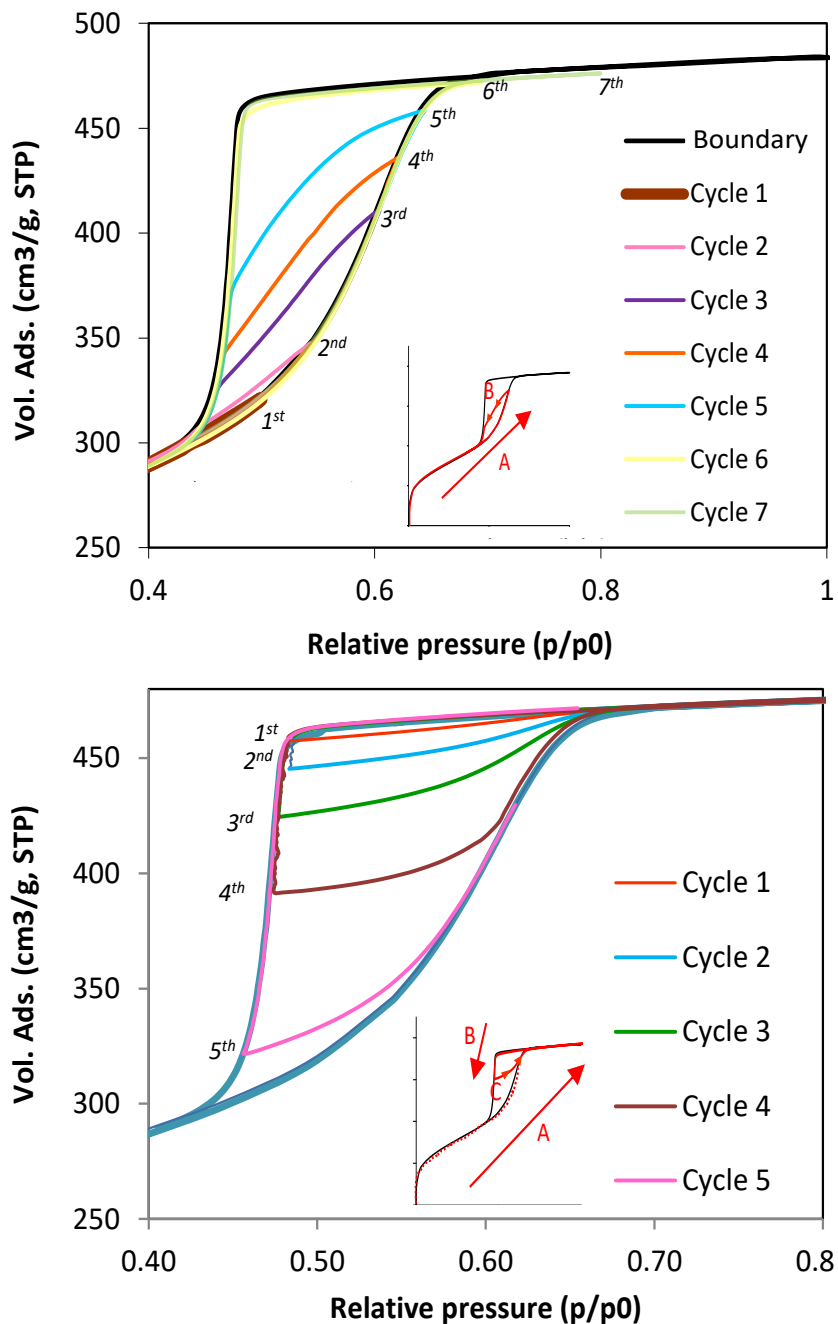
Figure 5.3.4. Scanning N_2 adsorption/desorption isotherms at -196 °C of sample C-THBA-0-0: (top) primary desorption scanning curves (partial pore filling); (bottom) secondary adsorption scanning curves (partial pore emptying).

This was confirmed by the shape of the secondary adsorption scanning curves (SASC) -where condensation stars when a fraction of the pores is still filled-; despite the desorption branch of the scans is similar to the boundary branch (thus large fraction of pores remain blocked), adsorption at

high relatives pressures still takes place, due to the fraction of pores that can be emptied/filled regardless the state of neighboring pores (not constricted pores).
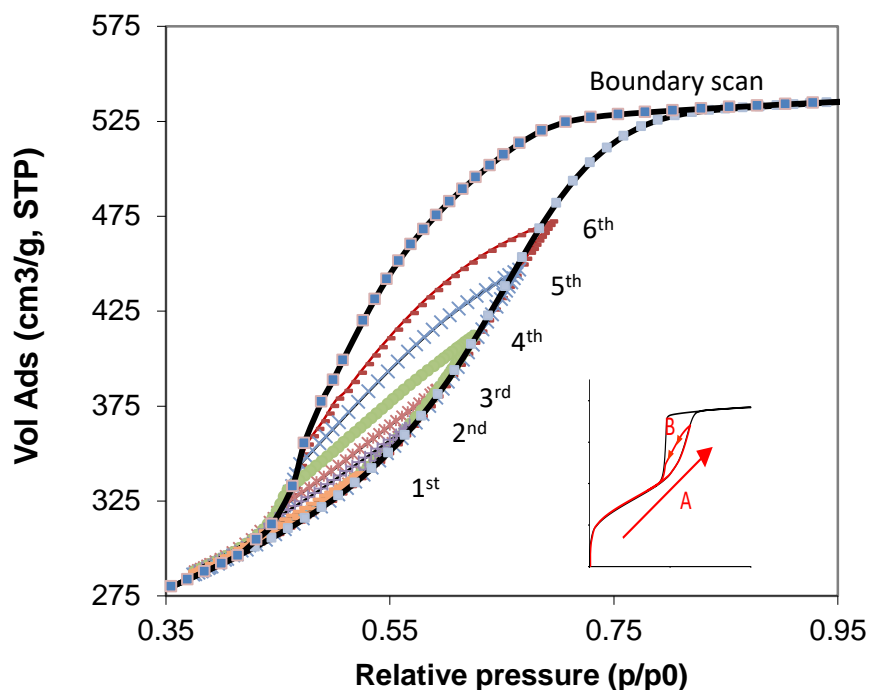
Figure 5.3.5. Primary desorption scanning curves (partial pore filling) of the N_2 adsorption/desorption isotherms at -196 °C of sample C-THBA-H-0.

In the case of sample C-THBA-H-0 (Figure 5.3.5), the shape of the boundary desorption curve is less abrupt, thus that of the primary desorption scanning curves follows a similar trend, with a much higher fraction of pores that evaporate freely (compared to the fraction of pores constricted). The fraction of mesoporosity that would evaporate freely at the different scans in Figure 5.3.5 is higher than in sample C-THBA-0-0, ranging from 80-90 %, pointing out a smaller fraction of blocked mesopores.

The Argon adsorption isotherms at -186 °C (87 K) carried out on these two samples also confirmed this observation. According to literature, performing adsorption/desorption experiments with different gases allows for detecting and separating the effects of pore blocking/percolation and cavitation evaporation phenomena. Since cavitation-controlled evaporation is a universal feature of the adsorptive, the pressure of evaporation does not depend upon the pore structure of the material or the neck size [Thommes 2006, 2010].
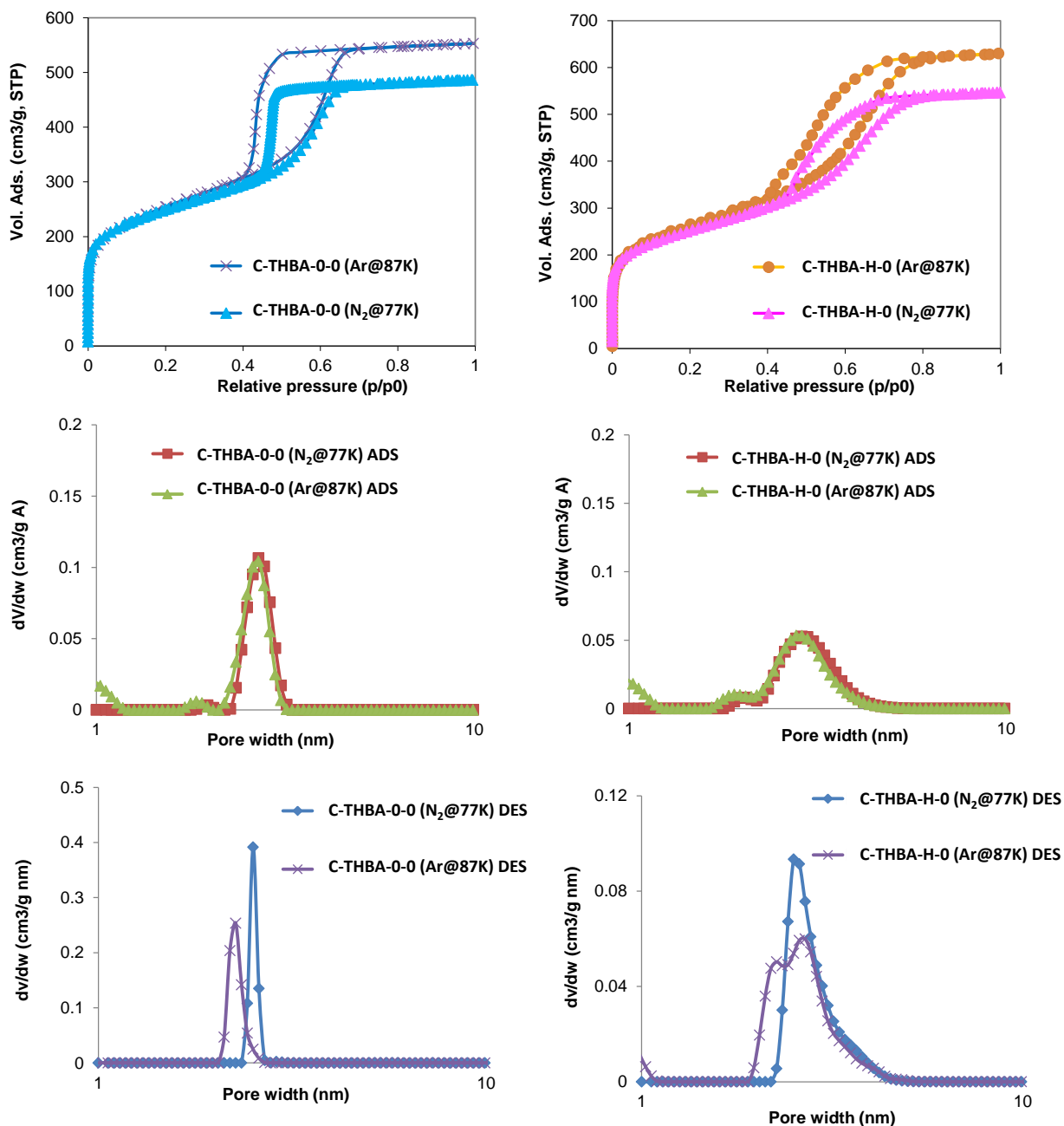
Figure 5.3.6. a) High resolution Ar adsorption isotherms at -186 °C of samples C-THBA-0-0 and C-THBA-H-0 (full symbol: adsorption branch; empty symbol: desorption branch). Data is compared to the N_2 adsorption isotherms at -196 °C; (down, left) Pore size distribution (PSD) evaluated using the QSDFT models for carbons with slit/cylinder geometry, applied to the adsorption (ADS) and desorption (DES) branches for the Ar and N_2 data.

The analysis of the pore size distribution for nitrogen at -196 ºC and argon at -186ºC (desorption branch) of samples C-THBA-0-0 and samples C-THBA-H-0 rendered similar profiles in the PSD when the adsorption branch of both gases was analyzed (Figure 5.3.5) and differences for the desorption branch, demonstrating that cavitation is occurring in the pores. Interestingly, the PSD obtained from N_2 and Ar isotherms from the desorption branch for sample C-THBA-H-0 overlap in a high range of pore width, but the distribution from argon shows a bimodal shape with a second peak featuring at lower pore widths. This would correspond to the fraction of pores that are blocked (where cavitation would occurs), in agreement with the analysis of the scanning curves.

5.3.2. Morphological characterization

The TEM micrographs of the carbons prepared under different chemical conditions revealed a typical 2D hexagonally ordered array mesoporous materials (Figure 5.3.7), with some differences among the samples.

For instance, sample C-THBA-0-0 presents a high range of order, with microdomains larger than 2 μm of the regular strip–shaped channels of around 5 nm each when viewed from the perpendicular channel direction, and hexagonally arranged when viewed along the channel direction. When the photoinitiator was employed (sample C-THBA-0-Ch), the degree of scope of order was still high but slightly decreased. The coexistence of ordered and disordered worm-like domains appears when HCl was used, being this effect more remarkable for sample C-THBA-H-Ch.

According to literature, at surfactant concentrations high enough to reach the critical micelle concentration (CMC), several structural transitions can be observed for Pluronic F127, shifting from a disorganized arrangement of the micelles, to an ordered hexagonal and/or cubic phase and then to the formation of cylindrical rods in a disordered structure when the cloud point is reached [Holmqvis 1997; Alexandridis 1995; Wanka 1994]. Based on this, it seems that the presence of photoinitiator and the strong acidic conditions reached when the HCl is incorporated would modify the polymerization rate of the aromatic resin, and thus the size and the mobility of the oligomers. Hence, the lack of order could be attributed to the rapid formation of high molecular weight polymer chains or cross-linked systems that would prevent the correct self-assembly with the template. In the case of long heavy and less crosslinked chains, the fast arrangement would lead to a disordered distribution around the micelles hindering the ordered micellar system [Liu 2010]. On the other hand, it has been reported for a phloroglucinol-formaldehyde resin that the crosslinking of the resin can freeze the mesostructure resin-surfactant, hindering any further reorganization [Long 2009; Liang 2006].
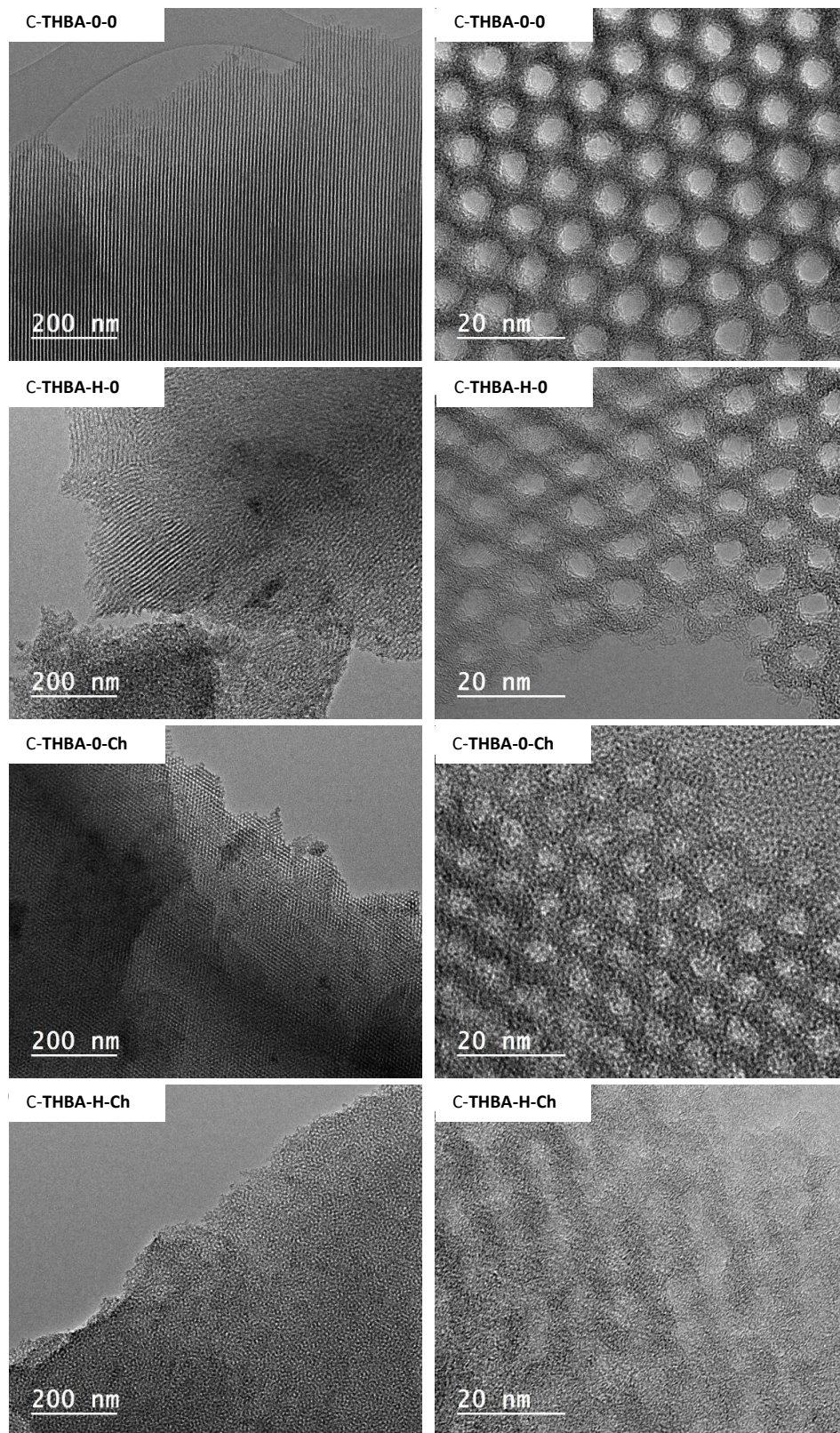
Figure 5.3.7. TEM images of the carbon materials obtained using THBA as precursor.

In view of our results, the coexistence of hexagonal and disorder worm-like mesopores would seem to be more related with an imperfect balance between the polymerization rate and the self-assembly with the pluronic micelles. As a result, a poor crosslinked resin is formed, which would not be able to overcome the stress of the backbone skeleton occurring during the carbonization step, thus rendering materials with imperfect ordered/disordered arrangements.

5.4. ^{13}C NMR study of the phenolic resins

The characterization of the prepared resins and carbon materials revealed that some of the precursors allowed to obtain carbon materials with an ordered mesoporous framework. To better understand these differences ^{13}C NMR experiments were carried out on the **phenolic resins** after the 60 minutes irradiation. To undertake this study, selected resins of the pyrogallol (PG), pyrogallo-4-carboxylic acid (PGA) and 2',4',6'-Trihydroxybenzoic acid (THBA) series we selected. Two different ^{13}C NMR experiments were performed: ^{13}C CP-MAS (cross polarization- magic angle spinning) and ^{13}C high-power proton decoupling- magic angle spinning (^{13}C hpdec- MAS).

Data corresponding to ^{13}C CP-MAS spectra is shown in Figures 5.4.1 to 5.4.3. As seen, all ^{13}C CP-MAS spectra showed the intense peak placed at ~71 *ppm* attributed to the carbon atoms of -CH$_2$ moieties bonded to oxygen atoms (**C**H$_2$-O-**C**H$_2$) in the hydrophilic PEO (polyethylene oxide) groups of Pluronic F127, as well as the peaks at ~76 and 74 *ppm* for both carbon atoms in –**C**H-**C**H$_2$ moieties of the hydrophobic PPO (polypropylene oxide) groups (-O**C**H(CH$_3$)-**C**H$_2$-) [Yihui 2014; Jiangxiu 2020]; and the peak at ~18 *ppm* of the methyl group (–**C**H$_3$) of the PPO bonded to –OCH(**C**H$_3$)-CH$_2$- [Yihui 2014; Niu 2020; Nomoto 2010].

Interestingly, while the signals attributed to pluronic are observed in all the polymeric resins; those corresponding to the formation of the phenolic resin (intense signals between 170-180 ppm) were only observed in some samples. More in detail, for the PG series, the ^{13}C CP-MAS NMR spectra of r-PG-0-0 and r-PG-H-0 (Figure 5.4.2) displayed the typical signals belonging to the pluronic F127, while those of the phenolic resin were only observed in sample r-PG-H-0. For the samples of the PGA series (Figure 5.4.3), the ^{13}C CP-MAS NMR spectra of both samples were almost the same, showing only the typical signals belonging to the surfactant. For the samples of the THBA series, the ^{13}C CP-MAS NMR spectra were also quite similar, showing in both samples the peaks assigned to the surfactant and those assigned to the phenolic resin. It is interesting to remark that the ^{13}C CP-MAS spectra showing only the signal assigned to the surfactant corresponded to **those ones that did not present an ordered mesoporous structure**. **This qualitative but valuable information**

suggests that the key step leading to the takes place during the illumination of the reactants, and before the thermal treatment to obtain the carbons.
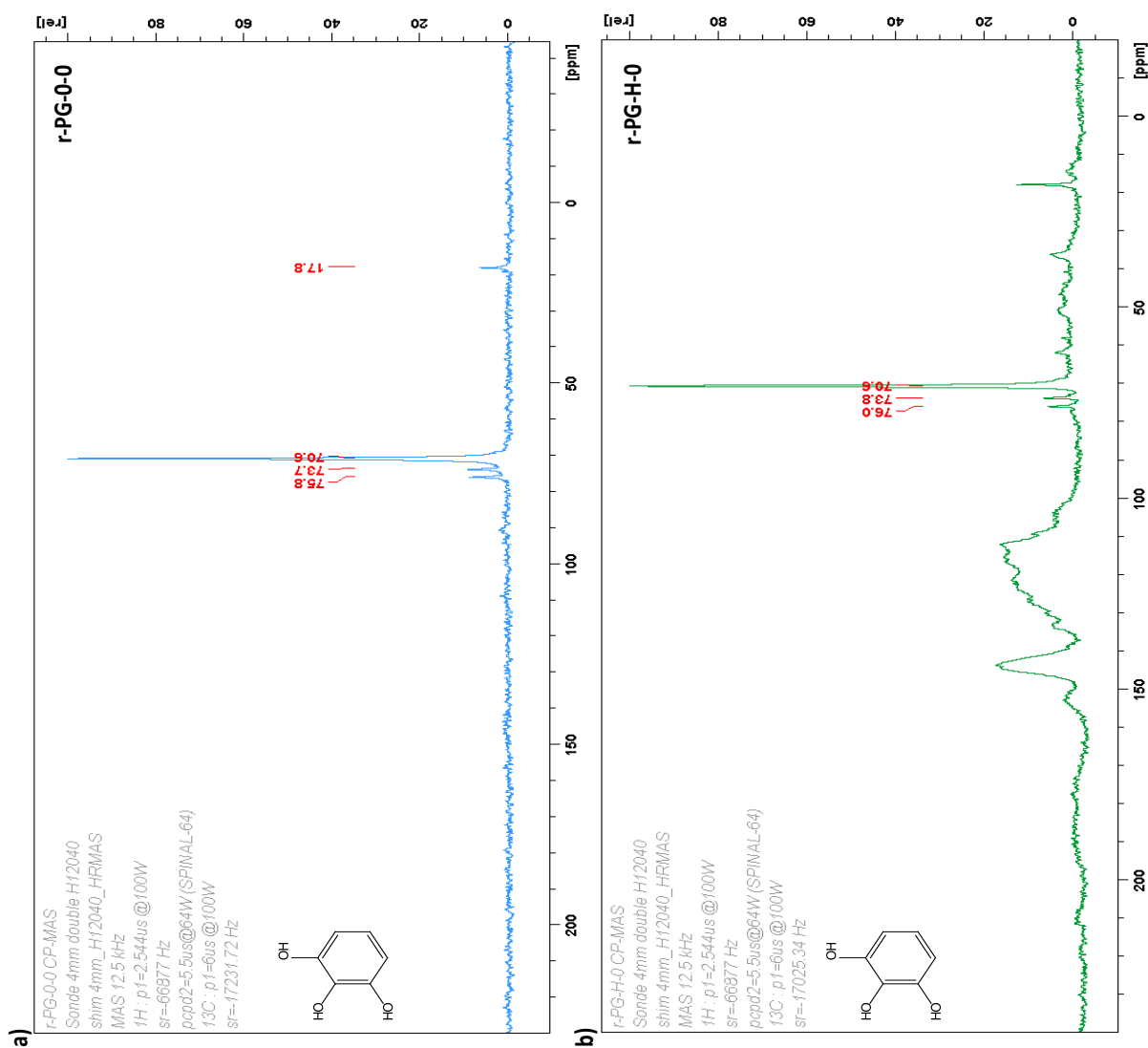
Figure 5.4.1. ¹³C CP-MAS NMR spectra of the phenolic resins prepared using PG as precursor: a) sample r-PG-0-0 and b) sample r-PG-H-0.
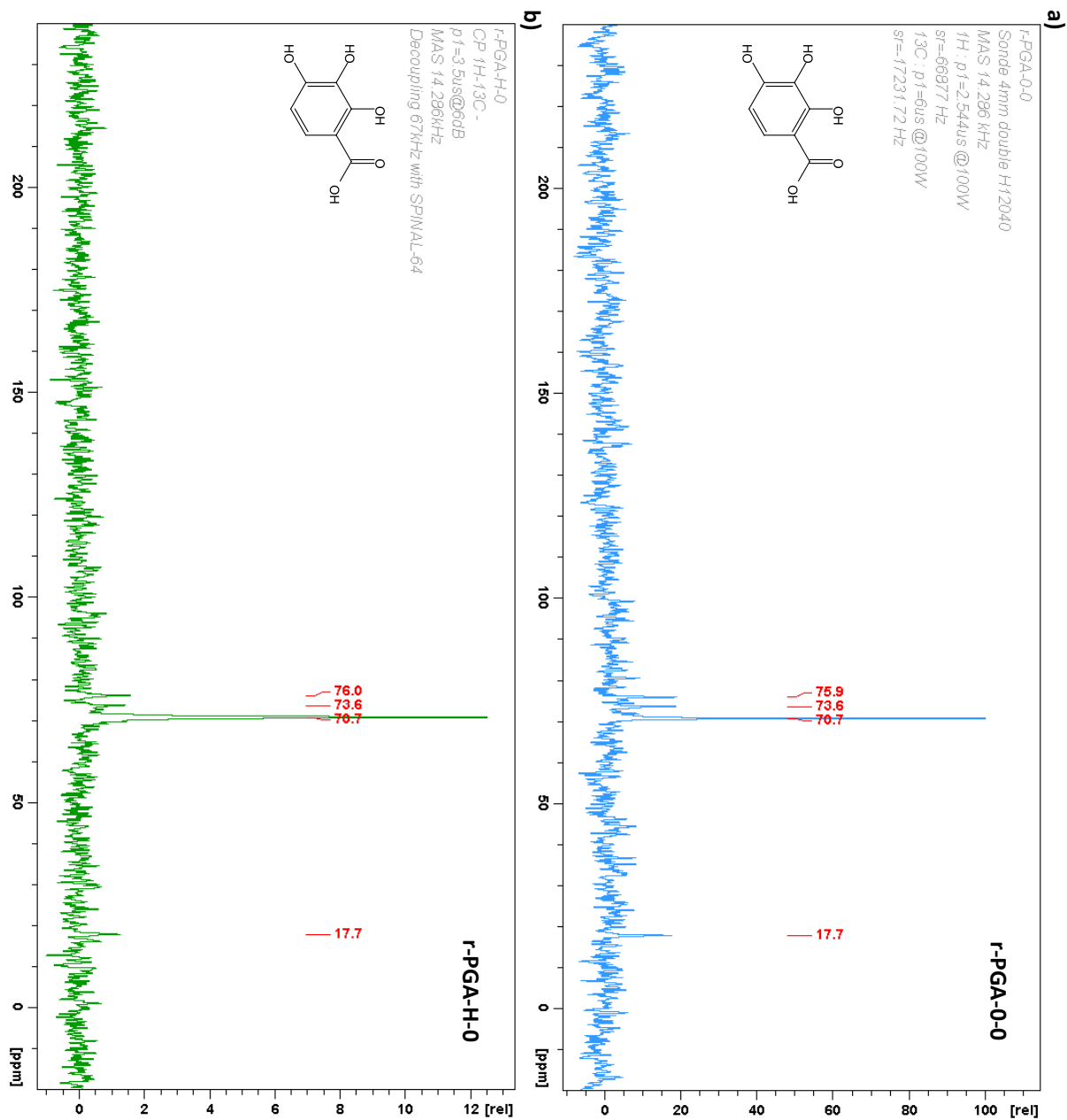
Figure 5.4.2. ^{13}C CP-MAS NMR spectra of the phenolic resins prepared using PGA as precursor: a) sample r-PGA-0-0 and b) sample r-PGA-H-0.
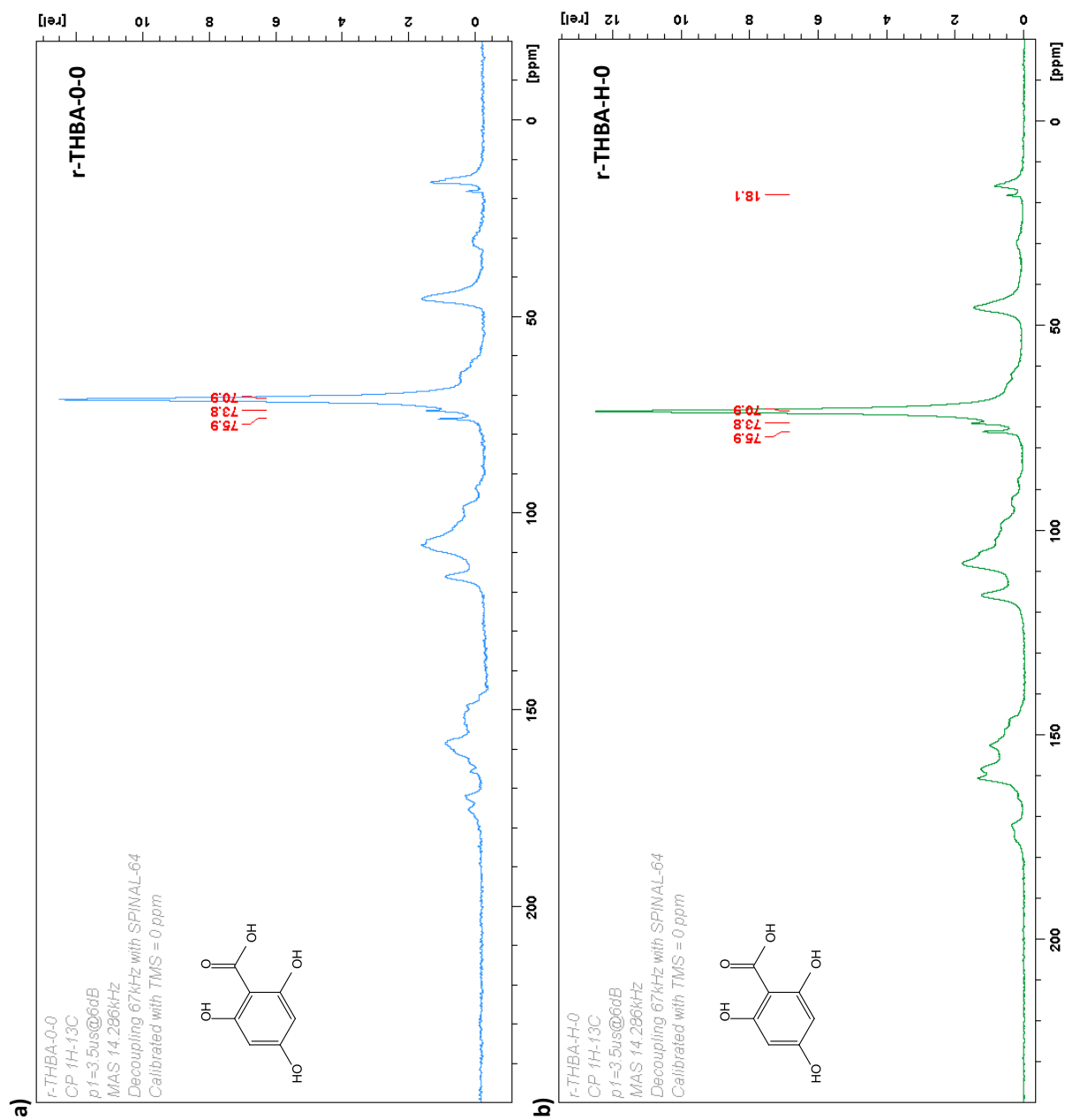
Figure 5.4.3. ^{13}C CP-MAS NMR spectra of the phenolic resins prepared using THBA as precursor: a) sample r- THBA -0-0 and b) sample r-THBA-H-0.

According to literature, the formation of a phenolic resin (resol or novolac type) through the electrophilic substitution of hydroxylated benzenes and an aldehyde proceeds through three different stages: i) addition of the aldehyde to the phenolic ring; ii) chain growth with successive condensation and addition reactions; iii) crosslinking (curing) of the resins [Zinke 1951; Maciel 1984; Ottenbourgs 1997]. Novolac type resins are obtained in acid medium and molar excess of

phenolic precursor, which disfavors the addition reaction and boosts the condensation step. However, the crosslinking (hardening) of novolac type resins cannot occur by heating and a hardening agent it is required. For resol resins, basic conditions and molar excess of the aldehyde are typically used [Maciel 1984; Pekala 1987], leading to a faster kinetics of the addition reaction, compared to the condensation reaction, and generating different types of linkage bridges [Zinke 1951]. In both cases, the curing (hardening) stage to take place if the aromatic rings in the polymer chain formed during the condensation reaction contains enough reactive positions on the aromatic ring (i.e. unsubstituted positions) to become cross-linked [Ottenbourgs 1997].

In our case, we work in excess of aldehyde (typical resol conditions) and in acid medium (typical novolac conditions) to favor the self-assembly of the reactants with the surfactant. Thus, we expect the addition reaction to proceed slower than the chain growth stage, which should allow us to observe differences in the overall polycondensation mechanism by the different NMR techniques.

In order to clarify the polymerization process, ^{13}C hpdec-MAS experiments were carried out (Figures 5.4.4 to 5.4.5). Data confirmed that the polymerization took place for all the studied samples; however, the lack of evidences by CP-MAS for certain samples indicated that the crosslinking (hardening) of the resin) did not take place for all of them within the illumination step.

For the samples of the PG series, hpdec spectra differences are observed in the samples depending on the pH of the reactants mixtures. The absence of peaks between 58-30 ppm for sample r-PG-0-0 indicates the lack of methylene bridges. In contrast, an incipient peak at 38 ppm was observed for sample r-PG-H-0. This confirms the polymerization of the reactants in both samples, but no signs of crosslinking (hardening) for sample r-PG-0-0 as observed by CP-MAS. This could be attributed to the unfavorable pH. Indeed, PG molecule has three reactive anchoring positions, but the lack of acidic pH would hinder the crosslinking of the polymer upon the 60 min irradiation. To further confirm this hypothesis, sample r-PG-0-0 was also recorded after thermal curing at 90 ºC overnight. As seen, new peaks around 30 and 90 ppm appeared, confirming the formation of glyoxal bridges (thus, the thermally induced cross-linking).

In the case of PGA series, hpdec spectra of both samples showed a similar trend, with no peaks in the area between 50-30ppm (as in the case of r-PG-0-0) despite both synthesis are in acidic medium (table 5.4.2). This could be attributed to the fact that PGA molecules has only one activated position in the aromatic ring; thus, the degree of polymerization to form the polymeric chains is expected to be low. This may also be related to the low pyrolysis values of these samples.
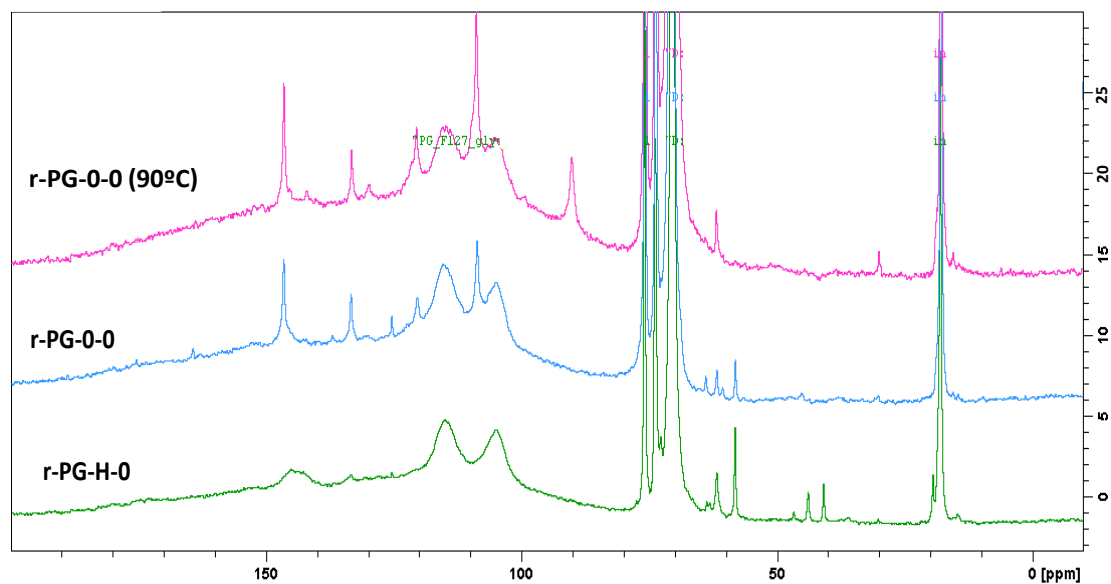
Figure 5.4.4. ^{13}C hpdec spectra of the phenolic resins prepared using PG as precursor: samples r-PG-0-0, r-PG-H-0 and r-PG-0-0 (90ºC) after a heating at 90ºC to verify reticulation.
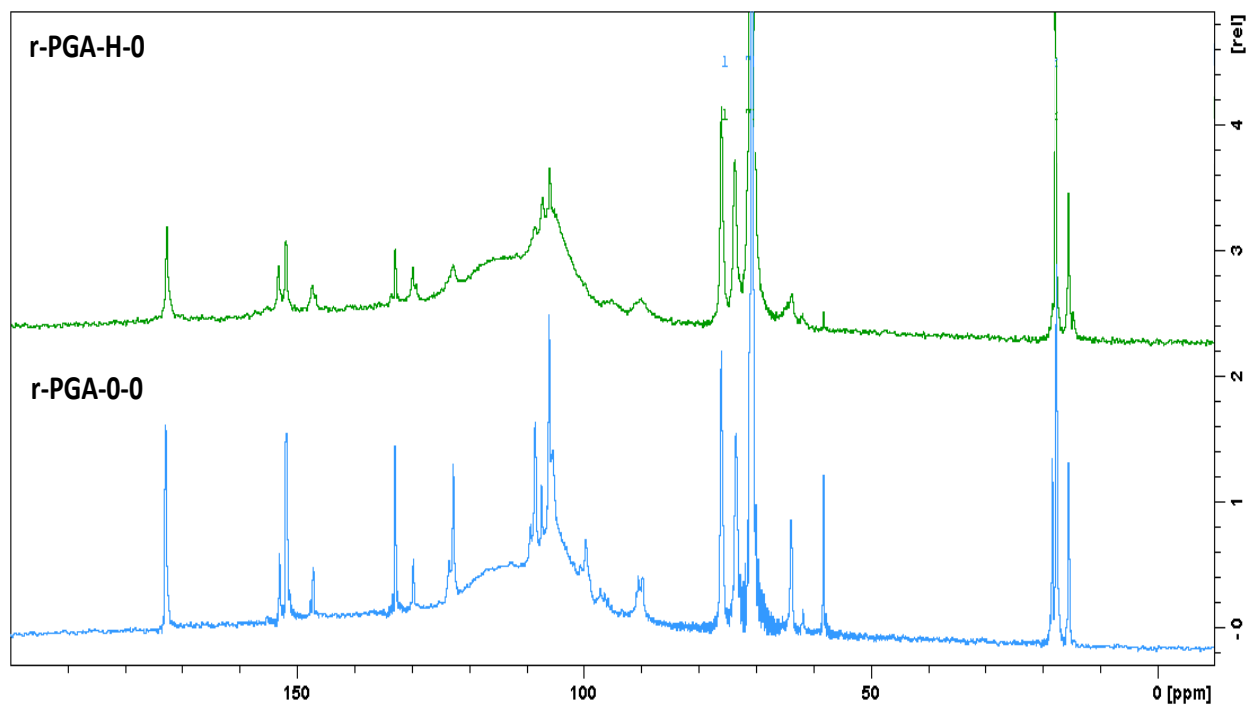
Figure 5.4.5. ^{13}C hpdec spectra of the phenolic resins prepared using PGA as precursor: a) sample r-PGA-0-0 and b) sample r-PGA-H-0.
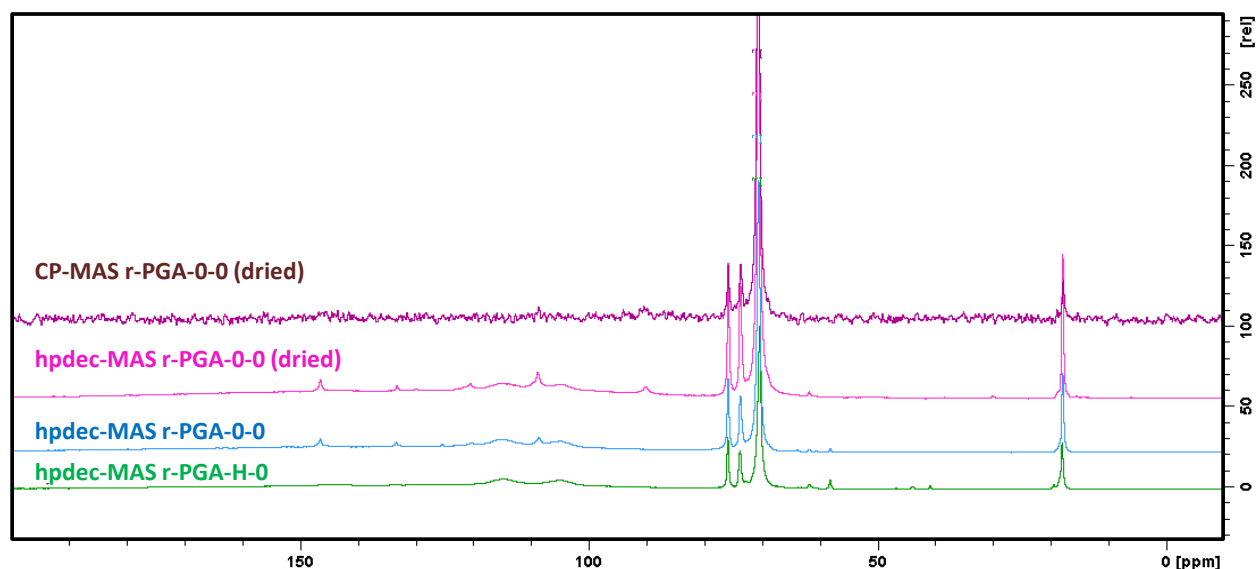
Figure 5.4.6. Comparison of the ^{13}C hpdec and CP-MAS spectra of the phenolic resins prepared using PGA as precursor.

Summarizing, data analysis of ^{13}C CP- MAS and ^{13}C hpdec- MAS spectra has shown the different reactivity of the precursor's mixtures upon illumination. The achievement of an ordered mesoporous structure would only be possible when the crosslinking of the polymeric resin takes place during the illumination period (ca. 60 min). Otherwise, when the resins present a low degree of reticulation, favoring the transition of the surfactant from an ordered (hexagonal) to an amorphous phase when the surfactant gets the cloud point upon carbonization of the resin [Holmqvist 1997; Long 2009; Kostko 2009], and/or a disordered arrangement of the final pore structure due to the stress of the backbone skeleton during the carbonization.

5.5. Conclusions

Mesoporous carbons of different pore sizes were obtained from PGA, TNA and THBA precursors through the UV assisted condensation with glyoxal in the presence of F127 and different synthetic parameters (i.e. by using HCl and/or a photoinitiator). PGA and TNA precursors rendered amorphous carbons, with slightly differences in terms of textural features. Indeed, larger mesopores were obtained for the carbons of the series PGA, as compared to those of the series TNA. Regarding the microporosity, all materials presented similar values. In general, low pH conditions favoured the formation of materials with more developed textural properties in mesopores range and higher total pore volume. The average pore size can be modified by changing the synthetic conditions, to obtain materials ranging from ca. 6-20 nm or even larger mesopores of ca. 38-40 nm.

Even with exactly the same functional groups the molecular structure which directs the polymerization path ways and could render completely different morphologies. This could be attributed to a stronger hydrogen bond interactions between TNA and Pluronic, compared to PGA, or to a slower reaction rate for the former (it has more reactive sites, but more steric hindrance), leading to longer assembling times between TNA and the PEO groups of Pluronic, while the polymer network is being formed. The action of the photoinitiator it is uncertain, but the self-assembly between the phenolic resin and the template determined the final mesopores structure of the carbons, and the self-assembly between the phenolic resin and the template is based on the interactions of the resin oligomers which are being formed, with the -PEO groups of the surfactant.

Considering these oligomers (disregarding hydrogen bonds interactions), the polymerization rate is expected to have an impact in the interactions between the resin and the template; TEM micrographs and the textural analysis indicated that the photoinitiator might increase the polymerization rate or favor the crosslinking, rendering denser oligomers and thus producing more compact fragments of phenolic resins around the surfactant. All this would provide thicker carbon walls around the mesopores after removing the template, which might bring about the decrease observed in the mesopore volume.

^{13}C CP- MAS and ^{13}C hpdec- MAS have allowed to explore the reactivity of the precursor's mixtures upon illumination. Data analysis revealed that the achievement of an ordered mesoporous structure is only possible when the curing of the resin takes place during the photoassisted reaction. Otherwise, when the resins present a low degree of reticulation the lack of ^{13}C CP- MAS signal confirmed that the resin was not able to stabilize upon the irradiation step. Such poor crosslinked resin would not be able to overcome the stress of the backbone skeleton during the carbonization, thus rendering materials with imperfect disordered arrangements.

CHAPTER 6
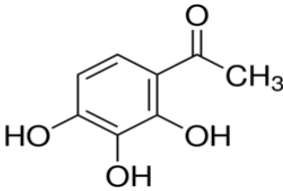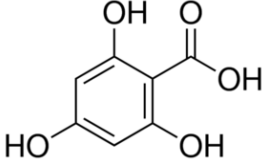
Synthesis of metal-nanoporous carbons *—one step incorporation of Ag and Au*

nanoparticles

6.1. Introduction

In the present chapter, we explore an in-situ light-assisted methodology for the preparation and **functionalization** of the phenolic resins with metallic salts (e.g., Ag or Au) to obtain metal-containing nanoporous carbons. It has been reported in the literature that metallic nanoparticles can be formed upon photo-reduction of a metal precursor [Roucoux 2002, Sakamoto 2009] in the presence of polymeric matrices, leading to the formation of NPs surrounded by a protective polymeric layer. Based on this, we have explored the photoreduction of the metallic precursors in the presence of the precursors' mixture for the formation a phenolic polymeric resin, aiming to obtain the simultaneous phot-assisted polycondensation of the resin and the photo-induced reduction of the metallic precursor to render nanoparticles and leading to a polymeric-metal NPs composite. The objective was to demonstrate the possibility of carrying out both photoinduced reactions, promoting the development of textural features in the resulting metal NPs-nanoporous carbons while optimizing the size and distribution of the metallic NPs.

For this purpose, we have selected gallacetophenone (GA) and 2', 4', 6'- trihydroxybenzoic acid (THBA) as precursors for the incorporation of the metallic nanoparticles (Table 6.1.1). Various experimental conditions were evaluated, modifying the concentration of the metallic precursors and the presence of photosensitizer.

Table 6.1.1. Nomenclature assigned to the organic precursors selected for the incorporation of the metallic nanoparticles, including molecular formula.

Organic Precursor (OP)	Nomenclature	Molecular Structure
Gallacetophenone IUPAC name: (2,3,4-trihydroxyphenyl)ethan-1-one $C_8H_8O_4$	GA	
Phloroglucinol carboxylic acid IUAC name: 2,4,6 Trihydroxybenzoic acid $C_7H_6O_5$	THBA	

6.2 GA-based composites containing Ag and Au nanoparticles

For the preparation of the metal- nanoporous carbon materials, the photopolymerization of phenolic resins was carried out in the presence of metal salts, (i.e. $AgNO_3$, $AuBr_3$). Details are indicated in the experimental section. Briefly, the preparation of the resins followed similar experimental conditions to those of the previously described for the GA series: glyoxal (40 wt.% aqueous solution) as linker, pluronic F127 as template and ethanol as solvent, with a glyoxal/EtOH molar ratio of 1:100 and a glyoxal: OP: Pluronic F127 molar ratio of 1.4: 1: 0.03. To avoid the precipitation of AgCl salt and the formation of Au (III) mixed chloride–bromide complexes during the photoinduced reaction, the synthesis was carried out in the absence of HCl [Usher 2009]. The nomenclature of the samples follows the same logic as before, indicating the type of metal (Ag or Au) and the concentration of the metallic salt (e.g., r-GA-0-0-Ag-0.25). For clarity, a summary of the experimental conditions and the nomenclature assigned for the samples is presented in Table 6.2.1.

Table 6.2.1. Summary of experimental conditions used in the synthesis of polymeric resins using GA as precursor in the presence of Ag and Au salts.

	HCl	*Photoinitiator*	*Metallic salt (wt.%)*	*pH of reactants' mixture*
r-GA-0-0-Ag-0.25	no	no	$AgNO_3$ (0.25 wt.%)	6.0
r-GA-0-Ch-Ag-0.25	no	yes	$AgNO_3$ (0.25 wt.%)	6.0
r-GA-0-Ch-Ag-0.12	no	yes	$AgNO_3$ (0.12 wt.%)	6.0
r-GA-0-0-Au-0.25	no	no	$AuBr_3$ (0.25 wt.%)	6.0
r-GA-0-Ch-Au-0.25	no	yes	$AuBr_3$ (0.25 wt.%)	6.0
r-GA-0-Ch-Au-0.12	no	yes	$AuBr_3$ (0.12 wt.%)	6.0

With the irradiation time, the crystalline solutions of the reactants' mixtures darkened, and a viscous solid was formed after 60 min of UV 365 nm irradiation (Figure 6.2.1). A similar behavior had already been observed in the case of the GA series in the absence of Ag (I) or Au (III) salts (see chapters 3 and 4). However, the color of the resins clearly showed a more dark brownish appearance than in the samples prepared in the absence of the metallic salts.

The progress of the photoassisted reaction was monitored via UV-visible absorption spectroscopy. In this case, the UV-vis spectra showed the typical absorption peaks of the plasmon for silver and gold (Figure 6.2.2), confirming formation of the Ag and Au NPs during the irradiation. Such surface plasmon appears at a wavelength range between 410-440 nm for Ag^0 [Balan 2008; Chibac 2012; Mustatea 2014] and between 500-600 nm for Au^0 (range of Au^0 nanoparticles size

from 5 nm to 100 nm)[Sakamoto 2009; Melinte 2015]. In the presence of the photoinitiator (i.e. GA-0-Ch-Au-0.25_rm and GA-0-Ch-Au-0.12_rm), all Au-containing reactant mixtures presented the typical yellow color of Au (III) (Figure 6.2.1). Further confirmation of the formation of Ag⁰ and Au⁰ nanoparticles was obtained by XPS (see annex I).
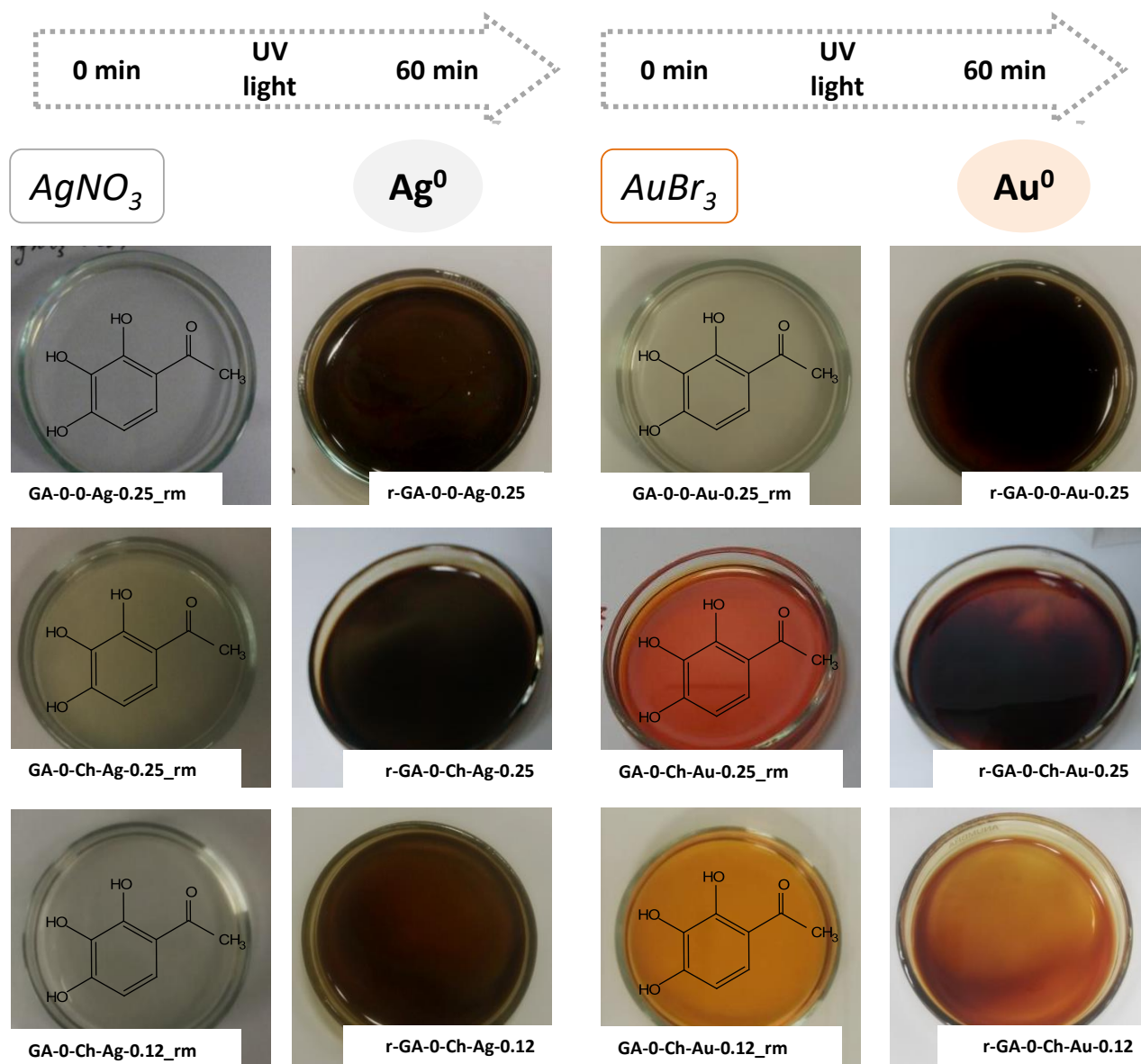
Figure 6.2.1 Visual changes between the GA metal-polymer reactant's mixtures before (series rm) and the resins after 60 minutes of UV irradiation.

The resins obtained after the irradiation were recovered and further pyrolysed at 600 °C under N_2 atmosphere (ca. 120 ml/min, heating rate 2 °C/min) during 2 hours to obtain the metal-hybrid

carbon materials. The pyrolysis yields of the photopolymerized resins after the carbonization at 600 °C, and the nomenclature of the materials are presented Table 6.2.2.
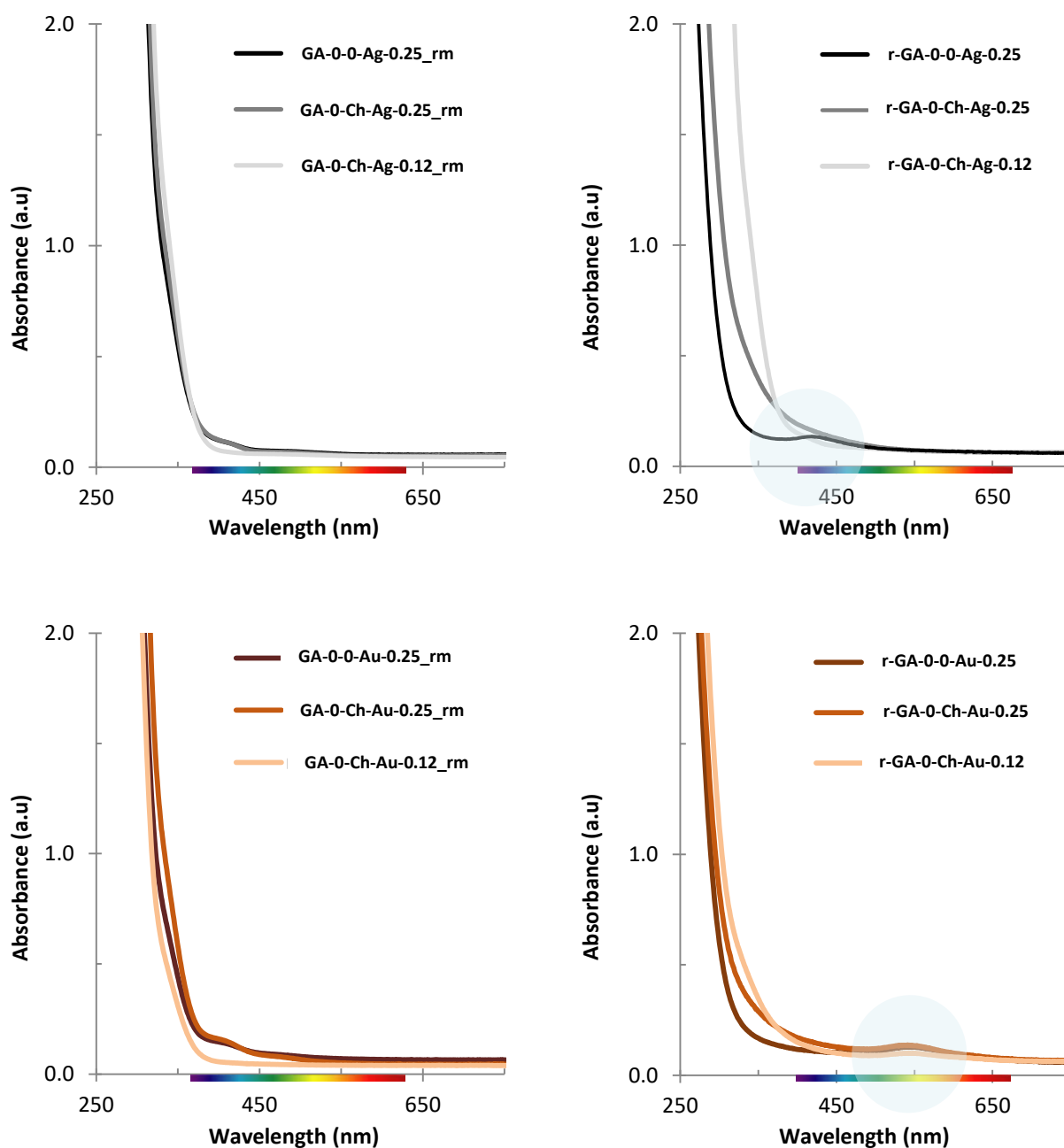
Figure 6.2.2 UV-VIS spectra of metal-containing GA reactant's mixtures before (series rm) and after 60 minutes of UV irradiation (series r).

The carbonization yields varied between ca. 11-14 wt. %; these values were slightly higher than those of the samples prepared in the absence of the metal salts (Table 6.2.2). This is reasonable, considering the molecular weight of the metals (even if they are in a low amount). The surface pH

was of a basic nature for all the materials, as in the case of the samples prepared in the absence of the metal salts. All this indicates that the incorporation of the metallic salts do not modify the characteristics of the resulting carbon materials.

Table 6.2.2. Carbonization yields (wt.%) and surface pH of the metal-containing materials prepared using GA as precursor.

	Carbonization Yield [a]	Carbonization Yield (resin basis)[b]	Surface pH
C-GA-0-0	8	18	9.2
C-GA-0-Ch	10	23	8.5
C-GA-0-0-Ag-0.25	14	33	8.7
C-GA-0-Ch-Ag-0.25	13	30	8.8
C-GA-0-Ch-Ag-0.12	13	30	8.6
C-GA-0-0-Au-0.25	12	28	8.2
C-GA-0-Ch-Au-0.25	12	28	8.7
C-GA-0-Ch-Au-0.12	11	26	8.7

[a] Experimental carbonization yield under N_2 atmosphere at 600°C yield
[b] Carbonization yield recalculated on the basis of the resin (i.e. without considering the mass of Pluronic F127)

6.2.1. Textural characterization

The porosity of the samples was characterized by adsorption-desorption isotherms of N_2 at -196 °C. The corresponding isotherms are shown in Figure 6.2.3 and 6.2.4 (compared to the samples prepared in the absence of metallic precursors). The main textural parameters are presented in Table 6.2.3. All the materials presented a high nitrogen uptake, indicating the presence of the metallic salt during the photopolymerization of the precursors did not hinder or blocked the cross-linking of the reactants, and allowed the formation of nanoporous materials, in both the micropore and mesopore range after pyrolysis at 600 °C.

All the materials them displayed type IV(a) nitrogen adsorption isotherms, with well-developed hysteresis loops of type H2 (b). It may be noted that the shape of the loop was similar in the samples containing metals. However, a significant decrease in the total pore volume was found for C-GA-0-0-Ag-0.25 and C-GA-0-0-Au-0.25 (ca. 0.48 and 0.58 cm³/g, respectively) in comparison with the sample without metals (ca. 0.70 cm³/g for C-GA-0-0). In the case of the samples containing Ag nanoparticles, the hysteresis loops shifted towards smaller values of relative pressure, indicating

narrower pore sizes. In addition, it is observed that the hysteresis loop (type H2) expands over a wider range of relative pressure (0.42-0.86) for sample C-GA-0-0-Au-0.25, compared to C-GA-0-0 (0.6-0.98).
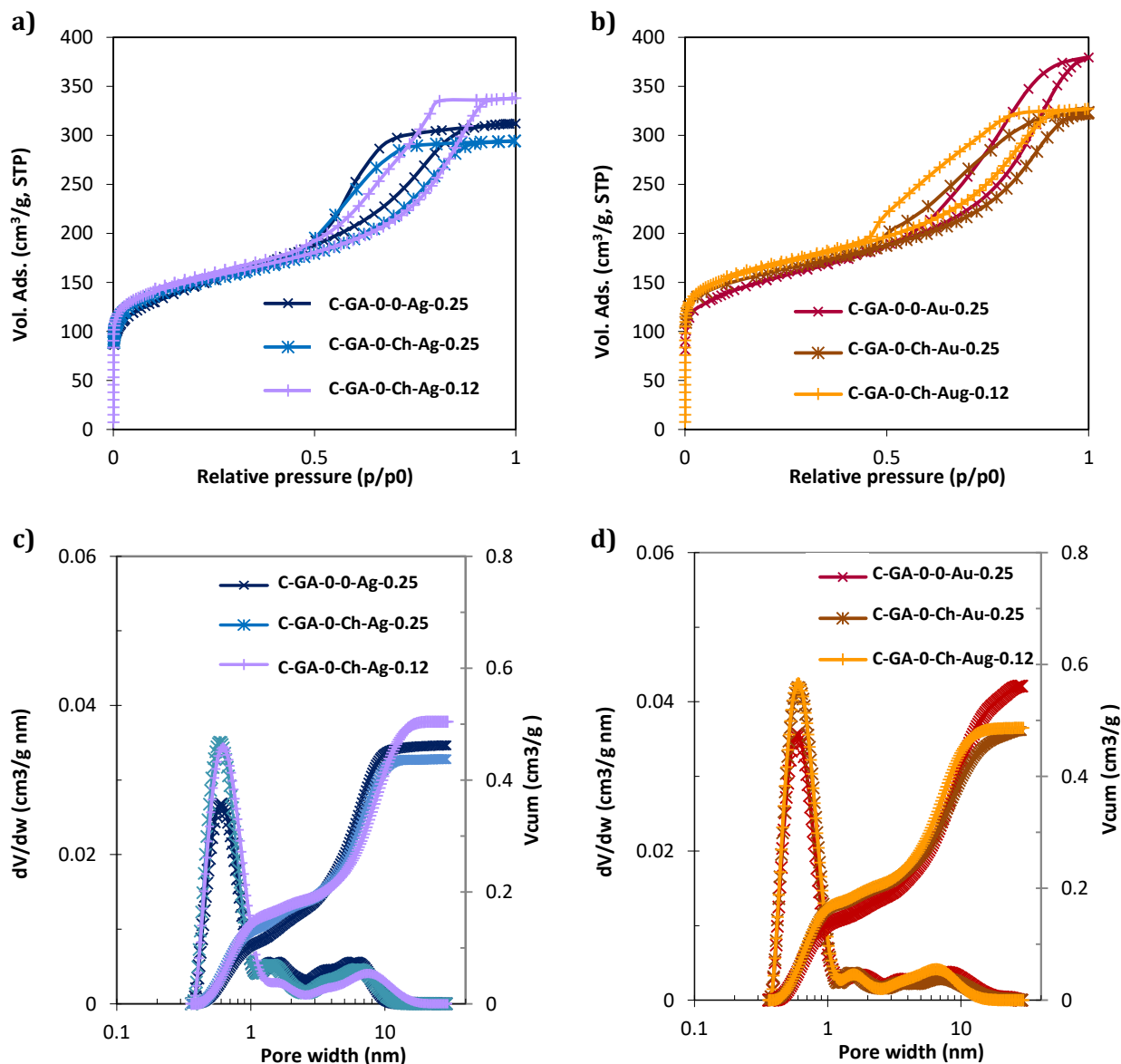
Figure 6.2.3. High resolution N_2 adsorption/desorption isotherms at -196 °C (a,b) and pore size distributions (c,d) evaluated using the 2D-NLDFT-HS method from the adsorption branch of the N_2 isotherms of the metal-containing GA series.
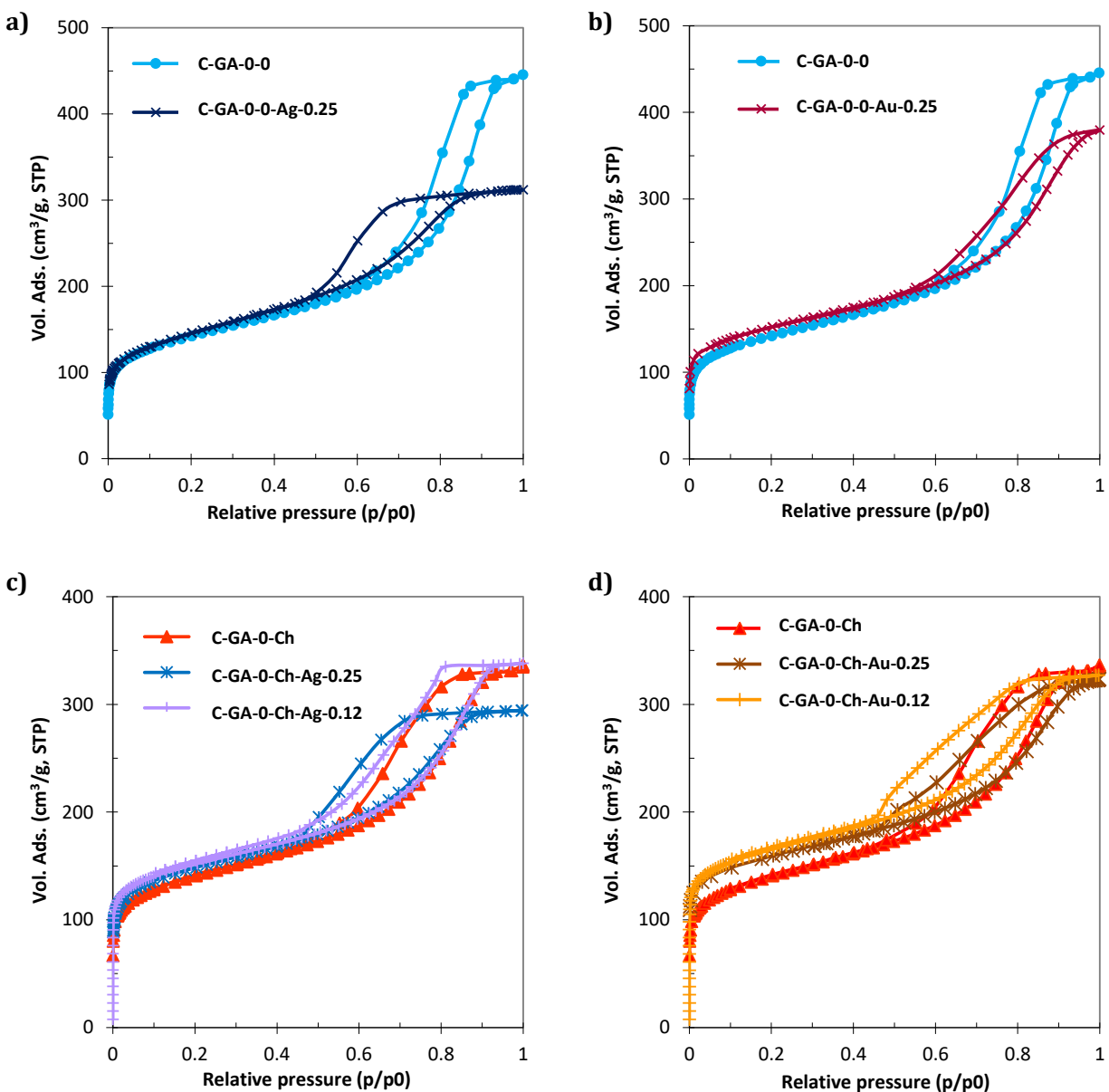
Figure 6.2.4. Comparison of the high resolution N_2 adsorption/desorption isotherms at -196 °C of the samples of the C-GA series obtained in the presence and absence of metallic salts.

When the synthesis is carried out in the presence of photoinitiator (series Ch), the variations in porosity are less marked. Again, lower total pore volumes were found for the samples prepared in the presence of the metal NPs, and the PSD also shifted slightly to smaller mesopore sizes. For the case of the samples prepared with a high Ag-loading (i.e. C-GA-0-Ch-Ag-0.25), such differences were more remarkable. However, the mesopore size distribution for sample C-GA-0-Ch-Au-0.12 with a low Au-loading, shifted towards smaller sizes. This fact may suggest that the gold NPs are located

inside the mesopores; this is consistent with the smaller size of the gold nanoparticles as observed by TEM (see morphological discussion below).

Table 6.2.3. Main textural parameters of the carbons of the metal-containing GA series obtained from gas adsorption analysis. Data corresponding to samples C-GA-0-0 are included for comparative purposes.

	S_{BET} (m²/g)	V_{PORES}[a] (cm³/g)	$V_{MICRO\,N2}$[b] (cm³/g)	V_{MICRO}[c] (cm³/g)	V_{MESO}[c] (cm³/g)	$W_{0\,CO2}$[d] (cm³/g)	L[e] (nm)
C-GA-0-0	513	0.70	0.19	0.15	0.52	0.62	0.14
C-GA-0-Ch	518	0.52	0.20	0.16	0.35	0.60	0.15
C-GA-0-0-Ag-0.25	527	0.48	0.15	0.15	0.310	0.57	0.19
C-GA-0-Ch-Ag-0.25	548	0.45	0.17	0.17	0.264	0.56	0.20
C-GA-0-Ch-Ag-0.12	565	0.52	0.18	0.19	0.326	0.56	--
C-GA-0-0-Au-0.25	557	0.58	0.17	0.17	0.39	0.57	0.21
C-GA-0-Ch-Au-0.25	589	0.49	0.19	0.20	0.29	0.59	0.22
C-GA-0-Ch-Au-0.12	616	0.51	0.17	0.17	0.33	0.56	--

[a] Evaluated at $p/p_0 \sim 0.99$ in the N_2 adsorption isotherms at -196 °C.
[b] Micropores volume, evaluated from DR equation applied to N_2 adsorption data at -196 °C.
[c] Evaluated from the 2D-NLDFT-HS method applied to N_2 adsorption data at -196 °C.
[d] Narrow micropores volume, from DR equation applied to CO_2 adsorption data at 0 °C.
[e] Evaluated using the Stoeckli-Ballerini equation applied to CO_2 adsorption data at 0 °C

Summarizing, the use photoinitiator and the silver salt produced the most significant changes in the porosity of the samples, favoring a decrease in the average mesopore size and a decrease in the total pore volume. Regarding the surface areas, the values remained rather unchanged, with the exception of the samples decorated with Au nanoparticles, although the changes are subtle. The volume of narrow micropores determined by CO_2 adsorption data followed a similar trend. When the metal loading was reduced to 0.12 wt.%, the effect on the decreased total pore volume become negligible.

6.2.2. Morphological characterization

TEM images of the samples are shown in Figure 6.2.5, showing the formation of metal nanoparticles of varied sizes dispersed within the carbon matrix.

Figure 6.2.5. TEM images of the metal-containing carbons obtained by using GA as organic precursor.

The samples C-GA-0-0-Ag-25 and C-GA-0-Ch-Ag-25 presented the formation of polydispersed spherical nanoparticles, with a bimodal size distribution with diameters in the 5-10 nm and the 25-30 nm range, being the former the dominant one. The dispersion of the NPs is more homogeneous for the sample prepared in the presence of the photoinitiator. When the metal loading of $AgNO_3$ was reduced to 0.12 wt.% in the presence of the photoinitiator (sample C-GA-0-Ch-Ag-12), an almost uniform and well-dispersed distribution of Ag nanoparticles of ca. 4-8 nm size was achieved, with a small contribution of nanoparticles with diameter between 15-20 nm (see example in Figure 6.25 of a 16 nm size nanoparticle).

At converse, in the case of the gold-loaded materials, at high metal-salt loadings (i.e. 0.25 wt.%), quite larger and more agglomerated metallic nanoparticles were obtained; as an example, for sample C-GA-0-0-Au-25 the images revealed highly agglomerated nanoparticles of around 25-100 nm size. This is attributed to the use of $AuBr_3$ as precursor and the bulk size of bromide ions that would contributes to a slow growth nanoparticles after the nucleation [Eustis 2006; Blosi 2011], and/or to the thermal treatment of the resins.

On the other hand, micrographs of sample C-GA-0-Ch-Ag-25 a better dispersion and a significant reduction of the nanoparticles size, compared to C-GA-0-0-Au-25 prepared in the absence of the photoinitiator, indicating the outstanding role of the photoinitiator. More in detail, sample C-GA-0-Ch-Ag-25 presented smaller nanoparticles, in a bimodal distribution of NPs of around 15-30 nm (agglomerated) and in the 6-12 nm range (well-dispersed). Such bimodal distribution is associated to processes were the photoreduction is fast, thus leading to the formation, nucleation and growth of numerous nuclei in a multiple-step stages (i.e. more than one nucleation/growth cycles) [Blosi 2011; LaMer 1950]. The material C-GA-0-Ch-Au-12 prepared with a gold loading of 0.12 wt.% and the photoinitiator to favor a good equilibrium between nucleation and growth of the NPs presented an uniform and well-dispersed distribution of Au nanoparticles of ca. 4-13 nm. The materials C-GA-0-Ch-Au-12 and C-GA-0-Ch-Ag-12 presented a well-dispersed distribution of small NPs.

On the other hand, the NPs appear to be randomly distributed within the carbon matrix, which showed the typical amorphous morphology of carbon materials (as in the case of the sample of the GA series prepared in the absence of metallic precursors).

6.3. THBA-based carbons containing Ag and Au nanoparticles

A summary of the experimental conditions and the nomenclature assigned for the metal-containing samples prepared using THBA precursor and is presented in Table 6.3.1. The color changes in the precurors' solutions upon illumination are shown in Figure 6.3.1.

Table 6.3.1. Summary of experimental conditions used in the synthesis of polymeric resins using THBA as precursor in the presence of Ag and Au salts.

	HCl	Photoinitiator	Metallic salt (wt.%)	pH of reactants' mixture
r-THBA-0-Ch-Ag-0.25	no	yes	$AgNO_3$ (0.25 wt.%)	2.0
r-THBA-0-Ch-Au-0.25	no	yes	$AuBr_3$ (0.25 wt.%)	2.0
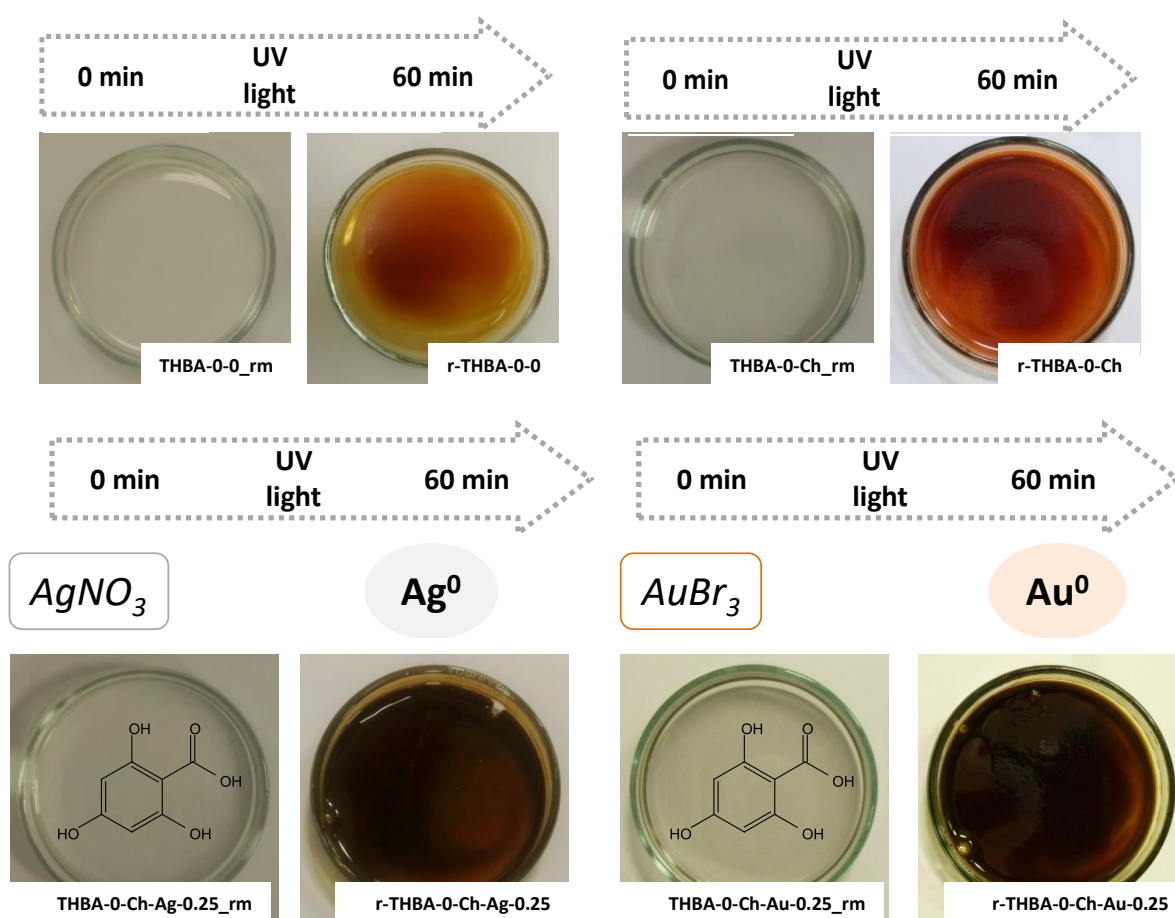
Figure 6.3.1 Visual changes between the THBA metal-polymer reactant's mixtures before (series rm) and the resins after 60 minutes of UV irradiation.

The progress of the photoassisted reaction was monitored via UV-visible absorption spectroscopy (Figure 6.3.2). The UV-vis spectra showed the typical absorption peaks of the plasmon for silver (410-440 nm) and gold (500-600 nm), confirming formation of the Ag and Au NPs during the irradiation. Further confirmation of the formation of Ag^0 and Au^0 nanoparticles was obtained by XPS (see annex I). The plasmon is more visible that in the samples of the series GA (Figure 6.2.2) Interestingly, the typical yellow color of Au (III) ions was not observed for the reactant mixtures of the series of THBA, as in the case of the GA series (Figure 6.2.1). This is attributed to the differences in the pH of the synthesis; giving the acidic nature of THBA precursor, the reactants mixture has a marked acidic character (pH~ 2) as opposed to the GA series (Table 6.2.1) with rather neutral pH.
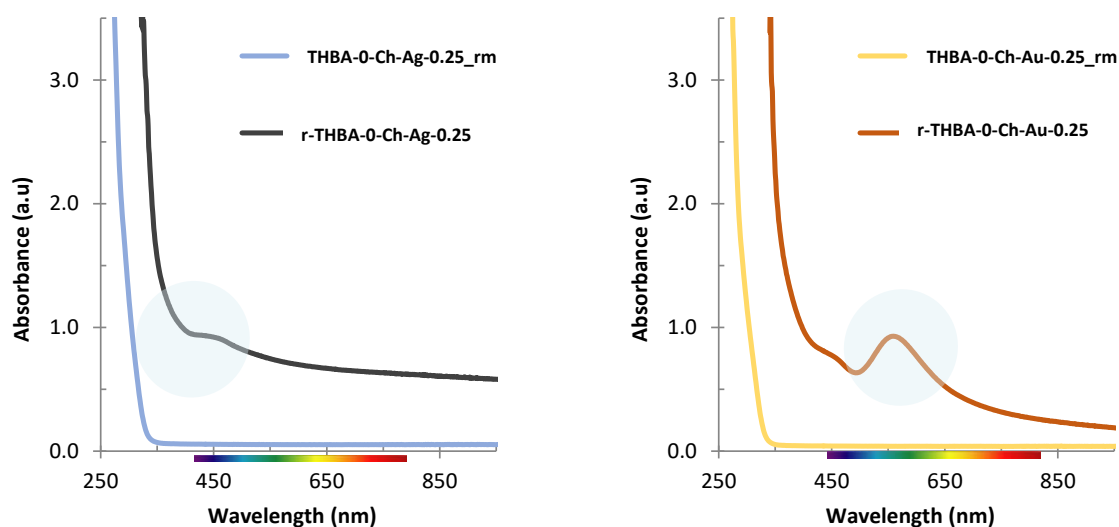
Figure 6.3.2 UV-VIS spectra of metal-containing GA reactant's mixtures before (series rm) and after 60 minutes of UV irradiation (series r).

The carbonization yields of the metal-loaded samples were similar to those in the absence of the metal salts (Table 6.3.2). The surface pH was neutral, as in sample C-THBA-0-Ch.

Table 6.3.2. Carbonization yields (wt.%) and surface pH of the THBA metal-containing materials.

	Carbonization Yield [a]	Carbonization Yield (resin basis) [b]	Surface pH
C-THBA-0-Ch	18	43	6.9
C-THBA-0-Ch-Ag-0.25	20	47	7.2
C-THBA-0-Ch-Au-0.25	19	45	7.4

[a] Experimental carbonization yield under N_2 atmosphere at 600°C yield
[b] Carbonization yield recalculated on the basis of the resin (i.e. without considering the mass of Pluronic F127)

6.3.1. Textural characterization

The nitrogen adsorption-desorption isotherms at -196 °C of the THBA-metal containing carbon materials are shown in Figure 6.3.3, and the main textural parameters are presented in Table 6.3.3. As in the case of the GA series, all the materials presented a high nitrogen uptake, indicating the presence of the metallic salt during the photopolymerization of the precursors did not inhibit the cross-linking of the reactants.
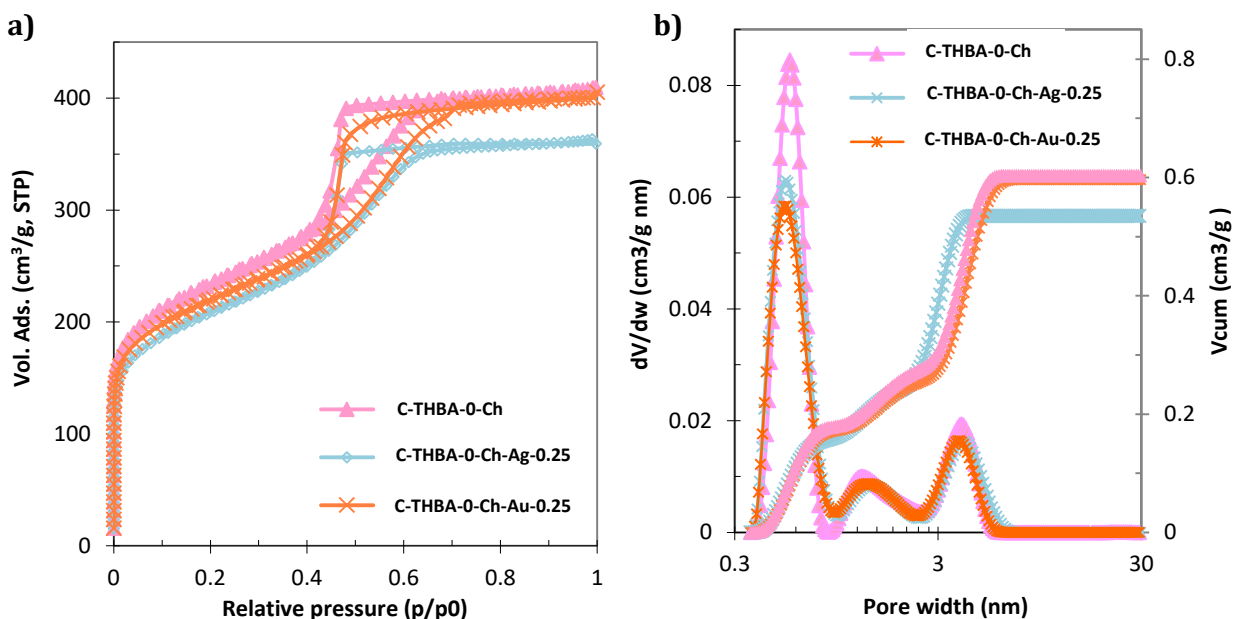
Figure 6.3.3. a) N_2 adsorption/desorption isotherms at -196 °C of the metal-containing carbons prepared using THBA as precursor; b) pore size distributions evaluated using the 2D-NLDFT-HS method from the adsorption branch of the N_2 isotherms.

All materials displayed type IV(a) nitrogen adsorption isotherms in the IUPAC classification, with H2(b) hysteresis loops. The incorporation of the metallic precursor did not modify the final porosity of the carbon, regardless the type of salt.

Only a slightly impact in the total pore volume was observed, with sample C-THBA-0-Ch-Ag-0.25 showing a slightly lower value (Table 6.3.2). The PSD showed an average mesopores size around 4-5 nm for all the samples.

Table 6.3.3. Main textural parameters of the carbons of the metal-containing THBA series obtained from gas adsorption analysis. Data corresponding to sample C-THBA-0-0 are included for comparative purposes.

	S_{BET} (m^2/g)	V_{PORES}[a] (cm^3/g)	$V_{MICRO\ N2}$[b] (cm^3/g)	V_{MICRO}[c] (cm^3/g)	V_{MESO}[c] (cm^3/g)
C- THBA -0-Ch	850	0.63	0.28	0.24	0.44
C- THBA -0-Ch-Ag-0.25	756	0.56	0.26	0.23	0.31
C- THBA -0-Ch-Au-0.25	798	0.62	0.27	0.24	0.36

[a] Evaluated at $p/p_0 \sim 0.99$ in the N_2 adsorption isotherms at -196 °C.
[b] Micropores volume, evaluated from DR equation applied to N_2 adsorption data at -196 °C.
[c] Evaluated from the 2D-NLDFT-HS method applied to N_2 adsorption data at -196 °C.

6.3.2. Morphological characterization

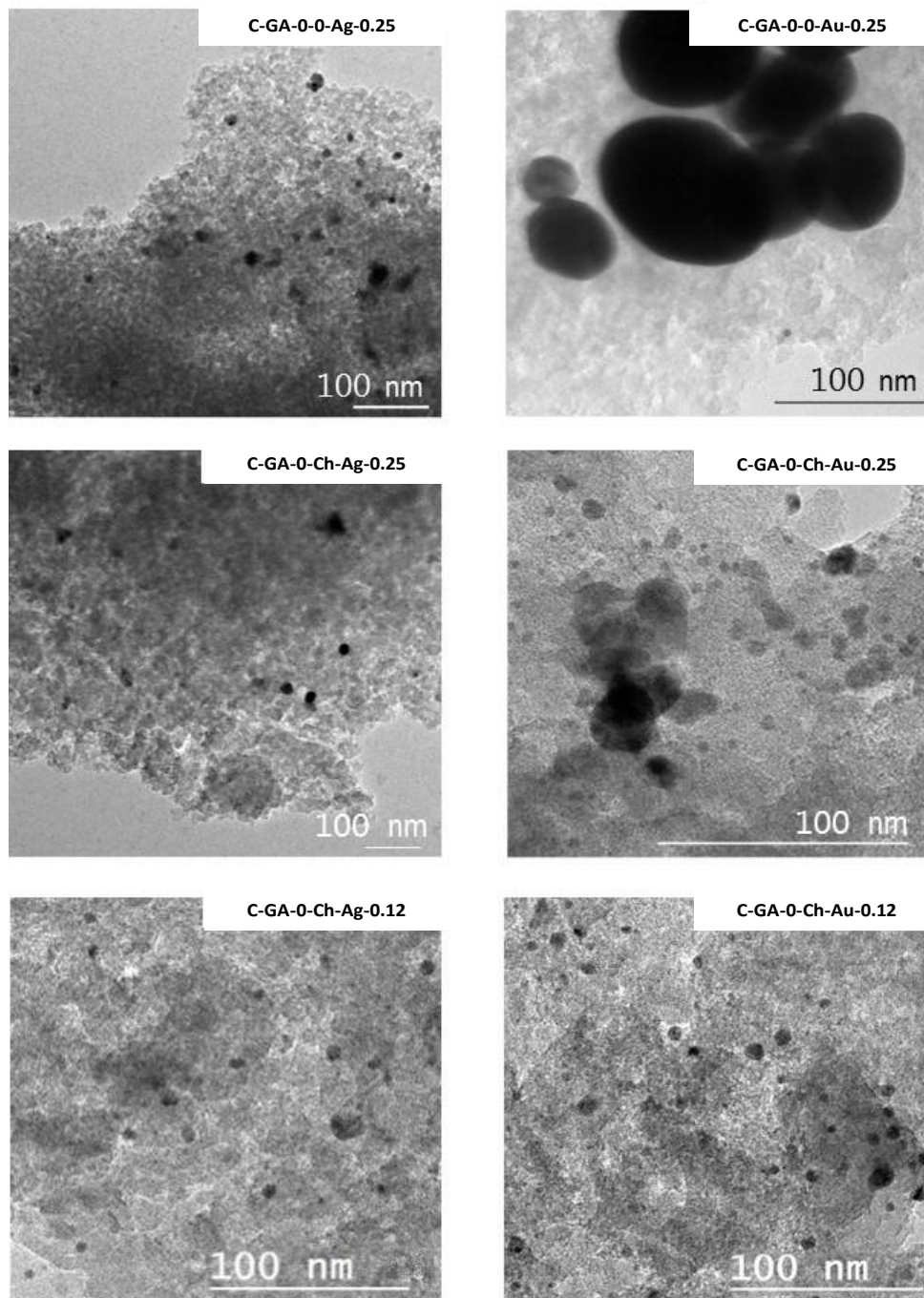TEM images of the samples confirming the formation of metal nanoparticles of varied sizes dispersed within the carbon matrix after the thermal treatment are shown in Figure 6.3.4.
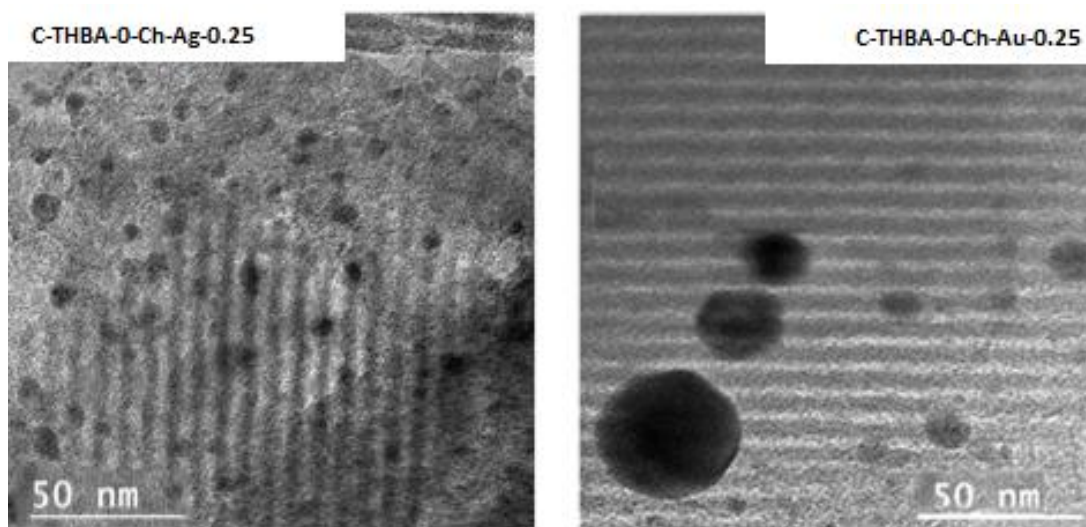
Figure 6.3.4. TEM images of the metal-loaded carbon materials prepared using THBA as precursor.

As seen, silver nanoparticles between 2-8 nm size and gold nanoparticles of 3-40 nm size were obtained. Comparatively, sample C-THBA-0-Ch-Ag-0.25 presented a more uniform and well-dispersed distribution of Ag NPs than sample C-THBA-0-Ch-Au-0.25, that presented polydispersed spherical nanoparticles of larger sizes. Despite the high metal loading, quite good results were achieved both in terms of dispersion and size of the nanoparticles. As for the carbon matrix, the regular parallel channels of around 4-5 nm characteristic of an ordered porous structure were observed, as in the case of the sample prepared in the absence of metals (Figure 5.3.7).

6.4 Conclusions

The incorporation of Au (III) and Ag (I) ions in the precursors' solutions allowed a simultaneous photoassisted polycondensation of the monomers and the photoreduction of the metallic ions rendering metal nanoparticles. The resulting carbon-metal composites displayed well-dispersed metal nanoparticles within the carbon matrix, of varying sizes depending on the synthetic parameters of the carbon materials. In addition, the incorporation of the metal nanoparticles induced slight modifications in the porosity of the carbon materials, mainly in the total pore volume and the average mesopore size.

CHAPTER 7

Conclusions and Perspectives

7.1. Conclusions

The most significant conclusions that can be inferred from this PhD thesis are summarized below:

- We have developed a simple and cost effective method for the synthesis of nanoporous carbons with varied textural and structural features based on the UV-assisted condensation of glyoxal and hydroxylated aromatic molecules (e.g., phenol, resorcinol, catechol, bisphenol A, dihydroxynaphthalene, pyrogallol, phloroglucinol, tannic acid...) at room temperature for 60 min and subsqeunet carbonization. Owing to the different reactivity of the precursors, their UV exposure give rise to polymeric resins and carbons of hydrophobic nature and varied porosity and morphology. By an adequate choice of the organic precursor, and synthetic parameters, it is possible to control the morphology and porosity of the final carbon materials within the full micro/mesoporous range.

- The degree of cross-linking of the reactants is determined by the composition and the reactive positions of the hydroxylated aromatic precursor and the pH, controlling the final physicochemical properties of the carbons. For example, the linear structure of bisphenol A gave rise to highly branched clusters that harden to form the phenol-like resin in a dense structure with close porosity mainly composed of narrow micropores. In contrast, other aromatic precursors assembled in large cross-linked clusters, rendering large pores.

- We have investigated the effect of the solution pH and a photoinitiator in the physicochemical characteristics of the nanoporous carbons obtained upon the photoinduced polycondensation of gallacetophone and pyrogallol with glyoxal. In both cases, a well-developed mesoporosity can be successfully obtained without the need of using acidic conditions or a photoinitiator. This constitutes an advantage towards the preparation of materials through green synthetic routes and using less chemical reagents.

- Strong acidic conditions have demonstrated the feasibility to produce carbon materials with high specific surface areas and total pore volumes, characterized by large mesopores, while the photoinitiator has little impact on the properties of the resulting carbons.

- In the case of gallacetophenone, the synthesis can be carried out at high glyoxal/ EtOH ratio (i.e., concentrated conditions), which allows to reduce the solvent consumption of solvent without sacrificing the mesoporosity of the carbons -despite there is a slight influence of the glyoxal/ EtOH ratio on the average mesopore size and total pore volume-.

- In the case of pyrogallol and THBA, the acidic conditions enabled the formation of an ordered arrangement of the mesoporosity. This is attributed to modifications in the polucondensation mechanism upon the pH: acidic conditions favor the crosslinking of the polymeric resin before the spinodal decomposition occurs, avoiding the transition from the wormlike packing micelles of the surfactant to a hexagonal crystalline arrangement. Too long or too fast polymerization rates will be unable to provide ordered mesostructures, rendering amorphous materials.

- Mesoporous carbons of different pore sizes were obtained from PGA, TNA and THBA precursors: PGA and TNA rendered amorphous carbons, with larger mesopores for the carbons of the series PGA (similar values of microporosity). In general, low pH conditions favoured the formation of materials with more developed textural properties in mesopores range and higher total pore volume.

- 13C CP- MAS and 13C hpdec- MAS allowed to explore the reactivity of the precursor's mixtures upon illumination. Data analysis revealed that the achievement of an ordered mesoporous structure is only possible when the curing of the resin takes place during the photoassisted reaction. Otherwise, when the resins present a low degree of reticulation, the lack of 13C CP- MAS signal confirmed that the resin was not able to stabilize upon the irradiation step. Such poorly crosslinked resin would not be able to overcome the stress of the backbone skeleton during the carbonization, thus rendering materials with imperfect disordered arrangements.

- Nanoporous carbon-metal composites were obtained through a one pot one step photoassisted methodology. The photo-reduction of Ag (I) and Au (III) ions simultaneously during the photoassisted condensation of the polymeric resins rendered the formation of metal nanoparticles on the polymeric matrix. The carbonization of those hybrid metal-polymer composites resulted in obtaining the nanoporous metal-carbons which displayed well-dispersed metal nanoparticles within the carbon matrix.

- The incorporation of the metal salts during the synthesis induced slight modifications in the porosity of the carbon materials, mainly in the total pore volume and the average mesopore size, but in any case, it does not prevent the mesoporosity development. Indeed it was even possible to obtain OMC-metal composites.

7.2 Perspectives

In this PhD thesis photoassisted approaches have been explored to obtain materials with high porosity using different organic molecules as precursors. In this regard, some research activities have been initiated in the framework of this PhD thesis that would need to be further completed and would constitute the activities of the future work that will be worth continuing. A summary can be found below:

• *Utilization of solar light*

Light is without a doubt a reagent to consider: photons are near-ideal reagents and photochemistry can contribute efficiently to the growing field of Green Chemistry. Thus, after having demonstrated the usefulness of UV light in the synthesis of carbon materials upon the photoassisted polycondensation of aldehydes and hydroxylated precursors, it seems reasonable to explore the extent of the reactions using solar light. The preliminary tests have shown successful results.

To this aim, similar experimental procedures were applied, selecting GA, PG and THBA as precursors (ca. 1.6 g of the precursor dissolved in 40 mL of ethanol; 3.2 g of surfactant; 1.6 mL glyoxal 40 wt.% aqueous solution). The reactants mixtures were irradiated using simulated solar light (300 W Xe lamp) for 60 minutes and pyrolysed at 600 °C. The nomenclature of the samples is similar to the one following in the thesis, incorporating S for referring to the solar light. For instance, sample C-GA-0-0-S refers to gallacetophenone in the absence of acid and photoinitiator, and using simulated solar light. The yields of pyrolysis were ca. 9.7 wt.% , 19.5 wt.% 10.2 wt.% and 23.4 wt.%, for GA, PG, PGA and THBA, respectively; the values were very similar to those ones obtained through UV polycondensation. Most importantly, the characterization of the porosity revealed that the carbon materials displayed a well-developed porous structure (Table 7.2.1).

Table 7.2.1. Summary of the textural parameters of selected samples prepared upon irradiation under simulated solar light.

Material	S_{BET} (m^2/g)	V_{PORES}[a] (cm^3/g)	$V_{MICRO\ N2}$[b] (cm^3/g)
C-GA-H-0-S	514	1.0	0.16
C-PG-H-0-S	595	0.52	0.23
C-THBA-0-0-S	872	0.78	0.30

[a] Evaluated at p/p0 ~ 0.99.
[b] Micropores volume, evaluated from Dubinin Radushkevich (DR) equation applied to N_2 adsorption data.

Further characterization studies are ongoing to compare the characteristics of the obtained materials with those prepared under UV light.

• *Utilization of N-doped precursors*

Besides the control of porosity, an important challenge in material's design is the preparation of materials with specific surface groups. Thus, the next step is to extend this fast photochemical approach to control the effect of different functionalization, as incorporating N-, O- or S-functional groups on the carbon surface. Based on the preliminary studies of the group on the synthesis of carbon gels using melamine [Rasines 2015b], we have selected this molecule as N-doping agent.

Several protocols are being employed to optimize the synthetic parameters, as different solvent conditions, from ethanol to ethanol: water mixtures at different molar ratios, adding the melamine previously solved in water to the reactants mixtures at different times (e.g., before pluronic, after pluronic and before glyoxal, after the addition of all other reagents), or employing various temperatures to dissolve the melamine in water (e.g., 25, 30, 35 and 40 ° C). We have worked in the presence and absence of 1 %wt. HCl, and also the incorporation of metal salts was carried out to evaluate the impact on the stabilization of the metal NPs by the possible nitrogen groups formed after the thermal treatment. The characterization of the samples needs to be finalized (e.g., TEM, XPS, elemental analysis), although we can confirm that nanoporous carbons are formed as evidenced by gas adsorption data.

• *Incorporation of conductive additives*

Nanoporous carbons with high porosity and improved conductivity are interesting candidates for a variety of electrochemical applications, as they show better performance over many competitors (e.g., metals, metal oxides). However, the synthesis of nanoporous carbons with high electrical conductivity is still a challenge. Based on the experience of the group, the incorporation of conductive additives during the synthesis of carbon materials is a good approach to attain this goal [Macias 2013; Rasines 2015a].

For this purpose, we have investigated the incorporation of carbon black as conductive additive incorporated to the reactants' mixture and exposed to solar light illumination during 60 min; THJBA was selected for this proof of concept. Briefly, about 0.83 g of THBA were dissolved in 40 mL of ethanol, and then a carbon black (Super P, TIMCAL, ca. 0.18 and 1.8 g corresponding to 1 and 10 wt.%) was dispersed in the solution by stirring for 10 min. Subsequently ca. 1.64 g of surfactant are added to the dispersion and stirred for 30 min. Finally, 0.83 mL of glyoxal (40 wt.% in aqueous

solution) is incorporated to the mixture and allowed to stir for 60 min under dark conditions. The reactants mixture is transferred to glass disses and irradiated under simulated solar light (300 W Xe lamp; aliquots of 8.8 g) for 60 minutes. The agitation was maintained during the illumination, although after 10 min of light exposure the viscosity of mixture increased significantly and the agitation stopped. The black solid recovered after 60 min irradiation was pyrolysed at 600 °C.

The yield of pyrolysis was ca. 27 and 51 % for the samples prepared with 1 and 10 wt.% of additive, respectively; the values are much higher than that obtained for the control carbon material prepared in the absence of carbon black (ca. 19 wt.%). Most importantly, the prepared carbons presented a well dispersion of the carbon black additive (even the one prepared with 10 wt.%). The N_2 adsorption/desorption isotherms at -196 °C revealed that the samples are mainly mesoporous (as in the case of sample C-THBA-0-0 in the absence of the carbon additive); interestingly, the incorporation of the carbon black had a strong impact in the mesoporosity of the materials. The specific surface area and the total pore volume decreased significantly upon the incorporation of 10 wt.% of carbon black, although both samples still displayed a notable porous character. It is worth noticing that the decrease in the pore volumes mainly affected the microporosity, whereas the volume of mesopores remained almost the same. A summary of the main textural features is presented in Table 7.2.2.

Table 7.2.2. Summary of the textural parameters of selected samples prepared in the presence of carbon black additive.

Material	S_{BET} (m^2/g)	V_{PORES}[a] (cm^3/g)	$V_{MICRO\ N2}$[b] (cm^3/g)	$V_{MESO\ N2}$[c] (cm^3/g)
C-THBA-0-0	903	0.75	0.31	0.44
C-THBA_CB-1%	714	0.71	0.25	0.43
C-THBA-CB-10%	296	0.54	0.12	0.47

[a] Evaluated at p/p0 ~ 0.99.
[b] Micropores volume evaluated from Dubinin Radushkevich equation applied to N_2 adsorption data.
[c] Mesopores volume, calculated by difference between V_{TOTAL} - $V_{MICOR\ N2\ DR}$.

• *Metal-loaded nanoporous carbons: impact of metal content*

After the successful incorporation of Au0 and Ag0 metal NPs by simultaneous photoreduction of metal salts during the photoassisted polycondensation of the monomers (chapter 6), we envisaged to extend the protocol to other precursors, synthetic conditions and metallic contents aiming to explore the impact on the dispersion of the metallic nanoparticles. For this purpose THBA, PGA, and TNA were selected as precursors. A summary of selected synthetic parameters currently under

investigation is compiled in Table 7.2.3 (nomenclature of the samples is similar to that used in chapter 6).

The textural characterizations of the materials (Table 7.2.4) showed that porous features similar to those of the corresponding counterparts of each series without metallic salts. For all the series, the surface area (S_{BET}) decreases slightly when the metal load was reduced up to 0.06 wt.%; the total pore volume remained almost at the same (or slightly higher) than the value for the nanoporous carbon without the metal.

Table 7.2.3. Summary of experimental conditions and main textural parameters of selected metal-containing carbons.

Material	Metal salt& content (wt.%)	Pyrolisis yield (wt.%)	S_{BET} (m²/g)	V_{PORES}[a] cm³/g)	$V_{MICRO N2}$[b] (cm³/g)
C-THBA-0-Ch	--	18	850	0.63	0.28
C-THBA-0-Ch-Ag_0.25	AgNO₃ (0.25 wt.%)	20	756	0.56	0.26
C-THBA-0-Ch-Ag_0.12	AgNO₃ (0.12 wt.%)	18	814	0.59	0.27
C-THBA-0-Ch-Ag_0.06	AgNO₃ (0.06 wt.%)	18	826	0.61	0.28
C-THBA-0-Ch-Au-0.25	AuBr₃ (0.25 wt.%)	19	798	0.62	0.27
C-THBA-Ch-Au_0.12	AuBr₃ (0.12 wt.%)	19	841	0.63	0.23
C-THBA-Ch-Au_0.06	AuBr₃ (0.06 wt.%)	19	840	0.64	0.27
C-PGA-0-Ch	--		559	0.89	0.20
C-PGA-0-Ch-Au_0.12	AgNO₃ (0.06 wt.%)	12	547	0.96	0.20
C-PGA-0-Ch-Au_0.06	AuBr₃ (0.06 wt.%)	12	532	0.80	0.20
C-TNA-0-Ch	--		565	0.38	0.21
C-TNA-0-Ch-Au_0.12	AgNO₃ (0.06 wt.%)	15	556	0.38	0.23
C-TNA-0-Ch-Au_0.06	AuBr₃ (0.06 wt.%)	12	548	0.35	0.20

[a] Evaluated at p/p0 ~ 0.99.
[b] Micropore volume evaluated from Dubinin Radushkevich equation applied to N_2 adsorption data.

Further characterization is planned including TEM to explore the morphology, size and distribution of the metallic nanoparticles, and well as XPS to corroborate the photoreduction of the metallic precursor and the formation of zero-valence metal nanoparticles.

• ***Utilization of tannins as natural precursors***

In the line with the development of green chemistry- based processes, the substitution of the phenolic monomers by bio-sourced polymers (e.g. polyflavonids tannins, lignine) has been reported in the literature with success [Braghiroli 2013, 2016, 2019; Saha 2014]. In this regard, in the framework of a collaboration with the group of Prof. Alain Celzard and Dr. Vanessa Fierro from Vanessa Fierro Institut Jean Lamour belonging to CNRS in Epinal (France), we have initiated the investigations on the possibility of the use of mimosa tannins (a natural and non-toxic bio-oligomer obtained from mimosa tree bark) as precursor for the development of carbon materials using photoinduced methods. This group has a large expertise in the preparation of mesoporous carbons by soft-templating methods from mimosa tannins [Braghiroli 2016; Sánchez-Sánchez 2018]. Another advantage of this natural precursor is that it is able to undergo the condensation reaction without the need to incorporate the linker (the aldehyde).

The experimental protocol followed was adapted from that used in our previous approaches to mimic the previous work of Celzard and Fierro. Briefly, ca. 2 g of mimosa tannin were dissolved in 8 or 16 mL of ethanol; 2 g of surfactant pluronic F127 dissolved in 8 or 16 mL of EtOH and added to mimosa dispersion (mass ratio MT: pluronic: EtOH of 1 1:1:4 and 1:1:8); 1 wt.% HCl was added to the pluronic solution when required. The mixture was stirred for 30 min under dark conditions; after that the reactants mixture was transferred to glass disses and irradiated for 60 and 30 minutes using two different light sources (UV-vis and simulated solar light). After that the resins were pyrolysed at 600 °C. The nomenclature of the carbon materials is C-MT-AA-X-Y, where C- refers to carbon, MT- stands for mimosa tannin; AA refers to UV or SS for simulated solar light; X stands for the MT: pluronic: EtOH ratio, i.e. 1 for diluted and 2 for concentrated conditions; Y stands for the HCl (catalyst), 0 working in the absence or H in the presence of HCl.

The pyrolysis yields were very similar for all of them from ~19 wt.% for the materials prepared under concentrated conditions (MT: pluronic: EtOH of 1 1:1:4) to ~23 wt.% for those prepared under diluted conditions (MT: pluronic: EtOH of 1 1:1:8). The evaluation of the textural features was carried out after the pyrolysis. The main textural parameters from the N_2 and CO_2 adsorption-desorption isotherms at -196 °C and 0 °C are presented in Table 7.2.4.

The samples presented type IV isotherms (Figure 7.2.1) with well-define hysteresis loops expanding in a large range of relative pressures. This confirmed the formation of porous carbon within the micro and mesopore range. Furthermore, selected samples displayed a pronounced bimodal distribution in the mesopore range, as inferred by the shape of the nitrogen adsorption

isotherms. Almost all the materials presented similar values of specific surface area (ca. 500 m^2/g) and pore volumes ranging from 0.4-0.5 cm^3/g. Only under concentrated conditions and upon illumination using simulated solar light remarkable differences were found, with an increase of both parameters (ca. 800 m^2/g and 0.65 cm^3/g).
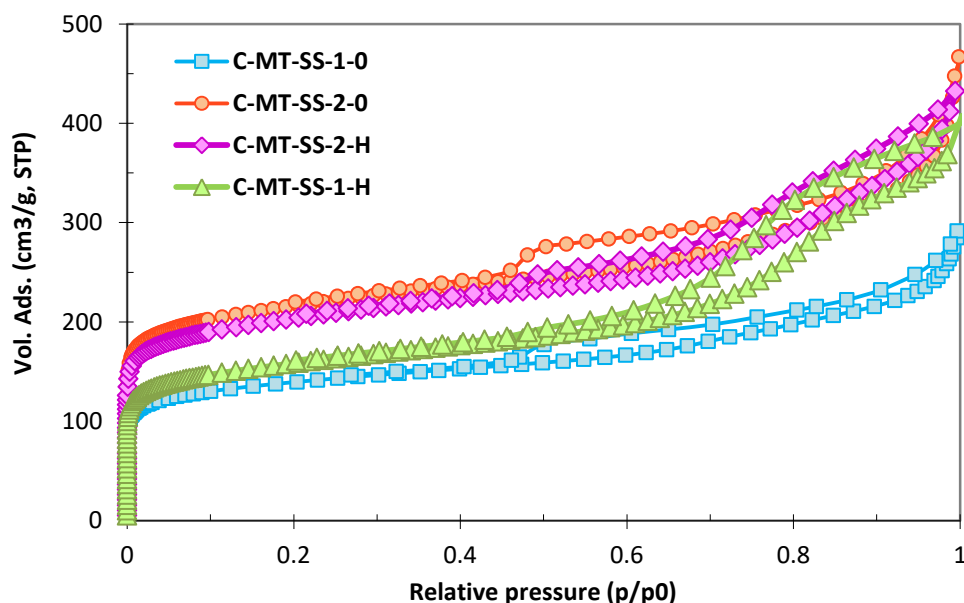
Figure 7.2.1. High resolution N_2 adsorption/desorption isotherms at -196 ºC of selected samples prepared from mimosa tannin under simulated solar light.

Table 7.2.4. Summary of the textural parameters of selected samples prepared from mimosa tannin under UV and simulated solar light.

Material	S_{BET} (m^2/g)	V_{PORES} [a] (cm^3/g)	V_{MICRO} [b] (cm^3/g)	W_{0CO2} [c] (cm^3/g)	$V_{MICRP\ N2}$ [d] (cm^3/g)	$V_{MESO\ N2}$ [d] (cm^3/g)
C-MT-UV-1-0	547	0.44	0.19	0.18	0.21	0.23
C-MT-UV-2-0	545	0.41	0.21	0.17	0.20	0.23
C-MT-UV-1-H	573	0.54	0.21	0.18	0.18	0.34
C-MT-SS-1-0	539	0.46	0.19	0.18	0.19	0.25
C-MT-SS-2-0	815	0.66	0.29	--	0.29	0.34
C-MT-SS-1-H	590	0.59	0.21	0.17	0.20	0.38
C-MT-SS-2-H	763	0.65	0.27	--	0.27	0.36

[a] Evaluated at $p/p_0 \sim 0.99$ in the N_2 adsorption isotherms at -196 °C.
[b] Micropores volume, evaluated from DR equation applied to N_2 adsorption data at -196 °C.
[c] Micropores volume, evaluated from DR equation applied to CO_2 adsorption data at 0 °C
[d] Evaluated from the 2D-NLDFT-HS method applied to N_2 adsorption data at -196 °C.

Indeed, under simulated solar light, the behavior of this precursor was very interesting. In any case, the concentrated conditions under simulated solar light clearly favored the development of the microporosity giving rise to higher specific surface areas; the use of HCl as catalyst did not seem to have a marked impact on the development of the porosity. This fact might be due to the fact that high concentration already "directs" the self-assembly of the pair MT- pluronic due to the limited solvent. However under diluted conditions (samples C-MT-SS-1-0 and C-MT-SS-1-H), the acidic pH favored the formation of a mesoporous network. Further characterization of the samples is ongoing to compare the photoinduced method with the conventional soft-templating method previously reported for mimosa tannins.

• *Elucidation of the mechanisms*

As discussed in chapter 5.4, solid state NMR characterization of the resins and the carbons has allowed to propose some hypothesis about the reactions that take place during the polycondensation of the precursors, and that are responsible for the different characteristics of the resulting carbon materials (after carbonization). Further investigations in both liquid and solid state (at different irradiations times) have been initiated for a better understanding of the mechanisms, to elucidate the formation of intermediates during the photoinduced reactions.

Studies of the phenolic resins crosslinked by glyoxal have been initiated; we expect to get information about the reaction mechanism, the position(s) of the aromatic substitution, the reactivity of glyoxal in the glyoxal-derived bridges (i.e. which reaction take places during the chain growth and hardening of the resin). According to the literature, two different linkages could be present in phenolic resins, due to the formation of the reactive methylol groups or, occasionally, dimethylene-ether (diethylene in our case). With the NMR study, we should be able to contribute to elucidate these questions.

Measurements of the ^{13}C NMR spectra of the reactant's mixture at the beginning (no light exposure) and at the end (i.e. the condensed product after irradiation) of reaction have been recorded for the different precursors (at least in duplicate). Theoretical chemical shifts from the bibliography using the spectral database for organic compounds (SDBS) and software Mestrenova NMR predictor software have been used to support the correct assignment of the signals. It has been possible to identify each different carbon signal present in the precursor's mixture before the irradiation, with a good linear correlation between the experimental values in comparison with the theoretical ones (Figure 7.2.2). Data on the system glyoxal/ethanol (solvent) in the presence and absence of HCl has allowed to observe that glyoxal exists in the equilibrium pair acetal/hemiacetal,

with no NMR evidences of C=O carbonyl group [Ramires 2010]. The hemiacetal species are dominant in acidic conditions (ratio hemiacetal/acetal around 2:1), which would seem to indicate a higher reactivity of these mixtures. Further analysis is necessary to quantify the ratio hemiacetal/acetal pairs and correlate with the polymerization extent of the resins.

ReactionMix_0min.2.1.1r
Pyrogallol+glyoxal+EtOH+HCl+PluronicF127+irradiation 0min
shim file: updated shims for glyoxal
13C 360 deg: 37.9 us <=> 100 W
MAS 4kHz

ReactionMix_180min.7.1.1r
Pyrogallol+glyoxal+EtOH+HCl+PluronicF127+irradiation 180min
shim file: updated shims for glyoxal
13C 360 deg: 37.9 us <=> 100 W
MAS 12.5kHz
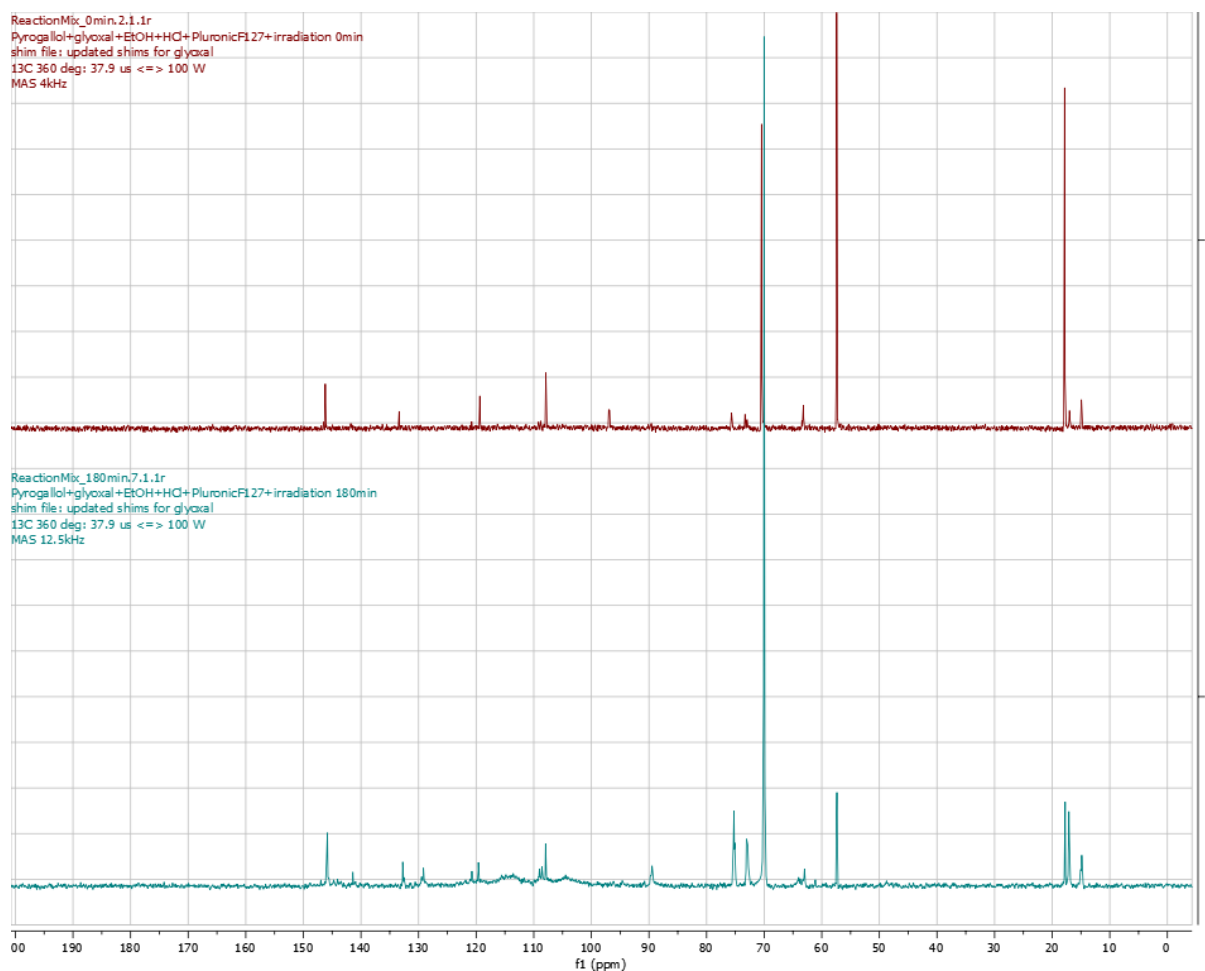
Figure 7.2.2 **[13]C** NMR spectra of the precursors mixture (i.e. before irradiation) and the photopolymerized resin.

We have also initiated kinetic studies on the polymerization of pyrogallol upon various times of light exposure. These kinetic studies will contribute to elucidate different questions about:

- Which are the most favorable substitution positions for the growth of the polymer chain?
- Detect the occurrence of different reactions during the addition of the glyoxal to the phenolic ring through the formation of ether-bridges or enolic bridges (diolic

146

crosslinking and subsequent enolic aducts) as proposed in the literature [Ramires 2010]. Our preliminary data has confirmed that the keto- enolic equilibrium does not take place in our systems (Figure 7.2.3).

- Determine how the dialdehyde reacts to connect the phenolic molecules: through only one of the carbonyl functional group, using only one carbon to connect two aromatic rings and the other remains free (e.g. acetal form) or through the two carbonyl-carbons, connecting the two rings for each of the two carbons (Figure 7.2.3).
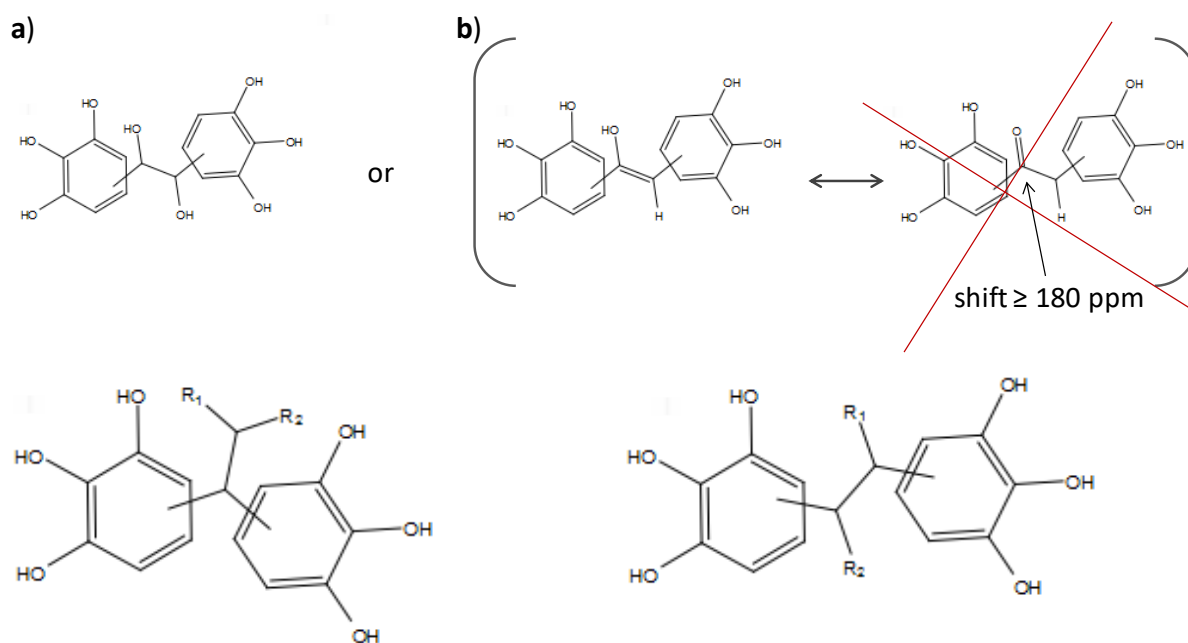
Figure 7.2.3 Structural element proposed for a (a) diolic crosslinking or (**b**) keto-enolic equilibrium; Structural elements/units proposed for glyoxal-pyrogallol binding through (c) only one carbonyl group of glyoxal and **d**) each of the two carbonyl-carbons.

Variations in the degree of reticulation as a function of different "post-synthetic" times have been investigated, to provide information about the degree/extent of reticulation. This should show us if there is any variation in terms of reticulation (bonds destroyed/formed) with time, once the solid (resin) has already formed; but also, carried out during the photopolymerization we can establish if the reaction is only photo-induced or also photo-sustained (thermal).

Comparing the spectra of the initial and final states of reaction, structural changes have been observed. For instance, the appearance/disappearance of peaks and shifts after the formation of the

hard viscous solid. In this regard, analysis of the signals at the shift of the region assigned to aromatic carbon atoms (ca. 115.5 and 104.8 ppm) allow to assign each of the new molecular bonds formed during the condensation reaction, to determine if the substitution takes place preferentially in most reactive position of the aromatic rings (e.g., -C4-6 or -C5 carbon atoms).

On the other hand, it is also necessary to study the behavior of glyoxal to understand the linkage between the polyphenolic molecules. The formation of [(OC2H5)2HC–CH(OC2H5)2] and [HC(OC2H5)(OH)–CH(OC2H5H)(OH)] species due to acetal form of glyoxal in ethanol has been detected. This information will help us to understand which is the main conformation of the glyoxal on the bridges PG-PG. For instance, the formation of a vinyl group (-CH2=CH2) between the pyrogallol molecules should give rise to a chemical shift between 100-140 ppm. On the other hand, iolic [-CH(OH)–CH(OH)-, -CH(OC2H5)–CH(OC2H5H)-], enolic [-CH=CH(OH)-] or ether [-R2HCb-CaHR1-O-R1HCa-CbHR2)] crosslinks are expected within 70 to 103 ppm [Ramires 2010].

In the carbon matrix, the broad intense signals between 100 and 145 ppm are assigned to sp2 (aromatic and olefinic) carbon atoms, and a shoulder at around 151 ppm is typically assigned to C-OH moieties in an aromatic structure. The main signal between 110 and 145 ppm can be divided into different peaks accounting for carbon atoms in various configurations (ca. 145-125 ppm accounting for substituted aromatic carbons; 113-120 ppm for unsubstituted aromatic carbons). No other peaks at higher or lower fields were observed. Qualitative information based on the intensity of the peaks corresponding to unsubstituted and substituted ring carbons can be correlated to the substituted character in the resin.

References

Agarwal V, Zetterlund PB. 2021. Strategies for reduction of graphene oxide – A comprehensive review. Chem. Eng. J. 405, 127018.

Albini A, Dichiarante V, 2009. The 'belle époque' of photochemistry†, Photochem. Photobiol. Sci., 8, 248-254.

Alexandridis P, Hatton TA. 1995. Poly(ethylene oxide)·poly(propylene oxide)·poly(ethylene oxide) block copolymer surfactants in aqueous solutions and at interfaces: thermodynamics, structure, dynamics, and modelling, Colloids Surfaces A: Physicochem. Eng. Aspects 96, 1-46.

Al-Muhtaseb SA, Ritter JA. 2003. Preparation and Properties of Resorcinol–Formaldehyde Organic and Carbon Gels. Adv Mater 15, 101–114.

Allen S, 2010. Photochemistry and Photophysics of Polymer Materials, John Wiley & Sons, Inc.

Altintig E, Arabaci G, Altundag H. 2016. Preparation and characterization of the antibacterial efficiency of silver loaded activated carbon from corncobs. Surface and Coatings Technology 304, 63–67.

Andrade M, Parra JB, Haro M, Mestre AS, Carvalho AP. 2012. Characterization of the different fractions obtained from the pyrolysis of rope industry waste. J Anal Appl Pyrol 95,31-37.

Andrew ER, Bradbury A, Eades RG. 1959. Removal of Dipolar Broadening of Nuclear Magnetic Resonance Spectra of Solids by Specimen Rotation. Nature, 183, 1802-1803.

Ania CO, Cabal B, Parra, JB, Pis, JJ. 2007. Importance of the hydrophobic character of activated carbons on the removal of naphthalene from the aqueous phase. Adsorpt. Sci. & Technol. 25, 155–167.

Ania CO. 2013. Surface Chemistry of Green Carbons, in: Rufford, T.E., Hulicova-Jurcakova, D., Zhu, J. (Eds.), Green Carbon Materials: Advances and Applications. CRC Press Taylor & Francis Group, pp. 1–33.

Ania CO, Bandosz TJ. 2006. Metal-loaded polystyrene-based activated carbons as dibenzothiophene removal media via reactive adsorption. Carbon 44, 2404, 2412.

Ania CO, Parra, JB, Pis, JJ. 2002. Effect of texture and surface chemistry on adsorptive capacities of activated carbons for phenolic compounds removal. Fuel Proc. Technol. 77–78, 337–343.

Ania CO, Raymundo-Pinero E. 2019. Nanoporous Carbons with Tuned Porosity, in K. Kaneko, F. Rodriguez-Reinoso (Eds.), Nanoporous Materials for Gas Storage, Springer, Green Energy and Technology series, pp 403.

Ania CO, Seredych M, Rodríguez-Castellón E, Bandosz TJ. 2014. Visible light driven photoelectrochemical water splitting on metal free nanoporous carbon promoted by chromophoric functional groups. Carbon 79, 432–441.

Ávila-Brande D, Arenas-Esteban D, Otero-Díaz LC, Guerrero-Martínez A, Tardajos G, Carretero-González J. 2015. Activated nanoporous carbon–gold nanoparticle composite electrode with enhanced volumetric capacitance. RSC Advances 5, 86282–86290.

Bach T, Hehn JP. 2011. Photochemical Reactions as Key Steps in Natural Product Synthesis. Angew. Chem. Int. Ed. Review 50, 1000-1045.

Balan L, Malval JP, Lougnot DJ. 2010. In situ photochemically assisted synthesis of silver nanoparticles in polymer matrixes. Silver Nanoparticles ISBN:978-953-307-028-5.

Balan L, Schneider R, Lougnot DJ. 2008. A new convenient route to polyacrylate/silver nanocomposites by light-induced cross-linking polymerization. Prog. Org. Coat. 62, 351-357.

Bandosz TJ, Jagiello J, Contescu C, Schwarz JA. 1993. Characterization of the surfaces of activated carbons in terms of their acidity constant distributions. Carbon 31, 1193–1202.

Bandosz TJ, Ania CO. 2006. Surface chemistry of activated carbons and its characterization, Ch. 4. Interface Science & Technology 7, 159–229.

Barta J, Procházková L, Vaněček V, Kuzár M, Nikl M, Čuba V. 2019. Photochemical synthesis of nano- and micro-crystalline particles in aqueous solutions, Appl. Surf. Sci. 479, 506-511.

Batisse N, Guérin K, Dubois M. 2010. Fluorination of silicon carbide thin films using pure F2 gas or XeF2. Thin Solid Films 518, 6746–6751.

Belloni J, Mostafavi M, Remita H, Marignier JL, Delcourt, MO. 1998. Radiation-induced synthesis of mono- and multi-metallic clusters and nanocolloids, New J. Chem., 22, 1239-1255.

Bergius F. 1913. Die Anwendung hoher Drücke bei chemischen Vorgängen und eine Nachbildung des Entstehungsprozesses der Steinkohle, In: Knapp W. (Ed.), Wilhelm Knapp, Halle a. d. Saale, Germany pp 41-58.

Berl E, Schmidt A, Koch H. 1932. The development of carbon. Angew. Chem, 45, 0517–0519.

Berthon S, Barbieri O, Ehrburger-Dolle F, Gerissler E, Achard P, Bley F, Pajonk GM. Pinto N, Rigacci A, Rochas C. 2001. DLS and SAXS investigations of organic gels and aerogels. J Non-Cryst Solids 285, 154–161.

Blosi M, Albonetti S, Dondi M, Martelli C, Baldi G. 2011. Microwave-assisted polyol synthesis of Cu nanoparticles. J. Nanopart. Res. 13, 127-138.

Bommier C, Xu R, Wang W, Wang X, Wen D, Lu J, Ji X. 2015. Self-activation of cellulose: a new preparation methodology for activated carbon electrodes in electrochemical capacitors. Nano Energy 13, 709-717.

Braghiroli FL, Fierro V, Pizzi A, Rode K, RAdke W, Delmotte L, Parmentier J, Celzard A. 2013. Condensation reaction of flavonoid tannins with ammonia, Ind. Crop. Prod 44, 330-335.

Braghiroli FL, Fierro V, Parmentier J, Pasc A, Celzard A. 2016. Easy and eco-friendly synthesis of ordered mesoporous carbons by self-assembly of tannin with a block copolymer, Green Chemistry 18, 3265-3271.

Braghiroli FL, Amaral-Labat G, Boss AFN, Lacoste C, Pizzi A. 2019. Tannin gels and their carbon derivatives: a review, Biomolecules 9, 587.

Braslavsky SE. 2007. Glossary of Terms Used in Photochemistry Third ed. (IUPAC recommendations 2006). Pure and Appl. Chem. 79, 293-465.

Cao L, Brasic DN, Guichard AR, Brongersma Ml. 2007. Plasmon-assisted local temperature control to pattern individual semiconductor nanowires and carbon nanotubes, Nano Lett. 7, 3523-3527.

Carriazo D, Gutiérrez MC, Ferrer ML, del Monte F. 2010. Resorcinol-based deep eutectic solvents as both carbonaceous precursors and templating agents in the synthesis of hierarchical porous carbon monoliths. Chem Mater 22, 6146–6152.

Cazorla-Amorós D, Alcañiz-Monge J, Linares-Solano A. 1996. Characterization of activated carbon fibers by CO2 adsorption. Langmuir 12, 2820–2824.

Chaikittisilp W, Ariga K, Yamauchi Y. 2013. A new family of carbon materials: synthesis of MOF-derived nanoporous carbons and their promising applications. J. Mater. Chem. A 1, 14–19.

Chatani S, Kloxin CJ, Bowman CN. 2014. The power of light in polymer science: photochemical processes to manipulate polymer formation, structure, and properties Polym. Chem. Rev. 5. 2187-2201.

Chibac A, Melinte V, Buriana T, Balan L, Buriana EC. 2012. One-pot Synthesis of phtocrosslinked sol-gel hybrid composites containin silver nanoparticles in urethane-acrylic matrixes. Chem. Eng. J. 200-202, 577-588.

Chuenchom L, Kraehnert R, Smarsly BM. 2012. Recent progress in soft-templating of porous carbon materials. Soft Matter 8, 10801–10812.

Ciamician G. 1908. Sur le Actions Chimiques de la Lumiere, Bulletin de la Société Chimique de France, IV Série, Tome III.

Ciamician G. 1912. The Photochemistry of the future, Science, 36, 385.

Cimino K, Thommes M. 2013. Colloids and Surfaces A: Physicochem. Eng. Aspects 437, 76– 89.

Contescu A, Contescu C, Putyera K, Schwarz JA. 1997. Surface acidity of carbons characterized by their continuous pK distribution and Boehm titration. Carbon 35, 83–94.

Contescu C, Jagiełło J, Schwarz, JA. 1993. Heterogeneity of Proton Binding Sites at the oxide/solution interface. Langmuir 9, 1754–1765.

Cui X, Antonietti M, Yu SH. 2006. Structural effects of iron oxide nanoparticles and iron ions on the hydrothermal carbonization of starch and rice carbohydrates. Small 2, 756–759.

Kulkarni DD, Kim S, Fedorov AG, Tsukruk VV. 2012. Light-Induced Plasmon-Assisted Phase Transformation of Carbon on Metal Nanoparticles Adv. Funct. Mater. 22, 2129–2139.

Demir-Cakan R, Baccile N, Antonietti M. 2009. Carboxylate-rich carbonaceous materials via one-step hydrothermal carbonization of glucose in the presence of acrylic acid. Chem Mater 21, 484–490.

Dinjus E, Kruse A, Troeger N. 2011. Hydrothermal carbonization. Influence of lignin in lignocelluloses. Chem Eng Technol 34, 2037–2043.

Dutra LMU, Ribeiro MENP, Cavalcante IM, Brito DHA, Semião LM, Silva RF, Fechine PBA, Yeates SG, Ricardo NMPS. 2015. Binary mixture micellar systems of F127 and P123 for griseofulvin solubilisation, Polímeros, 25(5), 433-439.

Enterría M, Figueiredo JL. 2016. Nanostructured mesoporous carbons: Tuning texture and surface chemistry, Carbon, 108, 79-102.

Eustis S, Hsu HY, El-Sayed MA. 2005. Gold nanoparticle formation from photochemical reduction of $Au3+$ by continuous excitation in colloidal solutions. A proposed molecular mechanism. J. Phys. Chem. B, 109, 4811-4815.

Eustis S, El-Sayed MA. 2006. Molecular Mechanism of the Photochemical Generation of Gold Nanoparticles in Ethylene Glycol: Support for the Disproportionation Mechanism. J. Phys. Chem. B 110, 14014-14019.

Falco C, Marco-Lozar J, Salinas-Torres D, Morallon E, Cazorla D. 2013. Tailoring the porosity of chemically activated hydrothermal carbons: influence of the precursor and hydrothermal carbonization temperature. Carbon 62, 346–355.

Fechler N, Wohlgemuth SA, Jäker P, Antonietti M. 2013. Salt and sugar: direct synthesis of high surface area carbon materials at low temperatures via hydrothermal carbonization of glucose under hypersaline conditions. J Mater Chem A 1, 9418–9421.

Ferrari AC, Robertson J. 2000. Interpretation of Raman spectra of disordered and amorphous carbon. Phys. Rev. B. 61, 14095.

Ferrari AC, Robertson J. 2004. Raman spectroscopy of amorphous, nanostructured, diamond-like carbon, and nanodiamond, Phil. Trans. Roy. Soc. Lond. 362, 2477-512.

Ferrari AC, Rodil SE, Robertson J. 2003. Interpretation of infrared and Raman spectra of amorphous carbon nitrides, J. Phys. Rev. B67, 155306-326.

Fouassier J-P. 1995. Photoinitiation, photopolymerization, and photocuring : fundamentals and applications. Hanser : Distributed by Hanser/Gardner Publications, Munich.

Fujino T, Calderon-Moreno JM, Swamy S, Hirose T, Yoshimura M. 2002. Phase and structural change of carbonized wood materials by hydrothermal treatment. Solid State Ion 151, 197-203.

Gachard E, Remita H, Khatouri J, Keita B, Nadjo L, Belloni J. 1998. Radiation-induced and chemical formation of gold clusters NewJ. Chem. 22, 1257-1265.

Galant O, Barca Donmez H, Barner-Kowollik C, Diesendruck CE. 2020. Flow Photochemistry for Single-Chain Polymer Nanoparticle Synthesis. Angew. Chem. 132, 1–6.

García-Martínez J, Cazorla-Amorós D, Linares-Solano A. 2000. Further evidence of the usefulness of CO_2 adsorption to characterize microporous solids. Stud. Surf. Sci. Catal. 128, 485–494.

Garrido J, LLinares-Solano A, Martin-Martinez JM, Molina-Sabio M, Rodriguez-Reinoso F, Torregrosa R. 1987. Use of nitrogen vs. Carbon dioxide in the characterization of activated carbons, Langmuir 3, 76-81.

Gogotsi Y, Nikitin A, Ye H, Zhou W, Fischer JE, Yi B, Foley HC, Barsoum M.W. 2003. Nanoporous carbide-derived carbon with tunable pore size. Nature Materials 2, 591–594.

Gomis Berenguer A, PhD Thesis. 2016a. Photochemical response of nanoporous carbons. Role as catalysts, photoelectrodes and additives to semiconductors. University of Alicante, Spain. http://hdl.handle.net/10045/63668

Gomis-Berenguer A, Celorrio V, Iniesta J, Fermin DJ, Ania CO. 2016b. Nanoporous carbon/WO3 anodes for an enhanced water photooxidation. Carbon 108, 471–479.

Gomis-Berenguer A, Garcia-Gonzalez R, Mestre AS, Ania CO. 2017. Designing micro- and mesoporous carbon networks by chemical activation of organic resins. Adsorption 23:303-312

Gomis-Berenguer A, Celorrio V, Iniesta J, Fermin DJ. Ania CO. 2018. Photoelectrochemical response of WO_3/nanoporous carbon anodes for photocatalytic water oxidation. C – J. Carbon Research 4, 1–14.

Gomis-Berenguer A, Elian, I, Lourenço VF, Carmona RJ, Velasco LF, Ania CO. 2019. Insights on the use of carbon additives as promoters of the visible-light photocatalytic activity of Bi2WO6. Materials 12, 1-14.

Granado L, Tavernier R, Henry S, Auke RO, Fogyer G, David G, Caillol S. 2019. Towards Sustainable Phenolic Thermosets with High thermal Performances. ACS Sust. Chem. Eng. 7, 7209-7217.

Gray H. 2009. Erratum: Powering the planet with solar fuel. Nat. Chem., 1, 112.

Guardia L, S. Villar-Rodil, J.I. Paredes, R. Rozada, A. Martínez-Alonso, J.M.D. Tascón. 2012. UV light exposure of aqueous graphene oxide suspensions to promote their direct reduction, formation of graphene–metal nanoparticle hybrids, Carbon 50, 1014-1024.

Quezada-Renteria JA, Ruiz-Garcia C, Sauvage T, Chazaro-Ruiz LF, Rangel-Mendez Jr, Ania CO, 2020. Photochemical and electrochemical reduction of graphene oxide thin films: tuning the nature of surface defects, Phys. Chem. Chem. Phys., 22, 20732-20743.

Guillot A, Stoeckli F. 2001. Reference isotherm for high pressure adsorption of CO_2 by carbons at 273 K. Carbon 39, 2059–2064.

Guo J, Morris JR, Ihm Y, Contescu CI, Gallego NC, Duscher G, Pennycook SJ, Chisholm MF. 2012. Topological Defects: Origin of Nanopores and Enhanced Adsorption Performance in Nanoporous Carbon. Small 8, 3283–3288.

Haro M, Rasines G, Macías C, Ania CO. 2011. Stability of a carbon gel electrode when used for the electro-assisted removal of ions from brackish water, Carbon 49, 3723-3730.

Hartman SR, Hahn EL. 1962. Nuclear Double Resonance in the Rotating Frame. Phys. Rev. 128, 5, 2042-2053.

Hasani A, Hamed Sharifi Dehsari, Ali Amiri Zarandi, Alireza Salehi, Faramarz Afshar Taromi, Kazeroni H. 2015. Visible Light-Assisted Photoreduction of Graphene Oxide Using CdS Nanoparticles and Gas Sensing Properties. J. Nanomaterials, Article ID 930306.

Hesse SA, Werner JG, Wiesner U. 2015. One-Pot Synthesis of Hierarchically Macro- and Mesoporous Carbon Materials with Graded Porosity. ACS Macro Letters 4, 477–482.

Hines D, Bagreev A, Bandosz TJ. 2006. Surface Properties of Porous Carbon Obtained from Polystyrene Sulfonic Acid-Based Organic Salts. Langmuir 20, 3388–3397.

Holmqvist P, Alexandridis P, Lindman B. 1997. Phase Behavior and Structure of Ternary Amphiphilic Block Copolymer-Alkanol-Water Systems: Comparison of Poly(ethylene oxide)/Poly(propylene oxide) to Poly(ethylene oxide)/Poly(tetrahydrofuran) Copolymers. Langmuir, 13, 2471-2479.

Hu B, Wang K, Wu L, Yu S-H, Antonietti M, Titirici M-M. 2010. Engineering Carbon Materials from the Hydrothermal Carbonization Process of Biomass. Advanced Materials 22, 813–828.

Isaacs Páez E, Haro M, Juárez-Pérez EJ, Carmona RJ, Parra JB, Leyva Ramos R, Ania CO. 2015. Fast synthesis of micro/mesoporous xerogels: Textural and energetic assessment. Microporous and Mesoporous Materials 209, 2–9.

IUPAC Recommendations. 1996. Glossary of terms used in photochemistry. Pure & Appl. Chem., 68 (12), 2223-2286.

Jagiello J, Olivier JP. 2013a. Carbon slit pore model incorporating surface energetical heterogeneity and geometrical corrugation, Adsorption 19, 777-783.

Jagiello J, Olivier JP. 2013b. 2D-NLDFT adsorption models for carbon slit-shaped pores with surface energetical heterogeneity and geometrical corrugation, Carbon 55, 70-80.

Jain A, Balasubramanian R, Srinivasan MP. 2016 Hydrothermal conversion of biomass waste to activated carbon with high porosity: A review. Chem Eng J 283, 789–805.

Jawhari T, Roid A, Casado J, 1995. Raman Spectroscopic Characterization of some Commercially Available Carbon Black Materials. Carbon, 33, 1561–65.

Jeon JW, Zhang L, Lutkenhaus JL. 2015. Controlling porosity in lignin-derived nanoporous carbon for supercapacitor applications. ChemSusChem 8, 428-432

Ji T, Chen L, Mu L, Yuan R, Knoblauch M, Bao FS, Zhu J. 2016. In-situ reduction of Ag nanoparticles on oxygenated mesoporous carbon fabric: Exceptional catalyst for nitroaromatics reduction. Applied Catalysis B: Environmental 182, 306–315.

Jia L, Mane GP, Anand C, Dhawale DS, Ji Q, Ariga K, Vinu A. 2012. A facile photoinduced synthesis of COOH functionalized meso-macroporous carbon filmsand their excellent sensing capability for aromatic amines, Chem. Commun. 48, 9029-9031.

Jiang H-L, Liu B, Lan Y-Q, Kuratani K, Akita T, Shioyama H, Zong F, Xu Q. 2011. From Metal–Organic Framework to Nanoporous Carbon: Toward a Very High Surface Area and Hydrogen Uptake. J. Am. Chem. Soc. 133, 11854–11857.

Jin RC, Cao YW, Mirkin CA, Kelly KL, Schatz GC, Zheng J. 2001. Photoinduced conversion of silver nanospheres to nanoprisms. Science, 294 (5548), 1901-1903.

Jin L, Zhao X, Qian X, Dong M. 2018. Nickel nanoparticles encapsulated in porous carbon and carbon nanotube hybrids from bimetallic metal-organic-frameworks for highly efficient adsorption of dyes. Journal of Colloid and Interface Science 509, 245–253.

Job N, Panariello F, Crine M. 2007. Rheological determination of the sol–gel transition during the aqueous synthesis of resorcinol-formaldehyde resins. Colloids Surf A: Physicochem Eng Aspects 293, 224–228.

Job N, Thery A, Pirard R, Marien J. 2005. Carbon aerogels, cryogels and xerogels: influence of the drying method on the textural properties of porous carbon materials. Carbon 43, 2481–2494.

Kärkäs MD, Porco JA. Stephenson CR. 2016. Photochemical Approaches to Complex Chemotypes: Applications in Natural Product Synthesis. J. Chem. Rev. 116, 9683-9747.

Khare P, Sharma A, Verma N. 2014. Synthesis of phenolic precursor-based porous carbon beads in situ dispersed with copper–silver bimetal nanoparticles for antibacterial applications. J. Colloid Interf. Sci. 418, 216–224.

Kozak DS, Sergiienko RA, Shibata E, Iizuka A, Hayasaka Y, Tsepelev VS, Nakamura T. 2017. Characterization of silver/carbon nanocomposite synthesized by non-electrolytic technique using surface plasma. Materials Chemistry and Physics 196, 288–294.

Kruk M, Celer EB, Matos J, Pikus S, Jaroniec M. 2005. Synthesis of FDU-1 silica with narrow pore size distribution and tailorable pore entrance size in the presence of sodium chloride, J. Phys. Chem. B, 109, 3838.

Kulkarni 2012. Light-Induced Plasmon-Assisted Phase Transformation of Carbon on Metal Nanoparticles Adv. Funct. Mater. 22, 2129–2139.

Kyotani T, Nagai T, Inoue S, Tomita A. 1997. Formation of New Type of Porous Carbon by Carbonization in Zeolite Nanochannels. Chem Mater 9, 609–615.

Kyotani T, Sonobe N, Tomita A. 1988. Formation of highly orientated graphite from polyacrylonitrile by using a two-dimensional space between montmorillonite lamellae. Nature 331, 331-333.

Langille MR, Personick ML, Mirkin CA.2013. Plasmon-mediated syntheses of metallic nanostructures. Angewandte Chemie Int. Ed. 2013, 52, 13910-13940.

Lee J, Kim J, Hyeon T. 2006. Recent Progress in the Synthesis of Porous Carbon Materials. Advanced Materials 18, 2073–2094.

Lewis N, Nocera D. 2006. Powering the Planet: Chemical Challenges in Solar Energy Utilization. Proc. Natl. Acad. Sci. USA, 103, 15729–15735.

Li H, Bubeck C. 2013. Photoreduction processes of graphene oxide and related applications, Macromolecular Research 21, 290–297.

Liang C, Hong K, Guiochon GA, Mays JW, Dai S. 2004. Angewandte Chimie 43(43), 5785–5789.

Liao Y-T, Chen JE, Isida Y, Yonezawa T, Chang, W-C, Alshehri SM, Yamauchi Y, Wu KC-W, 2016. De Novo Synthesis of Gold-Nanoparticle-Embedded, Nitrogen-Doped Nanoporous Carbon Nanoparticles (Au@NC) with Enhanced Reduction Ability. ChemCatChem 8, 502–509.

Libbrecht W, Verberckmoes A, Thybaut JW, Van Der Voort P, De Clercq J. 2017. Soft templated mesoporous carbons: tuning the porosity for the adsorption of large organic pollutants. Carbon 116, 528-546.

Lillo-Ródenas MA, Lozano-Castelló D, Cazorla-Amorós D. 2001. Preparation of activated carbons from Spanish anthracite: II. Activation by NaOH. Carbon 39, 751-759.

Liu L, Wang FY, Shao GA, Ma TJ, Yuan ZY. 2010. Synthesis of ultra-large mesoporous carbons from triblock copolymers and phloroglucinol/formaldehyde polymer. Carbon 48, 2660–2664.

Liu S, Zhang H, Meng X, Zhang YT, Ren L, Nawaz F, Li JH, Li Z, Xiao F-S. 2010. Ordered hexagonal mesoporous silica materials (SBA-15) with additional disordered large-mesopore networks formed by gaseous expansion, Microp. Mesop. Mater. 136, 126-131.

Liu T, Hao T, Liu J, Liou L, Liu S. 2016. Inorganic-Salts Assisted Self-Assembly of Pluronic F127-Organosilica into Ordered Mesostructures, J. Nanosci. Nanotechonol. 16, 9173-9179.

Liu J, Lu L, Wood D, Lin S. 2020. New Redox Strategies in Organic Synthesis by Means of Electrochemistry and Photochemistry ACS Central Science 6 (8), 1317-1340.

Long D, Qiao W, Zhan L, Laing X, Ling L. 2009. Effect of template and precursor chemistry on pore architectures of triblock copolymer-templated mesoporous carbons. Microp. Mesopr. Mater. 121, 58-66.

López-Salas N, Jardim EO, Silvestre-Albero A, Gutierrez MC, Ferrer ML, Ropdriguez-Reinoso F, Silvestre-Albero AJ, del Monte F. 2014. Use of eutectic mixtures for preparation of monolithic carbons with CO2 adsorption and gas-separation capabilities. Langmuir 30, 12220–12228.

Lopez-Salas N, Carriazo D, Gutierrez MC, Ferrer ML, Ania CO, Rubio F, Tamayo A, Fierro JLG, del Monte F. 2016. Tailoring the Textural Properties of Hierarchical Porous Carbons using DESs. J Mater Chem A 4, 478-489.

Lopez-Salas N, Carriazo D, Gutierrez MC, Ferrer ML, Ania CO, Rubio F, Tamayo A, Fierro JLG, del Monte F. 2017. Predicting the Suitability of Aqueous Solutions of Deep Eutectic Solvents for Preparation of Co-continuous Porous Carbons Via Spinodal Decomposition Processes, Carbon 132, 536-547.

Lowe IJ. 1959. Free Induction Decays of Rotating Solids, Phys.Rev. Lett. 2, 285-287.

Lu A-H, Schüth F. 2006. Nanocasting: A Versatile Strategy for Creating Nanostructured Porous Materials. Advanced Materials 18, 1793–1805.

Lu AH, Schuth F. 2006. Nanocasting: a versatile strategy for creating nanostructured porous materials, Adv. Mater. 18, 1793–1805.

Lukatskaya MR, Halim J, Dyatkin B, Naguib M, Buranova YS, Barsoum MW, Gogotsi Y. 2014. Room-Temperature Carbide-Derived Carbon Synthesis by Electrochemical Etching of MAX Phases. Angew Chem Int Ed 53, 4877-4880.

Ma Z, Kyotani T, Tomita A. 2000. Preparation of a high surface area microporous carbon having the structural regularity of Y zeolite. Chem Commun 0, 2365-2366.

Ma Z, Kyotani T, Tomita A. 2002. Synthesis methods for preparing microporous carbons with a structural regularity of zeolite Y. Carbon 40, 2367-2374.

Macias C, Haro M, Rasines G, Parra JB, Ania CO. 2013. Carbon-black directed synthesis of mesoporous aerogels, Carbon 63, 487-497.

Macias C, Rasines G, Garcia TE, Zafra MC, Lavela P, Tirado JL, Ania CO. 2016. Synthesis of Porous and Mechanically Compliant Carbon Aerogels Using Conductive and Structural Additives, Gels 2(1), 4.

Maciel GE, Chuang IS, Gollob L. 1984. Solid-state 13C NMR study of resol-type phenol-formaldehyde resins Macromolecules. 17, 1081-1087.

Mai Y, Eisenberg A. 2012- Self-assembly of block copolymers. Chem Soc Rev 41, 5969–5985

Marin ML, McGilvray KL, Scaiano JC. 2008. Photochemical strategies for the synthesis of gold nanoparticles from Au (II) and Au (I) using photoinduced free radical generation. J. Am. Chem. Soc. 130(49), 16572-16584.

Marsh, H., Rodríguez-Reinoso F. 2006. Activated carbon, 1. ed. ed. Elsevier, Amsterdam.

Matsuoka K, Yamagishi Y, Yamazaki T, Setoyama N, Tomita A, Kyotani T. 2005. Extremely high microporosity and sharp pore size distribution of a large surface area carbon prepared in the nanochannels of zeolite Y. Carbon 43, 876-879.

Melinte V, Chibac A, Buriana T, Hitruc G, Buriana EC. 2015. Triazene UV-triggered photogeneration of silver/gold nanoparticles in block copolymer templates. J. Nanopart. Res. 17, 422.

Meng Y, Gu Y, Zhang F, Shi Y, Yang H, Li Z, Yu C, Tu B, Zhao D. 2005. Ordered mesoporous polymers and homologous carbon frameworks: amphiphilic surfactant templating and direct transformation, Angew Chem Int Ed, 4, 44, 7053-7059.

Messner M, Walczyk DJ, Palazzo BG, Norris Z, Taylor G. 2018. Electrochemical Oxidation of Metal Carbides in Aqueous Solutions. J Electrochem Soc 165, H3107-H3114.

Morishige K, Tateishi M, Hirose F, Aramaki K. 2006. Change in desorption mechanism from pore blocking to cavitation with temperature for nitrogen in ordered silica with cagelike pores. Langmuir 22, 9220–9224.

Mulik S, Sotiriou-Leventis C, Leventis N. 2007. Time-Efficient Acid-Catalyzed Synthesis of Resorcinol–Formaldehyde Aerogels, Chem. Mater. 19, 6138–6144.

Mustatea G, Calinescu I, Diacon A, Balan L. 2014. Photoinduced siynthesis of silver/polymer nanocomposites Mat. Plastices 51, 17-21.

Nakagawa H, Watanabe K, Harada Y, Miura K. 1999. Control of micropore formation in the carbonized ion exchange resin by utilizing pillar effect. Carbon 37, 1455-1461.

Nishihara H, Kyotani T. 2012. Zeolite-Templated Carbon – Its Unique Characteristics and Applications. In: Tascon JMD (ed) Novel Carbon Adsorbents, 1st edn. Elsevier, The Netherlands, p 295-322.

Niu J. Yuan M, Chen C, Wang L, Tang Z, Fan Y, Liu X, Ma YJ, Gan Y. 2020. Berberine-Loaded Thiolated Pluronic F127 Polymeric Micelles for Improving Skin Permeation and Retention. Int. J. Nanomedicine, 15, 9987–10005.

Noah JS, Schwarz JA. 1990. Effect of HNO3 treatment on the surface acidity of activated carbon. Carbon 28, 675–682.

Noh JS, Schwarz JA. 1989. Estimation of the point of zero charge of simple and mixed oxides by mass titration. Powder Technology 130, 157–164.

Nomoto M, Fujikawa Y, Komoto T, Yamanobe, T. 2010. Structure and curing mechanism of high-ortho and random novolac resins as studied by NMR. J. Molecular Structure 976, 419-426.

O'Regan B, Grätzel M. 1991. A low-cost, high-efficiency solar cellbased on dye-sensitized colloidal TiO2 films. Nature, 353, 737–740.

Ottenbourgs B, Adriaensens P, Carleer R, Vanderzande D, Gelan J. 1998. Quantitative carbon-13 solid-state nmr and FT–Raman spectroscopy in novolac resins. Polymer 39(22), 5293–5300.

Parra JB, Ania CO, Arenillas A, Pis JJ. 2002. Textural characterization of activated carbons obtained from poly(ethylene terephthalate) by carbon dioxide activation. Studies in Surface Science and Catalysis 144, 537–543.

Parra JB, Ania CO, Arenillas A, Rubiera F, Palacios JM, Pis JJ. 2004. Textural development and hydrogen adsorption of carbon materials from PET waste. J. Alloys Comp. 79, 280–289.

Parra JB, de sousa, JC, Bansal RC, Pis JJ, Pajares JA. 1995. Characterization of activated carbons by BET equation an alternative approach. Adsorption Science and Technology 12, 50–66.

Pei L, Zhou J, Zhang L. 2013. Preparation and properties of Ag-coated activated carbon nanocomposites for indoor air quality control. Building & Envir. 63, 108–113.

Pekala RW. 1989. Organic aerogels from the polycondensation of resorcinol with formaldehyde. J. Mater. Sci. 24, 3221–3227.

Petkovich N, Stein A. 2013. Controlling macro- and mesostructures with hierarchical porosity through combined hard and soft templating. Chem Soc Rev 42, 3721–3739.

Pines A, Gibby MG, Waugg JS. 1972. A Method for High Resolution NMR of Dilute Spins in Solids. J. Chem Phys. 56, 1776.

Politano F, Oksdath-Mansilla G. 2018. Light on the horizon: Current research and future perspectives in flow photochemistry, Org. Process Res. Dev. 22, 9, 1045–1062.

Presser V, Heon M, Gogotsi Y. 2011. Carbide-Derived Carbons- From Porous Networks to Nanotubes and Graphene. Adv Funct Mater 21, 810-833.

Prier CK, Rankic DA, MacMillan DWC. 2013. Visible Light Photoredox Catalysis with Transition Metal Complexes: Applications in Organic Synthesis. Chemical Reviews, 113 (7), 5322–5363.

Pröbstle H, Schmitt C, Fricke J. 2002. Button cell supercapacitors with monolithic carbon aerogels. J Power Sources 105, 189–194.

Protti S, Dondi D, Fagnoni M, Albini A. 2007. Photochemistry in synthesis: Where, when, and why. Pure and Applied Chemistry, 79(11) 1929-1938.

Radovic LR. 2009. Active sites in graphene and the mechanism of CO2 formation in carbon oxidation. J. Am. Chem. Soc. 131 47, 17166-17175.

Radovic LR, Suarez A, Vallejos-Burgos F, Sofo JO. 2011. Oxygen migration on the graphene surface. 2. Thermochemistry of basal-plane diffusion (hopping). Carbon 49, 4226-4238.

Radovic LR, Bockrath B. 2005. On the chemical nature of graphene edges: Origin of stability and potential for magnetism in carbon materials. J. Am. Chem. Soc. 127, 5917–5927.

Radovic LR, Silva IF, Ume JI, Menéndez JA, Leon y Leon CA, Scaroni AW. 1997. An experimental and theoretical study of the adsorption of aromatics possessing electron-withdrawing and electron-donating functional groups by chemically modified activated carbons. Carbon 35, 1339–1348.

Ragucci R, Giudiciannia P, Cavalierebet A et a. 2013. Cellulose slow pyrolysis products in a pressurized steam flow reactor. Fuel 107, 122–130.

Ramamurthy V, S. Kirk, Organic, Physical, and Materials Photochemistry, CRC Press, 2000.

Ramires EC, Megiatto JD, Gardart C, Castellan A, Frollini E. 2010. Biobased composites from glyoxal-phenolic resins and sisal fibers. Bioresource Technology 101, 1998-2006.

Rasines G, Lavela P, Macias C, Tirado JL, Parra JB, Ania CO. 2015a. Mesoporous carbon black-aerogel composites with optimized properties for the electro-assisted removal of sodium chloride from brackish water. J Electroanal Chem 741, 42-50.

Rasines G, Lavel, P, Macías C, Zafra MC, Tirado JL, Parra, JB, Ania CO. 2015b. N-doped monolithic carbon aerogel electrodes with optimized features for the electrosorption of ions. Carbon 83, 262–274.

Raymundo-Piñero E, Leroux F, Béguin F. 2006. A high performance carbon for supercapacitors obtained by carbonization of a seaweed biopolymer. Adv Mater 18, 1877–1882.

Rodriguez-Reinoso F, Linares-Solano A, Molina-Sabio M, Lopez-Gonzalez JD. 1984. The two-stage air-CO$_2$ activation in the preparation of activated carbons. Characterization by gas adsorption. Adsorpt. Sci. Technol. 1, 211-222.

Rossum MV. 2005. Integrated circuits. Encyclopedia of Condensed Matter Physics Reference work. ISBN 978-0-12-369401-0.

Roucoux A, Schulz J, Patin H. 2002. Reduced transition metal colloids: a novel family of reusable catalysts. Chem Rev. 10, 3757-3778.

Rouquerol F, Rouquerol J, Sing KSW, Llewellyn P, Maurin G. 2014. Adsorption by powders and porous solids principles, methodology and applications, Second Ed. Elsevier Academic Press, Oxford, UK.

Ruiz B, Parra JB, Pajares JA. 2006. Effect of coal pre-oxidation on the optical texture and porosity of pyrolysis chars. J Anal Appl Pyrolysis 75, 27-32.

Sadezky A, Muckenhuber H, Grothe H, Niessner R, Poschl U. 2005. Raman microspectroscopy of soot and related carbonaceous materials: spectral analysis and structural information, Carbon 43, 1731-1742.

Saha D, Warren KE, Naskar AK. 2014. Soft-templated mesoporous carbons as potential materials for oral drug delivery, Carbon 71, 47-57.

Sakamoto M, Fujistuka M, Majim T. 2009. Light as a construction tool of metal nanoparticles: Synthesis and mechanism. J. Photochem. Photobiol. C: Photochem. Review 10, 33–56.

Sanderson K. 2011 Chemistry: It's not easy being green. Nature 469, 18–20.

Sanchez-Sanchez A, Izquierdo MT, Medjahdi G, Ghanbaja J, Celzard A, Fierro V. 2018. Ordered mesoporous carbons obtained by soft-templating of tannin in mild conditions, Microp. Mesop.s Mater. 270, 127-139.

Schaefer J, Stejskal OE. 1976. Carbon-13 nuclear magnetic resonance of polymers spinning at the magic angle. J. Am. Chem. Soc., 98, 1031-1032.

Schlicht S, Kireev A, Vasileva A, Grachova EV, Tunik SP, Manshina AA, Bachmann J. 2017. A model electrode of well-defined geometry prepared by direct laser-induced decoration of nanoporous templates with Au–Ag@C nanoparticles. Nanotechnology 28, 065405.

Sevilla M, Fuertes AB. 2009. Chemical and structural properties of carbonaceous products obtained by hydrothermal carbonization of saccharides. Chem Eur 15, 4195–4203.

Sevilla M, Fuertes AB. 2013. A general and facile synthesis strategy towards highly porous carbons: carbonization of organic salts. J. Mater Chem A 1, 13738–13741.

Sharmin E, Zafar F, Akram D, Alam M, Ahmad S. 2015. Recent advances in vegetable oils based environment friendly coatings: A review. Ind. Crops & Prod. 76, 215-229.

Sheng P, Li W, Tong X, Wang X. Cai Q. 2014. Development of a high performance hollow CuInSe 2 nanospheres-based photoelectrochemical cell for hydrogen evolution. J. Mater. Chem. A 2, 18974–18987.

Shukla V, Bajpai M, Singh DK, Singh M, Shukla R. 2004. Review of basic chemistry of UV - curing technology, Pigment & Resin Technol., 33, 272-279.

Sopronyi M, Felix Sima F, Vaulot C, Delmotte L, Bahouka A, Matei Ghimbeu C. 2006. Direct synthesis of graphitic mesoporous carbon from green phenolic resins exposed to subsequent UV and IR laser irradiations. Sci. Rep. 6, 39617.

Stein A, Wang Z, Fierke MA. 2009. Functionalization of Porous Carbon Materials with Designed Pore Architecture. Advanced Materials 21, 265–293.

Stephenson C. Yoon, T. 2016. Enabling Chemical Synthesis with Visible Light. Accounts of Chemical Research, 49(10), 2059–2060.

Szczurek A, Amaral-Labat G, Fierro V, Celzard A. 2011. The use of tannin to prepare carbon gels. Part I: carbon aerogels. Carbon 49, 2773–2784.

Tanaka H. 2015. Epitaxial Growth of Oxide Films and Nanostructures in Handbook of Crystal Growth: Thin Films and Epitaxy (Second Edition).

Tascón JMD (Ed.). 2012. Novel carbon adsorbents, 1. ed. ed. Elsevier, Amsterdam.

Thomberg T, Janes A, Lust E. 2010. Energy and power performance of electrochemical double-layer capacitors based on molybdenum carbide derived carbon. Electrochimica Acta 55, 3138–3143

Thommes M, Smarskly B, Groenewolt M, Ravikovitch PI, Neimark AV, 2006. Adsorption Hysteresis of Nitrogen and Argon in Pore Networks and Characterization of Novel Micro- and Mesoporous Silicas, Langmuir, 22, 756–764.

Thommes M. 2010. Physical Adsorption Characterization of Nanoporous Materials. Chemie Ing. Technik 82, 1059-1073.

Thommes M, KA Cychosz. 2014. Physical adsorption characterization of nanoporous materials: progress and challenges Adsorption 20, 233-250.

Thommes M, Kaneko K, Neimark AV, Olivier, JP, Rodriguez-Reinoso F, Rouquerol J, Sing KSW. 2015. Physisorption of gases, with special reference to the evaluation of surface area and pore size distribution (IUPAC Technical Report). Pure & Applied Chemistry 87, 1051-1069.

Titirici MM, Antonietti M. 2010. Chemistry and materials options of sustainable carbon materials made by hydrothermal carbonization. Chem Soc Rev 39, 103–116.

Titirici MM, Antonietti M, Baccile N. 2008. Hydrothermal carbon from biomass: a comparison of the local structure from poly- to monosaccharides and pentoses/hexoses. Green Chem. 10, 1204.

Trabesinger S, Juarez-Galan JM, Leis J, Rodriguez-Reinoso F. 2008. Porosity development along the synthesis of carbons from metal carbides. Micropor Mesopor Mat 113, 14-21.

Usher A, McPhail DC, Brugger J. 2009. A spectrophotometric study of aqueous Au(III) halide–hydroxide complexes at 25–80 °C. Geochim. Cosmochim. Acta 73, 3359–3380.

Vollhardt K, Schore PC, Neit E. 2007. Organic Chemistry: Structure and Function. New York: W.H, Freeman and Company.

Wang J, Kaskel S. 2012. KOH activation of carbon-based materials for energy storage, J. Mater. Chem. 22, 23710.

Wang X, Liang C, Dai S. 2008. Facile synthesis of ordered mesoporous carbons with high thermal stability by self-assembly of resorcinol-formaldehyde and block copolymers under highly acidic conditions, Langmuir 24, 7500–7505.

Wang K, Pang J, Li L, Zhou S, Li Y, Zhang T. 2018. Synthesis of hydrophobic carbon nanotubes/reduced graphene oxide composite films by flash light irradiation. Front. Chem. Sci. Eng. 12, 376–382.

Wanka G, Hoffmann H, Ulbricht W. 1994. Phase Diagrams and Aggregation Behavior of Poly(oxyethylene)-Poly(oxypropylene)-Poly(oxyethylene) Triblock Copolymers in Aqueous Solutions. Macromolecules, 27, 4145–4159.

Watanabe K, Menzel D, Nilius N, Freund H-J. 2006. Photochemistry on Metal Nanoparticles, Chem. Rev. 106, 10, 4301-4320.

Williams G, Seger B. Kamt PV, 2008. TiO2-Graphene Nanocomposites. UV-Assisted Photocatalytic Reduction of Graphene Oxide. ACS Nano 2, 7, 1487–1491.

Xia C, Shi SQ. 2016. Self-activation for activated carbon from biomass: theory and parameters. Green Chem 8, 2063-2071

Xia Y, Yang Z, Mokaya R. 2010. Templated nanoscale porous carbons. Nanoscale 2, 639–659.

Xue C, Millstone J E, Li S Y, Mirkin CA. 2008. Mechanistic study of photomediated triangular silver nanoprism growth. J. Am. Chem. Soc., 130, 8337-8344.

Yasser Mohamoud M, Attia YA, Nazer HA, Solum EJ. 2021. An Overview of Recent Development in Visible Light-mediated Organic Synthesis over Heterogeneous Photo-nanocatalysts", Current Organic Synthesis 18(1), 23-36.

Yihui D, Yanzhi S, Qingjing T, Zhenjun H, Di F, Zhennan S, Xinrong L, Xiaobo C, Yu, Bin Y. 2014. Self-assembled micelles of novel amphiphilic copolymer cholesterol-coupled F68 containing cabazitaxel as *a* drug delivery system. Int. J. Nanomedicine, 2307.

Yushin G, Nikitin A, Gogotsi Y. 2006. Carbide Derived Carbon. In Gogotsi Y (ed) Nanomaterials Handbook, CRC Press, Boca Raton, pp 237-280.

Zhai Y M, DuChene J S, Wang Y C, Qiu J J, Johnston-Peck A C, You B, Guo W X, DiCiaccio B, Qian K, Zhao E W, Ooi F, Hu D H, Su D, Stach E A, Zhu Z H, Wei W D. 2016. Polyvinylpyrrolidone-induced anisotropic growth of gold nanoprisms in plasmon-driven synthesis. Nature Materials, 15, 889-895.

Zhang P, Zhu H, Dai S. 2015. Porous Carbon Supports: Recent Advances with Various Morphologies and Compositions. ChemCatChem 7, 2788-2805.

Zhao T, Elzatahry A, Li X, Zhao D. 2019. Single-micelle-directed synthesis of mesoporous materials, Nature Rev. Mater. 4, 775–791.

Zhao J, Wu W. Sun J, Song G. 2013. Triplet photosensitizers: from molecular design to applications. Chemical Society Reviews, 42(12), 5323–51.

ANNEXES

Annex I. XPS data

Table A.I.1. Summary of atomic composition of certain metal-loaded carbons obtained from XPS analysis.

	Carbon (at.%)	Oxygen (at.%)	*Hydrogen* (at.%)
C-GA-0-0-Ag-0.25	90.9	5.9	2.4
C-GA-0-Ch-Ag-0.25	91.3	5.9	2.7
C-GA-0-0-Au-0.25	92.1	5.4	2.6
C-GA-0-Ch-Au-0.25	92.4	5.2	2.4

With Au

Figure 6. . Experimental XPS data and fitting of the C1s O1s and Au4f core level profiles under inert atmosphere of the resins after carbonization.

Figure A.I.1. XPS spectra of the Au-containing carbons of the GA series.
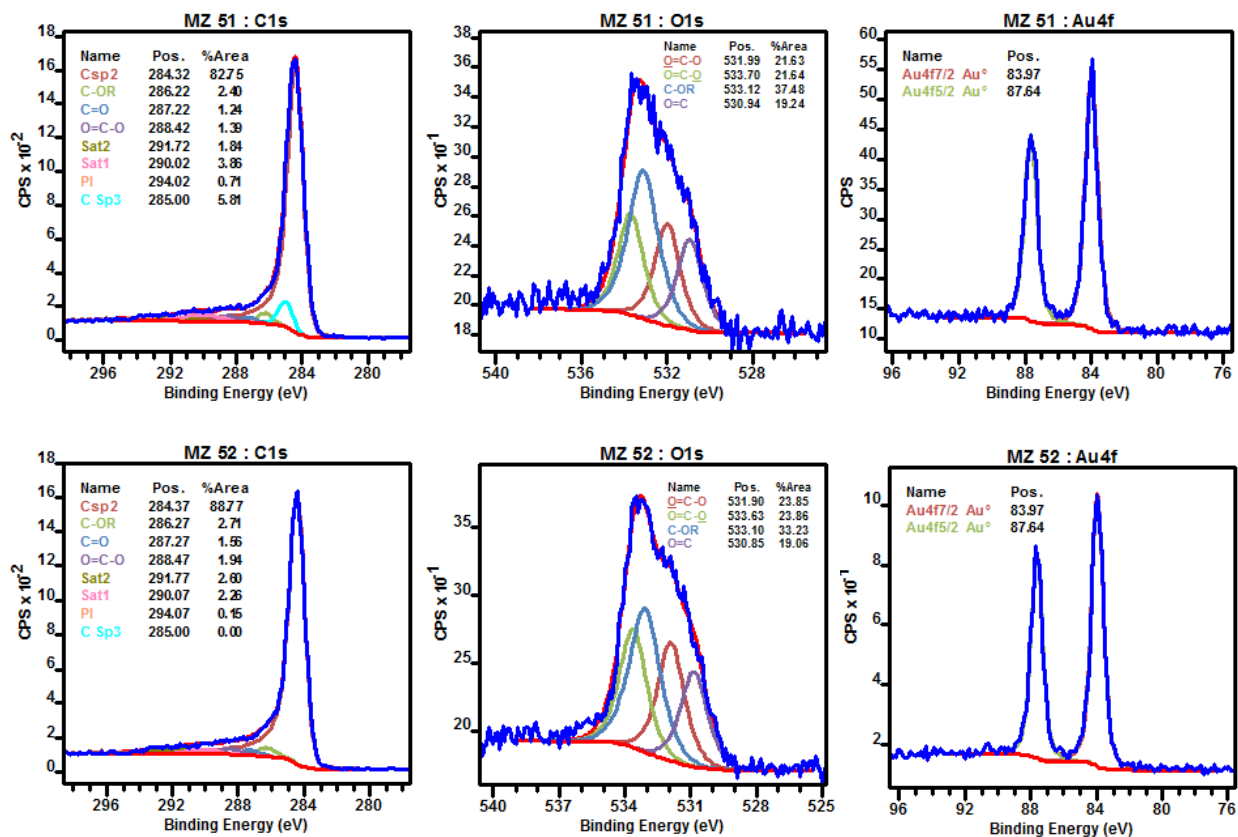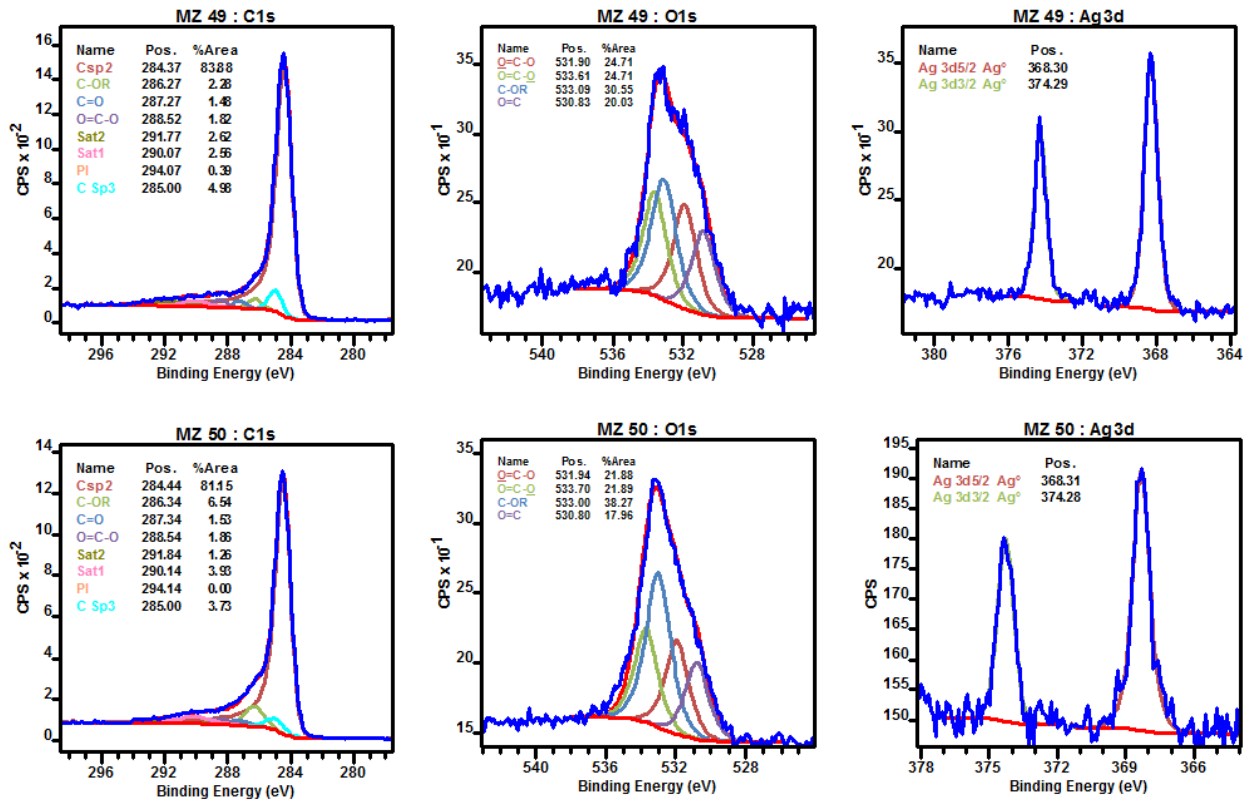
With Ag

Figure 6. . Experimental XPS data and fitting of the C1s O1s and Ag3d core level profiles under inert atmosphere of the resins after carbonization.

Figure A.I.2. XPS spectra of the Ag-containing carbons of the GA series.

Annex II. Publications

Balan L, Fernandez de Cordoba MC, Zaier M, Ania CO, A green and fast approach to nanoporous carbons with tuned porosity: UV-assisted condensation of organic compounds at room temperature, Carbon 116 (2017) 264-274.

A green and fast approach to nanoporous carbons with tuned porosity: UV-assisted condensation of organic compounds at room temperature

Lavinia Balan [a],[**], María C. Fernández de Córdoba [b], Mohamed Zaier [a], Conchi O. Ania [b],[*]

[a] CNRS Institut de Science des Matériaux de Mulhouse, UMR 7361, 15 rue Jean Starcky, 68057 Mulhouse Cedex, France
[b] Instituto Nacional del Carbon (INCAR, CSIC), 33011 Oviedo, Spain

ARTICLE INFO

ABSTRACT

This work reports a green and fast approach to the synthesis of nanoporous carbon materials based on the UV-assisted condensation of organic compounds as precursors. This new approach offers several improvements over the classical soft template and sol-gel routes for the synthesis of materials: versatility of organic precursors, shorter synthesis time, and ambient conditions. Owing to the specificity of the UV-assisted reactions mechanisms, organic compounds of varied chemical composition can be used as precursors in the preparation of nanoporous carbons with tuned porous features. The method consisted in the exposure of an aqueous solution of the organic precursors to UV light for 60 min at room temperature in the absence of a catalyst, allowing an outstanding shortening of the synthesis time compared to sol-gel routes. Furthermore, UV irradiation promoted the cross-linking of the polymer chains of precursors at room temperature, as opposed to classical methods that require an additional step at mild/ high temperatures. By changing the chemistry of the organic compound used as precursor, it was possible to modulate the surface area (from 10 to 720 m^2 g^{-1}) and the porosity of the synthesized carbons within the micro-/mesopore range. The obtained carbons also presented varied morphology depending on the precursor, from dense aggregates to ordered hexagonal arrangements of nanometric dimensions.

1. Introduction

Photochemical reactions are those caused by absorption of UV, visible of infrared radiation [1] and many of them occur in nature, such as photosynthesis in plants, human skin production of vitamin D, ozone formation and dissociation in the atmosphere, or photochemical smog (air pollution due to reaction of nitrogen oxides and some volatile organic compounds with sunlight). Most of them proceed through the formation of thermodynamically instable compounds (excited state species usually more reactive than the corresponding ground ones), allowing reactivity otherwise inaccessible by conventional methods [2−4].

In materials' chemistry, photochemical reactions are useful since many molecules and atoms are capable of undergoing chemical changes upon light absorption. Indeed, light-induced transformation of materials is a common phenomenon and the study of light-matter interactions has led to advances in several fields (heterogeneous catalysts, therapeutic applications, patterning of materials for semiconductor applications), and many ground-state reactions have also been studied (e.g. photocycloadditions, photodecarbonylations, photoenolizations, photoisomerizations, photoreductions) [2−6].

Recently, considerable efforts are being devoted to the fabrication of highly featured nanoporous carbon materials with a precise control of their physicochemical, textural and structural properties (uniformity in pore architectures, composition, particle size and shapes), due to their versatility and potential applications in multidisciplinary science and engineering fields (adsorption and separation, catalysis, sensing, energy storage [7,8]. The combination of large specific surface areas (microporosity) and pore volumes along with an adequate network of transport pores (mesopores) is most desirable to favor diffusion and/or adsorption of bulky

* Corresponding author. Current address: CEMHTI, CNRS (UPR 3079), Univ. Orléans, 45071 Orléans, France.
** Corresponding author.
E-mail addresses: lavinia.balan@uha.fr (L. Balan), conchi.ania@cnrs-orleans.fr (C.O. Ania).

molecules of strategic interest in multidisciplinary fields covering environmental remediation (e.g., hormones, pharmaceuticals, dyes), energy storage and conversion (e.g. electrocatalysis, super-capacitors) and sensing applications (e.g., immobilization of enzymes) [9,10]. In this context, the preparation of nanoporous carbons with well-defined pore architectures in the full micro-/mesopore range has become a subject of great interest. Porous carbon materials typically have relatively broad pore-size distributions, being the porosity mainly dominated by the micropore structure with classical methods showing almost no control over the porous features of the resulting carbons [11,12]. The control over the porous features of the carbons can be achieved to a certain extent by means of nanocasting procedures (soft and hard templating), self-assembling and sol-gel polycondensation reactions, among most representatives [13–16]. However, these are usually time consuming and complex reactions, therefore with quite scarce impact in the large-scale production and commercialization perspectives.

Recently, the use of light-induced reactions has become an interesting tool for the preparation and modification of carbon materials. For instance, Cao et al. showed a localized photothermal growth of carbon nanotubes and silicon nanowires on metal nanoparticles exposed to a focused light beam [17] due to the heat generated at the metallic surface plasmons exposed to irradiation. The same principle based on the light absorption properties of a metallic component has been used to induce the phase transformation of amorphous carbon deposited on nanoparticulated metal films, thereby obtaining carbon materials with enhanced electrical properties (graphitization) [18]. Vinu et al. reported the photofunctionalization of a carbon matrix with carboxylic moieties by exposing the sample to UV light and oxygen at room temperature [19]. The preparation of ordered porous carbons using phloroglucinol as precursor based on photoinduced evaporation reactions has also been reported [20] using a triblock copolymer as sacrificial template. The main advantage of the photoinduced synthesis, compared to the conventional endotemplating route (using the same precursors) is the time scale, since the aging step needed to induce the cross-linking of the polymeric precursor is significantly reduced due to the energy provided by the UV irradiation. Here, we demonstrate a fast and highly localized phase transformation of polyhydroxylated aromatic precursors on liquid phase by irradiation through condensation and spinodal decomposition of the precursor mixtures, to render aromatic resins and ultimately nanoporous carbons after a thermal treatment at 600 °C. We highlight the critical role of the polymeric precursors used in the homogenous liquid phase in bringing about a well connected network, sufficiently cross-linked to render a nanoporous carbon solid after densification of the resin. The difference in yields and porosity of the phenolic resins upon the pyrolytic treatment clearly demonstrates the role of the precursor on the photoassisted phase transformation and cross-linking of the polymers. Changes in composition, nanotexture and microstructure of the materials obtained after irradiation of the precursors were evaluated using Raman spectroscopy, solid state NMR and gas adsorption of several probes at various temperatures.

2. Experimental

2.1. Chemicals

Gallacetophenone (GA), 2,3-dihydroxynaphtalene (DN), pyrogallol (PG) and bisphenol A (BP), Pluronic F127 (poly(ethylene oxide)-block-poly(propylene oxide)-block-poly-(ethylene oxide, $PEO_{106}PPO_{70}PEO_{106}$, $Mw = 12\ 600$ Da), glyoxal aqueous solution (40%, $C_2H_2O_2$), absolute ethanol (C_2H_6O), and HCl (37%) were purchased from Sigma-Aldrich. The chemicals were used as received without any further purification.

2.2. Synthesis

GA, DN, PG and BP were selected as polymeric precursors for the photoassisted synthesis of nanoporous carbons. In a typical synthesis, the precursors (1.6 g) and the surfactant (3.2 g) were dissolved in ethanol containing HCl (37%). After complete dissolution at room temperature, a certain amount of glyoxal (1.6 mL) aqueous solution was added. Afterwards, the solutions were transferred to glass dishes and exposed to UV light for various periods (i.e., up to 70 min). The light source was a lightning cure device fitted with a 365 nm elliptical reflector. An anticaloric filter was used to avoid heating and evaporation during irradiation (monitored temperature was constant). The progress of the photoassisted reaction was monitored via UV–visible absorption spectroscopy using a Thermo Fisher Scientific Evolution 200 spectrophotometer.

The brownish viscous solids obtained after the irradiation were recovered from the dishes and further pyrolyzed at 600 °C under inert atmosphere (i.e., 120 ml/min Ar, heating rate 2°C/min, dwelling time 2 h) to allow the decomposition of the organic resins in carbon materials, and the generation of porosity. The nomenclature assigned for the resins after UV exposure is MM, where MM stands for the organic precursor (GA, PG, BP, DN); when the resins are carbonized, the nomenclature is MM-c600. To evaluate the eventual cross-linking of the organic precursors in the absence of UV light, blank reactions in were carried out for all the studied precursors (allowing the reaction to occur under darkness for several days).

2.3. Characterization techniques

The porosity of all the samples was determined by means of N_2 adsorption/desorption isotherms at -196 °C in a volumetric analyzer (Micromeritics). Before the experiments, the samples were outgassed at 120 °C for 17 h under vacuum (10^{-4} Torr). The specific surface area, S_{BET} and total pore volume, V_{total}, were calculated from the N_2 adsorption data. The pore size distribution in the full micro-/mesopore range was calculated from the N_2 adsorption isotherms using the 2D-NLDFT-HS (www.NLDFT.com) model assuming surface heterogeneity of carbon pores [21]. This model has been validated for the characterization of nanoporous carbons with similar porous features [21–23], and was chosen following IUPAC recommendations to use advanced methods based on NLDFT for the determination of pore size distributions of nanoporous carbons, rather than BJH method that underestimates the pore size for narrow mesopores [24]. The narrow microporosity was further assessed by CO_2 adsorption isotherms at 0 °C using the Dubinin-Radushkevich (DR) equation. All the gases were supplied by Air Products with ultrahigh purity (i.e., 99.995%).

Raman spectroscopy was performed by excitation with green laser light (532 nm) in the range between 1000 and 2000 cm^{-1} (InVia Raman Microscope, equipped with a Leica microscope). The samples were scanned between 10° and 90° (2θ) at a 0.02°/12 s scan rate.

Samples were chemically characterized by elemental analysis. The determination of carbon, hydrogen and nitrogen was carried out by a LECO CHNS-932 and oxygen was measured in a LECO VTF-900 CHNS-932 microanalayzer.

The surface pH of the carbon samples was measured in an aqueous suspension containing 0.4 g of carbon sample powder added to 20 mL of distilled water. After equilibration under stirring overnight, the pH value was measured using a glass electrode.

Thermogravimetric (TG) curves of all the samples were obtained

using a Setaram instrument thermal analyzer (Labsys), under a constant argon flow (100 mL/min). From the TG curves, differential TG (DTG) curves were derived.

The materials were also analyzed by transmission electron microscopy (TEM) with a Philips CM200 instrument working at 200 kV.

X-ray photoelectron spectroscopy (XPS) analysis was performed on a VG Scienta (Uppsala, Sweden) SES 200-2 X-ray photoelectron spectrometer under ultra-high vacuum (P < 10^{-9} mbar). The spectrometer resolution at the Fermi level is about 0.4 eV. The depth analyzed extends up to about 8 nm. The monochromatized AlKα source (1486.6 eV) was operated at a power of 420 W (30 mA and 14 kV) and the spectra of dried powdered samples were acquired at a take-off angle of 90° (angle between the sample surface and photoemission direction). During acquisition, the pass energy was set to 100 eV for high-resolution and 500 eV for wide scan spectra. During the processing of the XPS spectra, energy values were referenced to the C 1s peak of adventitious carbon located at 284.6 eV. CASAXPS software (Casa Software Ltd, Teignmouth, UK, www.casaxps.com) was used for acquisition and data analysis. A Shirley-type background was subtracted from the signals. Recorded spectra were always fitted using Gauss–Lorentz curves, in order to determine the binding energy of the different element core levels more accurately. The error in binding energy was estimated to be ca. 0.1 eV.

Solid-state ^{13}C CP/MAS NMR spectra of the carbonized resins were recorded at room temperature on a Bruker UltraShield Avance 400 spectrometer at 100 MHz. The CPMAS ^{13}C NMR experiments were run using a Bruker 4 mm double-resonance probe head at a spinning speed of 12 kHz. The cross-polarization contact time was 1 ms with a relaxation time of 5 s. The number of transients per spectrum was set to 2000, the acquisition time to 0.034 s, and the spectral width to 18500 Hz. The chemical shift of this signal was also employed to calibrate the shift of the aromatic signal, being 132.1 ppm from tetramethylsilane, and the p/2 pulse width (8.4 ms).

3. Results and discussion

3.1. Photo-assisted synthesis

The photoassisted approach described herein involves the UV irradiation of the precursors' mixture in liquid phase. Fig. 1 shows the UV-VIS spectra of the pristine organic precursor solutions before and after UV exposure at different times (see also Electronic Supplementary Information, Figs. S1 and S2). All the initial solutions of the reactants mixture present absorption between 300 and 400 nm, hence display absorption at the wavelength of the irradiation source used for the photopolymerization reaction (i.e., 365 nm). As the mixtures were exposed to UV light, the solutions progressively darkened, indicating that photoassisted reactions have started (likely polymerization and/or photooxidation of the precursor). Furthermore, the absorbance gradually increased with the irradiation time, indicating that the light favors the self-assembling of the —OH moieties of the hydroxylated precursors and glyoxal. Also, the polymerization rate increased with light (and hence the self-assembly rate). In all the cases the solutions gradually darkened with the illumination time, being this effect less pronounced in the case of gallacetophenone (Fig. 1). Furthermore, for all the organic compounds used as precursors, the solutions underwent spinodal decomposition forming a brownish solid (resin) after 60 min. Since an anticaloric filter was used to avoid the overheating and evaporation of the solutions during UV irradiation, the solid formed after 60 min irradiation is due to the UV-assisted cross-linking of the reactants. Longer exposures (i.e., 70 min) did

not modify the mass yield or spectroscopic properties of the solutions (in terms of absorbance), thus 60 min was chosen as optimized light exposure time. The obtained solids were recovered (scratched-out) from the glass dishes and analyzed (no need for solvent evaporation or further thermopolymerization). The eventual cross-linking of the organic precursors in the absence of UV light was evaluated by allowing the reaction of the precursors mixtures in the dark for several days at room temperature. The lack of color changes in the solutions -only a slight darkening for pyrogallol due to its oxygen sensitivity and propensity for self-oxidation [25]-, and of evidences for the formation of a solid phase (Fig. S3) confirmed that the cross-linking of the precursors does not occur in the dark.

Fig. 2 shows the thermogravimetric profiles (DTG curves) under inert atmosphere of the resins retrieved after UV irradiation of the precursors, to evaluate their thermal stability. The corresponding data of the as-received precursors (before UV exposure) is shown in Fig. S4 for comparison purposes. All the samples with the exception of gallacetophenone displayed one peak in the DTG profiles; for all of them, the peak corresponding main mass loss appears at higher temperature (ca. between 300 and 400 °C) than those of their corresponding organic precursors (ca. 200–300 °C), confirming the higher stability of the resins after the photopolymerization reaction. It is important to point out that the thermal profiles of all the precursors (Fig. S4) also displayed a single weight loss (similarly to the resins), despite their different composition. This indicates that the different structural motifs (i.e., hydroxyl and ketone moieties) of the organic precursors do not give rise to multi-stepped profiles, with differences only observed in the overall decomposition temperature (i.e., thermal stability).

In the case of the resin prepared using gallacetophenone, the DTG curve shows a hump at around 250 °C; the temperature of this peak is still higher than that of the as-received organic compound (ca. below 230 °C, see Fig. S4). Interestingly, the profile of the thermal decomposition of gallacetophenone showed only one broad peak (Fig. S4), despite the two structural motifs (i.e., hydroxyl and ketone moieties) of this compound. Thus, data suggests a different polymerization mechanism in this precursor, with the matrix of the resin displaying two moieties with different thermal stability, sufficiently separated to avoid an overlapping of the signal in the thermal profile.

For all the samples the decomposition of the volatile matter is almost complete above 500 °C as the mass loss remained almost unchanged at higher temperatures, thus 600 °C was the selected temperature for the synthesis of the carbons (via densification or pyrolysis).

3.2. Carbon materials

Table 1 shows the yields of carbonization of the photopolymerized resins after the carbonization at 600 °C to obtain the carbonaceous solids. The values differ depending on the precursor, ranging from 9 wt.% in the case of the resin prepared from gallacetophenone, to 24 wt% for pyrogallol. In any case, the yields of carbonization are of the same order of magnitude of the carbonization of polysaccharides, biomass, and other similar precursors with low carbon yields [26]. If the carbon content in the solids after carbonization measured by elemental analysis is recalculated versus the amount of carbon used in the synthesis (Table 1), a clear densification is obtained for all the samples, particularly in the case of gallacetophenone and pyrogallol (suggesting a higher cross-linking degree of the organic precursors). Interestingly, gallacetophenone solution showed a less notorious darkening upon UV irradiation (Fig. 1 and Fig. S2), pointing out to differences in the cross-linking rate of the precursors. This is also in agreement with the two peaks in the DTG profile (Fig. 2A) observed for this sample,
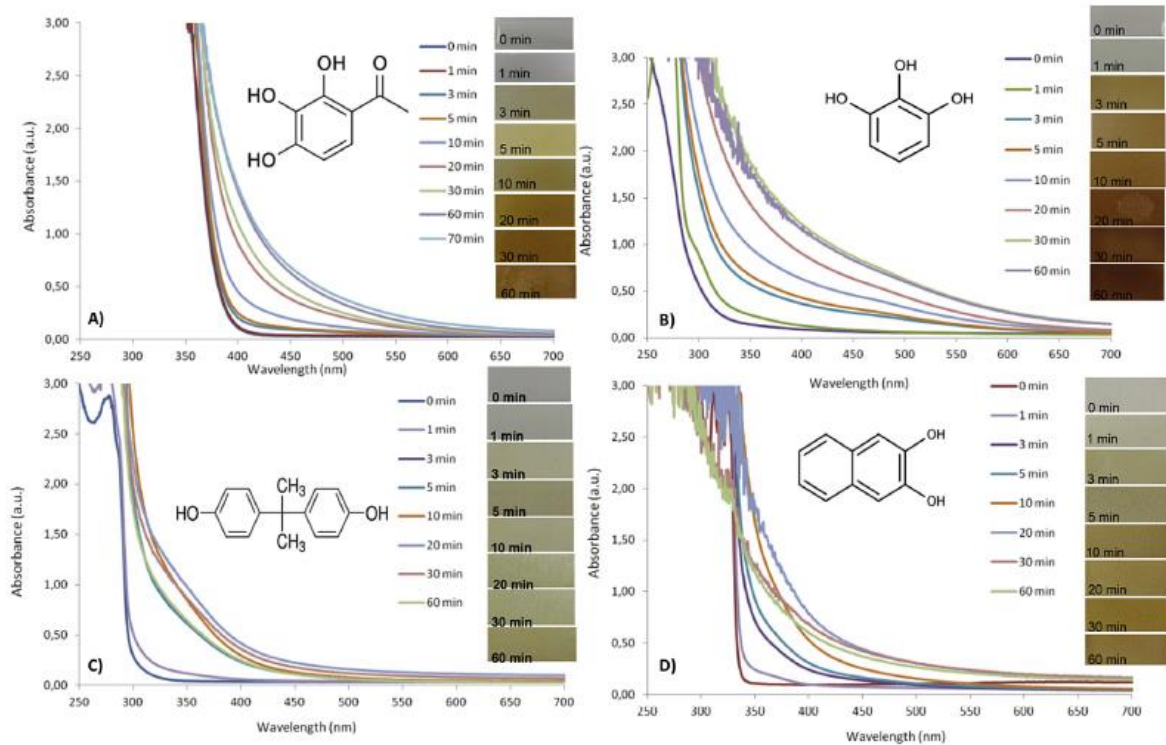
Fig. 1. Evolution of the UV-VIS spectra of the reactants mixtures with UV irradiation time for the different organic precursors: A) Gallacetophenone (GA); B) pyrogallol (PG); C) bisphenol A (BP), and D) 2,3-dihydroxynaphtalene (DN). (A colour version of this figure can be viewed online.)

suggesting that the lower cross-linking of this reactant would also affect the thermal stability of the obtained resin, in terms of lower carbonization yield. On the other hand, there is no clear correlation between the carbonization yields and other parameters such as the molecular weight of the precursors, their thermal stability (Fig. S4) or their functionalization.

The DTG curves of the solids after carbonization at 600 °C

(Fig. 2B) were quite similar for all the precursors, but significantly different from those of the photopolymerized resins. The main mass loss occurred above 600 °C and is attributed to the decomposition of volatile matter still remaining on the solids after the carbonization (since the materials were stabilized at this temperature) and/or to the decomposition of the O-surface functionalities anchored in the carbon matrix.
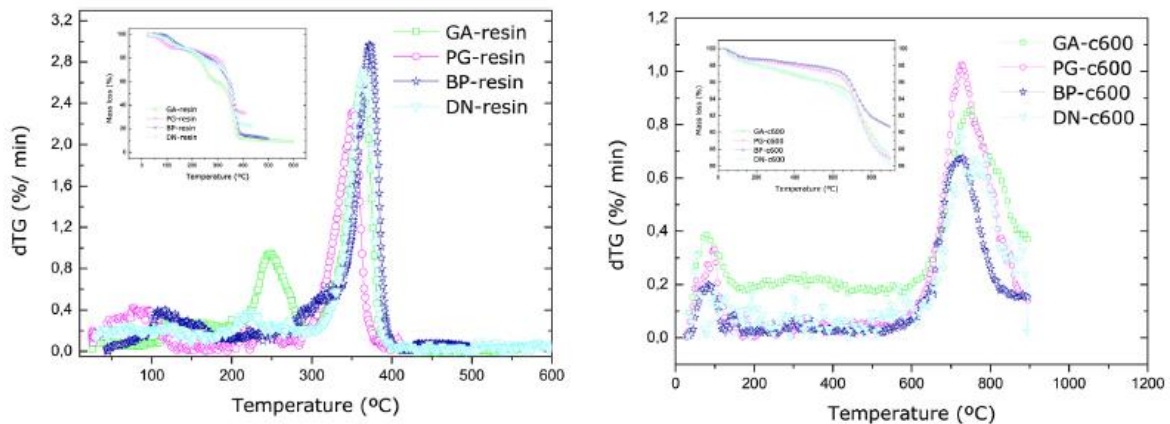
Fig. 2. Thermogravimetric profiles (DTG curves) under inter atmosphere of the photopolymerized resins before (left, series MM-resin) and after carbonization at 600 °C (right, series MM-c600). Insets show the corresponding mass losses. (A colour version of this figure can be viewed online.)

The chemical composition of the samples was analyzed by elemental analysis. The obtained materials exhibited moderate oxygen contents (Table 1), indicating the incorporation of O-groups in the carbonaceous matrix during the UV exposure and/or carbonization steps. Despite the oxygen content, the surface pH of the samples was rather basic, characteristic of hydrophobic carbon materials [27], suggesting that the oxygen is predominantly incorporated in the form of quinone, ether and/or O-bridge (groups of basic nature). Further information about the composition of the carbonized samples was obtained by XPS. The atomic concentrations of the surface elements are also provided in Table 1, and the relative distributions of the different species obtained by deconvolution of the C1s and O1s core level peaks of XPS spectra are shown in Fig. 3 (raw data and fitting of all the samples can be found in Fig. S5 and Table S1).

The amount of surface oxygen follows the trend: GA < DN < BP < PG, and the trend is similar to that obtained from elemental analysis (accounting for the oxygen content in the bulk). The results indicate a higher retention of oxygen in the samples prepared from the carbonization of GA and PG, which seems reasonable considering that both organic precursors present higher oxygen groups that are expected to be incorporated to the carbon matrix during the cross-linking reactions and/or carbonization. The C $1s$ core level spectrum was deconvoluted to various contributions (Fig. S5). The intense peak at 284.5 eV was assigned to carbon in sp^2 configurations, and the contributions at 286.3, 287.3 and 288.5 eV were assigned to phenolic and/or ether (C−OH and C−O−C), carbonyl (C=O) and carboxylic groups (O=C−O), respectively.

As seen in Fig. 3, for all the samples the majority of carbon is in C−C configurations and ca. 3−6% in oxidized forms in various oxygen environments. In addition, the O $1s$ core level broad peaks were decomposed in three contributions at 530.6−531.9 eV, 532.2−533.9 and 533.7−535 eV, assigned to carbonyl, phenol/epoxy, ether and carboxyl, water or chemisorbed oxygen species, respectively [28] (Fig. 3). The oxygen is predominantly in hydroxyl, epoxy and/or ether-like configurations, with equal distributions for all the samples. To further look into the influence of the precursor on the structure of the obtained carbons, the porosity was analyzed. The nitrogen adsorption isotherms, pore size distributions and the summary of the parameters of the pore structure are presented in Fig. 4 and Table 2, respectively.

With the exception sample BP-c600, all the samples can be considered as nanoporous materials, indicating the formation of porosity during the thermal treatment at 600 °C as a result of the decomposition of the volatile matter of the resins. It must be emphasized that no polymerization occurred when the solutions were kept in the dark at room temperature for at least 40 days. Likewise, the thermal heating of the solutions at 50 °C in the dark

for 60 min provoked the evaporation of the solvent, without evidence for the cross-linking of the precursors (Fig. S3). This observation excludes the intervention of any important effect in the dark and at room temperature. In the case of BP-c600, the N_2 uptake at −196 °C was negligible; this feature could be due to either poor textural development of this sample, or the presence of narrow micropores through which the diffusion of the gas at cryogenic temperatures is restricted. The latter was confirmed by CO_2 adsorption isotherms at 0 °C [29] (Fig. S6), using the DR method and Stoeckli-Ballerini equation to calculate the narrow micropore volume ($W_{o,CO2}$) and the average micropore size (L), respectively (Table 2).

We observed that, as a general trend, all the samples displayed similar volumes of narrow micropores with average pore sizes of ca. 0.6 nm. Thus, the porous structure of BP-c600 was composed of micropores of small dimensions not accessible to nitrogen. The rest of the samples of the series displayed high N_2 uptakes at -196 °C with important differences between them. For instance, sample DN-c600 has a type I(a) nitrogen adsorption isotherms according to the IUPAC classification [24], characteristic of microporous materials; the marked knee of the isotherm at relative pressures below 0.1 and the reversibility of the isotherm over the entire pressure range, indicates that the porosity is composed of micropores of small sizes with an almost negligible contribution of mesopores. In contrast, samples GA-c600 and PG-600 displayed type IV(b) nitrogen adsorption isotherms, and capillary condensation is accompanied in both cases by marked hysteresis loops indicating the occurrence of mesopores wider than 4 nm [30].

In the case of GA-c600, the hysteresis loop (type H2) expands over the range 0.64−0.98, with smooth almost parallel adsorption/desorption branches over the gas uptake, typically found in complex pore structures in which the desorption path is dependent on network effects (pore-blocking or cavitation induced evaporation) and thus the desorption mechanism is dictated by the pore neck size. The almost parallel adsorption/desorption branches over the gas uptake indicate a narrow range of uniform mesopores and the p/p0 of the end of the desorption branch suggests pore blocking effects (i.e., cylindrical mesopores with uniform bodies connected by narrower cylindrical necks of uniform widths). The hysteresis loop of sample PG-c600 displays a different shape expanding from ca. 0.5−0.85 (hence, the average mesopore size is smaller than for GA-c600), and the loop belongs to type H2(a) of IUPAC classification. The steep desorption branch closing the loop at relative pressures of about 0.5-the percolation threshold of N_2 at −196 °C-suggests that the mechanism of desorption from the larger mesopores is controlled by cavitation effects (i.e., the spontaneous nucleation and growth of gas bubbles in the metastable condensed fluid), where large ink-bottle mesopores have access to the external surface through narrow necks smaller than 5−6 nm) [31−33].

In such complex pore systems, the analysis of the PSD is not straightforward due to the complex pore-blocking or cavitation induced evaporation effects. In both cases, the analysis of the adsorption branch of the isotherm can be considered as a good approximation to get a realist distribution of the size of the mesopore bodies. However, in situations of pore blocking/percolation controlled evaporation (sample GA-c600), information about the size of the pore necks can be obtained from the desorption branch. On the contrary, no quantitative information about the neck size can be obtained in the case of cavitation from the analysis of the desorption branch of the N_2 isotherm, as the width of the pore size distribution would be still artificially narrow because the liquid evaporates from both the constrictions and the larger pores simultaneously [31].

Fig. 4 shows the corresponding PSD obtained from the adsorption branch of the isotherms of the samples, where the

Table 1
Carbonization yields, elemental analysis (wt.%), surface pH and surface concentration (at.%) of carbon and oxygen species obtained by XPS of the photopolymerized resins after carbonization at 600 °C.

Sample	GA-c600	PG-c600	DN-c600	BP-c600
Yield after carbonization[a] (wt.%)	9	24	18	11
Initial carbon content[b] (wt.%)	51.6	57.1	74.7	78.9
Carbon[c] (wt. %)	91.6	90.3	92.1	92.5
Oxygen[c] (wt.%)	6.1	7.4	5.0	4.7
Hydrogen[c] (wt. %)	2.3	2.4	2.9	2.8
Surface pH	9.1	8.3	7.3	8.3
Carbon[d] (at. %)	96.1	94.3	95.6	94.5
Oxygen[d] (at.%)	3.9	5.7	4.4	5.5

[a] Yield after the carbonization at 600 °C.
[b] Carbon content used in the synthesis (considering the precursor's formula).
[c] Evaluated from elemental analysis.
[d] Evaluated by fitting the C 1s and O 1s core level peaks of XPS spectra.
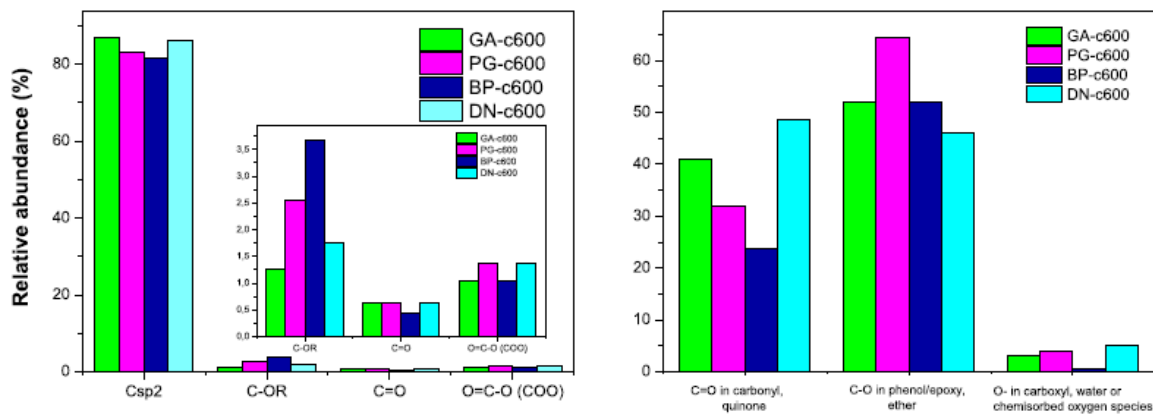
Fig. 3. Relative abundance (%) of carbon (left) and oxygen (right) species in various environments obtained by fitting the C1s and O1s and core level peaks, respectively, of the XPS spectra of the photopolymerized resins after carbonization at 600 °C. (A colour version of this figure can be viewed online.)
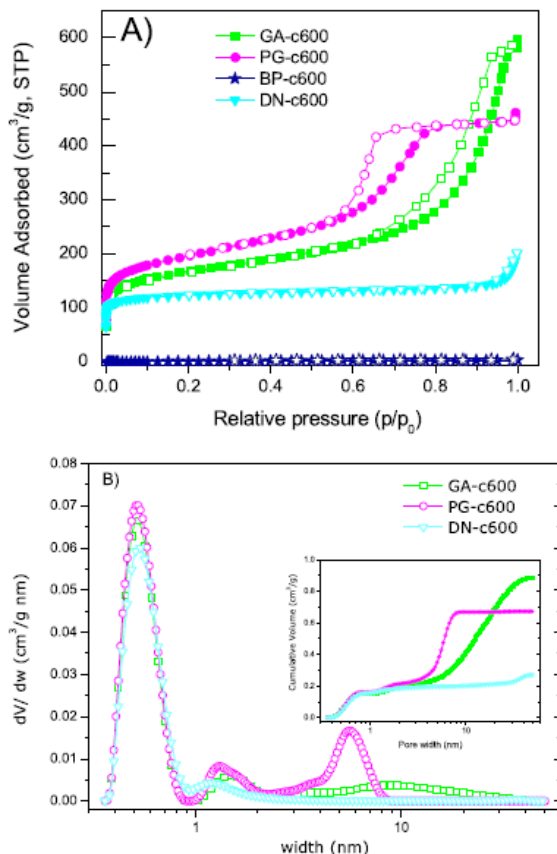

Fig. 4. (A) High resolution N_2 adsorption isotherms at −196 °C of the photo-polymerized resins after carbonization (full symbol: adsorption; empty symbol: desorption). (B) Distribution of pore sizes evaluated using the 2D-NLDFT-HS method applied to the adsorption branch of the nitrogen data (inset shows the cumulative pore volume). (A colour version of this figure can be viewed online.)

mesoporosity is cantered at about 10 and 6 nm for GA-c600 and PG-c600, respectively. The narrower distribution of mesopores of PG-c600 vs. GA-c600 and the smaller size of the pores (in average) is in excellent agreement with the analysis obtained from the observation of the gas adsorption isotherms (validating the application of the method for the assessment of the PSD). On the other hand, the analysis of the desorption branch (Fig. S7) showed the narrow distribution of PG-c600 cantered at about 5 nm, due to the cavitation effects, as opposed to the 9 nm for GA-c600 where pore blocking effects apply.

The TEM images revealed marked differences among the samples (Fig. 5). Sample BP-c600 displayed a dense structure composed of rectangular particles of nanometric dimensions, which is in agreement with the low porosity measured for this material by gas adsorption. Samples GA-c600 and DN-c600 show the typical structure of amorphous carbon materials with ill-defined aggregates in disorganized arrangement. In contrast, TEM images of sample PG-c600 showed a rather ordered pattern of well-aligned parallel channels, similar to the ordered hexagonal array of mesopores. TEM images confirmed the pore diameter of ca. 4–5 nm (and a lattice parameter of ca. 10 nm), which is in agreement with the data from N_2 adsorption. Similar textures are typically obtained for solids with long range ordering structures (such as SBA-15, CMK-3 carbons) with hexagonal symmetry [34].

The structural order of the carbons was also investigated by Raman spectroscopy (Fig. 6, Table S2) and X-ray diffraction (Fig. S8). For all the samples the Raman profiles are dominated by the characteristic D-bands and G-bands related to the sp^2 and sp^3

Table 2
Main textural parameters of the carbonized resins (series MM-c600) obtained from gas adsorption data.

Sample	S_{BET} (m^2/g)	V_{PORES}[a] (cm^3/g)	$V_{MICROPORES}$[b] (cm^3/g)	$V_{MESOPORES}$[b] (cm^3/g)	$W_{0, CO2}$[c] (cm^3/g)	L[d] (nm)
GA-c600	620	0.89	0.20	0.57	0.19	0.62
PG-c600	720	0.69	0.22	0.46	0.21	0.63
DN-c600	10	0.006	–	–	0.20	0.66
BP-c600	486	0.28	0.19	0.09	0.18	0.64

[a] Evaluated at p/p0 – 0.99.
[b] Evaluated from the 2D-NLDFT-HS method applied to N_2 adsorption data.
[c] Narrow micropores volume, evaluated from DR equation applied to CO_2 adsorption data.
[d] Evaluated using the Stoeckli-Ballerini equation applied to CO_2 adsorption data.

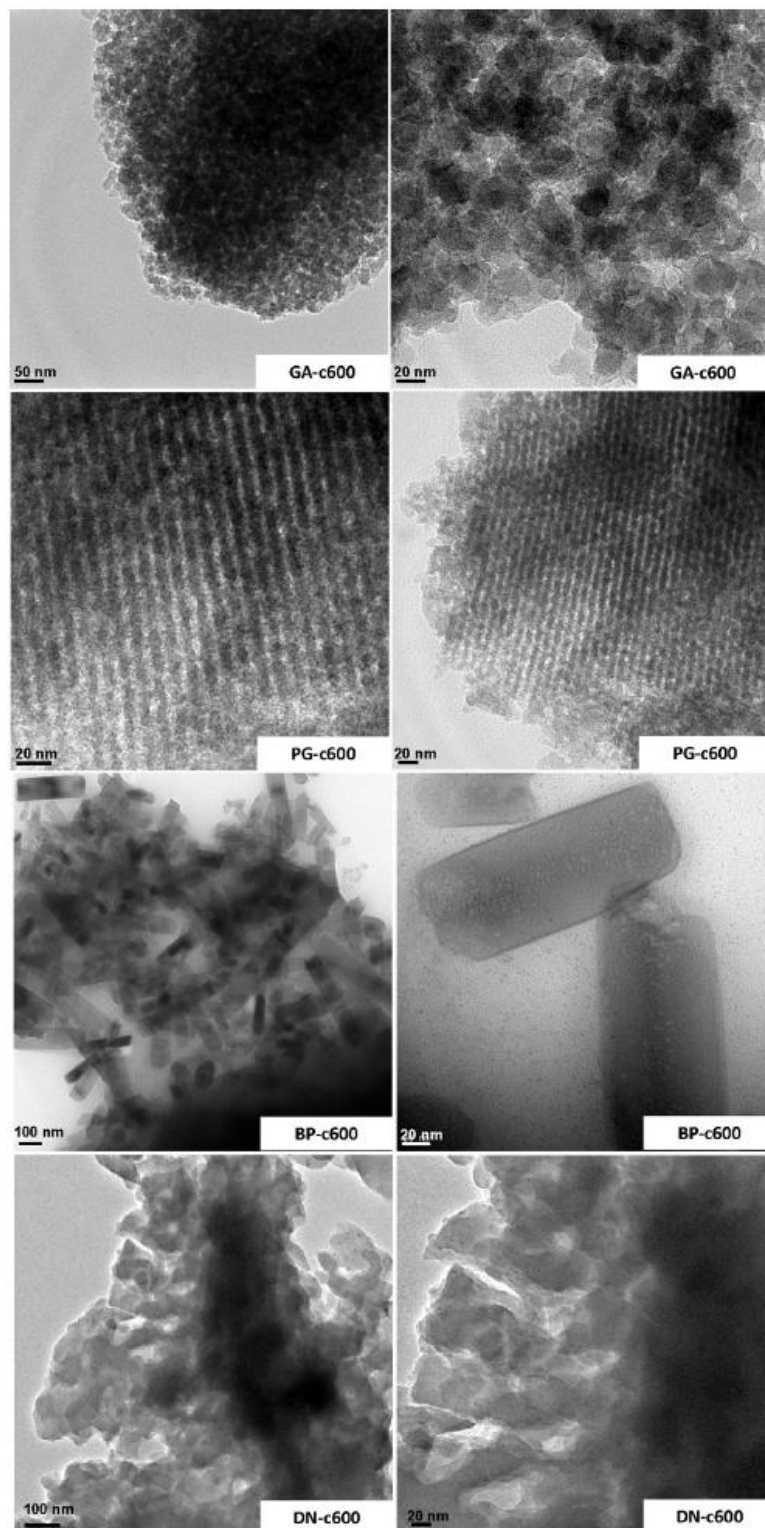270   *L. Balan et al. / Carbon 116 (2017) 264–274*

Fig. 5. TEM images of the photopolymerized resins after carbonization at 600 °C.
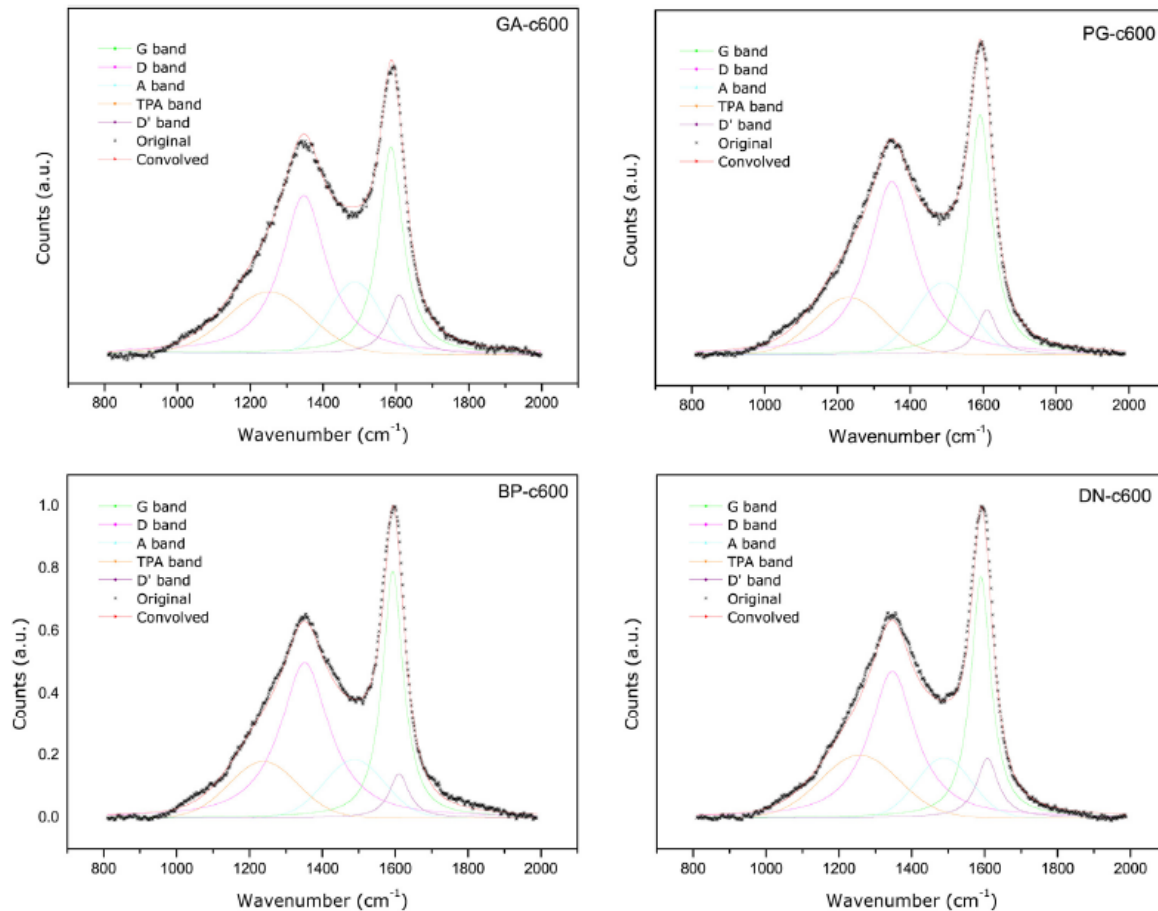
Fig. 6. Raman profiles of the photopolymerized resins after carbonization at 600 °C. (A colour version of this figure can be viewed online.)

content of carbon materials (Fig. 6). The large contribution of the D band in the spectra, indicates that the obtained materials do not present a long-range structural order, but rather features characteristic of disordered carbons [12]. The deconvolution of the first-order spectra allowed a precise evaluation of the I_G/I_D ratio as a measurement of the degree of structural ordering (Fig. 6, Table S2). The Raman spectra were deconvoluted using G, D, D', A and TPA bands as suggested in the literature for carbon materials [35–37]. The G band observed at 1585-1595 cm^{-1} is assigned to a Raman-allowed E2g resulting from 'in plane' displacement of the carbons strongly coupled in the hexagonal sheets. The position is slightly up-shifted relative to graphite (1580 cm^{-1}), as also seen for other sp^2-dominated carbons.

The D band appearing at ca. 1348 cm^{-1} is due to the lack of long range translation symmetry in disordered carbons. A careful decomposition of the spectra reveals two other additional Gaussian components. A band located at about 1500 cm^{-1} (A band) associated to sp^2-base point-like defects (single and double vacancies in non-hexagonal ring structures) in disordered carbons, and is The TPA band at 1230-50 cm^{-1} attributed to C–C and C=C stretching vibrations of polyene-like and transpolyacetylene-like structures. The variation of the I_D/I_G ratio is a measure of changes in the structural ordering of the carbon network, non-detectable by

classical powder X-ray diffraction. Samples showed I_D/I_G values following the trend (Table S2): GA-c600 (0.91) < PG-c600 (0.75) < BP-C600 (0.61) < DN-c600 (0.63), indicating the slightly higher structural order of the later. Nevertheless, all the samples showed the typical fingerprint of carbons with a rather disorganized (turbostratic) structure. This contrasts with the TEM images obtained from PG-c600 showing particles with an ordered pattern with aligned channels; this suggests that the ordered arrangement would correspond to morphological aspects of the particles (as also reported for solids with hexagonal symmetry [34]), rather than to structural order of the carbon matrix.

Useful information concerning the positions of linkage between the aromatic rings of the precursors that gave rise to the formation of the porosity of the carbons was obtained by ^{13}C NMR spectra of the samples. Data representative for PG-c600 and BP-c600 are shown in Fig. 7 (samples were selected given their differences in porosity and similarities in composition and structural order evidenced by XPS and Raman). The spectra of both samples is quite similar, showing a broad intense signal between 100 and 140 ppm corresponding to sp^2 (aromatic and olefinic) carbon and a shoulder at around 151 p.m. typical for C=C–O in an aromatic structures (furan rings or aromatic carbons bearing a hydroxyl group). The main signal between 100 and 140 ppm can be divided into different
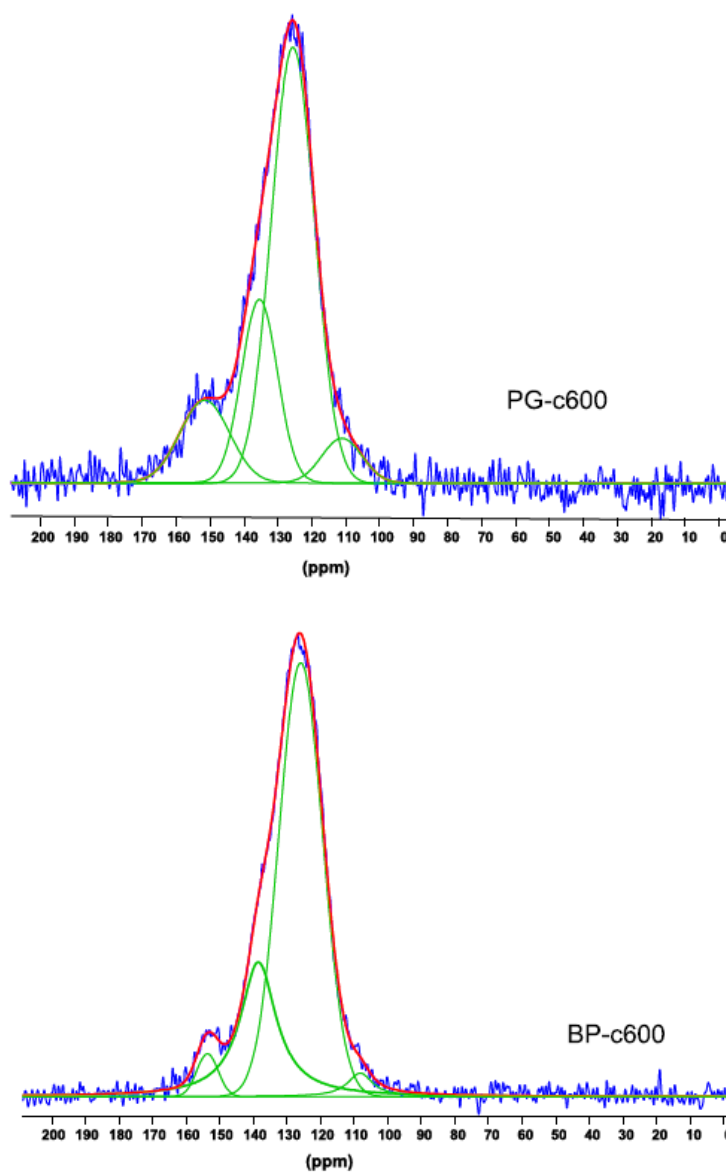
178

PG-c600

BP-c600

Fig. 7. ^{13}C solid-state NMR spectra of PG-c600 and BP-c600. (A colour version of this figure can be viewed online.)

peaks accounting for carbon atoms in various configurations: i) between 145 and 125 ppm accounting for *ortho*, *para* and *meta* substituted and aromatic carbons, and ii) between 120 and 113 for *ortho*, *para* and *meta* unsubstituted aromatic carbons (assignments are made based on the extensive data in the literature on related materials) [38,39]. No other peaks at higher fields (i.e., chemical shift below 90 ppm) were observed, indicating the negligible contributions of sp^3 +C—H moieties (e.g., aliphatic carbon).

This is in agreement with the high fraction of carbon in sp^2 configuration detected by XPS. The absence of signals around 91 ppm (assigned to unreacted glyoxal) and around 195—200 ppm (assigned to carbon in carbonyl groups, either free or directly attached to the phenol ring) also confirmed that the dialdehyde is

fully consumed during the photopolymerization. The contribution of the shoulder at 150 ppm is smaller for BP-c600 (Fig. S9), indicating a higher aromaticity of this sample (lower phenol-ring substitution). Also, the intensity corresponding to unsubstituted carbons compared to that of substituted ring carbons is relatively small for both samples, which is consistent with the highly substituted character of the resins (oxo-aromatic compounds, mainly phenol groups). The peak assigned to the resonances of unsubstituted aromatic carbons has a higher contribution for PG-c600.

Summarizing, ^{13}C solid-state NMR and gas adsorption data have revealed that the UV exposure of polyhydroxylated benzenes and glyoxal mixtures provokes the cross-linking of the reactants,

179

obtaining carbon materials with varied micro/mesoporosity depending on the aromatic precursor used. The reaction is sensitized by a colored product likely resulting from the condensation of the precursors, similar to that reported for phenolic resins [40,41]. When the precursors are mixed and exposed to UV light, intermediate species are photogenerated that are able to trigger the phenolic condensation between the precursors and glyoxal at room temperature, likely following a nucleophilic substitution between the hydroxylated compound and the dialdehdyde. The initial substitution reaction between aldehydes and hydroxylated benzenes is usually faster (in a catalyzed medium) than the subsequent condensation reaction between substituted phenol rings. The formed methylolphenols can further condense with other methylol groups to form ether linkages or with the reactive positions on the aromatic ring (unsubstituted positions *ortho* or *para* to the hydroxyl group) to form methylenebridges. Provided that there are enough reactive positions, they become cross-linked in the presence of the dialdehyde and harden to form phenol-like resins. In the case of BP, the photopolymerization occurs, but the resulting material did not show porosity (as in the case of the rest of the aromatic precursor). This could be attributed to the fact that bisphenol A displays a relatively long linear chain, that would allow a less efficient spatial packing of the colloidal aggregates, that would form dense form small clusters of branched polymeric species that would become more unstable in the nucleation regime easily undergoing spinodal decomposition. Consequently, the particles of BP-c600 show a dense structure and close porosity formed of narrow pores. In contrast, GA, PG and DN can assemble together in larger and highly cross-linked clusters, creating a more open porous structure due to the formation of clusters of larger sizes before spinodal decomposition.

Typically, heating or acidifications of the resins are used to promote the cross-linking of the network to form dense, interconnected and porous materials. One of the unique features of this photoassisted synthetic approach herein proposed is the ability to produce a variety of textural features and morphologies and the possibility to control both the structural order and pore size distributions of the obtained carbon materials operating at room temperature by using UV exposure after relatively short times (ca. 60 min of UV exposure).

4. Conclusions

We herein propose a simple and cost effective method for the synthesis of nanoporous carbon materials with varied textural and structural features based on the UV assisted condensation of organic polymeric precursors at room temperature for 60 min. Owing to the specificity of the organic precursors, they react differently upon UV exposure giving rise to resins, the carbonization of which renders nanoporous carbons of hydrophobic nature and varied porosity and morphology. By an adequate choice of the organic precursor, it is possible to control the morphology, structural order and the pore size distributions of the final carbon materials within the full micro/mesoporous range. Photolysis of polyhydroxylated benzenes and glyoxal mixtures triggers the photopolymerization of the reactants at room temperature, likely through a nucleophilic substitution mechanism, which provokes the formation of cross-linked aggregates or clusters that undergo spinodal decomposition. The degree of cross-linking of the reactant is determined by the structure (linear, cyclic) as well as the number of reactive positions (i.e., unsubstituted positions *ortho* or *para* to the hydroxyl moieties and aldehyde group) in the organic precursors. Thus, the linear structure of bisphenol A gave rise to highly branched clusters that harden to form the phenol-like resin in a dense structure with close porosity mainly composed of narrow micropores. On the other hand, the aromatic organic precursors are able to assemble in large cross-linked clusters, creating a more open structure.

One of the unique features of this photoassisted synthetic approach is the ability to produce a variety of morphologies and the possibility to control both the structural order and pore size distributions of the resulting carbon materials. The use of UV light to start the polymerization of the precursors enable to obtain a solid without the need for evaporation of solvents or further thermopolymeration (usually needed in the synthesis of phenolic resins to promote the cross-linking of the network). The future challenge is in controlling the synthesis conditions to achieve nanoporous carbon matrices in a controlled way, and to introduce surface functionalization through the incorporation of photosensitizers groups (heteroatoms and metallic doping) that could be active under different illumination conditions.

Appendix A. Supplementary data

Supplementary data related to this article can be found at http://dx.doi.org/10.1016/j.carbon.2017.01.088.

References

[1] S.E. Braslavsky, Glossary of Terms Used in Photochemistry, third ed., 2007, p. 79 (IUPAC Recommendations 2006). Pure and Applied Chemistry.
[2] J.-P. Fouassier, Photoinitiation, Photopolymerization, and Photocuring: Fundamentals and Applications, Hanser Publishers: Distributed by Hanser/Gardner Publications, Munich, 1995.
[3] V. Ramamurthy, S. Kirk, Organic, Physical, and Materials Photochemistry, CRC Press, 2000.
[4] Norman S. Allen, Photochemistry and Photophysics of Polymer Materials, John Wiley & Sons, Inc., 2010.
[5] S. Niu, R. Schneider, L. Vidal, L. Balan, Thioxanthone functionalized silver nanorods as smart photoinitiating assemblies to generate photopolymer/metal nano-objects, Nanoscale 5 (2013) 6538–6544.
[6] L. Balan, V. Melinte, T. Buruiana, R. Schneider, L. Vidal, Controlling the morphology of gold nanoparticles synthesized photochemically in a polymer matrix through photonic parameters, Nanotechnology 23 (2012) 415705.
[7] Carbon nanomaterials, in: Y. Gogotsi, V. Presser (Eds.), Advanced Materials and Technologies, second ed., CRC Press, 2013.
[8] K. Ishizaki, S. Komarneni, M. Nanko, Porous materials, in: R.G. Ford (Ed.), Materials Technology Series, vol. 4, Springer US, Boston, MA, 1998.
[9] W. Xin, Y.H. Song, Mesoporous carbons: recent advances in synthesis and typical applications, RSC Adv. 5 (2015) 83239–83285.
[10] C.D. Liang, Z.J. Li, S. Dai, Mesoporous carbon materials: synthesis and modification, Angew. Chem. Int. Ed. 47 (2008) 3696–3717.
[11] J. Wang, S. Kaskel, KOH activation of carbon-based materials for energy storage, J. Mater. Chem. 22 (2012) 23710–23725.
[12] H. Marsh, F. Rodríguez-Reinoso, Activated Carbon, Elsevier Science & Technology books, Oxford, 2006.
[13] S. Tanaka, A. Doi, N. Nakatani, Y. Katayama, Y. Miyake, Synthesis of ordered mesoporous carbon films, powders, and fibers by direct triblock-copolymer-templating method using an ethanol/water system, Carbon 47 (2009) 2688–2698.
[14] S.A. Al-Muhtaseb, J.A. Ritter, Preparation and properties of resorcinol–formaldehyde organic and carbon gels, Adv. Mater. 15 (2003) 101–114.
[15] A.-H. Lu, D. Zhao, P. O'Brien, H. Craighead, H. Kroto, Nanocasting; RSC Nanoscience & Nanotechnology, 2009. The Royal Society of Chemistry.
[16] C.J. Brinker, G.W. Scherer, Sol-gel Science: the Physics and Chemistry of Sol-gel Processing, Gulf Professional Publishing, 1990.
[17] L. Cao, D.N. Barsic, A.R. Guichard, M.L. Brongersma, Plasmon-assisted local temperature control to pattern individual semiconductor nanowires and carbon nanotubes, Nano Lett. 7 (2007) 3523–3527.
[18] D.D. Kulkarni, S. Kim, A.G. Fedorov, V.V. Tsukruk, Light-induced plasmon-assisted phase transformation of carbon on metal nanoparticles, Adv. Funct. Mater. 22 (2012) 2129–2139.
[19] L. Jia, G.P. Mane, C. Anand, D.S. Dhawale, Q. Ji, K. Ariga, A. Vinu, A facile photo-induced synthesis of COOH functionalized meso-macroporous carbon films

and their excellent sensing capability for aromatic amines, Chem. Commun. 48 (2012) 9029–9031.

[20] Patent Application BFF 14P0494 PP « Procédé de preparation de matériaux » 2014.

[21] J. Jagiello, J.P. Olivier, Carbon slit pore model incorporating surface energetical heterogeneity and geometrical corrugation, Adsorption 19 (2013) 777–783.

[22] J. Jagiello, J.P. Olivier, 2D-NLDFT adsorption models for carbon slit-shaped pores with surface energetical heterogeneity and geometrical corrugation, Carbon 55 (2013) 70–80.

[23] G. Rasines, C. Macias, M. Haro, J. Jagiello, C.O. Ania, Effects of CO_2 activation of carbon aerogels leading to ultrahigh micro-meso porosity, Microp. Mesop. Mater. 209 (2015) 18–22.

[24] M. Thommes, K. Kaneko, A.V. Neimark, J.P. Olivier, F. Rodriguez-Reinoso, J. Rouquerol, K.S.W. Sing, Physisorption of gases, with special reference to the evaluation of surface area and pore size distribution (IUPAC technical report), Pure Appl. Chem. 87 (2015) 1051–1069.

[25] Ullmann's Fine Chemical, 3 Volume Set; Wiley-VCH, John Wiley & Sons, 2014.

[26] P. Shuttleworth, A. Matharu, J.A. Clark, Polysaccharides based porous materials, Ch. 10, in: Polysaccharides Building Blocks, John Wiley and Sons, 2012, p. 271.

[27] T.J. Bandosz, C.O. Ania, Surface chemistry of activated carbons and its characterization. In interface science and technology, in: T.J. Bandosz (Ed.), Activated Carbon Surfaces in Environmental Remediation, vol. 7, Elsevier, 2006, pp. 159–229. Chapter 4.

[28] J.F. Moulder, W.F. Stickle, P.E. Sobol, K.D. Bomben, Handbook of X-Ray Photoelectron Spectroscopy: a Reference Book of Standard Spectra for Identification and Interpretation of XPS Data; Physical Electronics Division, Perkin-Elmer Corporation, 1992.

[29] J. Garrido, A. Linares-Solano, J.M. Martin-Martinez, M. Molina-Sabio, F. Rodriguez-Reinoso, R. Torregrosa, Use of nitrogen vs. Carbon dioxide in the characterization of activated carbons, Langmuir 3 (1987) 76–81.

[30] M. Thommes, K.A. Cychosz, Physical adsorption characterization of nanoporous materials: progress and challenges, Adsorption 20 (2014) 233–250.

[31] J. Landers, G.Y. Gor, A.V. Neimark, Density functional theory methods for characterization of porous materials, Colloids Surfaces A Physicochem. Eng. Aspects 437 (2013) 3–32.

[32] P.I. Ravikovitch, A.V. Neimark, Experimental confirmation of different mechanisms of evaporation from ink-bottle type pores: equilibrium, pore blocking, and cavitation, Langmuir 18 (2002) 9830–9837.

[33] P.A. Monson, Understanding adsorption/desorption hysteresis for fluids in mesoporous materials using simple molecular models and classical density functional theory, Microporous Mesoporous Mater. 160 (2012) 47–66.

[34] M. Impéror-Clerc, P. Davidson, A. Davidson, Existence of a microporous corona around the mesopores of silica-based SBA-15 materials templated by triblock copolymers, J. Am. Chem. Soc. 122 (2000) 11925–11933.

[35] C. Hu, S. Sedghi, A. Silvestre-Albero, G.G. Andersson, A. Sharma, P. Pendleton, F. Rodríguez-Reinoso, K. Kaneko, M.J. Biggs, Raman spectroscopy study of the transformation of the carbonaceous skeleton of a polymer-based nanoporous carbon along the thermal annealing pathway, Carbon 85 (2015) 147–158.

[36] J.N. Rouzaud, A. Oberlin, C. Beny-Bassez, Carbon films: structure and microtexture (optical and electron microscopy, Raman spectroscopy), Thin Solid Films 105 (1983) 75–96.

[37] M.S. Dresselhaus, A. Jorio, A.G. Souza Filho, R. Saito, Defect characterization in graphene and carbon nanotubes using Raman spectroscopy, Philos. Trans. A Math. Phys. Eng. Sci. 368 (2010) 5355.

[38] B. Ottenbourgs, P. Adriaensens, R. Carleer, D. Vanderzande, J. Gelan, Quantitative Carbon-13 solid-state N.m.r. and FT–Raman spectroscopy in novolac resins, Polymer 39 (1998) 5293–5300.

[39] G.E. Maciel, I.S. Chuang, L. Gollob, Solid-state Carbon-13 NMR study of resoltype phenol-formaldehyde resins, Macromolecules 17 (1984) 1081–1087.

[40] A. Gardziella, L.A. Pilato, A. Knop, Phenolic Resins, Springer Berlin Heidelberg, Berlin, Heidelberg, 2000.

[41] L.R.C. Barclay, M.R. Vinqvist, Phenols as antioxidants, in: Z. Rappoport (Ed.), The Chemistry of Phenols, John Wiley & Sons, Ltd, 2003, pp. 839–908.

Annex III. Communications in conferences

Oral communications (<u>Presenting author*</u>)

- <u>Fernandez de Cordoba MC</u>*, Balan L, Ania CO, Synthesis of ordered mesoporous carbons by a photoinduced strategy, CESEP 2019, Alicante (Spain), 20-24 Oct. 2019.
- Fernandez de Córdoba MC, Balan L, <u>Ania CO</u>*, Light-induced synthesis of ordered mesoporous carbons, Int. Carbon Conf. 2019, Lexington (USA) 15-19 July 2019.
- <u>Fernandez de Cordoba MC</u>*, Zaier M, Balan L, Ania CO, Synthèse de carbones mésoporeux ordonnés par une approche photoassistée, Societé Francophone des Etudes de Carbone (SFEC), Samatan (France), 23-26 April 2019.
- <u>Fernandez de Cordoba MC</u>*, Zaier M, Balan L, Ania CO, Photoassisted preparation of metal-containing nanoporous polymeric carbons, Int. Carbon Conf. 2018, Madrid (Spain), 1-6 July 2018.
- <u>Fernandez de Cordoba MC</u>*, Zaier M, Balan L, Ania CO, Carbones nanoporeux à architecture contrôlée obtenus par procedés photoassistés, Societé Francophone des Etudes de Carbone (SFEC), Obernai (France), 15-18 May 2018.
- <u>Fernandez de Cordoba MC</u>*, Zaier M, Velo-Gala I, Balan L, Ania CO, Using light to design the porosity of carbon/metal nanoassemblies, 2º Taller LatinoAmericano de Materiales de Carbono (TLMC-2), Termas de Chillan (Chile), 16-18 Nov. 2016.
- <u>Fernandez de Cordoba MC</u>*, Zaier M, Velo-Gala I, Balan L, Ania CO, Photoassisted preparation of pore controlled metal-decorated/nanoporous carbons, Reunion Iberica de Adsorcion, Evora (Portugal), 5-7 Sept. 2016.

Poster communications

- Fernandez de Cordoba MC, Ania CO, Sequential scanning of hysteresis loops in mesoporous materials, AFA 2020, Paris 30-31, Jan. 2020.
- Fernandez de Cordoba MC, Zaier M, Balan L, Ania CO, Synthesis and characterization of nanoporous carbons decorated with metal nanoparticles using room temperature photoinduced approaches, CESEP 2017, Lyon (France), 23-25 Oct 2017.
- Fernandez de Cordoba MC, Zaier M, Balan L, Ania CO, Photodesign of nanoporous carbons using metal/polymer nanoassemblies, Carbon 2016, Penn State (USA), 11-15 July 2016.

Communications in other scientific events (Presenting author*)

- <u>Fernandez de Cordoba MC</u>*, Zaier M, Balan L, Ania CO, Photodesigning the porosity and surface functionalization of nanoporous and metal-decorated carbons, Workshop "Beyond Adsorption: new perspectives and challenges for nanoporous carbons", New York City (USA), 16 Jul. 2016 (flash oral communication).
- <u>Fernandez de Cordoba MC</u>*, Balan L, Ania CO, Photoassisted Synthesis and Functionalization of Nanoporous Carbons, Journée des Doctorants et post-docs, CEMHTI-CNRS, Orléans (France), 18 Jun. 2017 (oral).
- <u>Fernandez de Cordoba MC</u>*, Balan L, Ania CO, A light-assisted process to control the pore architecture metal-carbon hybrid mesoporous materials, Journée des Doctorants et post-docs, CEMHTI-CNRS, Orléans (France), 22 Jun. 2018 (oral).
- <u>Fernandez de Cordoba MC</u>*, Balan L, Ania CO, A light-assisted process to control the pore architecture metal-carbon hybrid mesoporous materials, Journée des Doctorants et post-docs, CEMHTI-CNRS, Orléans (France), 17 Jun. 2019 (oral).

Maria COCINA FERNANDEZ DE CORBODA

Synthèse de matériaux carbonés nanoporeux

Résumé : L'objectif principal de cette thèse était d'explorer la possibilité d'utiliser des réactions photo-assistées pour préparer des carbones poreux et des nanohybrides métal/carbone. La polycondensation photoinduite par UV a été mise en œuvre pour figer les structures auto-organisées formées par certains polyphénols, capables de piéger des nanoparticules métalliques d'Ag ou d'Au. La pyrolyse de ces précurseurs organiques ouvre la voie vers des matériaux hybrides nanoporeux aux propriétés texturales et physicochimiques contrôlées. Par un choix approprié du précurseur organique et des paramètres de synthèse, il a été possible de contrôler la morphologie, l'ordre structurel et la distribution de taille des pores des matériaux carbonés finaux dans toute la gamme micro/mésoporeuse. Le degré de réticulation de la résine photopolymérisée est déterminé par la structure et par le nombre de positions réactives dans les précurseurs organiques. L'incorporation d'ions métalliques (Au^{3+}, Ag^+) au cours du processus "one-pot" a permis de réaliser simultanément la polycondensation photoassistée d'unités phénoliques et la photoréduction d'ions métalliques produisant des nanoparticules métalliques. Les matériaux obtenus contiennent des nanoparticules métalliques très dispersées dans la matrice de carbone, ce qui induit de légers changements dans la porosité, principalement dans le volume des pores et surtout dans la taille moyenne des mésopores. Des caractérisations morphologiques, texturales et physicochimiques des nouveaux nanomatériaux en carbone et hybrides métal/carbone ont également été réalisées afin d'évaluer l'influence des paramètres de synthèse sur les matériaux obtenus. Cette approche photoassistée rapide, simple et économique ouvre des perspectives intéressantes dans la synthèse de carbones poreux et de matériaux hybrides qui pourraient être utilisés, par exemple, comme photocatalyseurs dans le traitement des eaux usées et les processus d'oxydation avancés.

Mots clés : matériaux carbonés nanoporeux, nanoparticules métalliques, polycondensation photoinduite.

Photoassisted Synthesis of Nanoporous Carbon Materials

Summary: The main objective of this thesis was to explore the possibility of using photo-assisted reactions to prepare porous carbons and metal/carbon nanohybrids. Thus, UV photoinduced polycondensation was implemented to freeze the auto-organized structures formed by certain polyphenols, which are capable of trapping Ag or Au metal nanoparticles. The pyrolysis of these organic precursors opens the way to nanoporous hybrid materials with controlled textural and physicochemical properties. By the appropriate choice of the organic precursor and synthesis parameters, it was possible to control the morphology, structural order, and pore size distribution of the final carbon materials throughout the micro/mesoporous range. The degree of crosslinking of the photopolymerized resin was determined by the structure as well as the number of reactive positions in the organic precursors. The incorporation of metal ions (Au^{3+}, Ag^+) during the one-pot process allowed the simultaneous photoassisted polycondensation of phenolic units and photoreduction of metal ions yielding metal nanoparticles. The resulting materials contain highly dispersed metal nanoparticles in the carbon matrix, which induces slight changes in porosity, mainly in pore volume and especially in the average mesopore size. Morphological, textural and physicochemical characterizations of the new carbon and metal/carbon hybrid nanomaterials were also carried out in order to assess the influence of synthetic parameters on the resulting materials. This fast, simple and cost-effective photoassisted approach opens up interesting prospects in the synthesis of porous carbons and hybrid materials that could be used, for example, as photocatalysts in wastewater treatment and advanced oxidation processes.

Keywords: nanoporous carbon, metal nanoparticles, photoassisted polycondensation.